

Confinement Effects in Shallow Water Jets

*A thesis submitted to the College of Graduate Studies and Research in
partial fulfilment of the requirements for the degree of
Doctor of Philosophy
in the
Department of Mechanical Engineering
University of Saskatchewan*

by

Abdul-Monsif Shinneeb

August 2006

© Abdul-Monsif Shinneeb 2006. All rights reserved

Permission to Use

In presenting this thesis in partial fulfilment of the requirements for a postgraduate degree from the University of Saskatchewan, I agree that the libraries of this University may make it freely available for inspection. I further agree that permission for copying of this thesis in any manner, in whole or in part, for scholarly purposes may be granted by the professor who supervised my thesis work or, in their absence, by the Head of the Department or the Dean of the College in which my thesis work was done. It is understood that any copy or publication or use of this thesis or parts thereof for financial gain shall not be allowed without my written permission. It is also understood that due recognition shall be given to me and to the University of Saskatchewan in any use which may be made of any material in my thesis.

Requests for permission to copy or to make other use of material in this thesis in whole or part should be addressed to:

Head of the Department of Mechanical Engineering
University of Saskatchewan
Saskatoon, Saskatchewan S7N 5A9

ABSTRACT

The effects of vertical confinement on a neutrally-buoyant turbulent round jet discharging from a circular nozzle into quiescent shallow water were investigated. The focus was on identifying changes in the mean flow, turbulence characteristics, and large vortical structures of a horizontal water jet at different degrees of vertical confinement. The confinement resulted from the proximity of a lower solid wall and an upper free surface. The jet exit Reynolds number for all cases was 22,500. The depth of the water layer was the principal parameter. The axial and lateral confinements were negligible. Three different degrees of vertical confinement were investigated in addition to the free jet case. For the confined cases, the water layer depth was 15, 10 and 5 times the jet exit diameter. The centreline of the jet was located midway between the solid wall and the free surface. Particle image velocimetry (PIV) was used to investigate the flow behaviour. Measurements were taken on two orthogonal planes along the jet axis; one parallel and one perpendicular to the free surface. For each case, measurements were taken at three locations downstream of the jet exit where the effects of vertical confinement were expected to be significant. All image pairs were acquired at a frequency of 1 Hz using a 2048×2048 pixel camera. This rate was slow enough that the velocity fields were uncorrelated. At each location, two thousand image pairs were acquired in order to extract statistical information about the behaviour of the flow.

After completing the cross-correlation analysis of the PIV images and filtering outliers using a cellular neural network with a variable threshold, the statistical quantities such as mean velocities, turbulence intensities, Reynolds shear stress, centreline velocity decay, centreline turbulence intensities, and spread rate were obtained. The proper orthogonal decomposition (POD) technique was applied to the PIV data using *the method of snapshots* to expose vortical structures. The number of modes used for the POD reconstruction was selected to recover $\sim 40\%$ of the turbulent kinetic energy. An automated method was employed to identify the position, size, and strength of the vortices by searching for closed streamlines in the POD reconstructed velocity fields.

This step was followed by a statistical study to understand the effect of vertical confinement on the frequency of vortex occurrence, size, strength, rotational sense, and preferred locations.

The results showed that the structure of the flow underwent significant changes because of the vertical confinement. The axial velocity profiles in the vertical plane become almost uniform over the entire depth with a mild peak below the centreline of the jet for the shallowest case, while the axial velocity profiles in the horizontal plane are Gaussian but narrower than the free jet profile. The mean vertical and horizontal velocity profiles show that fluid is drawn from the sides of the jet to its centreline and then diverted upward and downward from the jet axis. The decay rate of the mean centreline velocity becomes slower at downstream locations and the jet width becomes narrower in the horizontal mid-plane compared to the free jet case. The mixing efficiency of the fluid in the vertical plane is significantly inhibited by the confinement while there is a slight effect in the horizontal plane. Also, with increasing vertical confinement, the wall jet characteristics become more dominant. Investigation of the coherent structures revealed that at intermediate distances from the exit the population of vortical structures of either rotational sense is almost identical for all vortex sizes. At downstream locations in the vertical plane, this distribution is changed by the vertical confinement which causes a significant increase in the number of small clockwise vortices. In addition, it was observed that, as the confinement increases, the total number of vortical structures decreases and their sizes increase. This is evidence of the pairing process. Moreover, with increasing confinement the circulation decreases as the flow proceeds downstream on the vertical plane with a corresponding increase in the horizontal plane. This behaviour is consistent with the turbulence intensity results.

ACKNOWLEDGEMENTS

First of all, I would like to thank God. I would like to express my sincere gratitude to my supervisors, Professor Jim D. Bugg and Professor Ram Balachandar for their support, advice, idea, and patience.

My sincere thanks go to my advisory committee members; Professors D. Bergstrom, D. Sumner, and T. Pugsley. Thanks should also go to Dave Deutcher for his technical assistance.

I gratefully acknowledge the financial support of Natural Sciences and Engineering Research Council (NSERC) of Canada. I would also like to thank the Department of Mechanical Engineering, University of Saskatchewan, for the financial support in the form of Graduate Teaching Fellowship (GTF). The assistance of the Bioinformatics Research Laboratory at the University of Saskatchewan with processing the PIV images is also gratefully acknowledged

Dedication

Dedicated to my parents, my wife, and my daughters

Table of Contents

Permission to Use	i
Abstract	ii
Acknowledgements	iv
Dedication	v
Table of Contents	vi
List of Tables	ix
List of Figures	x
Nomenclature	xvi
1 INTRODUCTION	1
1.1 GENERAL.....	1
1.2 OBJECTIVES.....	3
1.3 SCOPE OF THE PRESENT WORK.....	4
1.4 OUTLINE OF THE THESIS.....	5
2 LITERATURE REVIEW	6
2.1 INTRODUCTION.....	6
2.2 TURBULENT ROUND JET.....	8
2.2.1 Characteristics of Free Jets.....	8
2.2.2 Entrainment in Free Jets.....	14
2.3 EFFECT OF BOUNDEDNESS ON HORIZONTAL ROUND JETS.....	15
2.3.1 Free-Surface-Bounded Jets (Free-Surface Jets).....	15
2.3.2 Wall-Bounded Jets (Wall Jets).....	19
2.3.3 Wall and Free-Surface-Bounded Jets (Shallow Water Jets).....	21
2.4 COHERENT STRUCTURES.....	24
2.4.1 Coherent Structures in the Near-Exit Field of Jets.....	28
2.4.2 Coherent Structures in the Jet Far-Field.....	34

2.4.3	The Mechanism of Entrainment and Production	37
2.5	REYNOLDS NUMBER EFFECTS	38
2.6	EDUCTION OF COHERENT STRUCTURES	39
2.7	SUMMARY	42
3	EXPERIMENTAL APPARATUS AND INSTRUMENTATION	45
3.1	EXPERIMENTAL SETUP	45
3.1.1	General Remarks	45
3.1.2	Test Setup	45
3.1.3	Flowmeter Calibration	46
3.2	PARTICLE IMAGE VELOCIMETRY	48
3.2.1	General Remarks	48
3.2.2	PIV Image Acquisition	49
3.2.3	PIV Image Analysis	58
3.3	REMOVAL OF SPURIOUS VECTORS	63
3.3.1	Correlation-Based Correction (CBC) Technique	64
3.3.2	Post-Processing Analysis	65
3.4	UNCERTAINTY ANALYSIS	69
3.5	SUMMARY	76
4	IDENTIFICATION OF VORTICAL STRUCTURES	77
4.1	PRELIMINARY REMARKS	77
4.2	PROPER ORTHOGONAL DECOMPOSITION TECHNIQUE	78
4.2.1	The Direct Method	80
4.2.2	The Method of Snapshots	83
4.3	VORTEX IDENTIFICATION METHOD	85
5	RESULTS AND DISCUSSIONS	87
5.1	PRELIMINARY REMARKS	87
5.2	FREE JET CHARACTERISTICS	90
5.2.1	Jet Exit	90

5.2.2	Zone of Established Flow (ZEF).....	91
5.3	SHALLOW WATER JETS-MEAN VELOCITY FIELDS	99
5.3.1	Flow Properties along the Jet Centreline	100
5.3.2	Mean Velocity Profiles	106
5.3.3	Turbulence Profiles.....	117
5.4	SHALLOW WATER JETS-COHERENT STRUCTURES.....	139
5.4.1	Correlation between the Velocity Fields.....	139
5.4.2	Energy Content of Large-Scale Structures.....	140
5.4.3	Ensemble Size for the POD Analysis	141
5.4.4	Vortex Definition and Identification Method	143
5.4.5	Examples of POD Reconstructed Velocity Fields.....	147
5.4.6	Quantitative Investigation of Coherent Structures.....	150
6	CONCLUSIONS AND RECOMMENDATIONS	167
6.1	CONCLUSIONS.....	167
6.2	CONTRIBUTIONS	174
6.3	RECOMMENDATIONS FOR FUTURE WORK	175
	REFERENCES	177
APPENDIX A	AXIAL DEVELOPMENT OF SELECTED VELOCITY FIELDS	188
APPENDIX B	COPYRIGHT PERMISSIONS	191

LIST OF TABLES

Table		Page
2.1	Comparison of decay results for a free round jet.....	13
3.1	Characteristics of the seeding particles and the laser.....	55
3.2	Characteristics of the real and simulated images.....	73
3.3	Summary of uncertainties in the PIV data (in pixels).....	74
3.4	Error estimation in the quantities used for the exit velocity U_e calibration	75
5.1	Summary of the characteristics of the velocity fields.....	88
5.2	Number of educed structures, modes, percentage of kinetic energy contained in the modes used for the reconstruction of the velocity fields, and ratio of positive to negative vortices. The POD analysis was applied to two thousand velocity fluctuation fields for each case.....	142

LIST OF FIGURES

Figure		Page
2.1	Schematic definition of a free jet.....	9
2.2	Coherent structure cross-section in a plane mixing layer (adapted from Hussain, 1984, page 457).....	27
2.3	Plane mixing layer physics; (a) a picture of ideal ribs connecting rolls, and (b) a more realistic picture of ribs and rolls (adapted from Hussain, 1986, page 334).....	27
2.4	Dominant vortical and helical modes in axisymmetric jet flow, basic structural modes (adapted from Fiedler, 1988, page 250).....	28
2.5	Development of axisymmetric oscillations in the near-exit region of a round jet, rolling up into vortex rings, and then abruptly becoming turbulent (adapted from Van Dyke, 1982, page 60).....	29
2.6	A side view of a round free jet visualised using LIF. The arrow indicates a streamwise structure at $x/D = 3.5$ (adapted from Liepmann & Gharib, 1992, page 650).....	32
2.7	Cross-sectional images of a round free jet at $x/D = 3.25$ showing the ring and braid region (adapted from Liepmann & Gharib, 1992, page 654).....	33
3.1	Schematic description of the apparatus used to study shallow water jets..	47
3.2	Schematic of flow conditioner and jet exit.....	47
3.3	Variation of the Stokes number St in the far field of the free jet; (a) Radial profiles of St at different axial locations, and (b) St along the centerline of the jet.....	53
3.4	Generation of a light sheet with spherical and cylindrical lenses.....	56
3.5	Analysis of two typical singly-exposed PIV images.....	59
3.6	The cross-correlation function.....	61

5.1	Axial velocity and turbulence intensity profiles near the jet exit ($x/D = 0.2$). Velocities are normalised by the exit velocity (2.5 m/s) and distances by the jet exit diameter (9 mm).....	92
5.2	Decay of centreline velocity of the free jet in the axial direction. The solid line is the free jet case taken from Hussein <i>et al.</i> (1994).....	92
5.3	Variation of axial and radial turbulence intensities of the free jet along jet centreline.....	94
5.4	Spread of the present free jet along downstream distance. The solid line is the free jet case taken from Hussein <i>et al.</i> (1994).....	94
5.5	Normalised mean axial velocity profiles for a turbulent free jet in the zone of established flow (ZEF).....	96
5.6	Normalised mean radial velocity profiles for a turbulent free jet in the zone of established flow (ZEF).....	96
5.7	Normalised mean axial turbulence intensity profiles in the ZEF. The solid line is the free jet case taken from Hussein <i>et al.</i> (1994).....	98
5.8	Normalised mean radial turbulence intensity profiles in the ZEF. The solid line is the free jet case taken from Hussein <i>et al.</i> (1994).....	98
5.9	Normalised Reynolds shear stress profiles in the ZEF. The solid line is the free jet case taken from Hussein <i>et al.</i> (1994).....	99
5.10	Decay of centreline velocity of shallow water jet cases ($H/D = 15, 10,$ and 5) in the axial direction compared to the free jet.....	101
5.11	Spread of the shallow jet cases ($H/D = 15, 10,$ and 5) along downstream distance. The symbolic line represents the free jet data. The data was extracted from horizontal planes.....	101
5.12	Variation of axial turbulence intensity u_{rms}/U_c of shallow water jet cases ($H/D = 15, 10,$ and 5) along jet centreline. The symbolic line represents the free jet data.....	103
5.13	Variation of vertical turbulence intensity v_{rms}/U_c of shallow water jet cases ($H/D = 15, 10,$ and 5) along jet centreline. The symbolic line represents the free jet data.....	103

5.14	Variation of horizontal turbulence intensity w_{rms}/U_c of shallow water jet cases ($H/D = 15, 10,$ and 5) along jet centreline. The symbolic line represents the free jet data.....	104
5.15	Variation of the fluctuation velocity ratios of the free and shallow jet cases along the jet centreline; (a) $v_{\text{rms}}/u_{\text{rms}}$ and (b) $w_{\text{rms}}/u_{\text{rms}}$	105
5.16	Downstream development of the normalised mean axial velocity U/U_c profiles on the vertical plane for the shallow water jet cases; (a) $H/D = 15,$ (b) $H/D = 10,$ and (c) $H/D = 5$	107
5.17	Downstream development of the normalised mean vertical velocity V/U_c profiles on the vertical plane for the shallow water jet cases; (a) $H/D = 15,$ (b) $H/D = 10,$ and (c) $H/D = 5$	110
5.18	Colour contour representing the development of the mean vertical velocity V in the axial direction for the shallowest jet case ($H/D = 5$).....	112
5.19	Downstream development of the normalised mean axial velocity U/U_c profiles on the horizontal plane for the shallow water jet cases; (a) $H/D = 15,$ (b) $H/D = 10,$ and (c) $H/D = 5$	113
5.20	Profiles of the normalised mean axial velocity U/U_c of free and shallow jet cases on the horizontal plane at axial locations; (a) $x/D = 40,$ and (b) $x/D = 60$	114
5.21	Downstream development of the normalised mean horizontal velocity W/U_c profiles on the horizontal plane for the shallow water jet cases; (a) $H/D = 15,$ (b) $H/D = 10,$ and (c) $H/D = 5$	116
5.22	Colour contour representing the development of the mean horizontal velocity W in the axial direction for the shallowest jet case ($H/D = 5$).....	118
5.23	Profiles of the normalised mean horizontal velocity W/U_c of free and shallow jet cases on the horizontal plane at axial locations; (a) $x/D = 40,$ and (b) $x/D = 60$	119
5.24	Downstream development of the relative axial turbulence intensity u_{rms}/U_c profiles on the vertical plane for the shallow water jet cases; (a) $H/D = 15,$ (b) $H/D = 10,$ and (c) $H/D = 5$	120

5.25	Behaviour of the relative axial turbulence intensity u_{rms}/U_c of free and shallow jet cases on the vertical plane at axial locations; (a) $x/D = 40$, and (b) $x/D = 60$	123
5.26	Downstream development of the relative axial turbulence intensity u_{rms}/U_c profiles on the horizontal plane for the shallow water jet cases; (a) $H/D = 15$, (b) $H/D = 10$, and (c) $H/D = 5$	124
5.27	Behaviour of the relative axial turbulence intensity u_{rms}/U_c of free and shallow jet cases on the horizontal plane at axial locations; (a) $x/D = 40$, and (b) $x/D = 60$	125
5.28	Downstream development of the relative vertical turbulence intensity v_{rms}/U_c profiles on the vertical plane for the shallow water jet cases; (a) $H/D = 15$, (b) $H/D = 10$, and (c) $H/D = 5$	127
5.29	Behaviour of the relative vertical turbulence intensity v_{rms}/U_c of free and shallow jet cases on the vertical plane at axial locations; (a) $x/D = 40$, and (b) $x/D = 60$	129
5.30	Downstream development of the relative horizontal turbulence intensity w_{rms}/U_c profiles on the horizontal plane for the shallow water jet cases; (a) $H/D = 15$, (b) $H/D = 10$, and (c) $H/D = 5$	131
5.31	Behaviour of the relative horizontal turbulence intensity w_{rms}/U_c of free and shallow jet cases on the horizontal plane at axial locations; (a) $x/D = 40$, and (b) $x/D = 60$	132
5.32	Downstream development of the relative Reynolds shear stress $\langle uv \rangle / U_c^2$ profiles on the vertical plane for the shallow water jet cases; (a) $H/D = 15$, (b) $H/D = 10$, and (c) $H/D = 5$	134
5.33	Behaviour of the Reynolds shear stress $\langle uv \rangle / U_c^2$ of free and shallow jet cases on the vertical plane at axial locations; (a) $x/D = 40$, and (b) $x/D = 60$	136
5.34	Downstream development of the relative Reynolds shear stress $\langle uw \rangle / U_c^2$ profiles on the vertical plane for the shallow water jet cases; (a) $H/D = 15$, (b) $H/D = 10$, and (c) $H/D = 5$	137

5.35	Behaviour of the Reynolds shear stress $\langle uw \rangle / U_c^2$ of free and shallow jet cases on the horizontal plane at axial locations; (a) $x/D = 40$, and (b) $x/D = 60$	138
5.36	Variation of the correlation C_{ij} of the velocity field $j = 1000$ with the velocity field number i . Note that i and j also represent time of the velocity fields. For clarity, only the correlation values of one hundred velocity fields before and after the velocity field $j = 1000$ are shown.....	140
5.37	The effect of sample size M on the eigenvalue spectra for the first ten modes. The eigenvalue problem was calculated for ensembles of different sizes taken from a single data set.....	143
5.38	Illustration of the effect of the threshold T on (a) the mean size R_{mean} , and (b) the mean circulation Γ_{mean} of vortices. These mean values are calculated from the vortices that exist in sixteen-grid-unit intervals of the axial distance x indicated.....	146
5.39	Examples of POD reconstructed velocity fluctuation fields for the $H/D = 15$ case; (a) Vertical plane, and (b) Horizontal plane. The circles represent the size of identified vortices. Red and blue circles represent positive and negative rotational sense, respectively.....	148
5.40	Examples of POD reconstructed velocity fluctuation fields for the $H/D = 5$ case; (a) Vertical plane, and (b) Horizontal plane. The circles represent the size of identified vortices. Red and blue circles represent positive and negative rotational sense, respectively.....	149
5.41	Two examples showing the centre positions of identified vortices of two sets of data extracted from 2000 velocity fields on (a) a vertical plane, and (b) a horizontal plane of the shallowest case $H/D = 5$. Note that $y/D = z/D = 0$ represents the centreline of the jet	150
5.42	Variation of the number of vortices in the normalised axial direction x/D for the free and shallow jet cases on (a) the vertical plane, and (b) the horizontal plane.....	152

5.43	The distribution of vortex size R in the axial direction x . Each figure represents data extracted from 2000 velocity fields on (a) a vertical plane, and (b) a horizontal plane of the shallowest case ($H/D = 5$). Note that positive R/D represents positive rotational sense.....	153
5.44	Percentage of vortices for (a) the free jet, and shallow jets on the vertical plane of depths; (b) $H/D = 15$, (c) $H/D = 10$, and (d) $H/D = 5$. Each figure shows three profiles (i), (ii), and (iii) taken at different ranges of axial distances.....	156
5.45	Percentage of vortices for the shallow jets on the horizontal plane of depths; (a) $H/D = 10$ and (b) $H/D = 5$. Each figure shows three profiles (i), (ii), and (iii) taken at different ranges of axial distances.....	158
5.46	Variation of the normalised mean radius R_{mean}/D of vortices in the normalised axial direction x/D on (a) the vertical plane, and (b) the horizontal plane.....	160
5.47	Distribution of vortex circulation Γ of the shallowest case ($H/D = 5$) extracted from 2000 velocity fields on a vertical plane of two adjacent fields-of-view (a) $28 < x/D < 44$, and (b) $44 < x/D < 61$. Note that positive Γ/DU_e represents positive rotational sense.....	162
5.48	Distribution of vortex circulation Γ of the shallowest case ($H/D = 5$) extracted from 2000 velocity fields on a horizontal plane of two adjacent fields-of-view (a) $29 < x/D < 45$, and (b) $46 < x/D < 61$. Note that positive Γ/DU_e represents positive rotational sense.....	162
5.49	Variation of the normalised mean circulation $\Gamma_{\text{mean}}/DU_e$ of vortices in the normalised axial direction x/D on (a) the vertical plane, and (b) the horizontal plane.....	164
5.50	Distribution of normalised circulation Γ/DU_e associated with the identified vortices of different sizes at two adjacent fields-of-view for the free jet (a) and (b), the shallowest jet case ($H/D = 5$) on the vertical plane (c) and (d), and the shallowest jet case on the horizontal plane (e) and (f).....	165

NOMENCLATURE

Roman

A	The number of bits in the binary representation of the intensity level
$a^{(k)}(t_l)$	Time-dependent orthonormal amplitude coefficients
\mathbf{C}	The temporal correlation matrix
C_{ij}	Components of the temporal correlation matrix \mathbf{C}
\check{C}	Seeding concentration [particles/m ³]
$CC(\mathbf{s})$	PIV cross-correlation function
C_μ	A model coefficient, $C_\mu = 0.09$
D	Jet exit diameter [m]
d_l	Interrogation area size [pixels]
d_p	Particle diameter [m]
\ddot{E}	Voltage [volt]
E	Energy of vortical structures [m ² /s ²]
Fr	Froude number
FOV	Field-of-view
f_d	Particle drag coefficient
g	Gravitational acceleration (= 9.81 m/s ²)
$I(\mathbf{X})$	Intensity of the interrogation area image
IA	Interrogation area
K	A constant added to a threshold field
K_d	The velocity decay coefficient
K_s	The growth rate of the jet
k	Turbulent kinetic energy [m ² /s ²]
L_{ij}	The distance between points i and j
L_v	An eddy lengthscale
M	Ensemble size
m	Number of basis functions for the POD analysis
\dot{m}	Mass flow rate of a jet at any axial cross-section [kg/s]

\dot{m}_e	Exit mass flow rate of a jet [kg/s]
N	Number of velocity vectors in a PIV flow field
N_I	Number of particles per IA
n	The total number of connected neurons to the candidate neuron
\check{r}	Distance between a neuron and its immediate neighbours
Re	Reynolds number
$R(\mathbf{X}, \mathbf{X}')$	The two-point time-averaged spatial correlation function
\widehat{R}_{ij}^u	The absolute difference between a velocity component u at i and j
$r_{1/2}$	Half-width of the jet measured at $0.5 U_c$ [m]
r, x	Cylindrical coordinate system
St	Stokes number
S_i^u	The sum of the weight functions for the i th neuron
T_i^u	A threshold for the velocity component u
ΔS	Displacement vector of the seeding particle [pixel]
\widetilde{T}_i^u	A mean deviation in the u -velocity component for each vector location i
t	Time [s]
Δt	PIV image time separation [s]
U, V, W	Axial, vertical, and horizontal mean velocity components [m/s]
U_c	Mean centreline velocity [m/s]
U_e	Mean exit velocity [m/s]
U_f	The flow velocity measured by the flowmeter [m/s]
U_v	An eddy velocity scale [m/s]
u_T	The terminal velocity [m/s]
u', v', w'	Axial, vertical, and horizontal fluctuating velocity components
$u_{\text{rms}}, v_{\text{rms}}, w_{\text{rms}}$	Axial, vertical, and horizontal root-mean-squared velocities
$u_{\text{POD}}, v_{\text{POD}}, w_{\text{POD}}$	Axial, vertical, and horizontal POD reconstructed velocity components
$\langle uv \rangle, \langle uw \rangle$	Reynolds shear stress
$\mathbf{V}(\mathbf{X})$	Mean velocity vector
$\widetilde{\mathbf{V}}(\mathbf{X}, t)$	Instantaneous velocity vector
$\widehat{\mathbf{V}}(\mathbf{X}, t)$	Fluctuating velocity vector
$\mathbf{V}_{\text{POD}}(\mathbf{X}, t)$	POD reconstructed velocity vector

\mathbf{X}	Position vector
x, y, z	Cartesian coordinate system
x_0	Distance from the nozzle opening to the virtual origin of the jet
y_c	Vertical position of the centreline velocity [m]
ZFE	Zone of flow establishment
ZEF	Zone of established flow
δz	Laser sheet thickness

Greek

ρ	Density of the water [kg/m ³]
ρ_p	Density of the seeding particles [kg/m ³]
ρ_0	Density of entrained fluid [kg/m ³]
μ	Dynamic viscosity of the water [kg/m.s]
ν	Kinematic viscosity of the water [m ² /s]
ν_t	Turbulent viscosity [m ² /s]
ε	Turbulent energy dissipation [m ² /s ²]
γ_j^k	The state of neuron j at iteration k
χ	Ratio of the particle density to the fluid density
η	Non-dimensional coordinate (= $y/(x-x_0)$)
τ_p	Particle response time [s]
τ_f	Fluid timescale [s]
σ	The width of the Gaussian filter
α	The Gaussian function
$\Psi^{(k)}(\mathbf{X})$	Time-independent orthonormal basis functions
κ	Average least-squares error
Ω	The domain of interest for calculating the correlation $R(\mathbf{X}, \mathbf{X}')$
δ_{kp}	The Kronecker delta
$\lambda^{(k)}$	Eigenvalue at the k-th mode
$\Phi^{(k)}$	The k-th eigenvector corresponding to the eigenvalue $\lambda^{(k)}$ of \mathbf{C} .

Chapter 1

INTRODUCTION

1.1 GENERAL

Jets encountered in nature and in technological applications are usually confined due to the presence of rigid boundaries, free surfaces, or strong stratification. Among the most important of these is the shallow water jet which is a frequently encountered problem in engineering practice and consists of a jet that enters a body of water of finite depth where the proximity of the bottom solid wall and the top free surface are expected to influence the flow. For instance, jet discharges from industrial and domestic sources often enter shallow rivers and coastal bays (Dracos *et al.*, 1992). In contrast to the existing body of knowledge on unconfined turbulent jets, shallow water jets demonstrate flow behaviour that depends strongly on the bounding surfaces.

Discharges in shallow waters are of primary importance in environmental fluid mechanics because most of the waste flow is discharged into shallow bodies of water where the mixing is influenced by the shallowness. Jet mixing processes are complicated since two boundaries (free surface and bed) simultaneously influence the development of the jet. Shallow water produces a significant difference in the horizontal and vertical growth rates of the jet because the horizontal and vertical half-widths develop differently. A reduction in entrainment into the jet would be anticipated as a consequence of the restricted volume above and below the jet. The behaviour of this kind of jet has received considerable attention by hydraulic engineers. The concern is

often the influence of buoyancy on the spreading and mixing of jets since the jet is generally warmer than the receiving fluid. However, very little information is available on the turbulence structure of shallow water jets.

For as long as turbulence has been known, turbulent jets have been investigated extensively to understand just how turbulence is generated at the expense of the mean motion and how it is dissipated. The classical view that turbulence is essentially a stochastic phenomenon having a randomly fluctuating velocity field superimposed on a well-defined mean has changed in the last few decades. The discovery of large-scale, quasi-deterministic, coherent structures in flows which were previously considered chaotic is quite exciting because their evolution might be mathematically tractable (Hussain, 1986). These coherent structures have been the primary focus of recent turbulence research. This has been motivated by the expectation that coherent structures dominate turbulence effects of technological interest (drag, heat transfer, entrainment, mixing, aerodynamic noise, etc.) and that understanding coherent structures dynamics is essential for developing turbulence models and flow control strategies. The key feature of coherent structures is that they are vortical. Therefore, studying vortex interactions is obviously crucial for understanding basic turbulence phenomena such as transport, mixing, turbulence production, and generation of aerodynamic noise.

The overwhelming majority of the studies of coherent structures to date have been based on flow visualisation and not on quantitative data. Motivated by convenience, flow visualisation of coherent structures has been performed only at low Reynolds numbers. The development of quantitative visualisation techniques like particle image velocimetry (PIV) provides new possibilities for studying these structures. PIV is well suited for identifying vortical structures because it provides instantaneous global velocity fields which are not possible with pointwise techniques.

In this study, the velocity field was measured using the particle image velocimetry (PIV) technique. This technique can provide instantaneous two-dimensional velocity fields with excellent spatial resolution which is relevant for this kind of study. A number of

images were taken in selected planes in order to extract statistical information about the behaviour of coherent structures and mean flow turbulence. The proper orthogonal decomposition (POD) technique was used for exposing the coherent structures.

1.2 OBJECTIVES

Jet discharges from industrial and domestic sources into shallow bodies of water are certainly influenced by the proximity of the solid wall and free surface boundaries. These problems are usually complicated by the difference in density between the effluent and the receiving fluid. In this situation, buoyancy effects are of considerable importance. At present, there is a significant lack of understanding of round jets in shallow water. The purpose of this work is to increase the understanding of the turbulent structure of shallow water jets. Specifically, the objective of the present work is to characterise the effects of the vertical confinement on a neutrally-buoyant turbulent round jet discharging horizontally into a stagnant water tank. The objectives may be achieved by:

- investigating the mean flow characteristics such as velocity, turbulence intensity, and Reynolds stress fields as well as spread rate, centreline velocity decay, etc, and
- investigating the dynamics of coherent structures which can be performed by:
 - exposing vortical structures using the proper orthogonal decomposition (POD) technique,
 - identifying and measuring the vortical structures including vortex centre location, radius, strength (circulation) and rotational sense, using a vortex identification algorithm, and
 - conducting a statistical analysis to investigate the distribution of number, size, strength, and rotational sense of the vortical structures.

1.3 SCOPE OF THE PRESENT WORK

The present investigation focuses on a shallow water jet with perhaps its most elementary geometry – a round jet discharging horizontally from a vertical side wall into a flat-bottomed stationary body of water. The jet was free to expand laterally while the depth of the water H was an adjustable parameter. The Reynolds number was selected according to the maximum flow rate obtainable by the water supply system. PIV measurements were taken at several positions downstream of the jet exit.

The flow conditions can be represented non-dimensionally by the source Reynolds number, $Re_D = \frac{U_e D}{\nu}$, and the depth of the water layer H/D , where U_e is the jet exit velocity, D is the jet exit diameter, H is the water layer depth, and ν is the kinematic viscosity.

The scope may be summarised as follows:

- A neutrally-buoyant water jet discharging horizontally from a nozzle of diameter $D = 9$ mm was studied.
- The depth of the water layer H was the principal variable. Three different values of $H/D = 15, 10,$ and 5 were investigated in addition to the free jet case ($H/D = 60$).
- One exit Reynolds number ($Re_D = 22,500$) was investigated.
- In all experiments, the centreline of the jet was located midway between the solid wall and the free surface (see Figure 3.1).
- Measurements were taken on two orthogonal planes along the jet axis (x - y and x - z), where x , y , and z represent axial, vertical, and horizontal locations, respectively.
- Measurements were taken at several axial distances downstream of the jet exit ($10 < x/D < 80$). At each location, two thousand images were taken in order to extract statistical information about the behaviour of the flow.

1.4 OUTLINE OF THE THESIS

The thesis begins with a comprehensive review of the literature presented in Chapter 2. This chapter is divided into two main sections. The first section reviews turbulent round jets in a free environment and in the presence of bounding surfaces. This includes a comprehensive review of free jets in the near-exit and far-field regions. This section is followed by a review of coherent structures in the near-exit and far-field regions of free jets as well as Reynolds number effects and techniques of educing coherent structures.

In Chapter 3 of the thesis, the details of the experimental setup, instrumentation, and means of data analysis and processing are discussed. This includes the variable threshold technique proposed by Shinneeb *et al.* (2004a) for post-processing of PIV data. The analysis techniques chosen for the present study for educing and measuring the coherent structures are presented in Chapter 4, and the experimental results are presented in Chapter 5. The experimental results include the jet exit conditions, mean velocity, turbulence intensity, and Reynolds shear stress profiles as well as a coherent structure investigation on vertical and horizontal planes. To show the effect of the vertical confinement on the flow field, all shallow jet profiles are compared with the free jet results obtained in the same experimental setup, together with previously published results. The coherent structures section starts by discussing the correlation between velocity fields, the energy content of large-scale vortices, the ensemble size required for the POD analysis, and the vortex identification method. Then, a statistical study is presented, which includes distributions of vortex number, size, and circulation. The thesis ends with a summary of the major conclusions and contributions of the research, and some recommendations for future study.

Chapter 2

LITERATURE REVIEW

2.1 INTRODUCTION

It has been recognised long ago that most flows in large-scale applications are *turbulent*. Turbulent flow is prevalent in the natural environment and is one of the least understood problems in fluid mechanics. In 1883, Osborne Reynolds demonstrated the *transition* from laminar to turbulent flow in a pipe as a result of instability. He also introduced the *Reynolds number* as a similarity parameter, which allowed experiments at different scales to be correlated. Even before Reynolds' experiment, it was recognised that turbulent flow results from instability, and scientists such as Kelvin, Helmholtz, and Rayleigh initiated the discipline of flow stability theory.

Turbulence is still an unresolved problem of classical physics. In the words of John Lumley (see Gad-el-Hak, 2000); "*Turbulence is a difficult problem that is unlikely to suddenly succumb to our efforts. We should not await sudden breakthroughs and miraculous solutions but rather keep at it slowly building one small brick at a time*". The struggle to understand turbulence has been long with some achievements and much frustration. However, the progress made so far does not match the effort expended, reflecting the fundamental complexity of turbulence phenomena.

Most turbulence research has been accomplished using one of two main approaches. The first one is the search for models of the *Reynolds Averaged Navier-*

Stokes (RANS) equations, first derived by Reynolds, which address the mean flow quantities. The other one is the so-called *statistical theory* of turbulence which seeks statistical descriptions of the turbulence itself, mainly through correlations of fluctuating velocity, in anticipation of ultimately contributing to understand the turbulence phenomena. The main goal of the RANS approach is to understand the mean flow field which exhibits the effects of enhanced transport by turbulence in terms of growth rate, entrainment, etc. The statistical description of turbulence, which was introduced by G.I. Taylor in 1930, describes properties of the fluctuating flow field. This approach seeks equations and relations for correlations of the velocity fluctuations. Indeed, both approaches have provided many insights into turbulence. However, a complete understanding of turbulence phenomena has remained out of reach.

The discovery of large-scale coherent structures and the integration of the digital computer as an active component of turbulence research have had a profound impact on turbulence research. Coherent structures have been the primary focus of turbulence research in the past few decades. This has been motivated by the expectations that coherent structures dominate turbulence effects of technological interest (drag, heat transfer, entrainment, mixing, aerodynamic noise, etc.), and that understanding coherent structure dynamics is essential for developing turbulence models and flow control strategies. The key feature of coherent structures is that they are vortical; i.e. underlying the random vorticity field that constitutes turbulence, there is an instantaneously phase-correlated vorticity field. Accordingly, understanding vortex interactions is crucial for understanding basic turbulence phenomena such as transport, mixing, turbulence production, and generation of aerodynamic noise.

Section 2.2 of this chapter gives a comprehensive review of the characteristics of free round turbulent jets from the near-exit region to the far-field region. The effect of boundedness on horizontal round jets is reviewed in Section 2.3. This includes the effect of a free surface, a plane solid wall, or both simultaneously on the round jet. Section 2.4 provides descriptions and definitions of coherent structures, and reviews the characteristics of coherent structures in the near-exit and far-field regions of round free jets. The concept of Reynolds number similarity is discussed in Section 2.5. Finally, the

techniques commonly used for detection of coherent structures are reviewed in Section 2.6.

2.2 TURBULENT ROUND JETS

2.2.1 Characteristics of Free Jets

Numerous experimental and computational investigations of jet behaviour exist for a variety of bounded and free geometries. The free round (axisymmetric) turbulent jet, which results when fluid issues from a round orifice into infinite space, is a classical prototype of turbulent free shear flow. Its simple geometry makes it an attractive subject for the study of turbulence (see for example Abramovich, 1963 and Rajaratnam, 1976 for comprehensive reviews). Classically, the development of a free jet is characterised by two regimes; the zone of flow establishment (ZFE) near the jet orifice, followed by the zone of established flow (ZEF) far away (see Figure 2.1).

The ZFE has been investigated less than the ZEF. One of the probable reasons is that no suitable theory is available for the ZFE because of the dependence of flow structure on the jet orifice geometry. Generally, there exists a potential core at $0 < x/D < 5$, where x is the axial distance measured from the orifice and D is the orifice diameter. Some investigators take the potential core region as the ZFE (Kuang *et al.*, 2001). However, Browne *et al.* (1984) argued that there is a transition region after the potential core before the jet becomes self-similar in the ZEF. For simplicity, the ZFE is usually taken as the portion that consists of the potential core and transition regions.

Zone of flow establishment (ZFE)

The key to the growth rate of jets is a topic that has created much excitement, and a lot of argument, in the past. There is some documentation of the effect of initial conditions on round jets (Hussain & Zedan, 1978a,b; Xu & Antonia, 2002). It has been found that there exist significant differences between jet flows having different initial conditions (e.g. top-hat, fully-developed turbulent, etc.). Bradshaw earlier wrote (see Hussain & Zedan, 1978a), "*it is clear that turbulent initial boundary layers are to be avoided when*

one is trying to set up a self-preserving mixing layer”, suggesting dependence of the flow on the initial condition for attaining self-preservation, i.e., the jet achieves self-preservation earlier in case of an initially laminar shear layer. Hussain & Zedan (1978a,b) found that the spread rate and peak turbulent intensity in the self-preserving region are dependent on whether the initial boundary layer is laminar or turbulent. Also, the virtual origin and the distance required to attain self-preservation depends noticeably and systematically on the initial momentum thickness and turbulence intensity. The mean velocity and turbulence intensity profiles appear to reach self-similarity together when the initial boundary layer is laminar, but not when the initial boundary layer is turbulent. They argued that the initial turbulence intensity has a much more dramatic effect on the evolution and average characteristics of the free shear layer than does the initial momentum thickness.

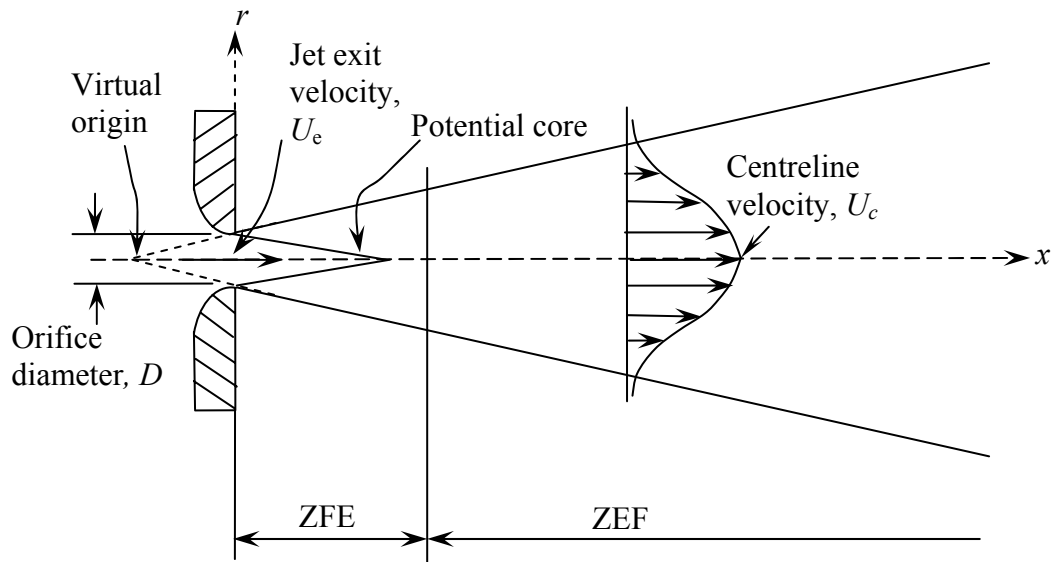


Figure 2.1: Schematic definition of a free jet.

George (1989) discovered a shortcoming in the original similarity theory which implicitly assumed that the self-preserving state was independent of the details of the

initial conditions. The analysis showed that there exists a multiplicity of self-preserving states for a particular type of flow and that each state is uniquely determined by the initial conditions. Recently, Ferdman *et al.* (2000) investigated the effect of non-uniform initial velocity profiles issued from a pipe on the downstream evolution of round jets; one with axisymmetric profile and the other with an asymmetric profile. Several turbulence quantities were compared between these two jets as well as with those of top-hat jets obtained by other researchers. It was found that the initial asymmetry of the second jet vanished nine jet diameters downstream, and the far-field decay rates of the two jets were smaller than those with top-hat initial velocity distributions. Later, Xu & Antonia (2002) compared the characteristics of a jet issuing from a nozzle with a smooth contraction to a jet exiting from a long pipe. The former produced a top-hat velocity distribution while the latter produced a fully-developed turbulent pipe flow profile. It was found that the jet produced by the smooth contraction approached self-preservation more rapidly than the jet produced by pipe flow. The differences are associated with differences in turbulence structure in both the near-exit and far fields of these two flows. The pipe jet possesses a thicker initial shear layer and larger turbulence intensity. This larger initial shear layer thickness produces a lower instability frequency. The regular vortex formation and pairing processes needed for mixing are disrupted by turbulence. Furthermore, they indicated that the streamwise vortices which enhance entrainment and mixing are absent in the case of initially turbulent boundary layers.

The effect of placing a circular nozzle flush with the wall or extending it inside the tank was investigated experimentally at Reynolds numbers from about 1000 to 10,000 by Romano (2002) using laser induced fluorescence (LIF), laser-Doppler anemometry (LDA), and particle tracking velocimetry (PTV). The former is called a no-slip jet and the latter is called a free-slip jet. The velocity profiles were the same at the jet exit in both cases. The focus was on the behaviour of the near-exit flow field. It was found that, for the free-slip jet, the large scale vortices grow and break up closer to the nozzle than for the no-slip jet. This is the reason for enhanced mixing for the free-slip case compared to the no-slip jet. Moreover, the measured centreline velocity decreases more slowly, with a longer potential core and a higher shear layer thickness for the free-slip case.

Zone of established flow (ZEF)

The characteristics of a turbulent free jet in the ZEF have been the subject of many investigations. The mean and turbulent flow properties in this region have been measured by several investigators. Wygnanski & Fiedler (1969) performed a comprehensive study of the self-similar region of a round jet and reported moments, energy balance, intermittency, microscales, and integral scales. The possibility of self-preserving solutions to the free turbulent round jet equations was recognised by Tollmien in 1926 and others (see Schlichting, 1979). *Self-preservation* means a continuing similarity in turbulent structure during the decay or development of a turbulent flow, i.e. there is equilibrium between viscous decay and the generation of turbulent energy through turbulent shear stresses. The premise of this theory is that, when properly scaled, flow variables such as the mean velocity profile can be expressed in terms of a unique function at each downstream distance along the jet axis. In brief, the mean velocity profiles, turbulence intensities, and shear stresses at various axial stations in the ZEF collapse onto a single profile when normalised by proper length and velocity scales (Hussein *et al.*, 1994). The velocity and length scales that are usually used are the local mean centreline velocity U_c and the half-width of the jet $r_{1/2}$. Wygnanski & Fiedler (1969) reported self-similarity at a distance from the nozzle exit of $x/D \approx 70$. It was argued that a given body of fluid is said to be in a self-preserving state when all of its turbulent components (u' , v' , and w') are in equilibrium. They indicated that self-similarity is reached in steps. First, the mean velocity becomes similar, which leads to certain production of the axial fluctuating component u' . Only after a balance is reached between these two quantities may equilibrium be attained in the transverse components as well. Their experiments showed that the u' component attained self-similarity at $x/D \approx 40$ and v' component became self-similar only at $x/D \approx 70$. Their results were in accordance with Townsend (1956) and consequently their work became the standard reference for the quantitative description of mean velocities, turbulence stresses, and triple correlation coefficients of the round jet.

Hussein *et al.* (1994) reported measurements of the turbulent velocity field of a round jet to clarify the source of the discrepancy between previous studies of jets. They used

laser-Doppler anemometry (LDA) and stationary and flying hot-wire (SHW and FHW, respectively) techniques for this investigation. It was argued that the far-field data of Wygnanski & Fiedler (1969) failed to satisfy conservation of momentum and concluded that the differences between the results reported by earlier investigators could be attributed to the smaller enclosures used in their studies and the recirculation within them.

Properties along the centreline of a free jet in the ZEF

There are apparently few studies where there has been a systematic evaluation of the changes that occur from the near orifice region to far downstream. Most of the available results show that a turbulent jet does not attain a self-preserving state until some 40 jet diameters downstream (Rodi, 1982). Wygnanski & Fiedler (1969) showed that the ratios of the mean turbulent stresses on the axis of the jet to the mean centreline velocity become essentially constant. The ratio of u_{rms}/U_c (u_{rms} represents the root-mean-square of the axial fluctuating velocity) on the jet axis is in the range 0.28 – 0.29, which compares with the value of 0.29 found by Shinneeb *et al.* (2006). Wygnanski & Fiedler (1969) also found that v_{rms}/U_c and w_{rms}/U_c were close to equal and asymptotically constant at a value of about 0.25. In a careful assessment of errors and analysis of hot wire calibrations by Rodi in 1975 (see Rodi, 1982), it was concluded that this value is probably high and should be about 0.23. This is consistent with the results obtained by Hussein *et al.* (1994) and Shinneeb *et al.* (2006). Measurements of the maximum measured values of Reynolds shear stress by Wygnanski & Fiedler (1969) and Rodi (1982) show relative values of the order of 0.017 – 0.018. Hussein *et al.* (1994) and Shinneeb *et al.* (2006) show higher values of the maximum relative Reynolds stress of the order of 0.021 – 0.022.

The mean centreline decay in the ZEF is typically modelled by a simple decay equation with a $1/x$ decay profile such as given by Malmstrom *et al.* (1997)

$$\frac{U_c}{U_c} = \frac{1}{K_d} \left(\frac{x}{D} - \frac{x_0}{D} \right) \quad (2.1)$$

In this equation, U_e is the jet exit velocity, U_c is the local mean centreline velocity, K_d is the velocity decay coefficient, D is the nozzle diameter, x is the coordinate in the axial direction, and x_0 is the distance from the nozzle opening to the virtual origin of the jet. The parameter x_0 has a positive value if the virtual origin is in front of the nozzle. For most practical purposes, the virtual origin is considered to be the same as the jet exit. Table 2.1 lists some frequently cited measurement results for comparison purposes. These previous research results indicate that the measured K_d values are in the range 5.8 – 6.0.

The jet spread is usually quantified by the increase of the half-width points $r_{1/2}$ in the axial direction. The half-width of a free jet is defined as the radial location where the axial velocity equals one-half of the centreline velocity. It is found that the free jet spreads linearly in the ZEF. Table 2.1 gives some of previous published results of the spread rate K_s for free jets which lie in the range 0.080 – 0.102.

Table 2.1: Comparison of decay results for a free round jet.

Investigator	Substance	Re_D $\times 10^{-4}$	Decay rate (K_d)	x_0/D	Spread rate (K_s)	Initial condition
Shinneeb <i>et al.</i> (2006)*	water	2.19	5.84	-0.98	0.106	Top hat
Hinze (1975)	---	---	5.90	-0.50	0.080	---
Wynanski & Fiedler (1969)	air	10	5.70	3	0.086	---
Rodi (1982)	---	8.7	5.90	---	0.086	---
Panchapakesan & Lumley (1993)	air	1.1	6.06	-2.50	0.096	Top hat
Hussein <i>et al.</i> (1994) LDA	air	9.55	5.80	4	0.094	Top hat
Hussein <i>et al.</i> (1994) SHW	air	9.55	5.90	2.70	0.102	Top hat

* Note that this paper investigates a vertical axisymmetric jet while the free jet case discussed in this thesis was horizontal.

2.2.2 Entrainment in Free Jets

As the jet spreads, fluid from the surroundings is drawn radially inwards towards the jet across its conical surface. This process is known as entrainment. Entrainment is important in many practical situations; for example, it controls the flow pattern in combustion chambers and furnaces. Also, many mixing devices in the chemical industry rely on entrainment for their effectiveness. To improve the efficiency of these devices and processes, it is important to gain insight into this process.

Ricou & Spalding (1961) measured the entrained flow to the jet directly in the ZEF. The jet was surrounded by a concentric chamber, closed at one end except for the jet nozzle and open at the other end to the atmosphere. The chamber was double-walled with a porous inner wall through which the measured air entrainment was supplied to the jet. When the pressure inside the chamber (but remote from the jet) was equal to the atmospheric pressure, the rate of air entrainment supplied was presumed equal to that which would occur naturally in the absence of the chamber. Measurements were taken over a wide range of density ratio and axial distance. It was found that the mass flow rate of the jet increases linearly with the axial distance due to entrainment of the surrounding fluid according to the following relation:

$$\frac{\dot{m}}{\dot{m}_e} = 0.32 \frac{x}{D} \left(\frac{\rho_o}{\rho_j} \right)^{1/2} \quad (2.2)$$

Here \dot{m}_e represents the initial mass flow rate, \dot{m} is the total mass flow rate of the jet at any axial cross-section, and ρ_j and ρ_o are the densities of the jet fluid and entrained fluid, respectively.

Hill (1972) was able to measure the local entrainment rate in the initial region of round turbulent jets and reproduce the results of Ricou & Spalding (1961) in the region of fully-developed flow successfully. The method used was the same as the porous-wall technique of Ricou & Spalding (1961) except that the jet was directed through a short

chamber open to the atmosphere at both ends and could be moved axially. Results showed that the local entrainment rate increased nonlinearly in the initial region from zero at the exit until it reached the fully-developed value at about $x/D = 13$.

2.3 EFFECT OF BOUNDEDNESS ON HORIZONTAL ROUND JETS

The classical approach toward the problem of free jets commonly neglects the induced pressure gradients within the resulting fluid motion. This condition is met by ensuring that the dimensions of the receiving medium are sufficiently large compared to the characteristic jet dimensions. This fundamental assumption is not satisfied in numerous instances in applied problems because of the existence of boundaries. In such jets, significant modifications of the usual jet motion occur due to confinement and entirely new and unexplained flow phenomena may arise which require altogether different analytical approaches. Generally speaking, jets can be confined in either the axial or lateral direction. This may occur under non-buoyant or buoyant (positive or negative) jet conditions. The boundedness of the jet may arise in different fashions; solid boundaries, air-water interfaces, or interfaces produced by strong stratification. In this section, the proximity of a free surface and/or solid wall to a turbulent round jet discharging horizontally is reviewed.

2.3.1 Free-Surface-Bounded Jets (Free-Surface Jets)

The turbulent flow below a gas-liquid interface plays an important role in diverse areas ranging from environmental flows and industrial mixing processes to the remote sensing of ship wakes. The near-boundary influences upon transfer and diffusion at the interface are of primary concern in environmental and industrial applications, whereas remote sensing issues ultimately involve any surface motions that may be detectable. At present, there is a lack of understanding of the nature of the interaction of a turbulent shear flow, such as a ship wake, with a free surface (Walker *et al.*, 1995).

Investigations of turbulent jet flows near free surfaces have, until recently, been concerned primarily with flows of relevance to civil and hydraulic engineering, where the effects of buoyancy are often significant. Rajaratnam & Humphries (1984) studied the mean flow characteristics of a round jet discharging parallel to a free-surface when the free surface is located at the edge of the nozzle, i.e. the centreline of the jet is at 0.5 nozzle diameters below the free surface. In their investigation they did not study the free-surface motion caused by the jet/free-surface interaction. However, they reported a reduction of the mean velocity near the surface at high Froude numbers* ($Fr = U_e / \sqrt{gD}$, where g is the gravitational acceleration) which was attributed to surface wave generation. Moreover, they confirmed the same scaling for the maximum mean velocity decay as for the free jet or round wall jet measurements of Rajaratnam & Pani (1974). The growth rate in the direction perpendicular to the free surface was found equal to the wall jet growth rate ($r_{1/2} = 0.044$) while the growth rate in the direction parallel to the free surface was found to be approximately half of the wall jet growth rate ($r_{1/2} = 0.09$ and 0.20 for the free surface and wall jets, respectively).

Swean *et al.* (1989) reported measurements of mean velocities and turbulent fluctuations in a two-dimensional turbulent jet issuing at a free surface. Velocity measurements were taken using a dual sensor hot-film anemometer. They concluded that the growth rates of the length and velocity scales resemble those of a two-dimensional wall jet at the same Reynolds number. Anthony & Willmarth (1992) measured the mean and fluctuating velocities in the turbulent flow field of a round jet issuing beneath and parallel to a free surface using a three-component laser-Doppler velocimetry (LDV). They studied the effects of the free surface on the development of a jet (the centreline of the jet was at 2 diameters below the free surface) at an exit Reynolds number of 12,700 and a Froude number ($Fr = U_e / \sqrt{gh}$, where h is the jet depth measured from the centreline of the jet) of 5.66. The results showed that near the jet centreline the velocity fluctuations normal to the surface are reduced while those parallel to the surface are enhanced. They noted the existence of an outward flow away from the jet axis in a thin layer near the free

* The Froude number Fr is defined as the ratio of the inertial force associated with the liquid motion to the gravitational force controlling the height of waves.

surface. This was identified in near-surface measurements. It was concluded, on the basis of flow visualisation, that this outward flow or “surface current” was comprised mainly of vortical structures ejected from the main jet. The origin of the surface current was not identified. They also found that the surface current is suppressed by an insoluble surfactant.

Liepmann & Gharib (1994) investigated the entrainment and vorticity dynamics of near-surface round jets using particle image velocimetry (PIV). The jet was obtained by directing water through a nozzle of 1 inch diameter into stationary water in a tank. The Reynolds number was 6000 and the velocity profile at the exit was uniform. The measurements were taken at eight stations downstream of the nozzle and at two depths which corresponded to Froude numbers of 0.48 and 0.34, based on the jet depth. Results showed that the development of the jets was affected by the proximity of the free surface which modified the streamwise vorticity and attenuated the growth rate. It was found that the growth rate of the near-surface reaches maximum, decays, and then levels off. This behaviour follows closely the vorticity calculated near the free surface which indicates that the streamwise vorticity decays in the downstream direction. The location and degree of influence depends on the Reynolds number and depth of the jet.

A round turbulent jet issuing parallel to a free surface was examined by Madnia & Bernal (1994) using flow visualisation and single-component hot-film measurements. The experiments were conducted at a Reynolds number of 12,700 and Froude numbers of 8, 6.5, 5, and 4.3. The Froude number used in this study was based on the jet depth h as defined above, rather than the jet exit diameter D , as the characteristic length. Significant surface disturbances occurred where the large-scale structures in the jet first interacted with the free surface. These disturbances form approximately plane waves which propagate away from the jet axis. The angle at which the waves propagate varied with jet exit velocity and jet depth – the angle increases with increasing the Froude number. Using shadowgraph visualisation, they also noted the appearance of small circular dimples on the free surface. These dimples are a typical signature of a vortex with its axis normal to the free surface.

Walker *et al.* (1995) reported an experimental investigation of turbulent round jet interaction with a free surface when the jet issues parallel to the free surface. The objective of the study was to investigate the effects of the Reynolds and Froude numbers on the structure of near-surface turbulence. Three different jets, with different exit velocities and jet exit diameters, all located two jet exit diameters below the free surface were studied. At this depth the jet flow is fully turbulent before significant interaction with the free surface occurs. Froude number effects were identified by increasing the Froude number from $Fr = 1$ to 8 at $Re = 12,700$. Reynolds number effects were identified by increasing the Reynolds number from $Re = 12,700$ to 102,000 at $Fr = 1$. Qualitative features of the subsurface flow and free surface disturbances were examined using flow visualisation. Measurements of all six Reynolds stresses and three-mean velocity components were obtained in two planes 16 and 32 jet diameters downstream using three-component laser velocimetry (LDV). For all the jets, the interaction of vorticity tangent to the surface with its “image” above the surface contributes to an outward flow near the free surface. This interaction is also shown to directly relate to the observed decrease in the surface-normal velocity fluctuations and a corresponding increase in the tangential (axial and horizontal) velocity fluctuations near the free surface. At high Froude numbers, the larger surface disturbances diminish the interaction of the tangential vorticity with its image, resulting in a smaller outward flow and less energy transfer from the surface-normal to tangential velocity fluctuations near the surface. Energy is transferred instead to free-surface disturbances (waves) with the result that the turbulent kinetic energy is 20% lower and the Reynolds stresses are reduced compared to the low-Froude-number jets. At high Reynolds number, the rate of evolution of the jet interaction with the free surface was reduced. In addition, the decay of tangential vorticity near the surface is slower than for low Reynolds number so that vortex filaments have time to undergo multiple reconnections to the free surface before they eventually decay.

2.3.2 Wall-Bounded Jets (Wall Jets)

Although wall jets in quiescent surroundings have been studied extensively both experimentally and theoretically (for instance, a plane wall jet, a radial wall jet, a curved wall jet, and an annular wall jet), there have been relatively few investigations of three-dimensional wall jets (Sforza & Herbst 1970, Newman *et al.* 1972, Rajaratnam & Pani 1974, Davis & Winarto 1980, and Launder & Rodi 1983). A three-dimensional wall jet is produced by a round, square, or rectangular nozzle (of finite aspect ratio) or by a nozzle of comparable geometry along a solid wall. This configuration may be found in the disposal of effluent through a submerged round pipe where the pipe is secured near the bottom of the receiving ambient fluid. An example is the disposal of marine tailings (Law & Herlina, 2002). This subject may also be of interest in the transport of pollutants inside storm water hydraulic conveyance systems, where near-bottom outlets are a common occurrence. In addition, the fluid flow resulting from a series of circular orifices in line may produce a quasi-two-dimensional wall jet which is used for boundary layer control (blowing) and also for film-cooling and mixing problems (Knystautas, 1964).

A three-dimensional round wall jet with the jet orifice affixed parallel to the plane wall (i.e. the distance from the nozzle centreline to the wall is 0.5 nozzle diameters) was studied experimentally and theoretically by Newman *et al.* (1972). It was shown from similarity considerations (neglecting wall friction) that the two half-widths (normal and parallel to the plane wall) and the decay of the mean maximum velocity should grow linearly with distance from the orifice. Beyond the initial development region, experiments confirmed this behaviour. The most noticeable feature of the jet is that it exhibits a far greater lateral rate of spread than it does normal to the wall. A more recent study by Davis & Winarto (1980) showed that wall jets, with the jet nozzle positioned above the wall at heights ranging from 0.5 to 4.0 nozzle diameters measured from the jet centreline to the wall, become increasingly oblate with downstream distance. The growth rate of the half-width parallel to the wall is many times larger than that normal to the wall at large distances from the nozzle (the ratio approaches 8.5). Measurements of turbulence and Reynolds stress show that turbulent mixing parallel to the wall exceeds

that normal to the wall which is consistent with the normal and lateral spreading rates. Correlations measurements were made between the vertical component of velocity at a fixed reference position and horizontal velocity components. The vertical component was measured at the centre of the flow above the jet axis where maximum Reynolds stress was observed, while the horizontal component was measured at different horizontal points from the jet centre. At each horizontal location, a series of measurements was made at different vertical locations by a moving X-wire probe. It was shown that the interaction between the jet and the wall involves a relatively large-scale coherent motion in which the normal component of motion towards (or away from) the solid wall is associated with horizontal outflow (or inflow) along the wall. This motion provides a physical explanation for the much greater mixing rate parallel to the wall. The most recent study on the characteristics of three-dimensional turbulent wall jets was conducted by Law & Herlina (2002) using particle image velocimetry (PIV) and laser induced fluorescence (LIF). The measurements revealed that the direction of the vertical velocity component at the centreline plane was negative (acting downward towards the solid wall). This observation supported the existence of a secondary mean vortex as suggested by Launder & Rodi (1983), where the flow was being sucked in towards the wall and then diverted horizontally away from the centreline near the wall, which is responsible for the large lateral spread rate. Anthony & Willmarth (1992) observed the same large spreading phenomena in a free-surface jet near the free surface. It was argued that the mechanism acting to produce this observed spreading is the creation of substantial streamwise vorticity, either from bending of vortex lines or through inhomogeneities in the Reynolds stress field.

Another important aspect of the three-dimensional wall jet is the effect of Reynolds number on the rate of spread, particularly in the lateral direction. Newman *et al.* (1972) observed no detectable change in spread rate as the discharge Reynolds number was increased from 2800 to 16,400. This observation was also supported by Law & Herlina (2002) who found that the mean flow characteristics were independent of the Reynolds number. On the contrary, Launder & Rodi (1981, 1983) document the disparity in lateral and normal spread rates among wall jets, and show the lateral spreading angle to be

highly sensitive to Reynolds number. They attribute differences in the behaviour among various wall jets at the same Reynolds number to differing jet geometries at the discharge plane.

It is clear that the flow near the free surface resembles that found for a jet discharging parallel to a solid wall. In both cases, the spread rate parallel to the wall is significantly greater than normal to the wall. This similarity between the free-surface jet and the wall jet suggests that it is the presence of a boundary at which the normal velocity must tend to zero, rather than the conditions imposed on the tangential velocity or shear stress at the boundary, which leads to the formation of an outward flow parallel to the boundary. Furthermore, the thickness of the boundary layer near the wall is at least twice that of the thickness of surface current (Anthony & Willmarth, 1992). This is most likely a consequence of the differing tangential boundary conditions; a free surface allows fluid motion in the plane of the surface, whereas at a solid surface, a boundary layer must form along the wall.

2.3.3 Wall and Free-Surface-Bounded Jets (Shallow Water Jets)

Even though jets have received considerable attention in the literature, little attention has been given to shallow jets except for the hydraulic literature, where the concern is the influence of buoyancy on the spreading and mixing of jets. The absence of detailed studies of shallow jets is particularly surprising as these conditions are, in fact, the standard case in many geophysical and environmental engineering applications. Industrial effluents, e.g. cooling water discharged into a river, lake, or tidal bay or a pumped inflow into a water supply reservoir, where the proximity of the bed and the free surface are expected to influence the flow pattern, are some examples.

Buoyant discharges in shallow water are of primary importance in environmental fluid mechanics because most wastes are discharged into shallow bodies of water where the mixing is influenced by the shallowness (Rodi, 1982). The horizontal discharge of a round buoyant jet into shallow quiescent water is a subset of this class of problem and has received specific attention from some researchers (e.g. Balasubramanian & Jain,

1978; Sobey *et al.* 1988; and Johnston & Volker 1993). The horizontal discharge of a round non-buoyant jet into shallow water has received attention from Maxwell & Pazwash (1975) and Rajaratnam (1976). As mentioned in Swean *et al.* (1989), Chu & Baddour (1984) show that very small density differences (low Richardson numbers) have a pronounced influence on jet entrainment, and hence jet behaviour which renders most of that literature of limited value to the present problem.

As mentioned earlier, detailed studies of neutrally-buoyant shallow-water jets are very scarce in the literature. A study by Dracos *et al.* (1992) was conducted using laser-Doppler velocimetry (LDV) to investigate a plane turbulent jet discharging horizontally in a shallow environment of infinite lateral extent. The water jet was discharged through a vertical slot 1 cm wide. The slot extended over the entire depth of the water in all experiments. The depth was varied over the range from 2 to 36 slot widths. It was argued that the shallow plane jet may be divided into a near-, middle-, and far-field region. The development of the jet in the near-field region, which extends to approximately two times the depth, is similar to unconfined jets. From there to a distance of about ten times the depth (the middle-field region), the flow is dominated by secondary currents. The velocity distribution of the jet becomes three-dimensional and the jet undergoes a constriction in the mid-plane and widening near the bounding surfaces. The main effect of the secondary currents is transporting fast fluid from the jet axis towards the boundaries along the vertical mid-plane, and slow ambient fluid towards the axis of the jet along the horizontal mid-plane. This transport causes a deficit of momentum flux in the mid-plane. Beyond this region the secondary currents disappear and the jet starts meandering around its centre-plane (far-field region) which accompanied with the appearance of large counter-rotating vortices alternating on both sides of the jet. The size of these structures becomes larger than the water depth and they align in a direction perpendicular to the bounding surfaces. These vortical structures increase in size with the downstream direction by pairing.

Chen & Jirka (1993) studied the mixing characteristics of a plane jet discharging in shallow water of depths 2.5 to 10 slot widths using LIF. The Reynolds numbers were

around 10,000. The depth of water was found relevant for normalising the fluctuating concentration results. The jet flow was classified into three regimes; three-dimensional flow, two-dimensional meandering flow, and stabilised flow. Their instability analysis showed that the viscosity of a free jet at low Reynolds number and the wall friction of shallow jets at high Reynolds number have similar effects in suppressing the instability.

Foss & Jones (1968) and Holdeman & Foss (1975) experimentally investigated a jet issuing from a rectangular slot spanning two walls. It was found that secondary flow structures develop at some distance from the orifice and these were attributed to vortex interaction between the free shear layers and the wall shear layers. In the experiments conducted by Holdeman & Foss (1975) with a wall spacing equal to four slot widths, these secondary flows seem to fully decay at a downstream distance of approximately 40 slot widths. Beyond that distance, the jet seems to return to the usual two-dimensional flow condition of a plane jet with a relatively thin boundary layer near the plates. McCabe (1967) gave an alternative explanation to the hypothesis suggested by Foss & Jones (1968) for the method of producing secondary flows in bounded jets. It was argued that when the vortex tube loop at the jet exit is convected into the bounded surroundings it becomes influenced by the velocity distribution across the jet which varies from a maximum at the centre to zero at its peripheries, and the effects of the non-uniform velocity distribution must deform the loop. The stretching of the vortex tube filaments near the bounding surfaces produces a decrease in its cross-sectional area and, therefore, increases the rotation associated with these portions of the vortex tube loop. This angular rotation provides an explanation of the method by which fluid is entrained into the main body of the jet.

Shinneeb *et al.* (2004b) reported PIV measurements of an isothermal round jet entering a shallow layer of water of depths 5 and 15 times the jet exit diameter (9 mm). The upper and lower boundaries of the shallow layer were a free surface and a solid wall, respectively, and the exit Reynolds number was 9000. Measurements were made on vertical and horizontal planes – both containing the axis of the jet. Results showed that, at an axial location of 65 jet exit diameters, the shallowest layer displayed an almost-

uniform profile of axial velocity with depth with a mild peak midway between the jet axis and the lower boundary. In the horizontal plane, the velocity profiles at this location were only slightly different than a free jet data for both depths considered. The Galilean decomposition was also performed on the low-pass filtered instantaneous velocity fields in order to expose vortical structures. It revealed the presence of quite large vortices in the shallowest layer which spanned 30-50% of the liquid depth. Preliminary indications of this study suggest that these structures contribute directly to shifting the peak axial velocity below the jet centreline.

2.4 COHERENT STRUCTURES

It is now well accepted that turbulent shear flows are characterised by organised motions – large scale structures with instantaneous phase-correlated vorticity – called *coherent structures*. Since coherent structures are characteristic features of turbulent flows, understanding the physics of these structures is very important. Entrainment, mixing, heat transfer, combustion, chemical reaction, drag, and aerodynamic noise generation are fields in which a better understanding of coherent structures should produce substantial technological benefits.

Even though extensive research work has been done in this area, no generally accepted definition of what is meant by coherent motion has emerged. A number of different definitions for *coherent motion* or *coherent structures* are available in the literature (see Robinson, 1991 and references therein). A coherent structure is usually associated with regions of local swirling motion and, in a frame of reference moving with the convection velocity; it might be recognised as a region where streamlines describe circular patterns (Camussi, 2002). In this review two different definitions of coherent structures are provided. According to Robinson (1991), “*A coherent motion is defined as a three-dimensional region of the flow over which at least one fundamental flow variable (velocity component, density, temperature, etc.) exhibits significant correlation with itself or with another variable over a range of space and/or time that is significantly larger than the smallest local scales of the flow*”. Hussain (1983, 1984, and 1986) gave a more restrictive definition; “*A coherent structure is a connected, large-scale, turbulent*

fluid mass with instantaneously phase-correlated vorticity over its spatial extent". The apparent randomness of the flow field is due to the random size and strength of the different types of organised structures comprising that field.

In most studies of turbulent shear flows, coherent structures are considered to be those which are large compared to the physical extent of the shear flow. However, coherent motions at scales considerably smaller than the local characteristic flow length scale can occur. In other words, the term *large-scale structure* may mean a vortex ring and can also be used to describe a rather weak and transient large-scale coherence imposed on a wide range of more energetic small scales of turbulence. Thus, large-scale structures in the turbulent region lie between these two ranges (Yule, 1978).

Studies of coherent structures have persistently supported the idea that they are generated by instability mechanisms (Tso, 1984). These mechanisms determine the flow patterns and the formation frequencies of coherent structures. Since, in various turbulent shear flows, the generated structures were found to have large vorticity concentrations in two or three dimensions, the idea to consider them as *vortices* has been well accepted (Hussain, 1986) and the term *vortex* has often been used for coherent structures like *vortex rings* or *vortex pairs*.

Turbulent shear flows have been the focus of most studies of coherent structures. In particular, the mixing layer structure appears to be the only one documented in detail except that of the near wake of a cylinder (Hussain, 1984). An example of a coherent structure of a plane mixing layer is schematically shown in Figure 2.2 in a frame advected with it. Even though the following discussions address the plane mixing layer, these points equally apply to other shear flows. The contours shown in this figure denote constant vorticity. There are two critical points; the *saddle* "A" characterised by negligible vorticity and is like a two-dimensional stagnation line. The centre "B" identifies the location of the peak value of vorticity. The flow does have a *saddle* at the centre of the braid. The *braid* is the region that connects two vortex cores. The braids are subjected to strain produced by the rolls, so that vorticity is withdrawn from the braids

and transferred to the rolls. The lines connecting the two rolls shown in Figure 2.3(a) illustrate this roll-induced strain effect graphically.

Flow visualisation shows that the *braid* consists of vortices aligned with the main flow direction (Hussain, 1984). That is, the saddle area or the braid is not a two-dimensional continuous sheet but consists of slender discrete vortices aligned with the main flow as shown in Figure 2.3(a). Adjacent vortices in the *braid* have opposite circulations so that the net circulation in the y - z plane is zero. These vortices are called *ribs*. The braid surface is perforated and consists of ribs which are not only separated from each other in the z -direction, but also they do not all lie in a surface; they are apparently randomly displaced with respect to each other in a direction normal to their axis as illustrated in Figure 2.3(b). The mechanism for the formation of the ribs is still unclear (Hussain, 1984, 1986).

Coherent structures are spatially non-overlapping; each has its own territory. The interactions of coherent structures are intrinsically nonlinear, typically involving pairing or tearing. *Pairing* means amalgamation of two structures. In addition to *complete* pairing, it is sometimes *partial*, i.e. not all of the fluid associated with the two merging structures completely coalesces; one structure captures only a part of an adjoining structure (Hussain & Clark, 1981). Occasionally there is *fractional* pairing, the merging of parts torn from different coherent structures. Tearing occurs when a structure is torn into two or more parts. Thus, the interaction between coherent structures results in new structures of different scales via either pairing (complete, partial, or fractional) or tearing. The dominance of complete pairing seems to diminish with increasing Reynolds number (Hussain & Clark, 1981) because the coherent structures probably evolve through a combination of tearing, fractional pairing, or partial pairing. This probably occurs in most fully-developed free turbulent shear flows.

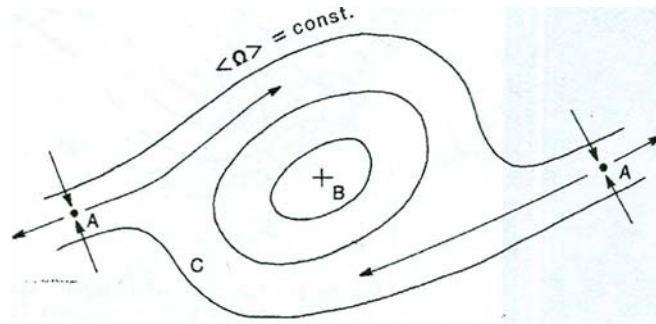


Figure 2.2: Coherent structure cross-section in a plane mixing layer (adapted from Hussain, 1984, page 457*).

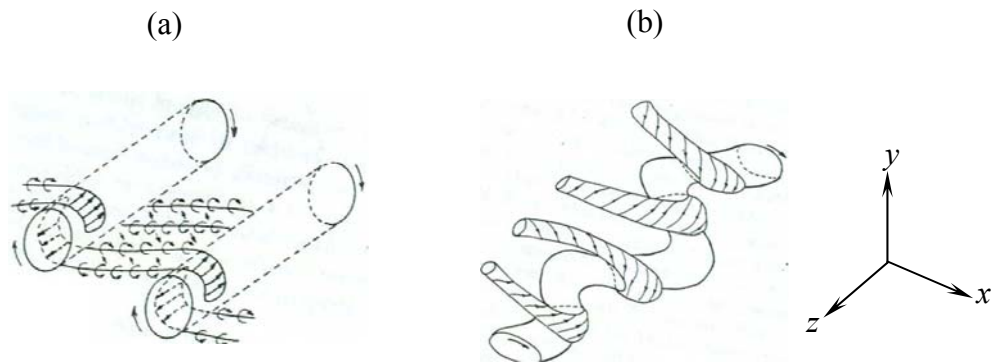


Figure 2.3: Plane mixing layer physics; (a) a picture of ideal ribs connecting rolls, and (b) a more realistic picture of ribs and rolls (adapted from Hussain, 1986, page 334**).

* Reprinted with the permission of Cambridge University Press (see written permission in Appendix B).

** Reprinted with the permission of Cambridge University Press (see written permission in Appendix B).

The structures in a turbulent flow typically have large differences in their geometrical and dynamical features (like size, shape, orientation, vortical strength, convection velocity, trajectory, lifetime, etc.). Such discrepancies impose formidable difficulties in the detection of the structures and in the understanding of their physics. A coherent structure is usually recognised via vortical flow patterns. One or more dominant patterns can usually be recognised in a flow which can be termed *preferred modes*. Thus, the preferred mode represents the most frequently occurring structure. For instance, modes 0, ± 1 , and ± 2 , sketched in Figure 2.4, are the dominant modes in axisymmetric jets. Mode 0 is known as the *axisymmetric mode*. Modes +1 and -1 represent the right-handed and left-handed *first helical mode*, respectively. Similarly, mode 2 represents two inter-twined helices. Modes +2 and -2 are then the right-handed and left-handed *second helical mode*, respectively.

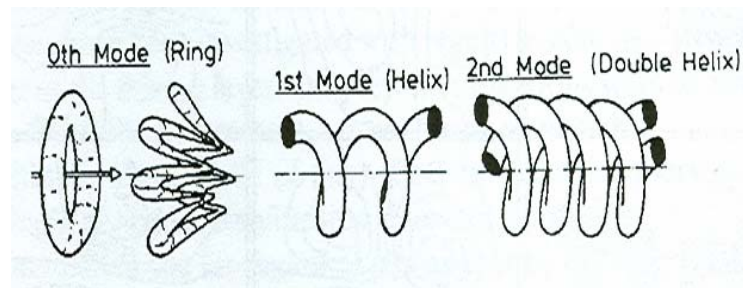


Figure 2.4: Dominant vortical and helical modes in axisymmetric jet flow, basic structural modes (adapted from Fiedler, 1988, page 250^{*}).

2.4.1 Coherent Structures in the Near-Exit Field of Jets

The existence of orderly, large-scale, vortical structures in the near-exit field, consisting of ten or so jet diameters, has been recognised for some time. This near-field organisation in the jet is often viewed as *transitional*. There is now overwhelming

^{*} Reprinted with the permission of Elsevier Press (see written permission in Appendix B).

evidence that the large-scale vortices, which control the initial growth of turbulent jets, are generated in the shear layer produced at the jet exit. The initial Kelvin-Helmholtz instability develops in the very early stages and the shear layer rolls up into primary vortical structures which appear as a sequence of vortex rings in a round jet as shown in Figure 2.5 (see for example Michalke & Freymuth, 1966; Becker & Massaro, 1968; Beavers & Willson, 1970). Hussain (1983) argued that the initial instability of the mixing layer in various jets has been found to be axisymmetric. Instantaneous velocity signals from a number of hot-wires aligned azimuthally in the shear layer near the exit of a large air jet reveal that the instability and rollup of a shear layer, as well as the large-scale structure following the rollup are instantaneously almost axisymmetric.

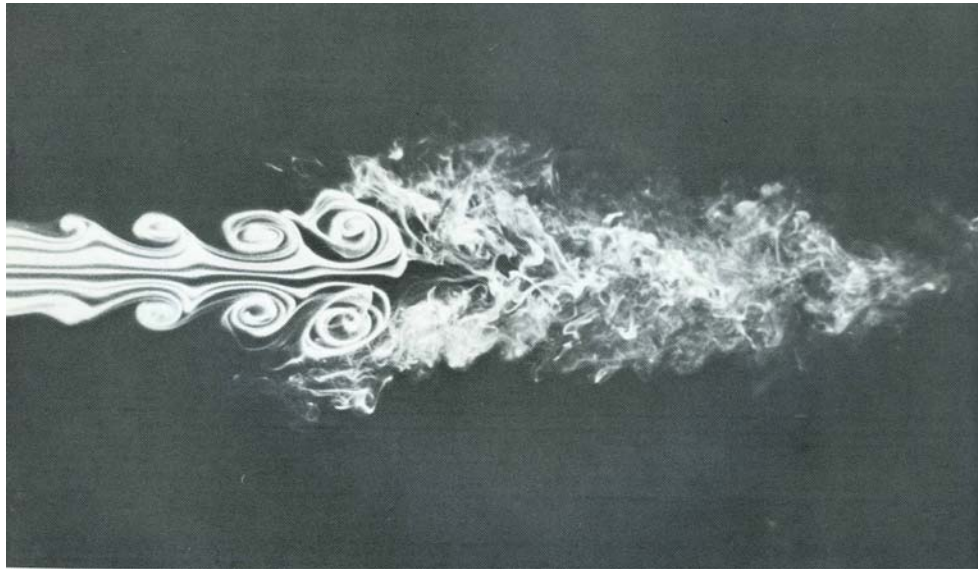


Figure 2.5: Development of axisymmetric oscillations in the near-exit region of a round jet, rolling up into vortex rings, and then abruptly becoming turbulent (adapted from Van Dyke, 1982, page 60^{*}).

^{*} Reprinted with the permission of Parabolic press (see written permission in Appendix B).

Crow & Champagne (1971), Petersen (1978), and Yule (1978) showed that this vortex structure, although produced by the laminar shear layer at the orifice, is in fact carried downstream and forms the basis of the phenomenon known as a large-scale structure. Becker & Massaro (1968) discovered ring vortices in the initial region of turbulent jets and determined that the boundary layer thickness at the jet orifice was a controlling factor in fixing the initial disturbances that produce ring vortices. Lau & Fisher (1975) and Davis & Davies (1979) confirm the basic nature of coherency in the near-exit flow field and show that the vortex production frequency f is given by a Strouhal number of fD/U_e in the range 0.3 – 0.5, where D is the jet exit diameter and U_e is the exit velocity. The most common value found for the Strouhal number is about 0.45 (Moore 1977).

As the vortices grow by entraining ambient fluid, the velocity field produced by each vortex influences other vortices so that one downstream vortex may sweep another into itself in a process called *vortex pairing*. In the initial region ($x/D < 2$) every two vortices usually pair. If the two upstream structures are close enough together, or one of the vortex rings is relatively small, three vortices will merge. The amalgamation process continues downstream until the resultant vortex ring is so large that its diameter almost spans the radius of the jet. The vortex ring then breaks down very abruptly into small structures. The location of the structural breakdown coincides with the end of the potential core and the start of mixing transition. Figure 2.5 shows rolling up of the shear layer into vortex rings and then breakdown. After the breakdown, the jet grows linearly with downstream distance. The final destruction of the initially laminar structure is a consequence of the pairing process which causes both contraction and expansion of the primary vortical rings. This contraction and stretching process might enhance the evolution of the secondary, three-dimensional structures (Liepmann & Gharib, 1992).

Yule (1978) and others have shown that the transition to turbulent flow in jets involves a relatively orderly three-dimensional deformation of the initial vortex rings. Their results show that after the growth of the primary instability, the vortex rings further develop a high degree of azimuthal structure whose breakdown may occur in a violent manner. During the breakdown process, they also observed that pieces of the core's vorticity can

pinch off to form small vortex loops. Yule (1978) then argued the importance of this azimuthal instability mode of the vortex rings, suggesting that transition in round jets involves entanglement of streets of vortex rings which have developed wave deformations along their cores.

The instability of the ring-like vortices observed in jets has further been associated with the azimuthal instability found in isolated vortex rings. For isolated vortex rings, the analytical and experimental studies of Widnall & Sullivan (1973), Widnall *et al.* (1974), Maxworthy (1972, 1974) and others have shown the existence of azimuthal instability which manifests itself in the generation of waves over the circumference of the ring. In these studies, attention is focused on the details of the generation and roll-up process to explain the instability. Maxworthy suggests that the instability may be due to vorticity of the opposite sign generated in the boundary layer on the outside of the orifice and swept into the core during the roll-up process. Widnall & Sullivan (1973) found that the number of waves around the perimeter in the unstable mode depends on the size of the vortex ring's core, i.e., the smaller the inner core, the larger the number of unstable waves. These waves are then amplified through the ring's instability.

Liepmann & Gharib (1992), in a flow visualisation study using LIF, show the formation of streamwise vortex pairs that grow from wave-like instabilities in the early development of the jet after the first rollup of the vortex sheet. The Reynolds number of the jet based on the exit condition was 5500. During the development of the primary structures, the jet core forms an azimuthal instability in the vortex sheet surrounding the flow. Once the shear layer is no longer round, small perturbations grow in the highly strained region between two vortex rings and form secondary instabilities. These secondary instabilities grow and form streamwise vortex pairs which appear as fingers of dyed fluid emerged from the braid region between two vortex cores and stretch around the following vortex (identified by an arrow in Figure 2.6). These streamwise structures are aligned in the flow direction and appear as thin periodic streaks spaced with a certain spanwise wavelength. Although they can extend outward from the centre of the jet, they are always connected to the main flow.

In order to show the distribution of the streamwise structures around the jet, cross-sectional images taken at an axial location $x/D = 3.25$ are shown in Figure 2.7. In this figure, the ring structure is shown on the left with the braid region shown on the right. This figure clearly illustrates the streamwise vortex pairs distributed around the jet. The streamwise structures in Figure 2.7(a) match the mushroom-shaped structures surrounding the braid in Figure 2.7(b). The ring exhibits azimuthal instabilities as spatial waves which are out of phase with the streamwise vortex pairs and, therefore, cannot result from the influence of the streamwise vortex pairs surrounding the ring. On the other hand, the streamwise structures in Figure 2.7(b) are in phase with the azimuthal instabilities of the potential core which supports the scenario that the streamwise structures grow out of the braid (Liepmann & Gharib, 1992).

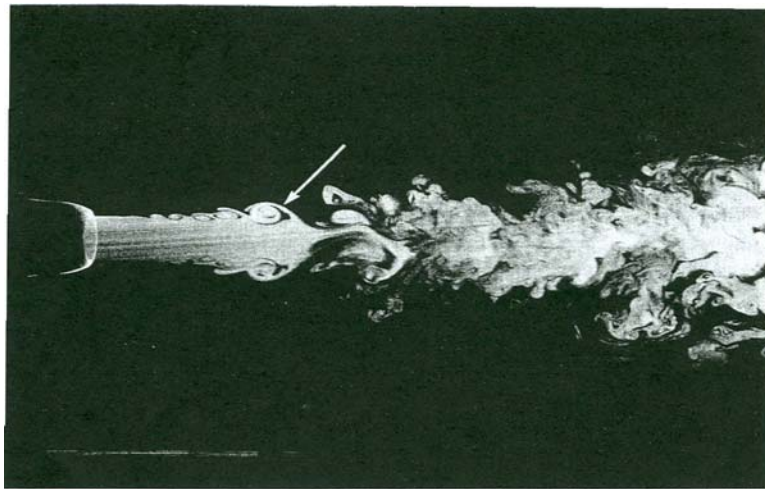


Figure 2.6: A side view of a round free jet visualised using LIF. The arrow indicates a streamwise structure at $x/D = 3.5$ (adapted from Liepmann & Gharib, 1992, page 650^{*}).

^{*} Reprinted with the permission of Cambridge University Press (see written permission in Appendix B).

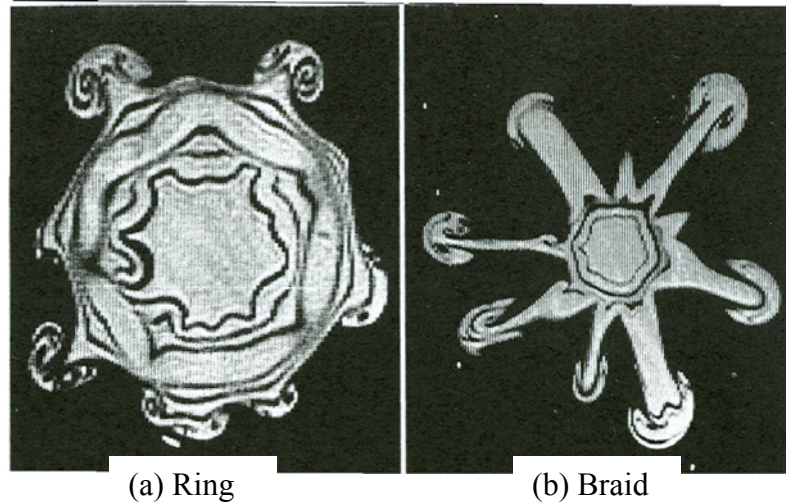


Figure 2.7: Cross-sectional images of a round free jet at $x/D = 3.25$ showing the ring and braid region (adapted from Liepmann & Gharib, 1992, page 654^{*}).

Recently, Ganapathisubramani *et al.* (2002) studied the evolution of three dimensionality in the near-exit region of a round air jet at a Reynolds number of 19,000 using stereoscopic PIV. Results showed that both the vortex cores and braids are three dimensional with a relatively large azimuthal velocity in the braid regions and also near the vortex cores. The braids contained streamwise vortex tubes aligned in the flow direction. The initial azimuthal perturbations were associated with straining regions immediately upstream of the vortex ring that formed at an axial location of $x/D \approx 0.5$. Zhou & Hitt (2004) applied the proper orthogonal decomposition (POD) technique to their large eddy simulation results for a buoyant jet. They identify an axisymmetric mode of instability near the exit and discuss the breakdown of these vortices with increasing downstream distance. Alternating direction vortices are evident in their decompositions of the predicted velocity fluctuations near the jet exit. Shinneeb *et al.* (2006) experimentally investigated vortical structures in the near-exit region of a round

^{*} Reprinted with the permission of Cambridge University Press (see written permission in Appendix B).

turbulent jet with a Reynolds number of 21,900. The measurements were made using the PIV technique and the data were analysed using the POD technique to expose the main energy-containing structures. Then, the identified structures were further quantified by computing their size, position, circulation, and direction of rotation using a vortex identification algorithm of Agrawal & Prasad (2002b). The data clearly showed the formation of alternating direction torodial vortices which begin to be resolved at a streamwise location of one-half the jet exit diameter. After this, the number of vortices decreased and their size and circulation increased as they move downstream. This is indicative of the vortex pairing process.

It should be pointed out that all the structures discussed above are axisymmetric (mode zero). However, some researchers gave evidence of the occurrence of helical modes in the transition region (see Tso, 1984 for a complete review). In a flow visualisation study by Browand & Laufer in 1975 (see Tso, 1984), it is found that mode one occurs possibly 50% of the time. In 1981, Drubka & Nagib also indicated the occurrence of mode one (see Tso, 1984). It was reported that mode zero is dominant at the jet initial region only when the Reynolds number and initial disturbance level were low. Otherwise, both modes were comparable. Hussain (1986) argued against the possibility of successive occurrence of axisymmetric and helical vortices in the jet near-exit field. It was also argued that the azimuthal phase signature of mode one can be due to tilted vortex rings which might be caused by instantaneous interactions of adjacent structures.

2.4.2 Coherent Structures in the Jet Far-Field

While considerable progress has been made toward understanding coherent motions in the transitional region of a turbulent axisymmetric jet, little is known about their nature in the fully-developed region. The explanation for this can be traced to the fact that previous measurement techniques, although successful in revealing and quantifying the coherent motions in the transitional region, were inappropriate in the fully-developed region. Another part of the problem may be attributed to the energy content of coherent structures in the far-field of jets. According to Fiedler's (1988) estimation, the energy contained in these structures is just 10% of the total turbulent kinetic energy compared

to 20% for mixing layer. Therefore, recognising structures in the far-field region is more difficult in the case of jets (Agrawal & Prasad, 2002b).

The existence of coherent motion in the fully-developed turbulent axisymmetric jet has been suspected by researchers probably ever since coherent motion became a major focus of experimental turbulence research. Tso *et al.* (1981) reported two-point correlation measurements of streamwise velocities using hot wires. The correlation curves with large streamwise separations along the half-width line were found to be similar when normalised by their peak correlations and corresponding local time scale ($2r_{1/2}/U_c$, where $r_{1/2}$ and U_c are the local half width and centreline velocity of the jet). From this similarity they inferred passage of large-scale structures of similar flow patterns in the fully-developed region. They also observed that the distribution of optimal correlations over a downstream cross-section has its maximum at the same azimuthal location as the upstream reference probe. Dimotakis *et al.* (1983), in a flow visualisation study of low Reynolds number jets ($Re = 650 - 2500$) using LIF, concluded the presence of vortices in the far field. Mungal & Hollingsworth (1989) provided experimental evidence of large coherent vortices in a very high Reynolds number ($Re = 2 \times 10^8$) jet indicating that large-scale organisation is an integral part of jet flows. These results suggested the occurrence of large-scale structures in the far-field of jets whose size was comparable to the local jet width.

Dimotakis *et al.* (1983) reported that the structures in the jet far-field are either the axisymmetric mode or the helical mode or in a transitional state between these two configurations. This conclusion was based on a visual observation of zig-zag flow patterns and symmetric flow patterns. Dahm & Dimotakis (1990) investigated the organisational modes in a jet, and suggested the presence of ring and helical modes with the jet perpetually switching between them. Yoda *et al.* (1992) found that helical and ring modes occur with almost equal probability, and that the structures maintain themselves for a large downstream distance. Based on three-dimensional concentration measurements, Yoda *et al.* (1994) proposed that the helical mode exists in pairs, such

that clockwise and counter-clockwise rotating spirals exist simultaneously. Further, they provided evidence of structures with an arrowhead shape (conical shape).

Tso & Hussain (1989) reported an experimental investigation of large-scale coherent vortical motions in the fully-developed region of a turbulent axisymmetric jet. Measurements were made in an air jet at exit Reynolds number $Re = 69,000$ by employing a radial rake of X-wires to obtain the azimuthal vorticity map. It was found that the helical mode was the most preferred and occurred 12% of the time. The double helical mode was found to occur 3% of the time. The ring mode, although present, was not considered to be dynamically important in the jet far-field. Experimental evidence showed that the helical structure has strong radial outward movement. This radial movement, in conjunction with simultaneous local ejection of turbulent fluid and subsequent entrainment of the ejected fluid with ambient fluid, appears to be a major means of jet spreading.

Agrawal & Prasad (2002a) examined the organisational modes of large vortices occurring in the axial plane of a self-similar axisymmetric turbulent jet. Measurements were conducted for a jet Reynolds number (based on the exit condition) of 3000. These large vortices were deduced by means of a Galilean transformation, i.e., by subtracting 15% of the mean centreline velocity from the low-pass filtered fields. It was found that both ring and helical modes occurred prominently in jets, with the helical mode being the more frequent. These modes were present in one-third of the ensemble size over a downstream length of four times the jet width* at the centre of the field-of-view. Despite the apparent inconsistency of these results with Yoda *et al.* (1992) and Tso & Hussain (1989), it was argued that the probability of mode occurrence correlates with the size of the field-of-view and concluded that the three studies are actually in close agreement with each other. It was also found that the low-pass filtered field occasionally exhibits arrowhead shaped structures. Furthermore, both ring and helical modes were also exposed using the linear stochastic estimation (LSE) technique.

* The jet width was defined as the radial location at which the mean axial velocity reduces to e^{-1} of the mean centreline velocity.

2.4.3 The Mechanism of Entrainment and Production

Entrainment is one of the most important properties of coherent structures. It is now believed to be mostly a result of large-scale engulfment of non-vortical fluid near the jet edge. In other words, it is the advection of the surrounding non-turbulent fluid into the body of the turbulent flow, which is responsible for the consequent expansion of the turbulent region. The entrapped fluid is then mixed completely with the core jet fluid (Agrawal & Prasad, 2002b).

The viscous diffusion of vorticity is important for the final digestion of external fluid into the turbulent flow. Once a non-turbulent blob is entrapped within the influence field of a coherent structure, the non-turbulent fluid is sheared into thin laminations with increased interface so that (molecular) diffusion of vorticity fluctuations by viscosity can effectively complete the turbulent entrainment process – the process of imparting random, three-dimensional vorticity to irrotational fluid (Hussain, 1986). Govindarajan (2002) argued that the entrainment process operates over three length scales. At the large scale, the coherent structures engulf parcels of ambient fluid. The engulfed parcels then mingle with original shear-flow fluid by breaking-up/stretching into smaller scales. Subsequently, the fluids mix at the molecular level when their characteristic sizes are comparable to molecular diffusion scales. It was also argued that vortical structures in the interior of the jet do not participate in the entrainment process, and the contribution of small-scale structures is negligible.

Hussain (1986) postulated that when entrained fluid at the saddle (see Figures 2.2 and 2.3) reaches the primary structure with large vorticity in shear flows, the interaction of the two orthogonal vortices produces three-dimensional turbulence and mixing. It was concluded that the point where the ribs connect with the rolls is the site of three-dimensional mixing. It was also found that turbulence production is maximum at the saddle which is also characterised by a very low value of vorticity. Since mixing, hence dissipation, occurs at the connection points of the ribs with the rolls, while production is maximum at the saddle, the sites of dominant production and dissipation seem to be different (Hussain, 1986).

The continual stretching of ribs (see Figure 2.3) causes them to spin faster due to conservation of angular momentum. This is equivalent to increasing velocity fluctuations and hence production of turbulence. This is the mechanism of continual replenishment of turbulence, which would otherwise decay due to dissipation. Thus one can say that coherent structures have a built-in mechanism for their own survival, albeit short-time survival. Based on these observations, Hussain (1986) claimed that *vortex stretching* is the physical mechanism for entrainment and production in all turbulent flows.

2.5 REYNOLDS NUMBER EFFECTS

The concept of Reynolds number similarity has been widely used in fluid dynamics research. Reynolds number similarity has been and is still the most fundamental hypothesis in turbulence. Reynolds numbers encountered in practice are usually very high. For the sake of convenience in education and/or flow visualisation, many coherent structure studies have been performed at very low Reynolds numbers.

The underlying concept in the similarity hypothesis is that the flow is dominated by large scales which remain unaffected with increasing Reynolds number that can only affect the fine scales. The increasing separation of the large (energy-transforming) and fine (energy-dissipating) length scales with increasing Reynolds number suggests decoupling of the two scales at high Reynolds number. The stability analysis and experiments of Widnall & Sullivan (1973) indicated that vortex rings studied at low Reynolds numbers are stabilised by viscous effects, and therefore, the results should not be extrapolated to high Reynolds numbers. Roshko (1976) argued that the large-scale processes and the resulting mean flow are very little affected by viscosity down to small values of Reynolds number. However, Hussain (1983) argued that when considering the instantaneous variable to consist of three components; the time-mean component, the coherent component, and incoherent turbulence, it was observed that smaller scales are produced in regions of intense shear within coherent structures and are concentrated in preferential regions of coherent structures, which indicates that incoherent turbulence is

produced and spatially organised by coherent structures in a turbulent shear flow. It was concluded that the coherent and incoherent turbulence are not totally uncoupled which is inconsistent with the underlying concept of the Reynolds number similarity hypothesis which states that the large and fine scales are decoupled.

Even though there appears to be a universal belief in Reynolds number similarity, there has not been any study to critically examine it. The range of Reynolds numbers in which the similarity hypothesis may hold is still a question to be answered. Therefore, one must be cautious of a straightforward extrapolation to higher Reynolds numbers (Hussain, 1986). Hussain (1983) observed that the detailed features of coherent structures in jets at Reynolds numbers significantly below 10^5 may not be totally relevant to high Reynolds number jets.

2.6 EDUCATION OF COHERENT STRUCTURES

The process of measuring the properties of a flow structure over its spatial extent is now popularly known as *eduction* (Hussain, 1986). Since the discovery of coherent structures, prescribing a method for describing and identifying these structures from a turbulent flow has been a challenge. In 1977, Zilberman *et al.* wrote (see Aubry *et al.*, 1988): “*We cannot unambiguously define the signature of an eddy without a priori knowledge of its shape and its location relative to the observation station and cannot map such an eddy because we do not have a proper criterion for pattern recognition*”. However, some methods of analysis have been employed to obtain useful information about the characteristics of these structures.

Perhaps more than any other tool available, flow visualisation employing dye, particles, bubbles, and smoke has played a major role in the study of turbulent coherent motions (Robinson, 1991). This technique is often combined with quantitative probe anemometry and is generally limited to low Reynolds numbers. Although visualisation is relatively simple and is capable of giving both global and local behaviour, it can be misleading (Holmes *et al.*, 1996). Furthermore, visualisation methods cannot provide quantitative information and pointwise measurements suffer from inadequate spatial resolution.

Recently, LIF has emerged as a useful tool which allows visualisation of coherent structures. This technique is usually coupled with simultaneous velocity field measurements, performed via particle image velocimetry (PIV).

A variety of statistical analysis tools has emerged to detect and characterise coherent motions. Among these techniques are; conditional sampling methods, the variable-interval time average (VITA) method, and the quadrant method (Robinson, 1991). More sophisticated statistical techniques employed to reduce the structure of organised turbulent motions include proper orthogonal decomposition (POD) and stochastic estimation of the single-point and two-point correlation tensors.

A modern statistical tool, which was introduced a little more than a decade ago, is wavelets. The wavelet transform is used in many fields, including signal processing, data compression, image coding, and numerical analysis (Gad-el-Hak, 2000). The wavelet transform is a mathematical tool which is capable of providing both a wavenumber and a physical space analysis simultaneously. This advantage makes it a suitable tool for detecting and analyzing coherent structures. On the other hand, the Fourier transform is not well suited for analysing coherent structures because its basis functions are perfectly localised in wavenumber space and it hides physical space information (Bonnet *et al.*, 1998). Wavelet analysis can be viewed as a multi-level or multi-resolution representation of a function.

The proper orthogonal decomposition (POD) was introduced by Lumley in 1967 (see Holmes *et al.*, 1996) as an unbiased method for extracting structures in a turbulent flow. In other disciplines the same procedure goes by the names; Karhunen-Loeve decomposition, principal components analysis, singular systems analysis, and singular value decomposition (Holmes *et al.*, 1996). POD has been of great use because it is the most efficient way of extracting the most-energetic components of an infinite-dimensional process with only a few modes (Adrian *et al.*, 2000 and Holmes *et al.*, 1996). The attractiveness of the POD lies in the fact that it is a linear procedure, i.e, a linear superposition of POD basis functions. However, the linear nature of the POD is

the source of its limitations. POD requires measurement of the spatial cross-correlation of the velocities in a turbulent flow field. The measurements are usually carried out at selected spatial positions in one or two lateral directions using multiple hot-wire probes, but this requires great experimental effort (Citriniti & George, 1999). PIV has also been used in the application of POD. The potentially high spatial resolution of PIV data makes it an ideal experimental technique for use with POD (Barker, 1998 and Bi *et al.*, 2003).

Bonnet *et al.* (1998) reported an experimental study to test and compare several coherent structure eduction methods using the same data base. The flow chosen was a plane, incompressible, fully-developed, turbulent, mixing layer. The data were collected from hot-wire rakes. The techniques chosen for discussion were; conditional sampling (vorticity-based and other methods), wavelets, pattern recognition analysis, proper orthogonal decomposition, stochastic estimation, topological concept-based methods, and full-field methods (e.g., pseudo flow visualisation). Good quantitative and qualitative agreement between the different methods was observed as well as some differences noted. As an example, the size of the averaged structures computed from the various methods compare to within 6%. It was also found that the wavelet transform is not efficient when it only uses the information obtained at a single location.

Camussi (2002) proposed a new technique to extract and characterise coherent structures from two-dimensional PIV data using the wavelet transform. This method is based on the analysis of the local energy content at separated scales. It is found that this method can correctly identify coherent structures, separate their energetic contribution scale-by-scale, and determine the length scale of the structures and the precise spatial localization of the vortex cores. From comparison of this method with more standard reference techniques, the agreement was satisfactory. The main shortcoming of this method is the resolution, a problem which is directly associated with the use of the wavelet transform. This means that this method is reliable only for structures whose length scale is much larger than the measurement resolution; otherwise the error will be of the same order as

the quantity to be measured. Another problem is that this method cannot separate structures with positive or negative vorticity.

Agrawal & Prasad (2002a) used the Galilean transformation to identify and visualise large vortices occurring in a self-similar region of a turbulent jet. This method may be summarised as follows. First, the instantaneous PIV frame is convolved with a Gaussian kernel to obtain a low-pass filtered field. This process removes the high frequency content and retains low frequencies which correspond to the largest vortices in the flow. Next, the low-pass field is Galilean transformed by subtracting the advection velocity of the vortices (about 15% of the local mean centreline velocity) from the low-pass filtered fields. In this method, only vortices larger than the cut-off filter size ($R > 5$ grid units) were exposed. The linear stochastic estimation (LSE) technique was then applied to the Galilean-transformed low-pass filtered fields in order to analyse the organisational modes of large-scale vortices. It was argued that stochastic estimation of PIV data is equivalent to conditional averaging of pointwise data.

2.7 SUMMARY

Although jets have received considerable attention in the literature, little attention has been given to shallow jets except for the hydraulic literature, where the concern is the influence of buoyancy on the spreading and mixing of jets. Studies of turbulent structure of shallow water jets are very scarce in the literature although these conditions are the standard case in many geophysical and environmental engineering applications. Previous studies indicated that the development of a plane turbulent jet in the axial direction discharging horizontally in a shallow environment was divided into three regimes; a near-, a middle- and a far-field region. The development of the jet in the near-field region, which extends to approximately two times the depth, is similar to unconfined jets. From there to a distance of about ten times the depth (the middle-field region), the flow is dominated by secondary currents. The velocity distribution of the jet becomes three-dimensional and the jet undergoes a constriction in the horizontal mid-plane and widening near the bounding surfaces. Beyond this region the secondary currents disappear and the jet starts meandering around its centre-plane (far-field

region), which accompanied with the appearance of large counter-rotating vortices alternating on both sides of the jet. The size of these structures becomes larger than the water depth and they align in a direction perpendicular to the bounding surfaces. These vortical structures increase in size with the downstream direction by pairing.

Most studies of turbulence have been performed by investigating either the mean flow quantities (the RANS approach) or through correlations of fluctuating velocity (statistical theory). These approaches have provided many insights into the turbulence phenomena. A basic flow for turbulence research that has received considerable attention by many researchers is the free round jet. Most of these studies have focused on the evolution and dynamics of coherent structures in turbulent jets. This is motivated by the role of coherent structures in processes of practical interest such as entrainment and mixing. The coherent vortical structures in the near-exit region of a round turbulent jet have received more attention compared to the far field. The reason may be attributed to the measurement techniques which are inappropriate in the fully-developed region. Despite the extensive work done in this area, there is no generally accepted definition of coherent structures. However, a number of definitions are available in the literature and two definitions are provided in this review. These structures are generated by instability mechanisms which determine the flow patterns and the formation frequencies. Coherent structures have large differences in their geometrical and dynamical features. One or more dominant patterns can usually be recognised in a flow which is termed *preferred modes*. These structures have large vorticity concentrations and it is well accepted to consider them as vortices. The interaction between coherent structures involves pairing (complete, partial, or fractional) and tearing.

Reynolds numbers encountered in practice are usually very high. For the sake of convenience in education and/or flow visualisation, many coherent structure studies have been performed at very low Reynolds numbers. Hussain (1983) found some evidence that is inconsistent with the underlying concept of the Reynolds number similarity hypothesis and warned against straightforward extrapolation of the low Reynolds number results to higher Reynolds numbers.

Some methods have been used to obtain useful information about the characteristics of coherent structures. The overwhelming majority of coherent structure studies have been based on flow visualisation using dye, particles, bubbles, and smoke. Another technique, which allows visualisation of coherent structures, is the Laser-Induced Fluorescence (LIF). In addition, a variety of statistical analysis tools to detect and characterise coherent structures is also available. Among these techniques are; conditional sampling methods, the variable-interval time average (VITA) method, and the quadrant method (Robinson 1991). More sophisticated statistical techniques employed to educe coherent structures include proper orthogonal decomposition (POD), stochastic estimation of the single-point and two-point correlation tensors, and wavelets.

Chapter 3

EXPERIMENTAL APPARATUS AND INSTRUMENTATION

3.1 EXPERIMENTAL SETUP

3.1.1 General Remarks

A turbulent water jet was generated using a closed-loop system. The purpose of the loop was to produce a steady-state turbulent jet issuing from a 9 mm diameter nozzle into a shallow layer of water. The depth of the shallow layer was adjusted to give different degrees of vertical confinement, while the lateral and axial confinements were negligible. The jet was at the same temperature as the receiving water and was therefore neutrally buoyant. The average jet exit velocity was $U_e = 2.5$ m/s yielding a Reynolds number of $Re_D = 22,500$.

3.1.2 Test Setup

The experiments were performed in a long, glass-walled water tank shown in Figure 3.1. The water tank has nominal interior dimensions of 0.7 m depth, 1 m width, and 4 m length. The apparatus consists of an insert placed in the water tank and a water supply system. The insert, which consists of a false floor and a vertical jet exit plate, was placed

inside the water tank as shown schematically in Figure 3.1. The false floor, which was made of glass to allow optical access from below, formed the bottom boundary while the top boundary was the free surface. This false floor was supported by a stainless steel frame (not shown). This frame hung from the top of the water tank by four threaded rods. The maximum deflection of the false floor due to its own weight was estimated to be only 1.1% of the jet exit diameter (~ 0.1 mm). The axial length of the false floor was 1 m and it was 0.863 m wide. The water layer depth H was controlled by varying the position of the false floor. Water was discharged through an orifice of diameter $D = 9$ mm into the fluid layer. The discharge nozzle was located at the centre of the vertical jet exit plate, i.e. it was midway between the false floor and the free surface.

The water supply system consisted of a submersible pump, a constant-head tank, a flow control valve, a turbine flowmeter, a flow conditioner, and the jet exit itself. The submersible pump supplied water from the water tank to the constant-head tank. The head tank provided a constant head of ~ 5 m. The jet flow was generated by the hydrostatic pressure difference between the head tank and the water tank.

A cross-section of the flow conditioner and jet exit is shown in Figure 3.2. The flow conditioner was attached directly to the jet exit plate (see Figure 3.1) and consisted of a 160 mm long, 112 mm diameter section. It contained three wire screens to break down the turbulence and a flow straightener which was made of drinking straws with a length to diameter ratio of 20. Following the flow conditioner, the jet was formed by a circular-arc exit with a radius equal to the exit diameter (9 mm). The exit plane of the jet was flush with the jet exit plate. As will be shown in Chapter 5, this configuration was successful in producing very uniform, top-hat velocity profiles (see also Shinneeb *et al.*, 2006). The jet exit turbulence level was only 0.3%.

3.1.3 Flowmeter Calibration

The flow rate was measured by a turbine flowmeter. The flowmeter was calibrated by weighing the quantity of water that passes through it during a period of time. The flow rate was regulated by a valve situated at the outlet of the flowmeter. The calibration was

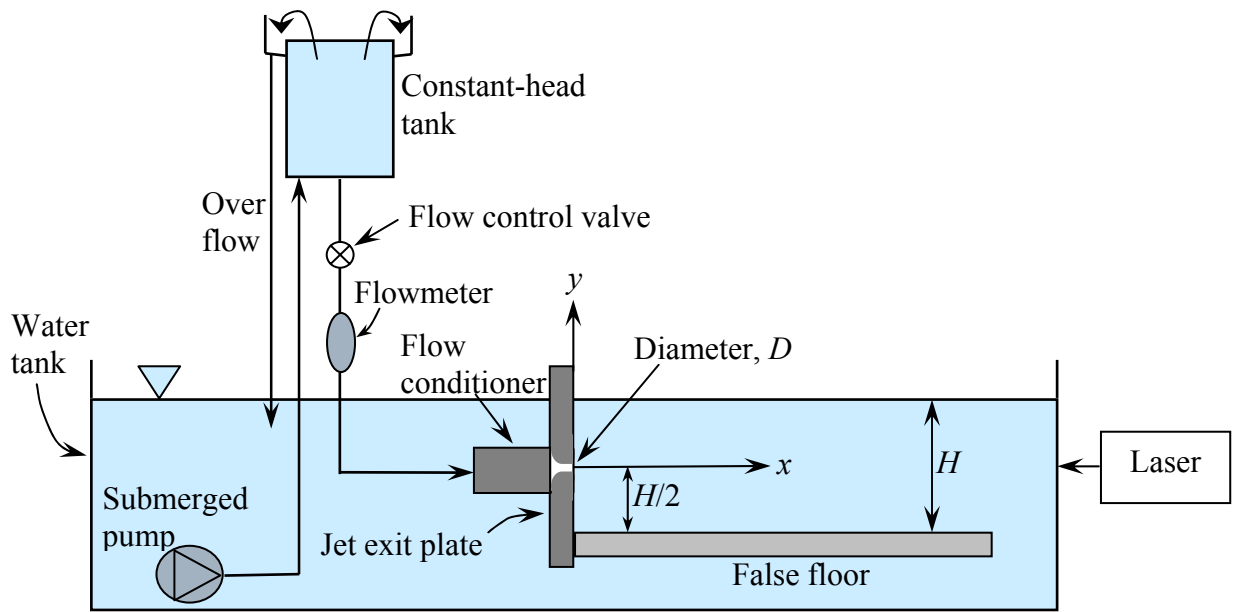


Figure 3.1: Schematic description of the apparatus used to study shallow water jets (not to scale).

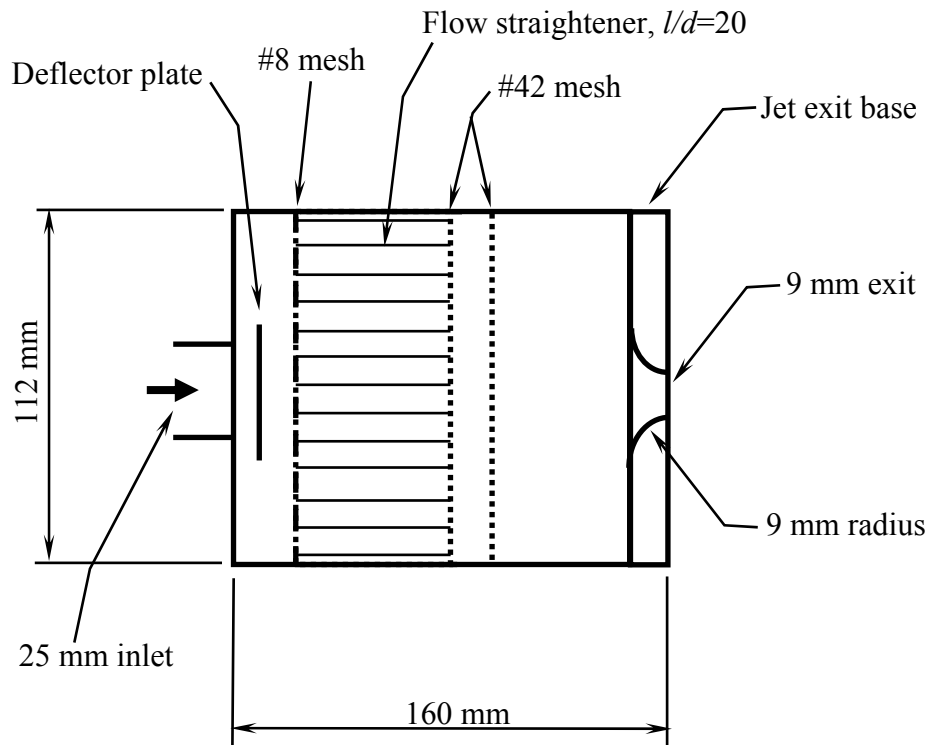


Figure 3.2: Schematic of flow conditioner and jet exit (not to scale).

carried out by collecting 11.8 kg of water in a container and recording elapsed time with a stopwatch. Measurements of the flow rate were recorded for ten different valve settings starting from fully-open. For each valve setting, ten repeated measurements were made and then averaged. The water temperature was monitored by a thermometer and there was negligible variation in the temperature during the experiment. The linear relationship between the flow velocity to the output voltage is

$$U_f = 1.1589\ddot{E} + 0.0349 \quad (3.1)$$

where U_f is the flow velocity (m/s) and \ddot{E} is the voltage (volts). The goodness-of-fit of the measured data can be assessed by the correlation coefficient of the linear fit (0.9992). The density of water used for converting the mass flow rate to flow velocity was determined at room temperature ($20 \pm 1^\circ\text{C}$), which is $\rho = 998 \text{ kg/m}^3$.

3.2 PARTICLE IMAGE VELOCIMETRY

3.2.1 General Remarks

Particle image velocimetry (PIV) is a non-intrusive technique to measure the velocity in a flow field at multiple points simultaneously. The basic premise of PIV is to measure the velocity of markers or seed particles in the flow within a plane. PIV provides an Eulerian description of the velocity, since the velocity vector is obtained by calculating correlations for interrogation areas (IA). Specifically, the velocity is determined using the basic definition

$$\tilde{\mathbf{V}}(\mathbf{X}, t) = \frac{\Delta\mathbf{S}(\mathbf{X}, t)}{\Delta t}, \quad \Delta t \rightarrow 0 \quad (3.2)$$

where $\tilde{\mathbf{V}}(\mathbf{X}, t)$ is the particle velocity vector at position \mathbf{X} and time t and $\Delta\mathbf{S}$ is the displacement vector of the seeding particle during the elapsed time Δt .

The theory of PIV was introduced by Adrian (1988) with the first experimental implementations followed shortly afterwards (Keane & Adrian, 1990 and 1991). At that stage, a single photographic frame was multiply exposed and analysed using auto-correlation. Improvements in image recording technology have allowed images to be captured on separate frames for analysis by cross-correlation techniques. The introduction of digital camera technology to PIV enabled the direct recording of particle images, at the expense of reduced spatial resolution, resulting in the development of digital PIV (DPIV). Along with these hardware advances, the speed and accuracy of PIV analysis techniques have significantly improved in the last decade because of development of new algorithms.

3.2.2 PIV Image Acquisition

PIV measurements are carried out in four steps; seeding the flow under investigation with particles, illuminating the tracer particles by a light sheet, capturing images, and analysing the images. The steps of the data acquisition are described in more detail below.

a) Seeding Considerations

In PIV, fluid velocity is inferred from the measurement of particle velocities. Hence, particle characteristics are important in determining their ability to follow the flow. The seeding particles must be small enough to accurately follow the flow and at the same time large enough to scatter sufficient light to be properly recorded by a camera (Raffel *et al.*, 1998). In addition, these particles must be small and their density close to the fluid density to be able to track the flow motion and minimise the difference between the flow and particle velocity. Moreover, their light scattering properties must be good to ensure that the particles are bright enough when captured by a camera (Raffel *et al.*, 1998).

The particle size should be selected such that the particle image diameter is approximately two pixels to ensure that each particle's position can be accurately determined. The particle image size becomes larger than the actual particle size because

of diffraction effects. The size of the particle image depends on its light scattering properties, the laser intensity, and the recording optics (Raffel *et al.*, 1998).

The capability of the seeding particles to follow the flow must be assessed. One measure of the particle's ability to track the flow effectively is its terminal velocity. Assuming a spherical particle, the Stokes settling velocity is given by (Clift *et al.*, 1978)

$$u_T = \frac{gd_p^2(\rho_p - \rho)}{18\mu} \quad (3.3)$$

where d_p is the particle diameter, ρ_p is the particle density, and μ is the fluid's dynamic viscosity. The particles used in this study had a specific gravity of 1.1 and a mean diameter of 10 μm . From equation 3.3, their settling velocity in stagnant water was approximately 0.0055 mm/s corresponding to a particle Reynolds number 0.000054.

The suitability of the seed particles to follow the turbulent fluctuations may be assessed by the following criterion (Clift *et al.*, 1978):

$$St \ll \frac{2\chi + 1}{9}. \quad (3.4)$$

Here χ is the ratio of the particle density ρ_p to the fluid density ρ . In this equation, St is the Stokes number which is defined as the ratio of the particle response time to an appropriate fluid timescale ($St = \tau_p / \tau_f$). The particle response time τ_p may be calculated by the following relation (Milojevic, 1990)

$$\tau_p = \frac{\rho_p d_p^2}{18\mu f_d} \quad (3.5)$$

where $f_d = 1.0 + 0.15Re_p^{0.687}$ is the particle drag coefficient and $Re_p = \frac{\rho d_p u_T}{\mu}$ is the particle Reynolds number calculated based on the terminal velocity of the particle.

A fluid timescale in the range $x/D \leq 3.8$ can be determined from (Longmire and Eaton, 1992)

$$\tau_f = \frac{L_v}{U_v} \quad (3.6)$$

where L_v is an eddy lengthscale and U_v is an eddy velocity scale. According to Longmire and Eaton (1992), the fluid velocity scale is assumed to be half of the jet exit velocity ($U_v = 0.5U_e$). Moreover, in the region up to $x/D = 3.8$, the vortex lengthscale L_v ranges from $0.26D$ to $1.2D$, where D is the jet exit diameter. They argued that the particles are influenced by the vortices in this region starting from $x/D = 1.6$. At this position the fluid lengthscale is given by $L_v = 0.655D$.

In the zone of established flow (ZEF), the Kolmogoroff timescale, which represents the smallest timescale of the motion, is the appropriate fluid timescale. It is calculated by (Milojevic, 1990)

$$\tau_f = \left(\frac{\nu}{\varepsilon} \right)^{1/2} \quad (3.7)$$

where ν is the fluid kinematic viscosity and ε is the turbulent energy dissipation and can be calculated by (Milojevic, 1990)

$$\varepsilon = C_\mu \frac{k^2}{\nu_t} \quad (3.8)$$

where $C_\mu = 0.09$ is a model coefficient, ν_t is the turbulent viscosity, and k is the kinetic energy of turbulence which is given by (Milojevic, 1990)

$$k = 0.5(u_{\text{rms}}^2 + v_{\text{rms}}^2 + w_{\text{rms}}^2) \quad (3.9)$$

Here u_{rms} , v_{rms} , w_{rms} are the root-mean-square fluctuating velocities in the axial, radial, and azimuthal directions, respectively. Since w_{rms} is not measured in this experiment, it will be assumed that $w_{\text{rms}} = v_{\text{rms}}$ in the absence of better information. The turbulent viscosity ν_t for free jets in the zone of established flow is defined by Schlichting (1979)

$$\nu_t = 0.0256r_{1/2}U_c \quad (3.10)$$

where $r_{1/2}$ is the half-width of the jet and U_c is the mean centreline velocity. This relation indicates that the turbulent viscosity is constant and, hence, independent of the axial direction x .

In order to assess the dynamic tracking characteristics of the particles, information about length and velocity scales of the flow must be known. For this reason, the following discussion will address only the free jet case since estimations of these scales are known. If the results demonstrate the capability of the particles to follow the turbulent flow in the free jet case, these results can be extrapolated to shallow jet cases. To ensure that these particles follow the turbulent fluctuations, the largest Stokes number St must be much smaller than 0.36 as suggested by equation 3.4. From equation 3.5, the particle response time τ_p equals 6.11×10^{-3} ms. At $x/D = 1.6$, the fluid velocity scale U_v is 1.25 m/s and the vortex length scale L_v is 5.895 mm. Therefore, the fluid timescale given by equation 3.6 is 4.72 ms yielding a value of St of about 1.30×10^{-3} .

Figure 3.3(a) shows the radial variation of the Stokes number St in the far field at $x/D = 12, 15, 20,$ and 25 . It is obvious that the highest Stokes number St occurs near the centreline of the jet. Figure 3.3(b) shows the axial variation of the Stokes number along the centreline of the jet in the far field. It can be seen that the Stokes number decreases in the downstream direction. This figure shows that the highest Stokes number occurs at $x/D = 12$ and its value is 7.56×10^{-3} . Since the highest values of the Stokes number in

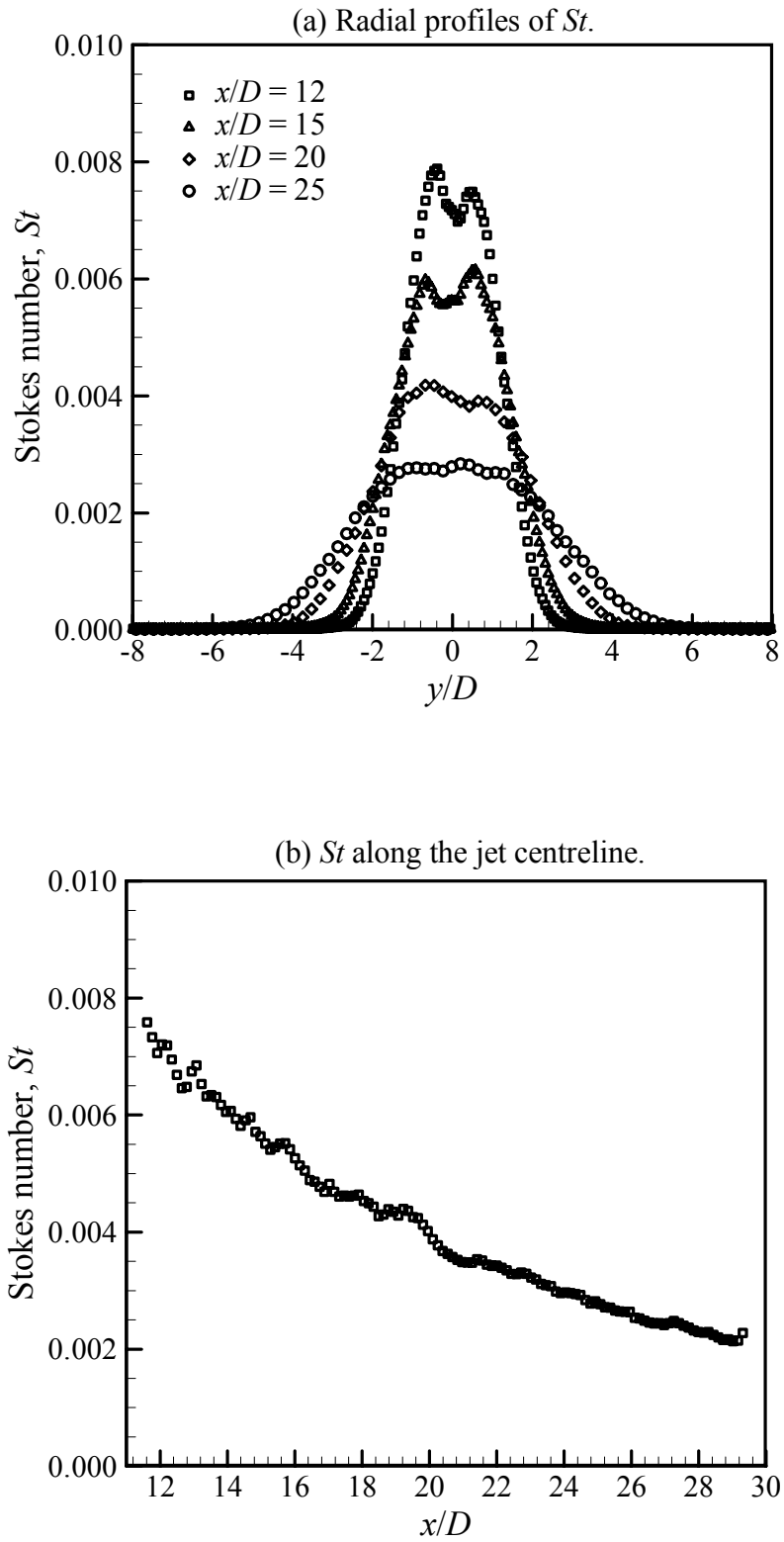


Figure 3.3: Variation of the Stokes number St in the far field of the free jet; (a) Radial profiles of St at different axial locations, and (b) St along the centreline of the jet.

the near-exit and far-field regions are much less than 0.36 as given by equation 3.4, this gives an indication that these particles are expected to follow the turbulence fluctuations faithfully in this application.

The spatial resolution of the velocity information obtained from PIV depends in part upon the number of particles per unit volume of the fluid. Each interrogation area must have a minimum number of particles (typically 10 to 20) to make successful velocity measurements. The concentration of particles should be large enough to ensure that every interrogation spot contains several particle images. The seeding concentration \check{C} is given by (Adrian, 1991)

$$\check{C} = N_1 / \delta z d_1^2 \quad (3.11)$$

where N_1 is the number of particles required per interrogation area, δz is the light sheet thickness, and d_1 is the interrogation area size. The quantity $\delta z d_1^2$ is the illuminated volume of the fluid for each interrogation area. The characteristics of the seeding particles and the laser used in this work are given in Table 3.1.

In this work, the seeding process was performed by preparing a high-concentration stock. The high concentration stock was prepared by mixing a known weight of the seeding particles (hollow glass spheres) in a known volume of water. One advantage of making this stock was to ensure that the particles are well mixed in the water. It is also convenient for increasing the seeding density in the case of not having enough seeding in the test section. First, the estimated amount of the prepared high-concentration stock was introduced to the water tank (see Figure 3.1). This step was performed after the water was carefully filtered through a 1 μm filter. Knowing the volume of water in the water tank, the required amount of the high-concentration stock was calculated according to equation 3.11 and then added to the water tank to ensure that each interrogation volume $\delta z d_1^2$ contains enough number of particles.

Table 3.1: Characteristics of the seeding particles and the laser.

Seed particles type	Hollow glass spheres
Particle mean diameter, d_p	8 to 12 μm
Specific gravity, χ	1.05 to 1.15
Refractive index	1.5
Number of particles in IA	10 to 20
Light sheet thickness, δz	~ 1 mm
Laser wavelength	532 nm
Laser energy	50 mJ/pulse
Laser repetition rate	15 Hz

b) Illumination

The requirements of the illumination system are as follows:

- The illumination pulse duration must be short to avoid image blur caused by motion of the seed particles during the exposure time,
- The separation time between the two illumination pulses must be such that the particles travel approximately 1/4 to 1/3 the length of the interrogation area, and
- The illumination intensity must be high enough so that individual particles can be detected.

These requirements were achieved using dual Nd:YAG lasers which provided a very short pulse duration of 6 ns with an average of 50 mJ/pulse at a wavelength of 532 nm (see Table 3.1). This high intensity light allows the use of small particles. Since the repetition rate achievable with a single laser of this type is only 15 Hz, two identical lasers, which share beam delivery optics, are used. In this way the time between the two illumination pulses can be made arbitrarily short. A Berkeley Nucleonics 500B pulse generator was used to trigger the two lasers and could be programmed to give any desired pulse separation.

The illumination must take the form of a thin sheet of light in the image recording device's field-of-view. To generate the light sheet, the laser beam passes through a spherical lens and a cylindrical lens as shown in Figure 3.4. The spherical lens controls the light sheet thickness while the cylindrical lens controls the light sheet height. The thickness of the light sheet is an important parameter. It needs to be thin enough to provide good spatial resolution and should be compatible with the depth of the field of the recording optics. The thinnest portion of the light sheet is located at the focal length of the spherical lens.

In this study, the light sheet was formed through a 1000 mm or 2000 mm spherical lens and a -6.4 mm, -12.6 mm, or -25 mm cylindrical lens depending on the size of the field-of-view desired. The light sheet was oriented vertically or horizontally according to the desired measurement plane. Both light sheet orientations included the axis of the jet in the light sheet. The light sheet entered the end of the water tank as shown in Figure 3.1, while the optical axis of the camera was positioned perpendicular to it – either at the side or underneath the tank. In some cases, the light sheet entered the side of the water tank to obtain brighter illumination by allowing the light source to be closer to the field-of-view.

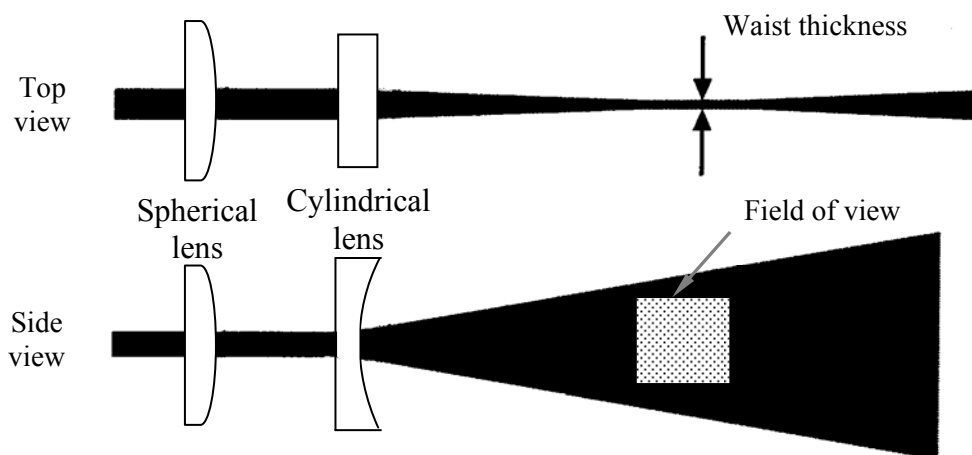


Figure 3.4: Generation of a light sheet with spherical and cylindrical lenses.

c) Image Recording

The light scattered by the seeding particles was captured on Charge Coupled Device (CCD) array which is referred to as digital PIV (DPIV). In DPIV, the particle images are digitized and sent to the computer during acquisition. With recent improvements in the speed and spatial resolution of digital cameras, the digital approach is becoming more favoured. Indeed, CCD arrays are now widely used for PIV recordings.

A CCD camera sensor consists of a very large number of light sensitive cells or pixels, each capable of producing an electric charge proportional to the amount of light falling on it. The pixels are arranged in a two-dimensional array and facilitate the capture of a single image with a single exposure. The resolution of a CCD camera is the total number of pixels which make up the light sensitive area of the camera sensor. A greyscale digital image is a matrix of pixels, each having a specific intensity. The number of distinct intensity levels is 2^A where A is the number of bits in the binary representation of the intensity level. There are 256 intensity levels for 8-bit greyscale images. Intensity level 255 represents white and zero represents black.

In this study, all measurements were acquired with a Roper ES4.0/E Megaplus camera operating in dual capture mode. The resolution of this camera is 2048×2048 pixels. A Berkeley Nucleonics 500B digital delay generator was used to trigger the lasers and provide synchronisation with the camera. The framegrabber was an EDT PCI DVC-Link. The camera was fitted with a 60 mm Micro-Nikkor lens and the object distance was adjusted to give the field-of-view required for each image. Image calibration was achieved by taking a picture of a steel ruler with 1 mm divisions and it was confirmed that there was negligible distortion over the field-of-view.

With the interrogation area size determined, the required time between the two laser pulses Δt was calculated. Δt was selected such that the particles would travel approximately 8 to 10 pixels in the interrogation area. The calculation of Δt was based on the maximum velocity in each field-of-view.

3.2.3 PIV Image Analysis

The main objective of the statistical evaluation of PIV recordings is to determine the displacement between two patterns of particle images, which are stored as a two-dimensional distribution of grey levels. It is common in signal analysis to determine the shift in time between two nearly identical time signals by means of correlation techniques. There are basically two correlation methods in use; the auto-correlation and cross-correlation methods. The auto-correlation method is used for multiple-exposure of the particle images on a single frame, while the cross-correlation technique is used for exposures on two separate frames.

The cross-correlation method

When two separate frames contain particle images from the respective light pulses (dual-frame PIV), it is possible to use cross-correlation techniques. This is the case for DPIV. The advantage of cross-correlation is that the signal-to-noise ratio is superior to auto-correlation. Also, no directional ambiguity exists.

The analysis of PIV images begins by subdividing the entire image into small “interrogation” areas. The interrogation area (IA) size should be chosen sufficiently small such that the second order effects such as displacement gradients can be neglected. A typical interrogation area would be a 64 by 64, 32 by 32, or 16 by 16 pixel region of the image. Each interrogation area should contain several particle images. The purpose of the analysis is to locally find the best match between the images in a statistical sense. This is accomplished through the use of the cross-correlation function $CC(\mathbf{s})$, which is determined by (Adrian, 1991)

$$CC(\mathbf{s}) = \iint_{IA} I_1(\mathbf{X}) I_2(\mathbf{X} + \mathbf{s}) dA \quad (3.12)$$

where $I_1(\mathbf{X})$ and $I_2(\mathbf{X})$ are the intensity of two interrogation area images extracted from separate frames. Essentially, the cross-correlation function statistically measures the

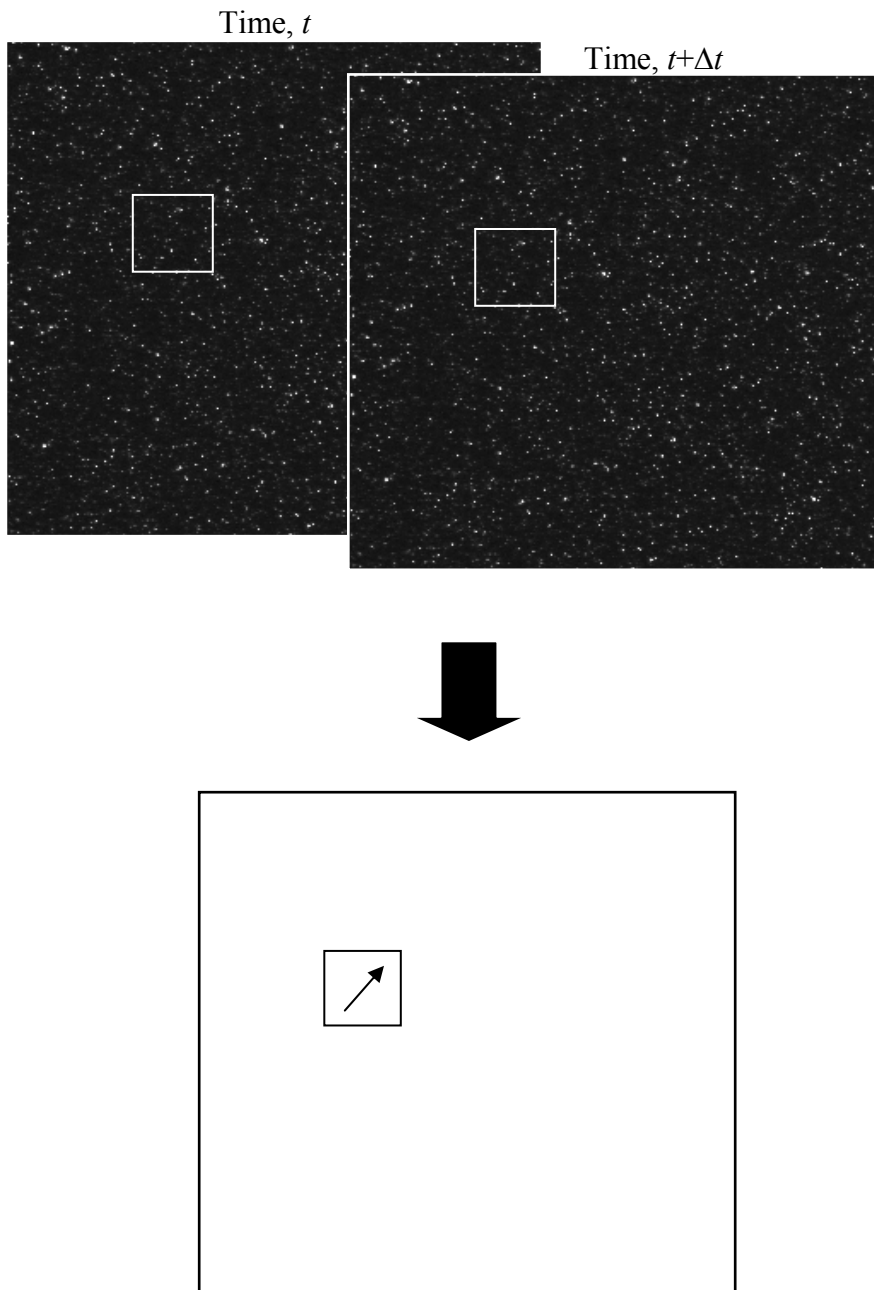


Figure 3.5: Analysis of two typical singly-exposed PIV images.

degree of match between the two images for a given displacement. The analysis of a pair of images can yield a field of linear displacement vectors. Knowing the time separation between the images enables the calculation of a velocity vector from the displacement vector. The computation of the cross-correlation between two images in the spatial domain requires significant computational resources. Cross-correlation can be performed much faster in the wave number domain using the fast Fourier transform (FFT) technique. Figure 3.5 shows two typical singly-exposed images with a single interrogation area highlighted. The time separation between the two images is Δt . Some aspects related to the cross-correlation analysis are discussed below.

Half-padded FFT-based cross-correlation

The interrogation process using this technique may be summarised as follows. The interrogation area (IA) of the first image is padded with zero elements to twice its original size. This padded IA is correlated with the corresponding IA of the second image. The size of the second IA is selected to be double of the original size of the first IA. The reason for the padding is because the Fourier transform of a finite data set treats the data as periodic, i.e, when the shift \mathbf{s} of the cross-correlation exceeds half of the IA size, the correlation wraps into the opposite side of the correlation function.

The correlation process starts by shifting the IA of the first image $I_1(\mathbf{X})$ around the IA of the second image $I_2(\mathbf{X})$ without extending over edges of $I_2(\mathbf{X})$ (see equation 3.12). For each choice of interrogation area shift $\mathbf{s}(s_x, s_y)$, the sum of the products of all overlapping pixel intensities produces one cross-correlation value $CC(s_x, s_y)$. Note that the product of the padded area of the first IA with the second IA is zero. The shift \mathbf{s} in pixels, required to align particle images in the second interrogation area with the corresponding particle images in the first interrogation area, is the displacement of the particle images in the time between the laser pulses. The pixel shift at which the interrogation areas are best aligned is indicated by the highest correlation peak in the cross-correlation plane as shown in Figure 3.6. The displacement of the highest correlation peak from the origin gives the mean displacement of the particles in the interrogation area. Dividing the displacement by the known time between the laser pulses gives the mean velocity of the

particles in pixels per pulse. An example of the half-padded FFT-based cross-correlation between two interrogation areas of 64×64 pixels is shown in Figure 3.6. The analysis of each interrogation area (IA) produces a single velocity vector as illustrated schematically in Figure 3.5. It should be noted that the displacement $\Delta\mathbf{S}$, determined using the cross-correlation analysis, represents an average displacement vector of all particles within the interrogation area (Adrian, 1991). Carrying out the analysis for all interrogation areas in the PIV image yields the flow velocity vector field in the plane of the laser light sheet. The accuracy of the resulting velocity vector is dependent on the accuracy of $\Delta\mathbf{S}$ and Δt . Δt is typically known to within 0.1%, hence the accuracy of $\tilde{\mathbf{V}}$ is mainly dependent on the evaluation of $\Delta\mathbf{S}$. This issue will be addressed in Section 3.4.

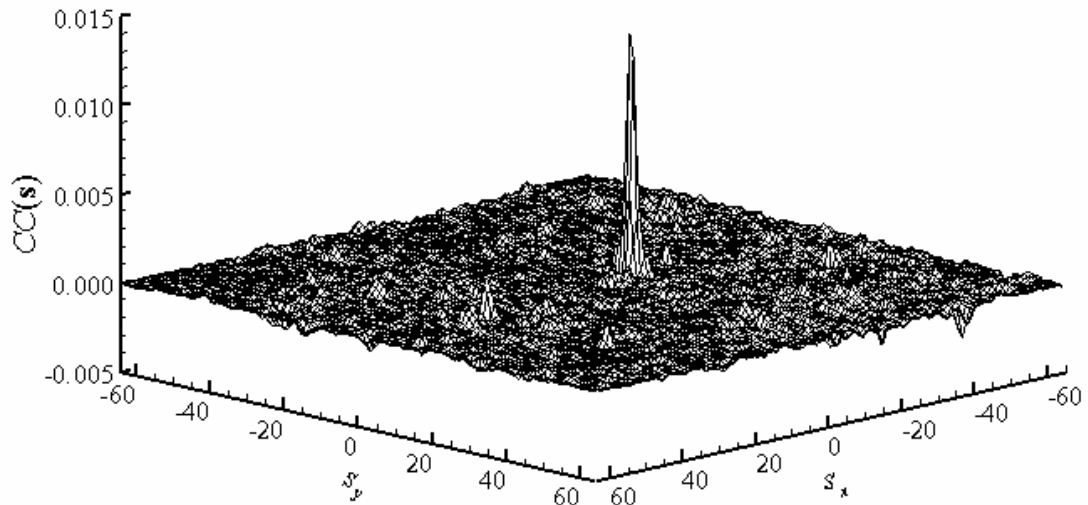


Figure 3.6: The cross-correlation function.

Interrogation area offset

The number of displacement vectors resulting from the interrogation process can be significantly increased by performing a second interrogation pass using an interrogation area offset equal to the local integer displacement in the first pass. The interrogation area offset refers to the relative positions that the interrogation areas are extracted from in the first and second exposure. By offsetting the interrogation areas, the fraction of matched particle images to unmatched particle images is increased, thereby increasing the signal-to-noise ratio of the correlation peak. This can be done by first performing a standard interrogation without interrogation area offset. The displacements obtained in this first pass serve only as estimates for the next higher resolution level. Note that the interrogation areas are made smaller with each pass. This displacement data is used to offset the interrogation areas with respect to each other. In the final interrogation pass, the IA offset vectors have generally converged to less than 1 pixel of the measured displacement thereby improving the evaluation of the PIV image. The choice for the final interrogation area size depends on the particle image density.

Peak detection and displacement estimation

In PIV, the location of the correlation peak is directly associated with the particle displacement. An error of ± 0.5 pixels is present in the correlation peak location provided by the discrete correlation function $CC(s)$ given in equation 3.12 (Huang *et al.*, 1997). The maximum of the discrete correlation function occurs at integer values of s_x and s_y . To increase accuracy, it is necessary to locate the correlation peak more precisely; that is, within sub-pixel accuracy. Sub-pixel interpolation involves fitting a function to the discrete cross-correlation function near the peak and finding the location of the maximum in that function. Some methods have been used to obtain the correlation peak to within sub-pixel accuracy, such as centre-of-mass, parabolic curve-fitting and Gaussian curve-fitting methods (Willert & Gharib, 1991). Among these methods, the Gaussian curve-fitting method is frequently used in the PIV analysis. This method has been recommended by Lourenco & Krothapalli (1995) after a detailed study on the

accuracy of different peak interpolation algorithms. In this study, the Gaussian curve-fitting method was employed for locating the correlation peak to sub-pixel accuracy.

Summary of the PIV analysis procedures

In this work, image analysis was performed with correlation analysis software developed in-house. The images were first analysed with 64×64 pixel interrogation areas using a half-padded FFT-based cross-correlation between successive images. The correlation-based-correction (CBC) method proposed by Hart (2000) was used to improve the signal-to-noise ratio and limit the number of spurious vectors (see Section 3.3.1 for more details). Then, using the displacement results from this rather coarse grid to determine a local interrogation area offset, the image was re-analysed with 32×32 pixel interrogation areas. In this way, rather small interrogation areas can be used even in regions where the particle displacement is larger than the interrogation area dimensions. This was especially important in this flow because of the wide range of velocities. This analysis process was repeated one more time for all cases except the velocity field at the jet exit (case FJ01 in Table 5.1) to complete a three-pass analysis and yield a final interrogation area size of 16×16 pixels. The interrogation areas were overlapped by 50%. The actual spatial resolution that this procedure yielded was dependent on the size of the measurement plane and will be reported when the results are introduced.

3.3 REMOVAL OF SPURIOUS VECTORS

PIV is based on the use of information contained in images of tracer particles to determine local flow velocities. Generally, the technique is subject to errors that arise from the finite number of tracer particles, interrogation area size, image resolution, excessive particle displacements normal to (or within) the light sheet, large velocity gradients, or poor image quality. In some cases, these errors are relatively easy to detect since the vectors vary substantially from their neighbours in both magnitude and direction. In other cases, the deviation from the local velocity may be more subtle. These “spurious” vectors occur regardless of how carefully the measurements are conducted and should be removed before extracting additional information from the velocity field.

Erroneous vectors are usually identified and eliminated from PIV data either directly from the correlation data during image analysis or after extracting the displacement field. The former are known as *correlation-based techniques* while the latter are known as *post-interrogation techniques*. Although the correlation-based algorithms are extremely useful, post-interrogation methods are usually still required to eliminate spurious vectors that are still contained in the data set.

Since PIV provides detailed spatial information and rather crude temporal information, detecting spurious vectors based on temporal information in post-processing analysis is not reliable. Instead, the nature of PIV data suggests that each displacement vector should be compared with neighbouring vectors and those that have an ‘unacceptably’ large deviation from their neighbours be labelled as spurious. The problem facing any post-interrogation technique is to distinguish between real variations in velocity from point-to-point and variations due to spurious vectors.

3.3.1 Correlation-Based Correction (CBC) Technique

Hart (2000) proposed a correlation-based correction (CBC) method for reducing sub-pixel errors and eliminating spurious vectors from PIV results. The method constructs a correlation plane which is the product of two overlapping correlation planes and searches the result for a signal peak. The principle is that, while the signal in the two constituent correlation planes should be correlated strongly, the noise will be correlated weakly. The resulting correlation planes tend to have very strong signal peaks. Because the method is implemented during the correlation process, it uses the information extracted from the correlation plane itself for improving signal-to-noise ratio and then eliminating bad vectors. However, this method still results in some erroneous vectors that need to be identified.

3.3.2 Post-Processing Analysis

Several algorithms have been proposed to identify and reject spurious vectors from PIV data sets (see Shinneeb *et al.*, 2004a for more details about these algorithms). Liang *et al.* (2003) applied the cellular neural network (CNN) method as a post-interrogation algorithm to detect spurious vectors in PIV measurements. CNN was found effective in detecting erroneous vectors when tested on artificial velocity fields. It was also applied to a measured PIV field of a two-dimensional flow around a semicircular cylinder that contained a considerable number of spurious vectors. A constant threshold was used across the whole velocity field and it was found that the performance of the CNN method was superior when compared to other post-processing methods.

In this study, the CNN method was applied to the PIV data. The threshold is the most important parameter in determining the success of any method. Decreasing the threshold makes these algorithms more aggressive in rejecting vectors. If a small threshold is used across the whole field they tend to remove many valid vectors in regions of large velocity gradients. Conversely, increasing the threshold retains more spurious vectors. The following sections describe the CNN method of Liang *et al.* (2003) and the variable threshold technique proposed by Shinneeb *et al.* (2004a).

The cellular neural network (CNN) method

The CNN method is a single layer, local feedback network, composed of $m \times n$ neurons in the two-dimensional case. When a neuron is linked only to the neurons within a distance \check{r} , and all weights with other neurons are zero, the network has only local feedback. If $\check{r} = 1$ each neuron connects only with its eight nearest neighbours and if $\check{r} = 2$ it connects to its 24 nearest neighbours. In the implementation described in Liang *et al.* (2003), each neuron connects with its immediate neighbours ($\check{r} = 1$) so that outlier rejection is based only on the nearby flow pattern. The final state of the network is determined by the interconnected weights among neurons.

Each neuron in the network corresponds to a vector in the velocity field and has two states, one and zero, which represent valid and spurious vectors respectively. Since the velocity has two components, one velocity field corresponds to two networks which separately show the validity of u and v . The velocity is regarded as spurious if either of these two components is shown to be erroneous by the network.

The method is fully described in Liang *et al.* (2003) and may be summarised as follows for the u component. At each neuron i , equation 3.13 is used to calculate the weight of this neuron with its neighbours j ($j = 1$ to n),

$$\widehat{W}_{ij}^u = \max(-T_i^u, T_i^u - \widehat{R}_{ij}^u) \quad (3.13)$$

where T_i^u represents the threshold for u and \widehat{R}_{ij}^u is the absolute difference between u at i and j ,

$$\widehat{R}_{ij}^u = |u_i - u_j|. \quad (3.14)$$

The sum of the weight functions for the i th neuron is given by

$$S_i^u = \sum_{j=1}^n \widehat{W}_{ij}^u \gamma_j^{k-1} \quad (3.15)$$

where n is the total number of connecting neurons and γ_j^{k-1} is the state (0 or 1) of neuron j from the previous iteration. For this method, \widehat{W}_{ii} is set to zero which means the network has no self feedback. All the neuron states are initially set to one which means that all the vectors are initially regarded as valid. The state of neuron i for iteration k is set according to

$$\gamma_i^k = 1 \text{ if } S_i^u \geq 0 \quad \text{and} \quad 0 \text{ if } S_i^u < 0. \quad (3.16)$$

Occasionally convergence is prevented by a very small number (less than 10) vectors whose states oscillate indefinitely. Usually, these occur in pairs of two neighbouring vectors with opposite states. In this work, such vectors are assumed to be spurious.

The variable threshold technique

This section describes a variable threshold technique proposed by Shinneeb *et al.* (2004a) that can be applied to any particle image velocimetry (PIV) post-analysis outlier identification algorithm. Although the CNN technique has been shown to work well with constant thresholds, the selection of the threshold is not clear when working with real data. Moreover, if a small threshold is selected, a very large number of valid vectors can be mistakenly rejected. Although careful monitoring may alleviate this danger in many cases, that is not always practical when large data sets are being analysed and there is significant variability in the properties of the vector fields.

In this study, the thresholds used by the CNN method just described above are functions of location in the field-of-view. The information used to determine this threshold field must come from the measurements themselves which, of course, initially contain spurious vectors. The method begins by calculating a provisional velocity field using an aggressive outlier rejection algorithm. At this stage, it is more important to reject any vector suspected of being an outlier than it is to minimise the number of good vectors mistakenly identified as outliers. For this purpose, a constant threshold CNN algorithm was used for preliminary rejection of outliers. The threshold was selected small enough to ensure that all bad vectors were removed. The velocity field that results from this procedure has suspect velocities replaced by a Gaussian-weighted average of their neighbours. For example, the u component of vector i becomes

$$u_i = \frac{\sum \alpha_{ij} u_j}{\sum \alpha_{ij}} \quad (3.17)$$

where

$$\alpha_{ij} = \exp\left(-\frac{1}{2}\left(\frac{L_{ij}}{\sigma}\right)^2\right) \quad (3.18)$$

Here $\sigma = 3\Delta x$ pixels is the width of the Gaussian filter and $L_{ij} = |\mathbf{X}_i - \mathbf{X}_j|$ is the distance between point i and its neighbouring point j . The sum is performed for all j within a 5×5 square region surrounding i . Velocities that are not identified as outliers are not altered in any way. Therefore, no general filtering is performed to arrive at this provisional velocity field.

The information that now needs to be extracted from the provisional field is the ‘expected’ difference between a velocity and its immediate neighbours. A mean deviation in the u -velocity component for each vector location i is calculated from this field using

$$\tilde{T}_i^u = \frac{1}{n} \sum_{j=1}^n |u_i - u_j| + K \quad (3.19)$$

where K is a constant and $n = 24$ neighbours. This threshold is then filtered by a Gaussian kernel as follows.

$$T_i^u = \frac{\sum \alpha_{ij} \tilde{T}_j^u}{\sum \alpha_{ij}} \quad (3.20)$$

where

$$\alpha_{ij} = \exp\left(-\frac{1}{2}\left(\frac{L_{ij}}{\sigma}\right)^2\right) \quad (3.21)$$

Here $\sigma = 3\Delta x$ pixels and $L_{ij} = |\mathbf{X}_i - \mathbf{X}_j|$. The sums in equation (3.20) are over a 5×5 region around i .

In summary, after the correlation analysis was complete, outliers were rejected using the cellular neural network (CNN) method as described above. The thresholds required for the CNN method were calculated for each velocity field using the variable threshold technique. The constant value K added to the threshold fields (see equation 3.19) was 2 pixels. The percentage of vectors rejected varied from 3% to 15%. Most of these rejected vectors were at the edges of the velocity fields.

Replacement schemes and data smoothing

After removing outliers from the data set, missing data must be replaced. The missing data can be estimated by using some sort of weighted average of the surrounding data, such as the Gaussian window technique (Raffel *et al.*, 1998). In this study, a 5×5 grid unit Gaussian window, given by equations 3.17 and 3.18, was used, with weighting based on the distance from the central grid point. The width of the Gaussian filter was selected to be $\sigma = 3\Delta x$, where the vector grid spacing $\Delta x = 8$ pixels.

Some form of data smoothing is commonly employed in the presentation of PIV velocity data, with its primary purpose to remove high frequency noise. This step should be performed before any further analysis particularly that uses the fluctuating velocity part of the PIV data such as the POD technique. The reason is that the experimental data are affected by noise and this could affect the results. In order to avoid removing real high frequency data, a simple convolution of the data with a rather narrow smoothing kernel with equal weights is generally sufficient for this purpose. A kernel size of 3×3 spatial window dimension and a Gaussian width equal to two grid units ($\sigma = 2\Delta x$) was employed in this study.

3.4 UNCERTAINTY ANALYSIS

One of the challenges in the application of the PIV is to determine its error. Error quantification is generally a function of the experimental conditions and the particle displacement detection algorithms (Huang *et al.*, 1997). Three forms of errors are

present in the PIV data. They are outliers, systematic errors, and random errors. Outliers are those velocity vectors which are obtained with poor correlations and usually appear random both in direction and magnitude (Huang *et al.*, 1997). This type of error was discussed in Section 3.3.1. Errors are also present in the velocity vectors obtained with sufficiently large correlation peaks. The analysis of this kind of errors is usually referred to as *uncertainty analysis*.

The measurement uncertainty is an assessment of the degree to which a measurement is representative of the true value and is usually expressed at the 95% confidence level. A complete uncertainty analysis of the PIV technique would involve identifying and quantifying both the systematic (bias) and random uncertainties. The uncertainty UN may be written as

$$UN = \sqrt{B^2 + (t_{95}\sigma)^2} \quad (3.22)$$

where B is the bias limit, t_{95} is the value of the t distribution at the 95% level of confidence, and σ is the standard deviation.

The uncertainty of the PIV data is influenced by a number of factors, such as particle image size, interrogation area size, particle seeding density, the number of particles in the interrogation area, computational and instrumentation effects, and flow properties such as velocity gradients, curvature of the particle trajectories, and three-dimensional (out of plane) motion. According to Willert & Gharib (1991), the displacement error may range from 1 to 10% depending on the seeding density and the maximum displacement being measured. Guezennec & Kiritsis (1990) first addressed the uncertainty of valid vectors by studying the PIV velocity error as a function of the image noise level, number of particles and particle displacement. In 1992, Willert analysed the error as a function of the particle density, particle displacement and velocity gradients (Huang *et al.*, 1997). Lourenco & Krothapalli (1995) studied the effects of various correlation peak-finding schemes on the velocity errors. Boillot & Prasad (1996) provided an optimisation procedure for pulse separation to minimise this error. Prasad *et*

al. (1992) found that the particle image diameter strongly influences the accuracy of the measured velocities and concluded that the optimum image size should be small but larger than the pixel size to reduce both bias and random errors. Huang *et al.* (1997) observed that the random error does not exhibit a dependence on the particle diameter. This result contradicts the findings of Adrian (1991), who concluded that the random error is proportional to the particle diameter.

The random error is influenced by many factors. Among them the method of implementing the discrete cross-correlation function and the method of locating the correlation peak to within sub-pixel accuracy are fundamental in determining the upper limit of the DPIV accuracy (Huang *et al.*, 1997). The maximum data point in a discrete correlation is an integer peak. To increase the PIV accuracy, it is necessary to locate the correlation peak more precisely; that is, to within a sub-pixel accuracy. This step significantly reduces the random error of the cross-correlation (Huang *et al.*, 1997). Agrawal & Prasad (2003) estimated the error after locating the correlation peak to sub-pixel accuracy to be about 0.1 pixels. Westerweel *et al.* (1997) found that the use of a window offset in the cross-correlation analysis improves its accuracy particularly for measurements of weak turbulence. They recommended combining the IA offset with a reduction of the interrogation area (IA) size in order to maintain the measurement error at a constant level

From the above discussion, it is clear that the error in the PIV data is a function of many parameters. This makes the task of error assessment difficult because the exact values are not known. For this reason, the error analysis was performed in this work by generating synthetic images with characteristics similar to the real images. In this way, the exact values of the displacements are known so that the error analysis is more realistic. This method is fully described in Bugg & Rezkallah (1998) and may be summarised here. The size of the simulated images was 2048×2048 pixels, the same as the real images. Each pixel was represented by 8 bits corresponding to 256 levels of grey. These images were analysed using the same procedures applied to the real ones as described in Section 3.2.3. Then, the outliers were detected and replaced using the

techniques described in Section 3.3.2. The percentage of the spurious vectors was ~6%. The characteristics of the simulated images were quantified by the following parameters.

1. *Background noise*: The images were initialised with Gaussian noise with a specified mean intensity μ_n and standard deviation σ_n .
2. *Number of paired particles*: These particles were distributed randomly in the first image and then positioned at a known displacement in the second image.
3. *Number of spurious particles*: Extra particles were distributed randomly in the images without pairs.
4. *Particle diameter*: The distribution of particle diameters was Gaussian with mean μ_d and standard deviation σ_d . The Gaussian distribution of particle sizes represents the variation in actual particle sizes.
5. *Particle intensity*: The distribution of particle intensities was Gaussian with mean μ_I and standard deviation σ_I intensity at the centre of the particle images.
6. *Displacement magnitude*: In this analysis, the displacements varied according to the following relations

$$\Delta S_x = 0.0048828125y \quad \text{and} \quad \Delta S_y = 0 \quad (3.23)$$

where ΔS_x and ΔS_y represents axial and vertical displacements in pixels, and y represents the vertical position in pixels. In this way, ΔS_x varied from 0 at $y = 0$ to 10 pixels at $y = 2048$ pixels. This is equivalent to the range of the displacements travelled by the seed particles in the real images. The quantities that characterise the quality of the real and simulated images are given in Table 3.2. These characteristics were obtained from the real images using *Matrox Inspector*® software. This software actually reports the particle image area A_p and $d_p = \sqrt{4A_p/\pi}$. All simulated images have the same characteristics as those given in Table 3.2. The members of the ensemble were made unique by seeding the random number generator with a different value. This made each image in the ensemble unique, but they still possess the same statistical properties.

Table 3.2: Characteristics of the real and simulated images.

Parameter	Real images		Simulated images	
	μ	σ	μ	σ
Background noise	23	11	18	19
Blob area, A_p	1.39	0.85	1.42	0.64
Particle amplitude, I_0	254	1	254	1
Number of paired particles, N_p	~79,000		70,000	
Ratio of spurious to paired particles, N_s/N_p	---		11%	

The purpose of the error analysis of the PIV data is to measure the uncertainty in the velocity vectors as a function of several parameters characterising image quality. Each image in the ensemble was analysed to measure the particle displacement and compared to the actual displacement to yield a single measurement of the error. The deviation of the mean from the actual displacement represents the bias while the standard deviation represents the precision index. There are four quantities to be determined; the bias limits for instantaneous B_{ins} and smoothed B_{smooth} axial displacement component u , and the standard deviation σ_{ins} and σ_{smooth} for the same variable. Note that the smoothed velocity fields are obtained by applying a rather narrow smoothing kernel to the instantaneous velocity fields.

The number of images required in an ensemble of images to give reliable statistics was assessed by ensuring that the calculated values of B and σ for four sets of data gave almost the same result. Accordingly, all calculations were done with an ensemble size of 2550. The biases, standard deviation, and uncertainties are given in Table 3.3. It was found that the uncertainty is independent of the displacement. This indicates that small velocities will have a higher relative uncertainty.

Table 3.3: Summary of uncertainties in the PIV data (in pixels).

	Instantaneous	Smoothed instantaneous
B	0.003	0.003
σ	0.15	0.08
UN	0.29	0.15

Table 3.3 shows that the systematic uncertainty is very small compared to the random uncertainty. It should be pointed out that the so-called *peak-locking effect* was observed in the present analysis. This effect indicates a preference for displacements calculated using sub-pixel (Gaussian) curve fitting (see Section 3.2.3) towards integer values. This error is more pronounced for particle image diameters smaller than two pixels (Prasad *et al.*, 1992). In this work, this effect is included in the calculations of the random error while the systematic error represents only the mean value of the error over the entire range of displacements.

The uncertainty in the jet exit velocity U_e was estimated from uncertainties in mass flow rate \dot{m} , water density ρ , and cross-sectional area A of the jet exit. The uncertainty of the mass flow rate was determined from uncertainties in water mass measurement m , filling time measurement t , voltage measurement \vec{E} , and calibration curve fitting. Also, the cross-sectional area A was determined from the nozzle diameter D . Table 3.4 lists the error estimation in these quantities. The uncertainty analysis of the jet exit velocity was determined to be 1.25% assuming negligible error in curve fitting compared with the other errors.

The characteristic velocity scale in the present flow (centreline velocity) corresponds to a displacement of about eight to ten pixels. The relative error in the characteristic velocity measurement is about 3.2% and 1.7% for the instantaneous and smoothed velocity fields, respectively. Including the error in the jet exit velocity, the relative errors for the instantaneous and smoothed normalised velocity fields become 3.4% and 2.1%, respectively. Moreover, the relative error in the fluctuating velocity components should

also be estimated because it is used for the POD analysis. The fluctuating velocity components are obtained by subtracting the mean velocity from the instantaneous (smoothed) velocity field. The characteristic velocity of the fluctuating velocity component decreases by about one order of magnitude, therefore the relative error of the fluctuating velocity field is amplified to about 21%.

Table 3.4: Error estimation in the quantities used for the exit velocity U_e calibration.

Quantity	Estimated error
Water density, ρ	0.2 kg/m ³
Jet exit diameter, D	0.02 mm
Collected mass, m	0.001 kg
Filling time, t	0.2 s
Voltage, \vec{E}	0.02 volts

The definition of the circulation Γ indicates that errors in measuring velocity and vortex radius R will contribute to the error of Γ (Agrawal & Prasad, 2003). The measurement of R is affected by the fact that the vortex centre may not lie exactly on a grid point. In addition, not all closed streamlines are perfectly circular or even perfectly closed due to the nature of the eduction process and the threshold employed therein. Furthermore, due to the discrete nature of the data, the true vortex radius may be slightly smaller or larger than the measured value. These effects can produce an additional random error in the value of Γ . Unfortunately, these errors cannot be quantified accurately without extensive investigations. However, the error in R is estimated to be equal to one grid unit (~ 0.6 mm). The relative error then varies according to the vortex size which is roughly estimated to be 10 to 30%. Moreover, the uncertainty in Γ around a perfect circle is equal to the uncertainty of a single fluctuating velocity uncertainty (21%). Thus, the cumulative measurement error in Γ is estimated to be 23 to 37%.

3.5 SUMMARY

The experimental apparatus was designed to generate shallow water jets discharging horizontally from a round nozzle (9 mm) into stagnant water. The confinement resulted from the proximity of the top free surface and the bottom solid wall while the lateral and axial confinement effects were negligible. The Reynolds number based on exit conditions was 22,500. The depth of the water H was an adjustable parameter. In all experiments, the jet axis was located midway between the confinement boundaries.

The velocity field was measured using particle image velocimetry (PIV) technique. Measurements were taken on two orthogonal planes along the jet axis; x - y and x - z planes. The process of making PIV measurements can be summarised in the following steps; seeding the flow with hollow-glass sphere particles, illuminating the measurement region with Nd:YAG lasers, capturing images using a digital camera of resolution 2048×2048 pixels, and analysing the images using FFT-based cross-correlation technique. The correlation-based-correction (CBC) algorithm proposed by Hart (2000) was used to improve signal-to-noise ratio and limit the number of spurious vectors. The data obtained from the analysis process were filtered from spurious vectors using the cellular neural network (CNN) method (Liang *et al.*, 2003). The threshold field used for this method was calculated using the variable threshold technique of Shinneeb *et al.* (2004). The missing vectors were then replaced using the Gaussian window technique. Finally, the data were smoothed using a narrow smoothing Gaussian kernel for further analysis.

Chapter 4

IDENTIFICATION OF VORTICAL STRUCTURES

4.1 PRELIMINARY REMARKS

Different methods have been used to decompose turbulent velocity fields in order to describe and/or study them. The Reynolds decomposition may be considered the standard method used to perform a statistical flow study. Unfortunately, it is not always the best method for studying the turbulent mechanics of a flow (Adrian *et al.*, 2000). Alternative methods include decomposition by Galilean transformation and by filtered fields. This filtering can be homogeneous as in large-eddy simulation (LES) or inhomogeneous as in proper orthogonal decomposition (POD). The advantage of POD is that it is very effective in inhomogeneous flows and can be used to construct inhomogeneous low-pass filters (Adrian *et al.*, 2000).

The POD is a statistical technique for determining a set of optimal basis functions for the reconstruction of a data set. The set is optimal in the sense that expansion in terms of these basis functions converges faster than expansion in terms of any other set of basis functions. This technique was introduced in the context of turbulence by Lumley in 1967 as an unbiased way for extracting structures in a turbulent flow (see Holmes *et al.*, 1996). The POD has been used in various disciplines that include fluid mechanics (Berkooz *et al.*, 1993), chemical engineering, oceanography, and image processing

(Cizmas *et al.*, 2003). Depending on the discipline, the POD is also known as Karhunen-Loeve decomposition, principal components analysis, singular systems analysis, and singular value decomposition.

The POD is a very powerful technique for extracting the energetically dominant modes in a flow. It is used to extract dominant spatial features and trends from experimental data. These features are also known as *coherent structures* (Holmes *et al.*, 1996). This method can then be used to reconstruct the coherent structures as mixtures of POD modes. The basis functions it yields are called; empirical eigenfunctions, empirical basis functions, or empirical orthogonal functions (Holmes *et al.*, 1996). When applied to turbulent velocity fields, the basis functions are the eigenfunctions of a Fredholm integral equation, where the kernel is the two-point correlation function of the velocity field.

While many of the more attractive properties of POD result from the fact that it is based on correlation functions that contain important information about the physics of a particular flow, the need to input the correlation functions also makes implementation of the POD difficult when applied to PIV data. This is because the high spatial resolution of the PIV data makes the *direct computation* of the correlation matrix difficult due to storage requirements. In contrast to direct POD, a popular technique called the *snapshot method* suggested by Sirovich (1987) is more relevant in this situation and gives equivalent results. Graftieaux *et al.* (2001) tested these two methods and found no significant differences, apart from the fact that greater computation time and memory are required for the direct technique. The following section discusses the implementation of the POD method in order to extract *coherent structures*.

4.2 PROPER ORTHOGONAL DECOMPOSITION TECHNIQUE

Consider a set of experimental turbulent velocity fields represented by discrete instantaneous velocity vectors $\tilde{\mathbf{V}}^l = \tilde{\mathbf{V}}(\mathbf{X}, t_l)$, where $l=1, \dots, M$. Since the current PIV system measures two-dimensional vector fields, only two of the three velocity

components $\tilde{\mathbf{V}}^l = \hat{\mathbf{e}}_1 u + \hat{\mathbf{e}}_2 v$ ($\hat{\mathbf{e}}_1$ and $\hat{\mathbf{e}}_2$ represent unit vectors) on one plane defined in physical space $\mathbf{X} = \hat{\mathbf{e}}_1 x + \hat{\mathbf{e}}_2 y$ and time t_l , will be considered. Assume that the number of vectors in each velocity field is N . By subtracting the ensemble average $\mathbf{V}(\mathbf{X})$ from each realisation, vectors $\hat{\mathbf{V}}^l = \hat{\mathbf{V}}(\mathbf{X}, t_l)$ containing the fluctuating part of all velocities in the domain are obtained.

The underlying problem is to identify coherent structures in a turbulent flow. The fundamental idea of the POD method is to find time-independent orthonormal basis functions $\Psi^{(k)}(\mathbf{X})$ and time-dependent orthonormal amplitude coefficients $a^{(k)}(t_l)$ such that the reconstruction is performed by (Kostas *et al.*, 2001)

$$\hat{\mathbf{V}}(\mathbf{X}, t_l) = \sum_{k=1}^M a^{(k)}(t_l) \Psi^{(k)}(\mathbf{X}) \quad (4.1)$$

Equation 4.1 is known as the proper orthogonal decomposition of $\hat{\mathbf{V}}(\mathbf{X}, t_l)$. This equation gives the best approximation of the data ensemble $\hat{\mathbf{V}}(\mathbf{X}, t_l)$ in the sense that the average least-squares error

$$\varepsilon_m = \overline{\left\| \hat{\mathbf{V}}(\mathbf{X}, t_l) - \sum_{k=1}^m a^{(k)}(t_l) \Psi^{(k)}(\mathbf{X}) \right\|^2} \quad (4.2)$$

is a minimum for any given number $m \leq M$ of basis functions over all possible sets of orthogonal basis functions (Cizmas *et al.*, 2003). Here $\| \cdot \|$ is the L^2 -norm and the overbar represents a spatial average of all N grid points in the velocity field. The value m specifies the number of basis modes included in the reconstruction.

One way to determine the functions $\Psi^{(k)}(\mathbf{X})$ is to project the ensemble on $\Psi^{(k)}(\mathbf{X})$, *i.e.* $(\hat{\mathbf{V}}^l, \Psi)$. Specifically, we seek $\Psi^{(k)}(\mathbf{X})$ such that the quantity

$$\frac{\langle \langle (\hat{\mathbf{V}}^l, \boldsymbol{\Psi})^2 \rangle \rangle}{(\boldsymbol{\Psi}, \boldsymbol{\Psi})} \quad (4.3)$$

is maximised. Here (\cdot, \cdot) is the inner product in the Hilbert space of square integrable functions and the operator $\langle \cdot \rangle$ is the ensemble average in time. Thus, the POD basis functions $\boldsymbol{\Psi}^{(k)}(\mathbf{X})$ are defined by the maximisation of their normalised mean-square projection on the velocity vector. The normalisation of the projection is done to eliminate amplitude dependence on the resulting functions and instead emphasise the degree of projection. The following sections review the methods of POD relevant to this work and discuss how POD can be applied to the PIV data in order to compute the POD modes in two different ways. Which of these requires less computational effort depends on the relative numbers of grid points N , and observations or snapshots M in the data ensemble.

4.2.1 The Direct Method

In 1967, Lumley proposed that a coherent structure is the one which has the largest mean square projection of the basis functions $\boldsymbol{\Psi}^{(k)}(\mathbf{X})$ on the velocity field. This maximisation problem leads to an integral equation of fixed limits, which is referred to as a Fredholm type integral equation, where the kernel is the correlation tensor. Thus, POD involves solving the following equation (Kostas *et al.*, 2001)

$$\int_{\Omega} R(\mathbf{X}, \mathbf{X}') \boldsymbol{\Psi}(\mathbf{X}') d\mathbf{X}' = \lambda \boldsymbol{\Psi}(\mathbf{X}) \quad (4.4)$$

where $R(\mathbf{X}, \mathbf{X}') = \langle \hat{\mathbf{V}}(\mathbf{X}, t_l) \bullet \hat{\mathbf{V}}(\mathbf{X}', t_l) \rangle$ known as the kernel and Ω represents the domain of interest. $R(\mathbf{X}, \mathbf{X}')$ is the two-point time-averaged spatial correlation function. Vector multiplication in this relation signifies the standard Euclidean inner product.

In practice, POD is implemented discretely. Since experimental data are always discrete and, in any case, integral equations are usually solved numerically by discretisation; therefore, the spatial correlation is replaced by the tensor product matrix (Cizmas, *et al.*, 2003)

$$R(\mathbf{X}, \mathbf{X}') = \frac{1}{M} \sum_{l=1}^M \hat{\mathbf{V}}(\mathbf{X}, t_l) \bullet \hat{\mathbf{V}}(\mathbf{X}', t_l) \quad (4.5)$$

where the dot denotes the standard vector inner product. Solution of equation 4.4 gives $\Psi^{(k)}(\mathbf{X})$ and $\lambda^{(k)}$ which are the empirical eigenfunctions and eigenvalues, respectively and (k) is the order of the orthogonal decomposition. The orthogonality condition implies that eigenfunctions of different order do not interact with each other in which case their scalar product is zero (Kostas *et al.*, 2001). Because of the normalisation, the scalar product of the empirical eigenfunctions with themselves is unity. Therefore,

$$\Psi^{(k)} \bullet \Psi^{(p)} = \delta_{kp} \quad (4.6)$$

where δ_{kp} is the Kronecker delta. The eigenfunction $\Psi^{(k)}(\mathbf{X})$ represents the spatial flow structures corresponding to mode k . The k -th eigenvalue represents the energy contained by the structures at this mode.

The time-dependent coefficients $a^{(k)}(t_l)$ are calculated by projecting the data set onto the eigenfunction space, i.e. (Kostas *et al.*, 2001)

$$a^{(k)}(t_l) = \frac{\sum_{n=1}^N (\hat{\mathbf{V}}(\mathbf{X}_n, t_l) \bullet \Psi^{(k)}(\mathbf{X}_n))}{\sum_{n=1}^N (\Psi^{(k)}(\mathbf{X}_n) \bullet \Psi^{(k)}(\mathbf{X}_n))} \quad (4.7)$$

where N is the number of vectors of the velocity field. Because $\Psi^{(k)}(\mathbf{X})$ is an orthonormal base, the coefficient $a^{(k)}(t)$ has the dimension of velocity. Therefore, since

the eigenvalue is defined by equation 4.8, the eigenvalue $\lambda^{(k)}$ has the dimension of kinetic energy. In fact, $\lambda^{(k)}$ provides the energy of the structures in the flow at the k -th mode projected onto the mathematical base represented by the associated eigenfunction (Sirovich, 1987)

$$\sum_{i=1}^M a^{(k)} a^{(p)} = \lambda^{(k)} \delta_{kp}. \quad (4.8)$$

The total energy captured in a proper orthogonal decomposition of the data set is defined as the sum of all eigenvalues (Kostas *et al.*, 2001)

$$E = \sum_{k=1}^M \lambda^{(k)} \quad (4.9)$$

while the relative energy captured by the k -th mode E_k is defined by $E_k = \lambda^{(k)} / E$.

Equation 4.9 illustrates an important property of the orthogonal functions obtained via the POD method. Since the eigenvalues are to be ordered and the sum over all eigenvalues gives the total turbulent kinetic energy in the flow, the first eigenvalue contains the largest amount of kinetic energy and successive eigenvalues contain a decreasing amount. This implies that the first few POD modes can be used to represent the *most energetic eddies* in the flow.

A problem with the direct method just described is that the dimension of the correlation matrix given by equation 4.5 is very large ($N \times N$) for PIV data. Therefore, the solution of the eigenvalue problem for such a large matrix is quite cumbersome and time consuming. An equivalent approach to overcome this difficulty is described next.

4.2.2 The Method of Snapshots

This method, which is also known as the *method of strobos*, was proposed by Sirovich (1987). It was introduced as an efficient method when the resolution of the spatial domain N is higher than the number of realisations M . This is the case for PIV data where a large number of vectors can be obtained in each velocity field but time resolution is generally low and the total number of images that can be processed is limited. This method is basically a numerical procedure which can save time in computation of the empirical eigenfunctions and give an equivalent solution to the direct method (Sirovich, 1987). The eigenvalue problem can be written as the following matrix function where \mathbf{C} represents the temporal correlation (Kostas *et al.*, 2001)

$$\mathbf{C}\Phi^{(k)} = \lambda\Phi^{(k)} \quad (4.10)$$

Here $\Phi^{(k)} = (\phi_1^{(k)}, \dots, \phi_M^{(k)})^T$ is the k -th eigenvector corresponding to the eigenvalue $\lambda^{(k)}$ of \mathbf{C} . Each component of the temporal correlation matrix C_{ij} is given by (Cizmas *et al.*, 2003)

$$C_{ij} = \frac{1}{M} \sum_{n=1}^N \hat{\mathbf{V}}(\mathbf{X}_n, t_i) \bullet \hat{\mathbf{V}}(\mathbf{X}_n, t_j), \quad i, j = 1, \dots, M \quad (4.11)$$

In words, each component of the matrix \mathbf{C} contains the results of the inner product of each field with all other fields. The symmetry of the correlation matrix \mathbf{C} implies that all eigenvalues are real and positive and can be ordered so that; $\lambda^{(k)} \geq \lambda^{(k+1)}$.

The empirical eigenfunctions $\Psi^{(k)}(\mathbf{X})$ can then be constructed from a linear combination of the snapshots using (Kostas *et al.*, 2001)

$$\Psi_i^{(k)}(\mathbf{X}) = \sum_{n=1}^M \Phi_n^{(k)} \hat{\mathbf{V}}_i(\mathbf{X}, t_n) \quad (4.12)$$

where i denotes the function component.

In summary, the problem has now been reduced to solving an $M \times M$ matrix eigenvalue problem instead of an $N \times N$ problem (where in most cases $N \gg M$). The direct method is computationally expensive for high resolution data on a large spatial domain while the snapshot method only becomes numerically expensive for large ensemble sizes.

Summary of the proper orthogonal decomposition (POD) procedure

In this study, the POD method was performed on the fluctuating velocity vector of a two-dimensional (x - y or x - z) PIV data using the method of snapshots. The components of the velocity vector used are either (u, v) or (u, w) . The aim was to extract the dominant spatial features directly from the velocity fields. The POD method was implemented as described below

1. Calculate the components of the $M \times M$ correlation matrix C_{ij} using equation 4.11.
2. Compute the eigenvalues $\lambda^{(k)}$ ($k = 1$ to M) of this matrix using the QR algorithm as described in Bronson (1991) (see also Golub & Van Loan, 1983). Then, order the eigenvalues as $\lambda^{(k)} \geq \lambda^{(k+1)}$. Note that the correlation matrix is symmetrical which means that all the eigenvalues are real and positive. Each eigenvalue represents a portion of the turbulent kinetic energy associated with it and, thus, the first modes are the most energetic ones.
3. Compute the eigenvectors $\Phi^{(k)}$ of equation 4.10 using the *Inverse Power Iteration* method. This method is generally used when one already has good eigenvalues and wants only a few selected eigenvectors. This can be done by decomposing the correlation matrix \mathbf{C} using the LU algorithm and following the procedures described in Press *et al.* (1998).
4. Construct the empirical eigenfunctions $\Psi^{(k)}(\mathbf{X})$ from a linear combination of the snapshots using equation 4.12.

5. Having constructed the orthonormal basis, this can be used with the velocity data to determine the coefficients (or amplitudes) $a^{(k)}(t)$ of the POD modes as a function of time using equation 4.7.
6. Finally, reconstruct the original realisations by a linear combination of the empirical eigenfunctions $\Psi^{(k)}(\mathbf{X})$ and the coefficients $a^{(k)}(t)$ using equation 4.1. The number of modes may be selected according to the energy content to be recovered.

4.3 VORTEX IDENTIFICATION METHOD

The method used in this thesis to identify and measure properties of vortex structures is described in Agrawal & Prasad (2002b). This method identifies vortical structures by searching for closed streamlines in the POD reconstructed velocity fields. This concept of using *closed streamlines* to identify vortices was proposed by Robinson (1991). It should be pointed out that the PIV data are discrete which means that the data are measured at fixed points on a two-dimensional plane. In the present data, the velocity vectors are distributed uniformly on the measurement plane with equal grid intervals ($\Delta x = \Delta y$). A code was developed to locate the positions of vortex centres, identify rotational sense, and measure the size and circulation of each vortex. The method may be summarised as follows.

- A grid point was identified as a vortex centre if the orientation of the reconstructed velocity vector $\mathbf{V}_{\text{POD}}(\mathbf{X}, t)$ varied monotonically from 0 to 2π while moving in a closed path around the point. The closed path is a square with sides of length $2\Delta x$ centred on the grid point. Eight velocity measurements exist on this path. At least six of the eight vectors must vary monotonically for the point to qualify as a vortex centre. The sign of rotation is assigned to the structure at this stage. The rotational sense is positive if a vortex is turning counter-clockwise.
- The radius of the vortex R was obtained by repeating the procedure just described for larger paths surrounding the identified centre. Due to the discrete nature of the data, the path was approximated by the polygon that best describes a circle and checking

whether the angle of the velocity vectors varied monotonically. The angular variation of the velocity vectors for at least 75% of the points had to vary monotonically to be considered a streamline closed. The largest radius at which this criterion was still satisfied was assigned as the vortex radius. Note that this procedure measures vortex radius to the nearest multiple of Δx .

- The line integral of the velocity along the outermost path of each structure identified above gives the circulation Γ of the structure. In discrete data, it is calculated by integrating along a polygon path as follows

$$\Gamma = \sum (u_{\text{POD}}\Delta x + v_{\text{POD}}\Delta y) \quad (4.13)$$

- In some cases, two or more structures are identified close to each other so that they overlap. If the identified centre of a structure is located inside the radius of a larger structure, the larger structure is retained while the smaller one is ignored. If the centres are very close to each other, a new centre is determined from the average position of the original centres, and a new radius that includes all vortices is obtained. Moreover, the new circulation will be the average of the overlapping structures. It is important to point out that the identified centres in the second case are usually about one grid unit apart. These cases occurred in about 10% of the identified vortices of each set of data. All the above procedures were performed automatically.

Chapter 5

RESULTS AND DISCUSSION

5.1 PRELIMINARY REMARKS

This chapter presents results of an experimental study of the behaviour of a turbulent round jet in a shallow body of water when the jet issues parallel to the free surface. In this study, water was the working fluid and the air-water interface will be referred to as the free surface. A series of experiments was conducted using the PIV technique. The depth of the water layer H was the principal parameter. The goal is to characterise the effect of vertical confinement, resulting from the shallowness, on the turbulence structure of shallow water jet flows. This objective is achieved by investigating the mean flow, turbulence characteristics and coherent structures. Experiments were conducted at a jet exit velocity of $U_e = 2.5$ m/s and jet exit diameter $D = 9$ mm ($Re_D = 22,500$) for water layer depths corresponding to $H/D = 15, 10,$ and 5 . In all experiments, the centreline of the jet was located midway between the solid wall and the free surface as shown in Figure 3.1. Multiple images were acquired at each location. All images were acquired at a sampling rate of 1 Hz and with a resolution of 2048 by 2048 pixels. This rate is slow enough that the images are uncorrelated. Table 5.1 summarises the number, location, size, and spatial resolution of the PIV images acquired for all the free and shallow water jet cases.

Table 5.1: Summary of the characteristics of the velocity fields.

(a) Vertical (x,y) planes						
H/D	Case Name	No. of images	Distance from jet exit*		Image size (mm \times mm)	Spatial resolution (mm)
			mm	Exit Diameters		
60	FJ01	1000	-1.9	-0.2	67.3 \times 67.3	0.526
	FJ02	2000	96.0	10.7	168.5 \times 168.5	0.658
	FJ03	2000	259.0	28.8	160.7 \times 160.7	0.628
	FJ04	2000	416.0	46.2	167.9 \times 167.9	0.656
15	SJ12	2000	246.0	27.3	157.9 \times 157.9	0.617
	SJ13	2000	399.0	44.3	165.4 \times 165.4	0.646
	SJ14	2000	561.0	62.3	159.2 \times 159.2	0.622
10	SJ22	2000	248.0	27.6	158.6 \times 158.6	0.620
	SJ23	2000	402.0	44.7	157.4 \times 157.4	0.615
	SJ24	2000	552.0	61.3	162.0 \times 162.0	0.633
5	SJ32	2000	94.0	10.4	153.9 \times 153.9	0.601
	SJ33	2000	244.0	27.1	157.5 \times 157.5	0.615
	SJ34	2000	395.0	43.9	155.1 \times 155.1	0.606
(b) Horizontal (x,z) planes						
15	SJ17	2000	254.0	28.2	156.4 \times 156.4	0.611
	SJ18	2000	405.0	45.0	155.1 \times 155.1	0.606
	SJ19	2000	562.0	62.4	155.2 \times 155.2	0.606
10	SJ27	2000	251.0	27.9	157.8 \times 157.8	0.616
	SJ28	2000	402.0	44.7	156.8 \times 156.8	0.613
	SJ29	2000	553.0	61.4	157.4 \times 157.4	0.615
5	SJ37	2000	105.0	11.7	156.2 \times 156.2	0.610
	SJ38	2000	254.0	28.2	156.5 \times 156.5	0.611
	SJ39	2000	405.0	45.0	155.5 \times 155.5	0.607

* This distance is measured from the jet exit plane to the left edge of the field-of-view.

In the velocity measurements presented in this thesis, instantaneous velocities are designated using lower-case letters (u, v, w), fluctuating velocities about the mean use primed-lower-case letters (u', v', w'), mean quantities are indicated by upper-case letters (U, V, W), and root-mean-square of the fluctuating velocities are designated using a subscript rms ($u_{\text{rms}}, v_{\text{rms}}, w_{\text{rms}}$). In these results, x is distance measured along the jet axis with the origin ($x = 0$) at the jet exit plane; the positive x direction will be referred to as the axial direction (see Figure 3.1) and the corresponding velocity component U is the mean axial velocity. The vertical direction (normal to the boundaries) is defined as the y direction, positive upward, with the origin on the jet axis. This will be referred to as vertical direction (see Figure 3.1) with corresponding velocity component V . The horizontal coordinate is z . The origin is again at the jet axis and the positive direction is defined according to the right-handed coordinate system. The mean horizontal velocity is given the symbol W .

The remainder of this chapter presents the results obtained by the PIV technique. A brief description of the contents is presented here. Section 5.2 provides the velocity measurements of the free jet at the jet exit and in the zone of established flow (ZEF) as well as the properties along the jet centreline such as the centreline velocity decay, variation of the axial and radial turbulence intensities, and spread of the jet. The behaviour of the shallow water jet cases along the jet centreline, and the mean velocity and turbulence characteristics (on vertical and horizontal planes) at different axial locations are provided in Section 5.3. As will be shown, the behaviour of these curves demonstrates the effect of the vertical confinement on the jet. In Section 5.4, the characteristics of large-scale structures in free and shallow water jets are investigated. This section starts by investigating the temporal correlation between the velocity fields. The energy content of large-scale vortices is also discussed as well as the ensemble size required for the POD analysis and the threshold used in the vortex identification technique. Then, a statistical investigation of the distribution of vortex number, size, and circulation is presented. The results show the effect of the vertical confinement on the turbulence structure of the flow field.

5.2 FREE JET CHARACTERISTICS

Before examining the coherent structures, it is necessary to characterise the mean features of the jet. These characteristics include the jet exit properties as well as the mean velocity, turbulence intensity, and Reynolds shear stress fields further downstream. The free jet will be taken as a reference case when investigating the shallow water jet results. Experiments were conducted at $H/D = 60$ to approximate a free jet and provide basic data for comparison with the shallow water jet cases.

The mean velocity was calculated from the ensemble of velocity fields acquired at each location. The mean axial velocity U at each point in the measurement plane was calculated using

$$U = \frac{1}{M} \sum_{i=1}^M u_i \quad (5.1)$$

where u_i represents the instantaneous axial velocity component in field i and M represents the number of velocity fields. The mean vertical and horizontal velocity components (V and W) were calculated by the same procedure. In addition to the mean velocity, the turbulence intensity in each direction (u_{rms} , v_{rms} , w_{rms}) and the turbulent shear stresses ($\langle uv \rangle$ and $\langle uw \rangle$) were calculated using

$$\begin{aligned} \frac{u_{\text{rms}}}{U_c} &= \frac{1}{U_c} \sqrt{\frac{\sum_{i=1}^M (u_i - U)^2}{M}}, \text{ and} \\ \frac{\langle uv \rangle}{U_c^2} &= \frac{1}{U_c^2} \sum_{i=1}^M \frac{(u_i - U)(v_i - V)}{M}. \end{aligned} \quad (5.2)$$

where U_c is the local mean centreline velocity. In these equations, the sum is taken over the ensemble of M velocity fields.

5.2.1 Jet Exit

PIV measurements were made at the jet exit. The purpose of taking measurements at this location is to document the initial condition of the jet since the flow at downstream

locations is dependent on the jet exit characteristics (see Xu & Antonia, 2002 and Shinneeb *et al.*, 2006). The size and spatial resolution of this field-of-view are given in Table 5.1 (case name FJ01).

Figure 5.1 shows the axial velocity component U just downstream of the exit plane ($x/D = 0.2$). This profile was extracted from the average of 1000 PIV velocity fields and is very close to uniform. The uncertainty in the mean velocity U was estimated to be 2.1% (see Section 3.4). The velocity in the core of the jet at this location is 2.62 m/s. Although the difference between the jet exit velocity (2.5 m/s) and the core velocity seems quite large, it is explained by the presence of a very thin boundary layer at the jet exit. A simple “displacement thickness” calculation shows that a boundary layer whose thickness was on the order of the spatial resolution of the PIV measurements at the exit will result in an accelerated core region of this amount. The maximum deviation of the velocity from the core velocity over the jet exit was 0.46%. Figure 5.1 also shows the axial turbulence intensity u_{rms} normalised by the jet exit velocity U_e and confirms that the high shear regions at the edges of the jet produce the highest turbulence intensity. The axial turbulence intensity in the core of the jet exit was only 0.3%. These data indicate that the flow conditioner was working quite well in that it achieved a uniform, low turbulence intensity jet exit condition.

5.2.2 Zone of Established Flow (ZEF)

This section presents measurements of the round free jet which will be used as a reference case for the shallow water jet results. The free jet was approximated by positioning the free surface and the solid wall as far as possible from the jet centreline. The axis of the jet was positioned in the middle of the water tank where the depth of the water layer was $H/D = 60$. Three fields-of-view were positioned on the vertical plane along the centreline of the jet and covered the range $10.7 \leq x/D \leq 64.9$. The size and spatial resolution of these fields-of-view are given in Table 5.1. Two thousand images were acquired at each location.

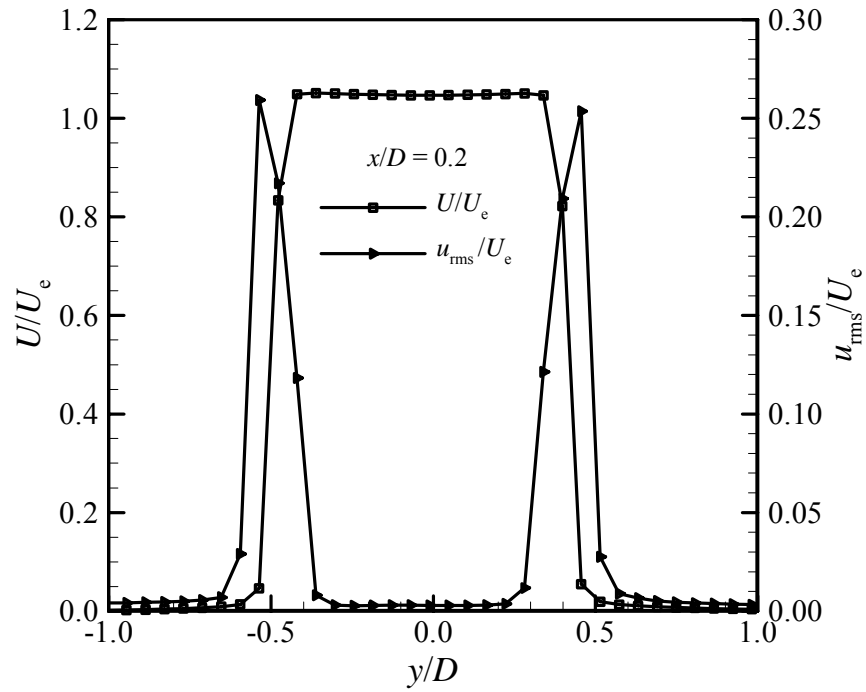


Figure 5.1: Axial velocity and turbulence intensity profiles near the jet exit ($x/D = 0.2$). Velocities are normalised by the exit velocity (2.5 m/s) and distances by the jet exit diameter (9 mm).

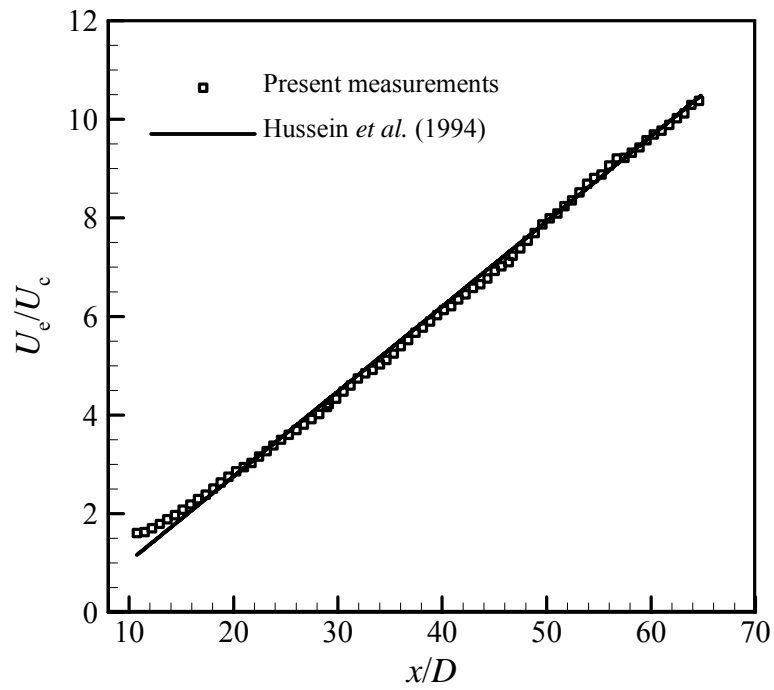


Figure 5.2: Decay of centreline velocity of the free jet in the axial direction. The solid line is the free jet case taken from Hussein *et al.* (1994).

Properties along the jet centreline

The variation of the mean centreline velocity U_c is shown by plotting U_c/U_c as a function of the normalised axial location x/D (see Figure 5.2). In this figure, the centreline velocity U_c was obtained by fitting the radial profiles of the mean axial velocity to the following Gaussian function:

$$U(y) = 1.359U_c \exp\left(-\left(\frac{y-y_c}{r_{1/2}}\right)^2\right) \quad (5.3)$$

where U is the mean axial velocity, U_c is the mean centreline velocity, y is the vertical coordinate, y_c is the vertical position of the centreline, and $r_{1/2}$ is the jet half-width measured at $U = U_c/2$. U_c , y_c , and $r_{1/2}$ were calculated using the non-linear, least-squares Levenberg-Marquardt algorithm (Press *et al.*, 1998).

Figure 5.2 shows that the mean centreline velocity measurements collapse very well onto a straight line within the range $10.7 \leq x/D \leq 64.9$. By modeling the centreline velocity according to equation 2.1, it exhibits a decay rate of $K_d = 5.90$ and a virtual origin $x_o/D = 3.57$ (x_o represents the distance from the jet exit to the virtual origin of the jet). Some frequently cited measurement results were listed in Table 2.1 for comparison purposes. The present results agree reasonably well with these previous K_d values which are in the range 5.8 – 6.0.

Figure 5.3 shows the axial turbulence intensity u_{rms}/U_c and the radial turbulence intensity v_{rms}/U_c along the jet centreline. Both curves demonstrate the same trend although the axial turbulence intensity u_{rms} is greater than the radial turbulence intensity v_{rms} . It should be remembered that the uncertainty in these values was estimated to be 21% (see Section 3.4). Both of them increase gradually in the region of $x/D < 40$. In the region of $x/D > 40$, the relative turbulence intensities reach almost constant values of $u_{rms}/U_c = 0.27$ and $v_{rms}/U_c = 0.21$, confirming the self-similarity of the jet in this region.

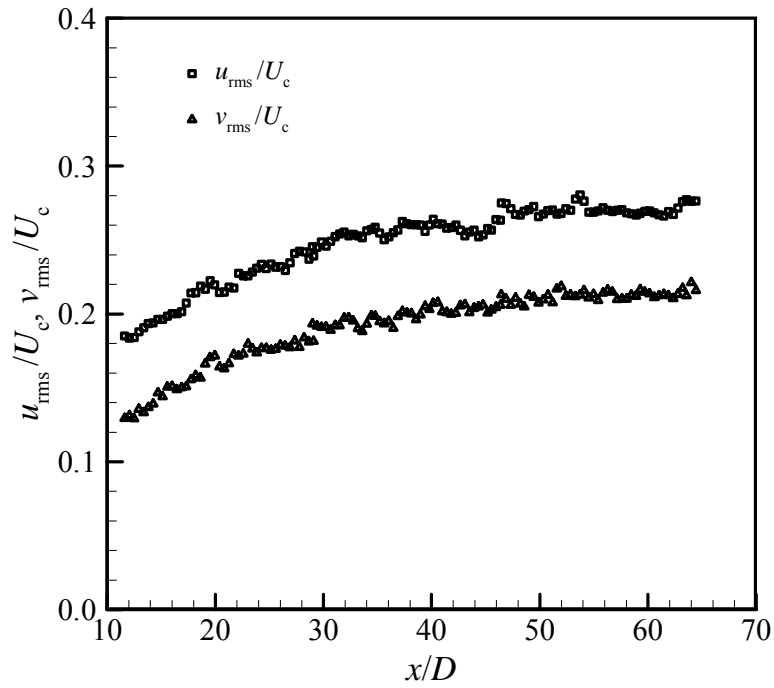


Figure 5.3: Variation of axial and radial turbulence intensities of the free jet along jet centreline.

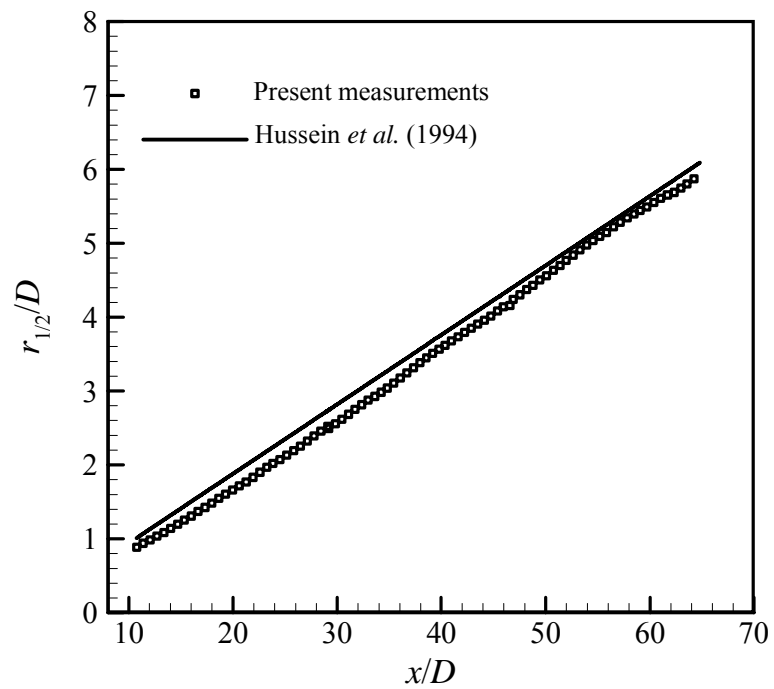


Figure 5.4: Spread of the present free jet along downstream distance. The solid line is the free jet case taken from Hussein *et al.* (1994).

This value is in excellent agreement with 0.28 and 0.22, respectively, for a turbulent free jet reported by Hussein *et al.* (1994).

The half-width of a free jet is defined as the radial location where the axial velocity equals one half of the centreline value. The jet spread accompanying the mean velocity decay is quantified by the increase of the half-velocity points $r_{1/2}$ with x . The value of $r_{1/2}$ was obtained from the fit to equation 5.3. The variation of the normalised half-width $r_{1/2}/D$ with the normalised axial distance x/D is plotted in Figure 5.4. This figure shows that the jet appears to spread linearly with a growth rate K_s of 0.096. The jet spread determined by Hussein *et al.* (1994) is also shown and corresponds to a growth rate K_s of 0.094. The agreement between the two growth rates is excellent. Table 2.1 gives some previous results of measured K_s values for free jets. These results lie in the range 0.080–0.102.

Radial profiles

The radial coordinate used to present radial profiles in this section is the non-dimensional η coordinate, which is given by

$$\eta = y/(x - x_0) \quad (5.4)$$

where y is the distance from the jet centreline, x is the axial distance measured from the jet exit, and x_0 is the location of the virtual origin.

Figure 5.5 shows radial profiles of mean axial velocity U at $x/D = 40, 50,$ and 60 . The self-similarity of the turbulent jet is clearly observed. The velocity profile for a free jet, given by Hussein *et al.* (1994), is also plotted in Figure 5.5. Good agreement between the present profiles and the free jet profile is found over most of the jet in this region. The narrower width of the profiles at the jet peripheries may be attributed to the different initial conditions and/or Reynolds number.

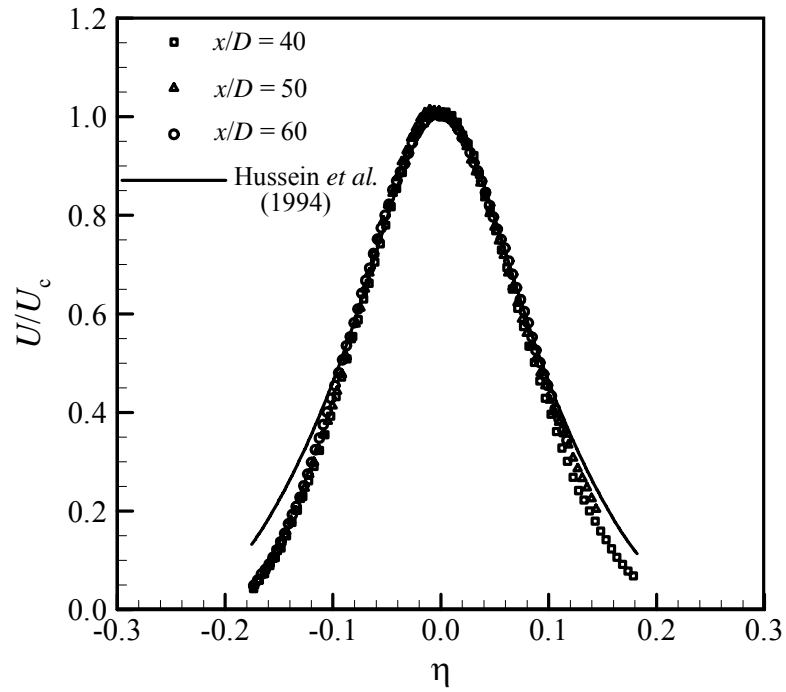


Figure 5.5: Normalised mean axial velocity profiles for a turbulent free jet in the zone of established flow (ZEF).

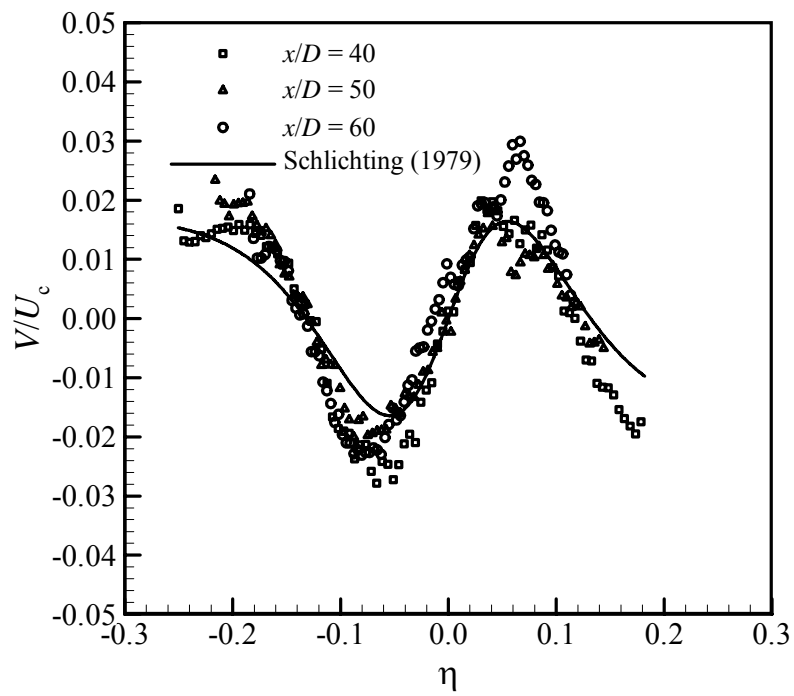


Figure 5.6: Normalised mean radial velocity profiles for a turbulent free jet in the zone of established flow (ZEF).

Radial profiles of the mean radial velocity V at $x/D = 40, 50,$ and 60 are shown in Figure 5.6. All profiles appear to collapse onto a single curve confirming the self-similarity of the flow. The mean radial velocity is weaker than the mean axial velocity by one order of magnitude and is also symmetrical about the jet centreline. This symmetry indicates that the flow near the jet centreline ($|\eta| < 0.11$) expands laterally outward and that the fluid surrounding the jet ($|\eta| > 0.11$) flows inward toward the jet centreline as a result of entrainment. The combined results of these two mechanisms lead to the profile shown in Figure 5.6. The theoretical prediction given by Schlichting (1979) is also plotted in the same figure. The comparison shows that the theory has predicted the basic features of the mean radial velocity although the predicted peak magnitude is smaller than the experimental results. The maximum relative radial velocity of the present jet is ~ 0.22 which occurs at $|\eta| \approx 0.073$, compared to ~ 0.164 which occurs at $|\eta| \approx 0.055$ for the theory. The higher values of the mean radial velocity are consistent with the relatively higher growth rate of the present jet compared to the published values given in Table 2.1.

Turbulent velocity fluctuations are plotted in the form of dimensionless turbulence intensities u_{rms}/U_c and v_{rms}/U_c , and turbulent shear stress $\langle uv \rangle / U_c^2$ in Figures 5.7, 5.8, and 5.9, respectively. The turbulence intensity at the centreline is approximately 0.27 and 0.21 for u_{rms}/U_c and v_{rms}/U_c . The data of Hussein *et al.* (1994) indicate that the maximum u_{rms}/U_c and v_{rms}/U_c are about 0.28 and 0.22, respectively, for free jets. The “flat top” and “cone top” profiles of turbulence intensity are clearly observed in Figures 5.7 and 5.8, respectively. Figure 5.9 shows that all the turbulent shear stress profiles collapse on a single line in this region as implied by self-similarity. The maximum value of $\langle uv \rangle / U_c^2$, which is located at $|\eta| \approx 0.073$, is equal to 0.022, which is in excellent agreement with the value of 0.021 reported by Hussein *et al.* (1994).

From the foregoing, it can be concluded that the free jet data for the present study are consistent with those of Hussein *et al.* (1994). The slight differences between the current

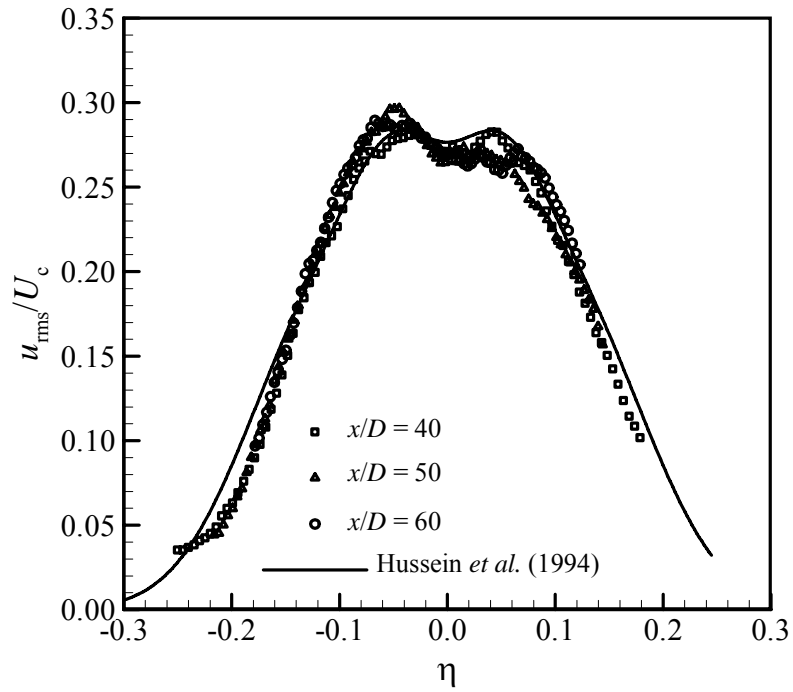


Figure 5.7: Normalised mean axial turbulence intensity profiles in the ZEF. The solid line is the free jet case taken from Hussein *et al.* (1994).

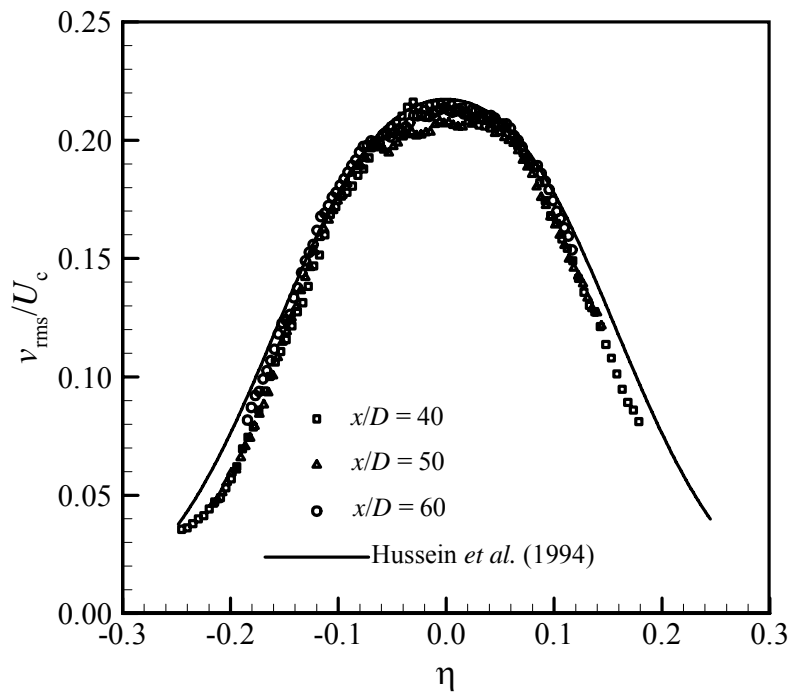


Figure 5.8: Normalised mean radial turbulence intensity profiles in the ZEF. The solid line is the free jet case taken from Hussein *et al.* (1994).

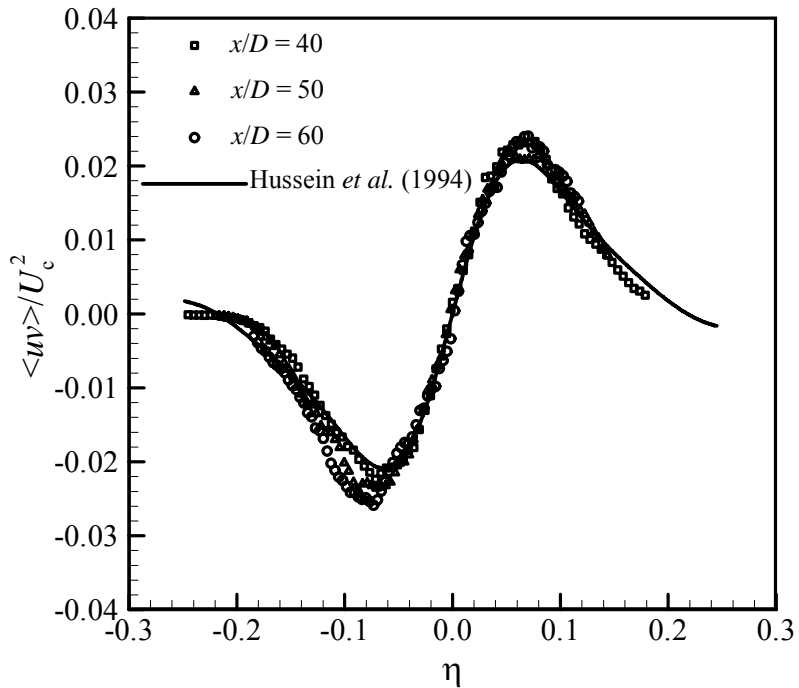


Figure 5.9: Normalised Reynolds shear stress profiles in the ZEF. The solid line is the free jet case taken from Hussein *et al.* (1994).

free jet results and those given in Table 2.1 may be attributed to different initial conditions, Reynolds numbers, and/or mild confinement effects resulting from smaller enclosures used in some studies. The last point was discussed in detail in Hussein *et al.* (1994).

5.3 SHALLOW WATER JETS – MEAN VELOCITY FIELDS

This section presents results of the mean velocity fields for shallow water jets. Three different degrees of vertical confinement were investigated, $H/D = 15, 10,$ and 5 . In all experiments, the centreline of the jet was located midway between the solid wall and the free surface as shown in Figure 3.1. Measurements were made on two orthogonal planes; vertical (x - y) and horizontal (x - z). Both measurement planes included the jet axis (x axis). The horizontal confinement in the water tank was negligible since the side walls were at $z/D \approx \pm 56$. Measurements were taken at three different locations downstream of

the jet exit where the effect of the vertical confinement started to be significant. The vertical plane was positioned to cover the entire depth from the solid wall to the free surface. As a reminder, the uncertainty in the mean velocities and turbulence intensities was estimated to be 2.1% and 21%, respectively (see Section 3.4).

5.3.1 Flow Properties along the Jet Centreline

Figure 5.10 shows the variation of the mean centreline velocity in the axial direction for the free and shallow water jet cases. In this figure, the vertical axis represents the mean centreline velocity U_c , which appears in the denominator, normalised by the jet exit velocity U_e . The centreline velocity U_c was obtained by curve fitting the mean axial velocity profiles measured on the horizontal plane using equation 5.3. It is clear that the centreline velocity measurements for all cases collapse very well onto a straight line in the beginning. Then the centreline velocity for the $H/D = 5$ and 10 cases started decaying at a lower rate at $x/D = 44$ and 55, respectively, compared to the free jet case. This is clearly the effect of the vertical confinement. This may be explained by the conservation of mass which demands an increase in the jet velocity because the cross-sectional area of the jet becomes constrained by the boundaries compared to the free case. However, the $H/D = 15$ case seems to follow the free jet decay rate in the range $28.2 < x/D < 79.6$ and is expected to decay at a slower rate at farther downstream locations. It can be concluded that the degree of the confinement affects the location at which the centreline velocity deviates from the free jet case.

The variation of the half-width $r_{1/2}$ of the jets with the axial distance x measured on the horizontal plane is shown in Figure 5.11. Both the half-width and the axial distance are normalised by the jet exit diameter D . It can be seen that both the free jet and the deepest shallow water jet ($H/D = 15$) appear to spread linearly although the growth rate of the free jet ($K_s = 0.096$) is higher than the $H/D = 15$ case ($K_s = 0.072$). The lower growth rate of the $H/D = 15$ case is consistent with the literature since the jet undergoes a constriction in the horizontal mid-plane and widening near the bounding surfaces because of the confinement. This behaviour may be explained by the presence of secondary flow currents which transport fluid from the axis towards the boundaries

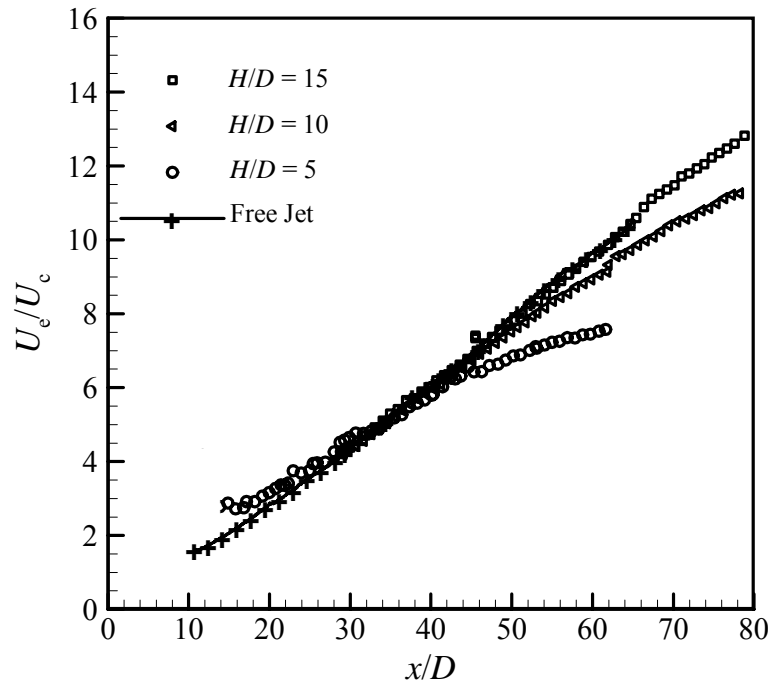


Figure 5.10: Decay of centreline velocity of shallow water jet cases ($H/D = 15$, 10, and 5) in the axial direction compared to the free jet.

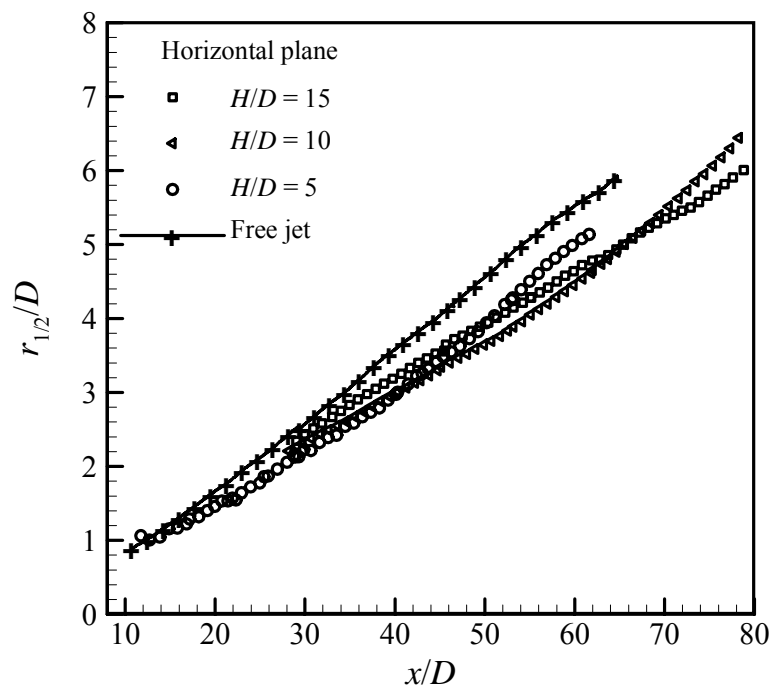


Figure 5.11: Spread of the shallow jet cases ($H/D = 15$, 10, and 5) along downstream distance. The symbolic line represents the free jet data. The data was extracted from horizontal planes.

(Dracos *et al.*, 1992). These secondary flow currents were formed by the interaction of jet vortices with the boundaries and subsequent stretching of the vortex filaments (Foss & Jones, 1968). The vertical confinement has a significant effect on jet spread for the shallower cases ($H/D = 10$ and 5). They appear to spread non-linearly with a lower growth rate compared to the free jet width. The only difference between the two cases is the location where the results depart from the free jet case. The departure from the free jet case has already occurred by $x/D = 30$ (where the data begin) for the $H/D = 10$ case, while it approximately occurs at $x/D = 12$ for the $H/D = 5$ cases. Generally, the deviation from the free jet case occurs earlier as the confinement increases.

Figure 5.12 shows the variation of the relative axial turbulence intensity u_{rms}/U_c along the jet centreline. It is clear that the relative axial turbulence intensity for all cases increases gradually before it becomes almost constant at downstream locations. This figure also shows that the axial turbulence intensity for the $H/D = 10$ case is slightly smaller than the free jet case because of the increased vertical confinement. For the $H/D = 5$ case, u_{rms}/U_c is further reduced by the vertical confinement and becomes $\sim 26\%$ lower than the free jet case. However, the vertical confinement has no effect on the $H/D = 15$ case ($u_{rms}/U_c = 0.27$). Generally, the vertical confinement has a mild effect on the axial turbulence intensity except that for the shallowest case which shows some suppression.

The variation of the relative vertical turbulence intensity v_{rms}/U_c along the jet centreline is shown in Figure 5.13. The vertical turbulence intensity for all the cases increased gradually before it became almost constant at downstream locations. By comparing the three shallow cases with the free jet, it is clear that the confinement has no effect on the vertical turbulence intensity for the $H/D = 15$ case ($v_{rms}/U_c \approx 0.21$), but it has a clear effect on the $H/D = 5$ case ($v_{rms}/U_c \approx 0.15$), a reduction of $\sim 29\%$. Note that the $H/D = 5$ case reached an asymptotic value earlier ($x/D \approx 19$) compared to the free jet which became constant at $x/D > 40$. The effect of the confinement on the $H/D = 10$ case is generally mild. v_{rms}/U_c seems to follow the free jet case in the beginning, then it starts slightly decreasing at axial location $x/D > 46$ which may be attributed to the increase of the mean centreline velocity.

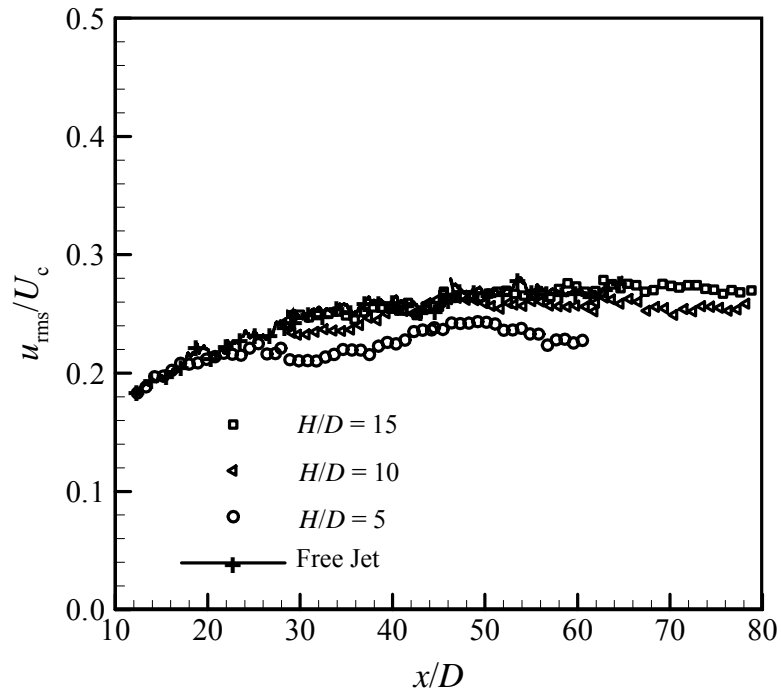


Figure 5.12: Variation of axial turbulence intensity u_{rms}/U_c of shallow water jet cases ($H/D = 15, 10,$ and 5) along jet centreline. The symbolic line represents the free jet data.

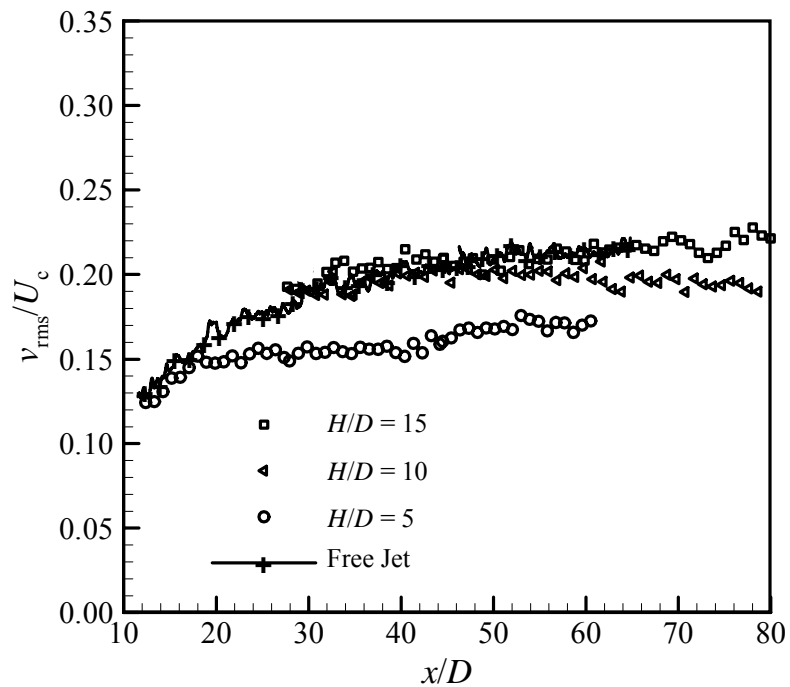


Figure 5.13: Variation of vertical turbulence intensity v_{rms}/U_c of shallow water jet cases ($H/D = 15, 10,$ and 5) along jet centreline. The symbolic line represents the free jet data.

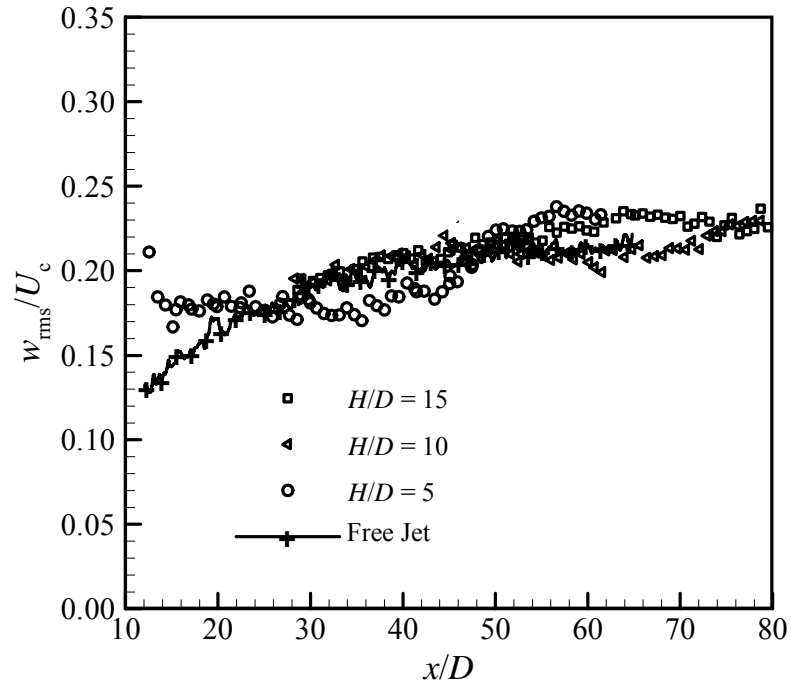


Figure 5.14: Variation of horizontal turbulence intensity w_{rms}/U_c of shallow water jet cases ($H/D = 15, 10,$ and 5) along jet centreline. The symbolic line represents the free jet data.

Figure 5.14 shows the variation of the relative horizontal turbulence intensity w_{rms}/U_c along the jet centreline. The relative horizontal turbulence intensity w_{rms}/U_c for the deeper cases ($H/D = 15$ and 10) increases gradually before it becomes almost constant at downstream locations. The results for u_{rms}/U_c and v_{rms}/U_c suggested that the vertical confinement should have no effect on w_{rms}/U_c for the $H/D = 15$ case, although it appears to have slightly higher values than the free jet case at downstream locations. For the shallowest case ($H/D = 5$), the relative horizontal turbulence intensity w_{rms}/U_c becomes constant earlier with a smaller value of turbulence intensity ($w_{\text{rms}}/U_c = 0.18$) compared to the other cases, then starts increasing at downstream locations ($x/D > 44$). Similar behaviour can also be observed farther downstream ($x/D > 71$) for the $H/D = 10$ case. This behaviour may be explained by the energy removed from the axial and vertical fluctuations being transferred to the horizontal component as will shown more clearly in Figure 5.15. As a result, the turbulence in the shallowest case is much more anisotropic at the centreline of the jet.

To show the degree of anisotropy of the fluctuation velocities along the jet centreline for the free and shallow cases, the vertical v_{rms} and horizontal w_{rms} turbulence intensities are plotted in Figures 5.15(a) and (b) against the normalised axial locations x/D . Both v_{rms} and w_{rms} are normalised by the axial turbulence intensity u_{rms} . Figures 5.15(a) shows that $v_{\text{rms}}/u_{\text{rms}}$ is almost constant for all free and shallow profiles. However, the free jet seems to be slightly less anisotropic with $v_{\text{rms}}/u_{\text{rms}} \approx 0.78$ compared to 0.76, 0.70, and 0.69 for $H/D = 15, 10,$ and 5 . These constant ratios indicate that the axial variation of u_{rms} and v_{rms} is similar. In contrast, Figures 5.15(b) shows that $w_{\text{rms}}/u_{\text{rms}}$ for the $H/D = 15$ and 10 cases increases with a low rate in the downstream direction, indicating a slow transfer of the kinetic energy from the axial and vertical fluctuations to the horizontal component. Moreover, this transfer occurs with a very high rate for the $H/D = 5$ case until the horizontal component w_{rms} becomes much higher than the axial component u_{rms} . This indicates that the degree of the anisotropy has increased significantly because of the confinement.

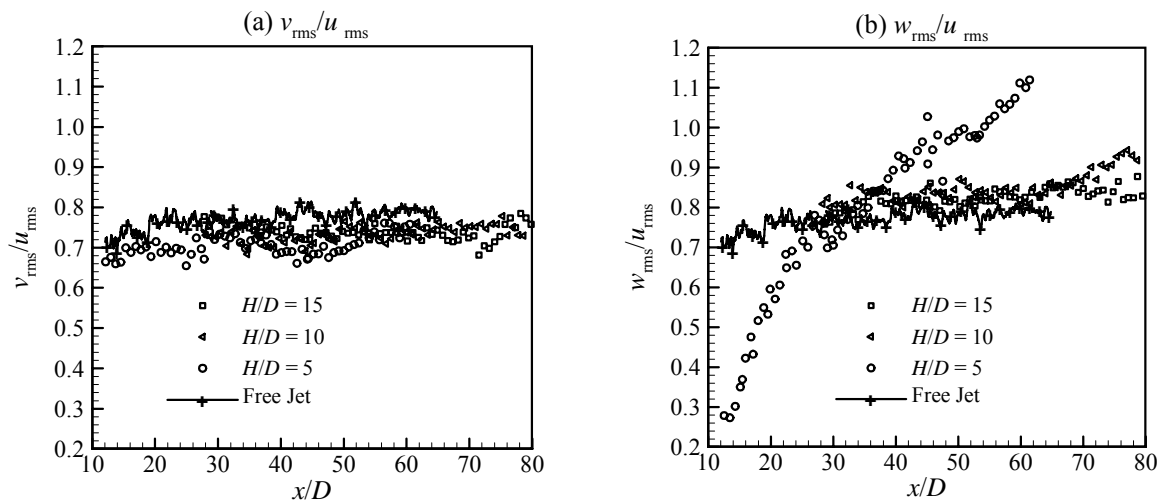


Figure 5.15: Variation of the fluctuation velocity ratios of the free and shallow jet cases along the jet centreline; (a) $v_{\text{rms}}/u_{\text{rms}}$ and (b) $w_{\text{rms}}/u_{\text{rms}}$.

5.3.2 Mean Velocity Profiles

Profiles of the mean velocity at selected downstream locations on the vertical (x - y) and horizontal (x - z) planes for the three shallow cases are presented in this section.

Vertical plane profiles

The development of the axial velocity U profiles in the axial direction for the three shallow cases ($H/D = 15, 10, \text{ and } 5$) is shown in Figure 5.16. All velocity profiles are normalised by the local mean centreline velocity U_c and are plotted against the vertical location y normalised by the water layer depth H . Figure 5.16(a) shows mean axial velocity U profiles in the vertical plane for the deepest shallow jet ($H/D = 15$) at different axial locations from $x/D = 30$ to 75 . To assess the effect of the confinement on the axial velocity field at $x/D = 30$, the free jet profile is also plotted at this location. Although the two profiles are almost identical over most of the water layer depth, the effect of the confinement can be observed near the solid wall ($y/H < -0.2$). As the flow evolves downstream, the jet spreads to the boundaries. The existence of these boundaries modifies the mean axial velocity so that it becomes zero at the solid wall and non-zero value at the free surface. It can also be seen that the symmetry of the velocity profiles around $y = 0$ has been lost at $x/D = 70$ and 75 because of the confinement. Moreover, this figure shows that the velocity profiles are still developing at these locations.

Figure 5.16(b) shows the mean axial velocity U/U_c on the vertical plane for $H/D = 10$ at different axial locations from $x/D = 30$ to 75 . By comparing to the free jet case at $x/D = 30$, the effect of the confinement is apparent. Downstream of this location, the normalised mean axial velocity above and below the jet centreline increases until the velocity becomes almost uniform at $70D$ and $75D$. The velocity profiles show only slight differences at these locations. The formation of the boundary layer near the solid wall can also be seen at $x/D > 50$, indicating that the jet has already spread to the solid

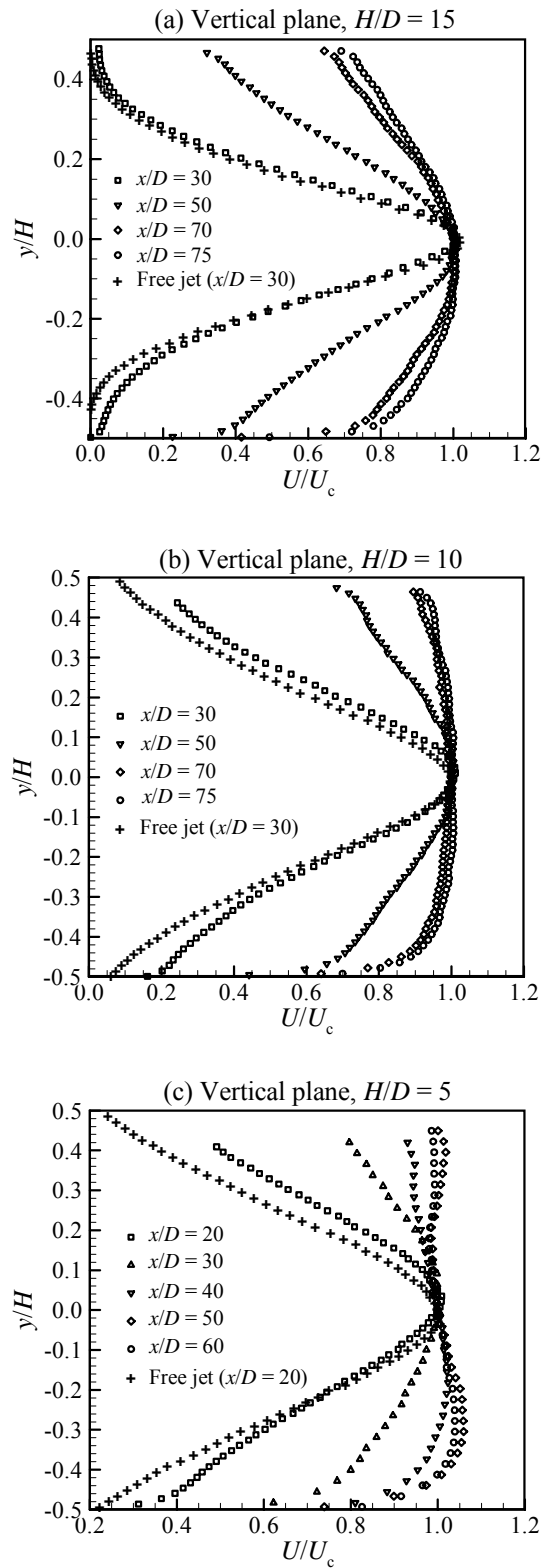


Figure 5.16: Downstream development of the normalised mean axial velocity U/U_c profiles on the vertical plane for the shallow water jet cases; (a) $H/D = 15$, (b) $H/D = 10$, and (c) $H/D = 5$.

boundary. The high spatial resolution of the present data allows the velocity gradient near the solid wall to be observed in these profiles.

Figure 5.16(c) shows the development of the mean axial velocity U/U_c on the vertical plane at different axial locations for the shallowest case ($H/D = 5$). At $x/D = 20$, the effect of the confinement on the velocity profile is clear compared to the free jet case. The confined profile appears wider and the location of the maximum velocity is slightly displaced above the jet axis. Downstream of this location, the normalised velocity above and below the centreline of the jet increases rapidly until it becomes almost uniform over the entire layer with a mild peak near the solid wall. The velocity becomes almost uniform earlier compared to the $H/D = 10$ case indicating very strong confinement in this case.

Profiles of the vertical component of the mean velocity V are shown in Figure 5.17. All velocity profiles are normalised by the local mean centreline velocity U_c and are plotted against the vertical location y normalised by the water depth H . Figure 5.17(a) shows the development of the vertical velocity profiles in the axial direction for $H/D = 15$. The vertical velocity profile for the free jet at $x/D = 30$ is also plotted in this figure. Note that only every third symbol is shown to avoid cluttering. It appears that the vertical flow is symmetrical about the jet centreline for all profiles. The free and shallow jet profiles (both plotted for $x/D = 30$) are similar in the core region ($|y/H| < 0.2$) of the jet. However, the mean vertical velocity for the shallow case is obviously affected by the proximity of the boundaries at this axial location. For the confined case, V/U_c differs from the free jet near the boundaries to become outward from the jet centreline indicating that the jet no longer expands beyond this axial location. Note also that the vertical component of velocity is more affected by the proximity of the solid boundary than the free boundary. This behaviour is consistent with the behaviour of the mean axial velocity at this location shown in Figure 5.16(a). At $x/D = 50$, the flow expands vertically outward over the entire depth indicating spreading of the jet without inward flow. $|V/U_c|$ reaches a maximum value at $|y/H| \approx 0.25$ then decreases gradually to zero at the boundaries. At this axial location, $|V/U_c|$ is relatively large over the entire depth. At

locations further downstream ($x/D = 70$ and 75), the behaviour of the mean vertical velocity profiles are similar to the one at $x/D = 50$. They become almost identical with a smaller relative velocity compared to the one at $x/D = 50$. The similarity between the vertical velocity profiles at $x/D = 70$ and 75 is also observed in the axial velocity profiles at the same locations shown in Figure 5.16(a). Generally, the vertical velocity profiles for $x/D \geq 30$ indicate that the vertical entrainment has stopped and only vertical outward flow from the jet axis takes place. This may explain the rapid increase of the axial velocity near the boundaries shown in Figure 5.16(a) and the reduction in the jet width on the horizontal mid-plane.

Figure 5.17(b) shows the behaviour of the normalised mean vertical velocity V/U_c at different downstream locations $x/D = 30, 50, 70,$ and 75 for $H/D = 10$. The velocity profile at $x/D = 30$ is similar to the free jet profile at the same location although the velocity magnitude is larger than the free jet case. Both of them are symmetrical about the jet centreline. This profile indicates that the flow near the jet centreline expands outward while there is no inward flow from the outer region toward the jet centreline compared to the free jet profile. The magnitude of the outward flow at this location reaches up to 3.7% of the centreline velocity at $|y/H| \approx 0.2$. Figure 5.17(b) also shows that with increasing axial distance, the vertical velocity profiles tend to a negative V over the depth (see $x/D = 75$). At this location, the peak magnitude of the relative vertical velocity ($V/U_c \approx -0.028$) is located at $y/H \approx -0.2$ and it is almost zero at $y/H \approx 0.1$ above the jet centreline. The negative sign of the vertical velocity profile at $x/D = 75$, which indicates that the flow is directed to the solid wall, is also observed by Law & Herlina (2002) in their experimental study on circular wall jets. It was explained by the existence of secondary vortices that suck the fluid towards the wall and then divert it horizontally away from the vertical mid-plane parallel to the wall. Note that the velocity profiles above the jet axis shown in Figure 5.17(b) change more rapidly than the velocity profiles below the jet axis to approach this state. This behaviour may be due to the different boundary conditions near the solid wall and the free surface.

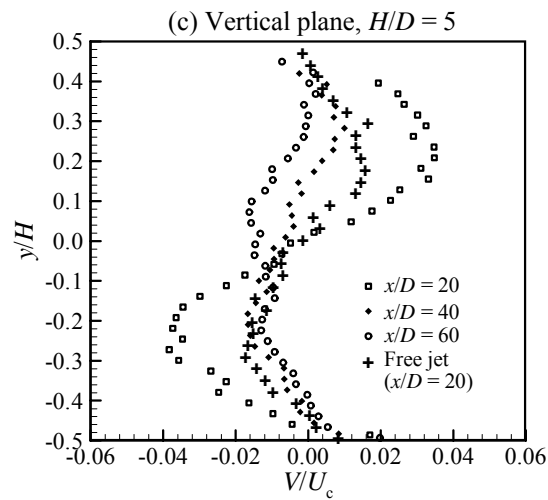
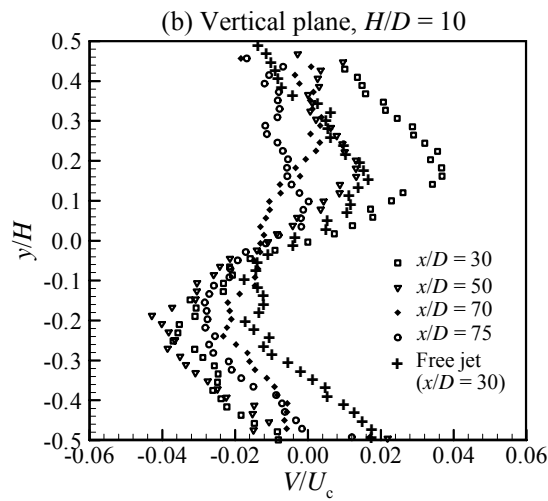
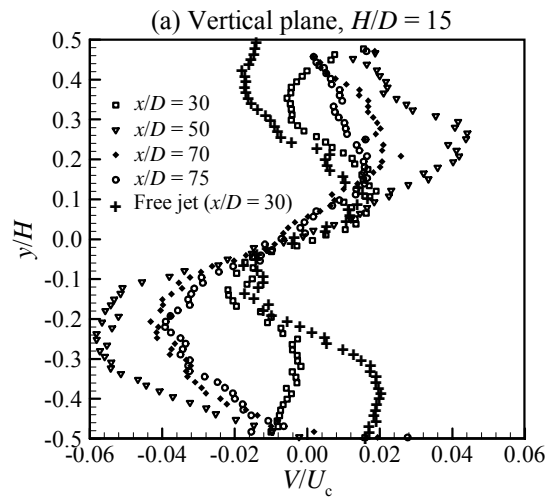


Figure 5.17: Downstream development of the normalised mean vertical velocity V/U_c profiles on the vertical plane for the shallow water jet cases; (a) $H/D = 15$, (b) $H/D = 10$, and (c) $H/D = 5$.

The mean vertical velocity profiles for the shallowest case $H/D = 5$ are shown in Figure 5.17(c) at axial locations $x/D = 20, 40,$ and 60 . It is apparent that the development of the velocity profiles shown in this figure is similar to the previous case. However, the interaction of the jet with the boundaries occurs earlier since the vertical confinement is stronger. Comparison between the shallow and free jet cases at $x/D = 20$ shows that the basic features are the same but the vertical velocity is larger for the shallow case and reaches about 3.6% of the centreline velocity. At locations further downstream, the velocity profiles above the jet centreline start decreasing until V becomes negative which indicates that the jet no longer expands. Below the jet centreline, $|V/U_c|$ seems to decrease then become almost constant at downstream locations. Generally, V becomes negative (with a magnitude close to zero) over almost the entire depth except near the solid wall where V is positive because of the formation of the boundary layer. As well, V seems to approach zero near the free surface. Unfortunately, the data near the free surface were removed due to reflection of the light sheet by waves on the free surface. A global representation of the behaviour of the mean vertical velocity V profiles is illustrated in Figure 5.18. It shows a colour contour of V/U_c which indicates that the jet spreads to the boundaries in the beginning. Then, V becomes negative over most of the water depth at downstream locations.

Horizontal plane profiles

Velocity profiles of the mean axial velocity on horizontal planes at different axial locations are shown in Figure 5.19. Each figure shows the development of the velocity profiles for each of the three shallow water jets ($H/D = 15, 10,$ and 5 respectively). The free jet profile is also plotted for comparison purposes. In these figures, the axial velocity U is normalised by the local mean centreline velocity U_c and is plotted against the non-dimensional coordinate $\eta = z/(x - x_0)$. The reason for using this coordinate system is to allow comparison with the free jet case. It is clear that all axial velocity profiles are similar and agree reasonably well with the free jet profile, suggesting that the vertical confinement has a negligible effect on the similarity of the axial velocity profiles on the horizontal plane.

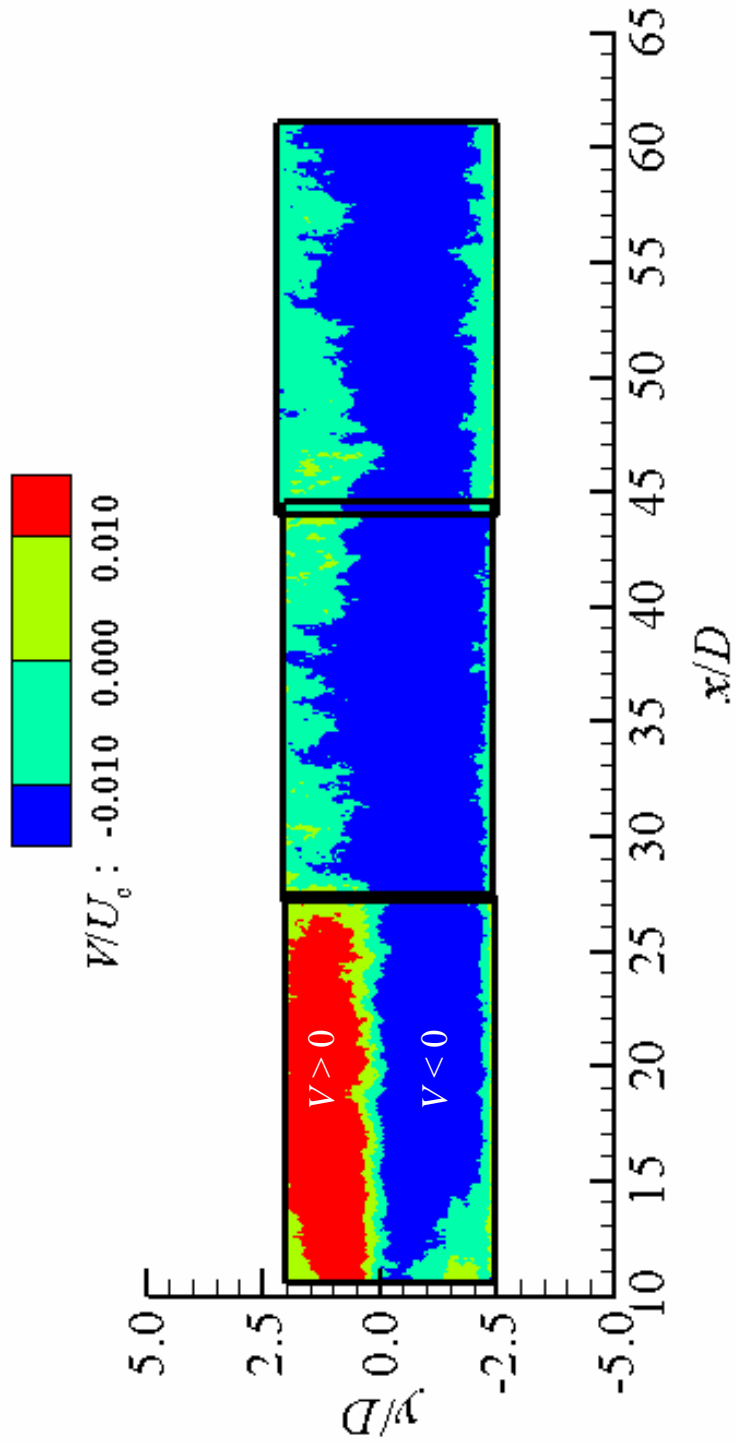


Figure 5.18: Colour contour representing the development of the mean vertical velocity V in the axial direction for the shallowest jet case ($H/D = 5$).

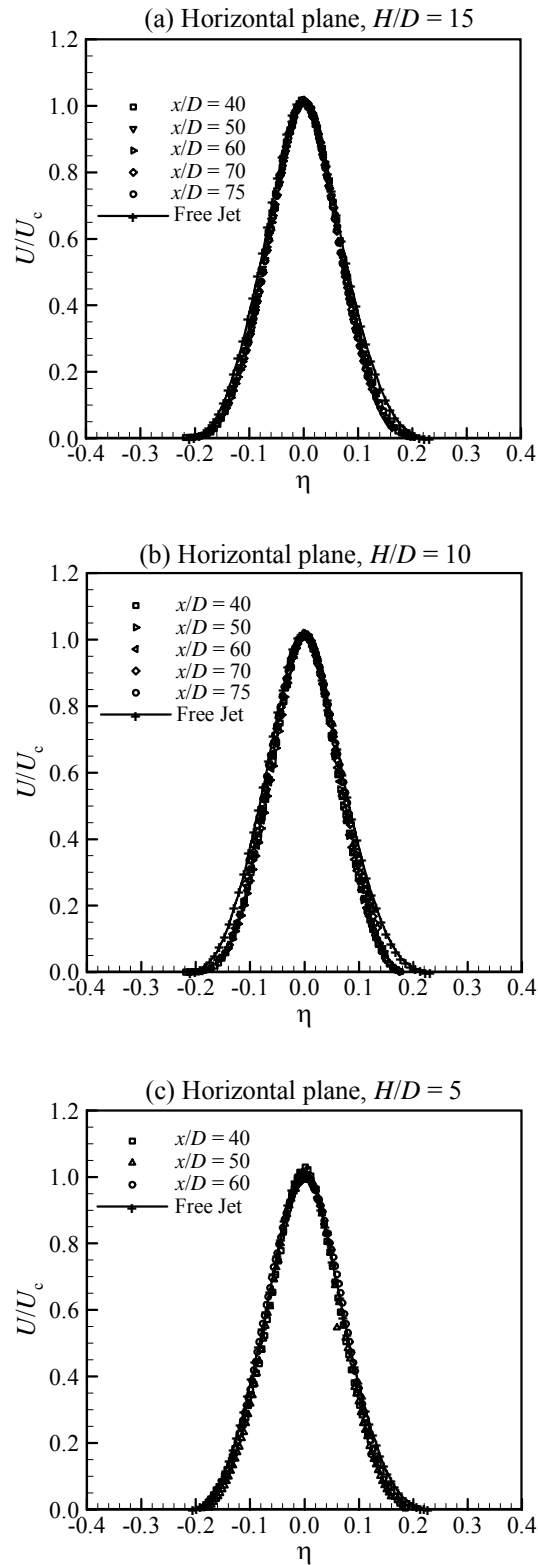


Figure 5.19: Downstream development of the normalised mean axial velocity U/U_c profiles on the horizontal plane for the shallow water jet cases; (a) $H/D = 15$, (b) $H/D = 10$, and (c) $H/D = 5$.

In order to show the effect of confinement on the velocity profiles, the profiles for $H/D = 15$, 10 , and 5 are plotted at the same axial locations. Figures 5.20(a) and (b) show the shallow jet profiles on the horizontal plane at $x/D = 40$ and 60 , respectively. The free jet profile is also plotted at the same locations. The velocity profiles are normalised by the mean centreline velocity U_c and are plotted against the vertical location y normalised by the jet exit diameter D . It is clear that the velocity profiles shown in Figure 5.20(a) are slightly narrower than the free jet profile at this location ($x/D = 40$). However, the shallow jet profiles are almost the same at this location, but are slightly different at the peripheries ($|z/D| > 4.2$). Further downstream ($x/D = 60$), Figure 5.20(b) shows that the jets become even narrower compared to the free jet case. The interesting feature shown in this figure is that the profiles of the $H/D = 15$ and 10 cases are narrower than the $H/D = 5$ case. The reason is because the $H/D = 5$ case started widening again at this location which is consistent with the jet spread shown in Figure 5.11 and the horizontal velocity W profiles to be shown in Figure 5.21(c). The narrow behaviour of the shallow jets shown in these figures is consistent with the behaviour of the vertical velocity in Figures 5.17(a), (b), and (c), which show outward flow from the jet axis without inward flow (entrainment). This indicates that the fluid is taken from the core of the jet and transported to the boundaries, which explains the reduction in the jet width in the horizontal plane.

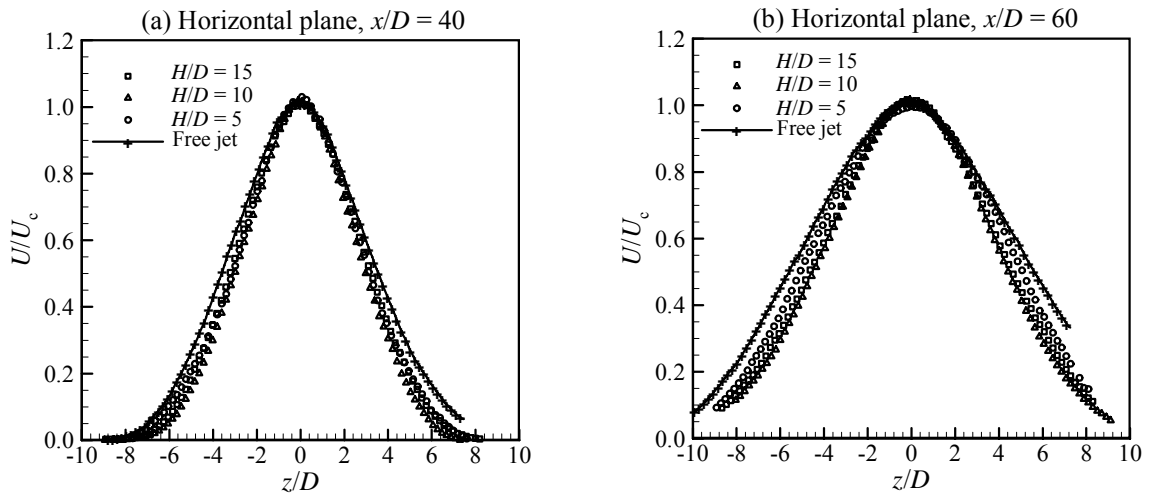


Figure 5.20: Profiles of the normalised mean axial velocity U/U_c of free and shallow jet cases on the horizontal plane at axial locations; (a) $x/D = 40$, and (b) $x/D = 60$.

Figure 5.21(a) shows the mean horizontal velocity W profiles extracted from the horizontal plane for $H/D = 15$ at axial locations $x/D = 40, 60,$ and 75 . In this figure, the velocities are normalised by the local mean centreline velocity U_c and plotted against the non-dimensional coordinate η . Again, the free jet case is also plotted for comparison. This figure shows that the horizontal velocity profiles are symmetrical about the jet centreline. For all cases, the mean horizontal velocity is near zero on the symmetry plane of the jet. These profiles indicate that the flow near the jet centreline expands outward ($|\eta| < 0.11$ for the free jet) while the fluid in the outer region flows inward toward the jet centreline as a result of entrainment. However, the region of outward lateral flow near the jet centreline shrinks in the downstream direction, indicating that the horizontal mid-plane of the jet undergoes a constriction (see Figure A.1 in Appendix A for a clearer view). This behaviour is consistent with the half-width curve which shows that the spread rate of this case is smaller than the free jet rate (see Figure 5.11). On the other hand, the inward horizontal flow at the peripheries of the jet increases in the axial direction. It should also be noted that the profiles at $x/D = 60$ and 75 are almost identical. This is consistent with the turbulence intensity results that approach constant values (shown in Figures 5.12 to 5.14).

Figure 5.21(b) shows velocity profiles of the mean horizontal velocity W on the horizontal plane for $H/D = 10$. The behaviour of the velocity profiles at this depth is similar to the previous case. The only difference is that the inward flow at the sides of the jet is larger than the previous case. The similarity between the velocity profiles at $x/D = 60$ and 75 is clear in this figure.

The development of the mean horizontal velocity W for the shallowest case $H/D = 5$ is interesting. Figure 5.21(c) shows that the velocity is zero at the centreline for all the profiles. It also shows that, although the outward flow is relatively weak and constrained to a small region near the jet axis, it narrows in the downstream direction until the mean flow is toward the jet centreline at $x/D \approx 40$ (see Figure A.2 in Appendix A for clearer view). Further downstream, it expands again in the axial direction as can be seen at

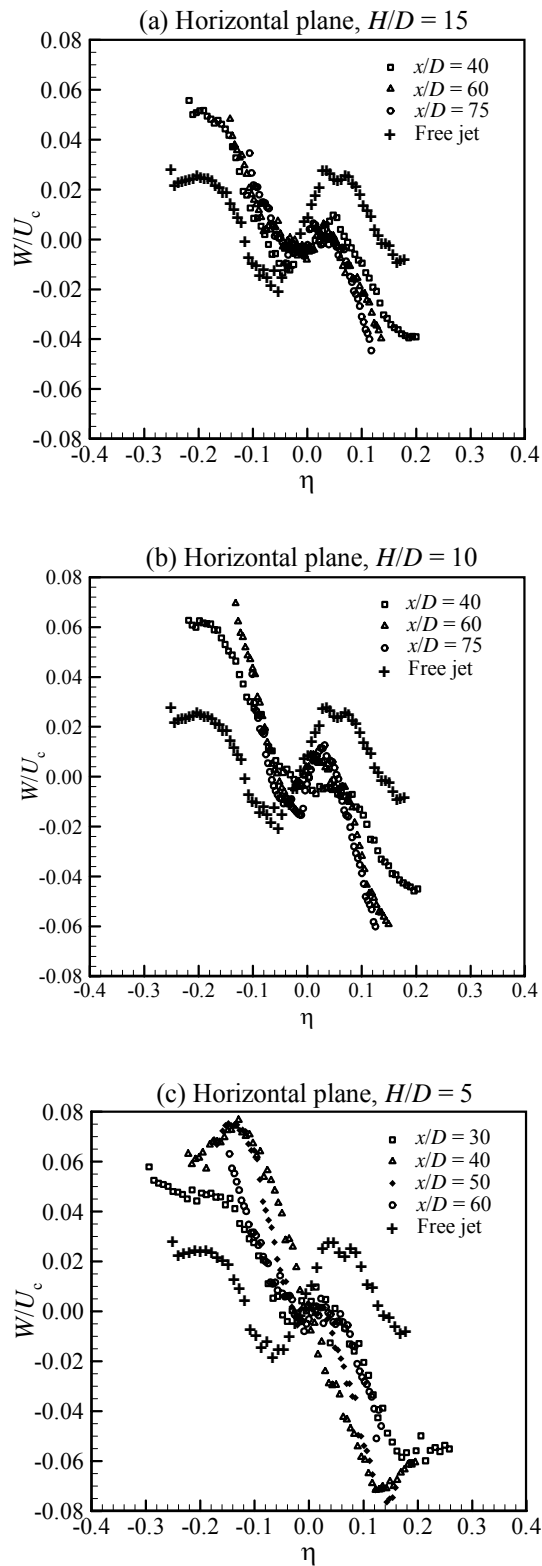


Figure 5.21: Downstream development of the normalised mean horizontal velocity W/U_c profiles on the horizontal plane for the shallow water jet cases; (a) $H/D = 15$, (b) $H/D = 10$, and (c) $H/D = 5$.

$x/D = 50$ and 60 . This behaviour is accompanied by first increasing the inward velocity at the sides of the jet until it reaches a maximum value at $x/D = 40$, then decreasing of the inward velocity ($|\eta| < 0.03$) as shown by the velocity profiles at $x/D = 50$ and 60 . Unfortunately, the velocity field was not measured beyond this axial distance. This behaviour is consistent with the non-linear spread of the jet for this case shown in Figure 5.11. This description of the behaviour of the mean horizontal velocity W profiles is shown more clearly in Figure 5.22. This figure shows the behaviour of W/U_c in the axial direction and confirms the reduction then expansion of the horizontal outward region near the jet axis and the existence of strong horizontal inward flow at the sides of the jet.

The effect of the vertical confinement on the mean horizontal velocity W is shown more clearly in Figures 5.23(a) and (b) for $H/D = 15, 10,$ and 5 . These figures show the behaviour of W/U_c for the shallow and free jet cases at axial locations $x/D = 40$ and 60 , respectively. In these figures, W/U_c is plotted against the horizontal distance z/D . At $x/D = 40$, Figure 5.23(a) shows that the region of outward lateral flow near the jet centreline shrinks while the magnitude of the inward horizontal flow at the peripheries increases as the confinement degree increases. It is also clear that the flow for the $H/D = 5$ case is only inward toward the jet centreline at this axial location. Further downstream ($x/D = 60$, Figure 5.23(b)), the mean outward flow near the jet centreline starts increasing and expanding again particularly for the $H/D = 10$ and 5 cases. This behaviour is accompanied by a decrease of the inward flow at the peripheries of the shallow cases compared to the results shown in Figure 5.23(a).

5.3.3 Turbulence Profiles

In this section, statistical quantities associated with the turbulent stresses are presented and compared with the free jet case. In the statistical description of turbulence, the instantaneous velocity is decomposed into mean and fluctuating components. The fluctuations are constructed as statistical measures of the local interactions due to unsteady behaviour. The root-mean-square velocities (turbulence intensities) and the Reynolds shear stresses (see equation 5.2) can provide insight into the physics of turbulent flow from a Reynolds-averaged point-of-view.

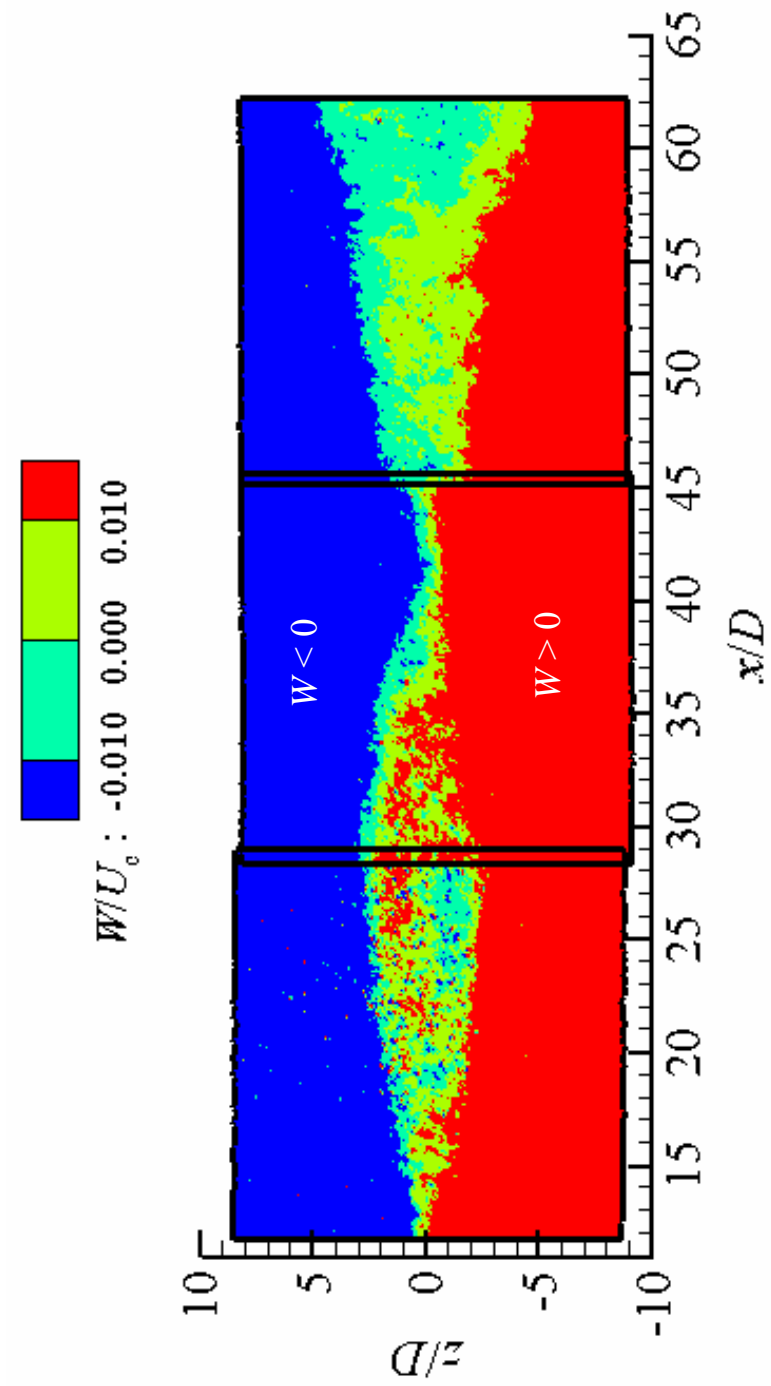


Figure 5.22: Colour contour representing the development of the mean horizontal velocity W in the axial direction for the shallowest jet case ($H/D = 5$).

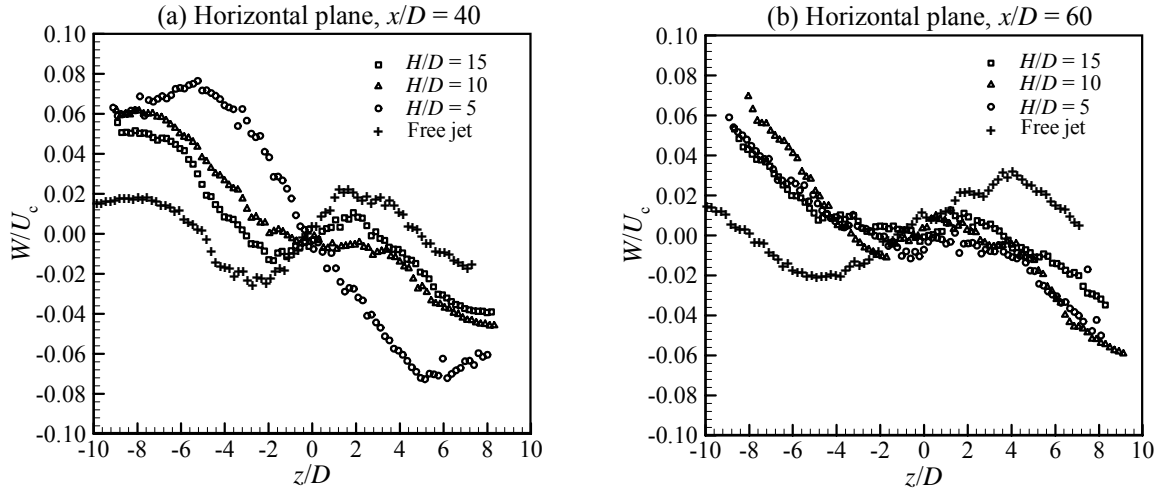


Figure 5.23: Profiles of the normalised mean horizontal velocity W/U_c of free and shallow jet cases on the horizontal plane at axial locations; (a) $x/D = 40$, and (b) $x/D = 60$.

Axial turbulence intensity u_{rms}/U_c on the vertical plane

Profiles of the relative axial turbulence intensity u_{rms}/U_c extracted from the vertical plane for the $H/D = 15, 10$, and 5 cases are shown in Figures 5.24(a), (b), and (c) at different axial locations. In these figures, the relative turbulence intensity is plotted against the vertical axis y normalised by the depth of the water layer H . The free jet profile is also shown in these figures for comparison purposes. Note that the free jet profile is normalised by the same depth H for each shallow jet case so that only a portion of the profile is shown. Comparing the relative axial turbulence intensity u_{rms}/U_c profiles for the shallow water and free jet cases at $x/D = 40$ (shown in Figure 5.24(a)) shows that u_{rms}/U_c for the shallow case is greater near the solid wall ($y/H < -0.42$) and near and above the jet axis ($y/H > -0.2$). The percentage of increase on the jet axis is $\sim 11\%$. The higher value of u_{rms}/U_c on the jet centreline at this location is not in agreement with the results to be shown on the horizontal plane at the same location, which shows only slight differences between the free and the shallow cases. This difference is seen only in this profile which may be due to bad data in this region. The off-axis peaks that occur in the free jet profile are not observed in the shallow jet profile. However, u_{rms}/U_c looks similar in the region $-0.42 < y/H < -0.2$. At locations further downstream, the relative axial turbulence intensity increases slightly in the inner region (near the jet axis) and rapidly

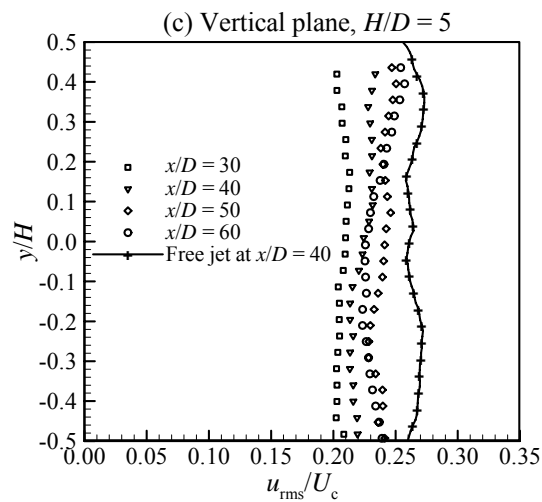
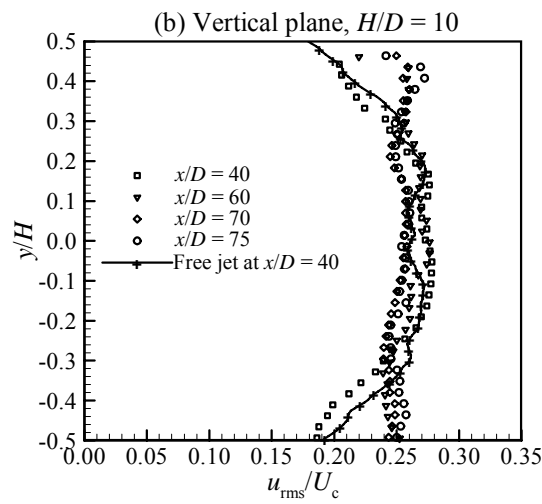
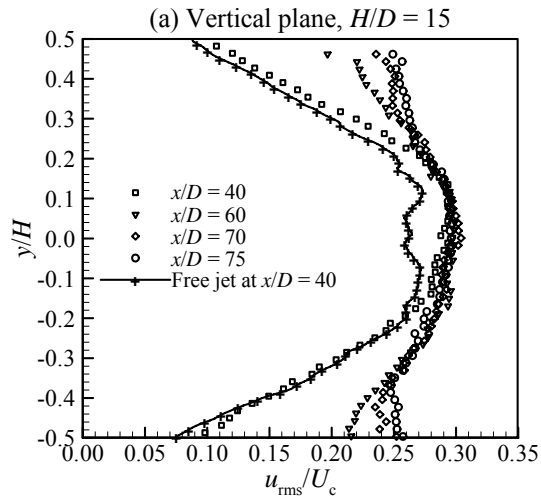


Figure 5.24: Downstream development of the relative axial turbulence intensity u_{rms}/U_c profiles on the vertical plane for the shallow water jet cases; (a) $H/D = 15$, (b) $H/D = 10$, and (c) $H/D = 5$.

in the outer region (near the boundaries) until the turbulence levels became relatively high across the entire depth with a mild peak located on the jet axis. The maximum value of u_{rms}/U_c is ~ 0.295 at $x/D = 70$ and 75 .

Figure 5.24(b) shows the downstream evolution of the relative axial turbulence intensity u_{rms}/U_c profiles for the $H/D = 10$ and free jet cases. The free jet data are extracted at $x/D = 40$. The shallow and free jet profiles at this location are slightly different because of the confinement. Farther away ($x/D > 40$), the vertical confinement becomes significant and the axial turbulence intensity profiles appear almost uniform over the depth ($u_{\text{rms}}/U_c \approx 0.25$). The profiles also show that the relative axial turbulence intensity u_{rms}/U_c near the boundaries slightly increases in the axial direction. At $x/D = 70$ and 75 , the slight increase of u_{rms}/U_c near the boundaries is accompanied by a slight decrease in the region near the centreline of the jet ($|y/H| < 0.25$). The two profiles look similar at these locations. The relatively low values of the axial turbulence intensity at $x/D = 60$, 70 , and 75 , compared to the values shown in Figure 5.24(a) at the same locations may partially be attributed to the mean centreline velocities used for normalising the profiles, which are greater than the free jet data because of the confinement.

Profiles of the relative axial turbulence intensity u_{rms}/U_c for the $H/D = 5$ case are shown in Figure 5.24(c). The free jet profile at $x/D = 40$ is also plotted. The effect of the vertical confinement is obvious by comparing the shallow and free jet profiles at $x/D = 40$, indicating very strong confinement in this case. The shallow jet profile at $x/D = 40$ looks almost uniform and has lower values of the relative turbulence intensity ($u_{\text{rms}}/U_c \approx 0.21$) than the free jet data. Further downstream, u_{rms}/U_c seems to increase slightly near the jet axis and with a greater rate near the boundaries. Moreover, the relative axial turbulence intensity profiles at $x/D = 50$ and 60 are slightly different near the centreline of the jet ($-0.24 < y/H < 0.16$). From this result and the behaviour of the relative turbulence intensities along the jet centreline shown in Figures 5.12 to 5.14, it can be concluded that the jet is still developing.

Profiles of the relative axial turbulence intensity u_{rms}/U_c on the vertical plane are plotted at $x/D = 40$ and 60 in Figures 5.25(a) and (b). Figure 5.25(a) shows the free and shallow jet ($H/D = 15, 10,$ and 5) profiles at $x/D = 40$. The deepest shallow jet profile ($H/D = 15$) does not show the off-axis peaks and looks greater than the free jet case near the jet axis ($-2.4 < y/D < 3.2$) and slightly greater for $y/D > 3.2$. The larger values at the jet centreline were attributed to bad data in that region. The $H/D = 10$ profile is obviously restricted by the depth of the water layer, but is still comparable to the free jet case at this location. For the $H/D = 5$ case, u_{rms}/U_c is significantly attenuated by the vertical confinement and has lost its Gaussian shape at this location. For this case, u_{rms}/U_c is slightly larger above the jet axis than below the jet axis. The reduction of u_{rms}/U_c at the jet centreline is estimated to be $\sim 15\%$ compared to the free jet case.

Figure 5.25(b) shows the u_{rms}/U_c profiles for the free and shallow cases at $x/D = 60$. In this figure, the off-axis peak above the jet axis for the free jet profile looks slightly smaller than below the jet axis which might be due to some bad data in this region. For the $H/D = 15$ case, the cone shape of the u_{rms}/U_c profile is observed. For the $H/D = 10$ and 5 cases, the Gaussian profile has been lost at this location and u_{rms}/U_c seems to decrease near the jet axis and increase near the boundaries compared to the $H/D = 15$ case. This is shown more clearly for the $H/D = 5$ case where u_{rms}/U_c becomes greater near the free surface compared to its value at the solid wall.

Axial turbulence intensity u_{rms}/U_c on the horizontal plane

The downstream development of the relative axial turbulence intensity u_{rms}/U_c extracted from the horizontal plane for the $H/D = 15, 10,$ and 5 cases is shown in Figures 5.26(a), (b), and (c), respectively, at different axial locations. These profiles are plotted against the non-dimensional coordinate $\eta = z/(x - x_0)$ in these figures and compared to the free jet profile at $x/D = 40$. The u_{rms}/U_c profiles for the $H/D = 15$ case are shown in Figure 5.26(a). This figure shows that the shallow and free jet profiles at $x/D = 40$ are similar in the core region ($|\eta| < 0.12$), but the shallow jet profile is narrower in the outer region

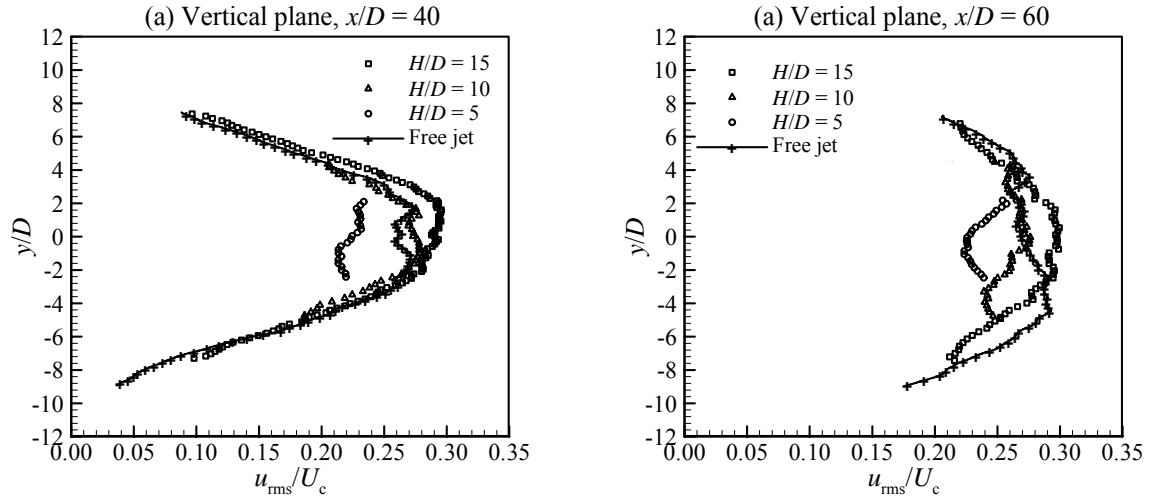


Figure 5.25: Behaviour of the relative axial turbulence intensity u_{rms}/U_c of free and shallow jet cases on the vertical plane at axial locations; (a) $x/D = 40$, and (b) $x/D = 60$.

($|\eta| > 0.12$). The u_{rms}/U_c profiles at $x/D = 60, 70$, and 75 collapse quite well onto a single line with $u_{\text{rms}}/U_c = 0.28$ at the centreline of the jet. The off-axis peaks become more distinct at these locations compared to the free jet profile. These profiles show an increase of u_{rms}/U_c in the core region ($|\eta| < 0.08$), but they match the free jet profile in the outer region.

Figure 5.26(b) shows that all the relative axial turbulence intensity u_{rms}/U_c profiles for the $H/D = 10$ case collapse quite well onto a single line from $x/D = 40$ to 75 . By comparing the collapsed profiles with the free jet profile, it can be seen that they almost match the free jet near the jet axis ($|\eta| < 0.1$), but they are narrower than the free jet case in the outer region. As shown in Figure 5.10, the mean centreline velocity for the $H/D = 10$ case decreases at a slower rate in the axial direction ($x/D > 49$) compared to the free jet case. This indicates that the axial turbulence intensity u_{rms} of the shallow cases must also decrease with the same rate in the axial direction in order to maintain a constant value of u_{rms}/U_c .

Figure 5.26(c) displays the behaviour of the relative axial turbulence intensity u_{rms}/U_c profiles in the axial direction for the $H/D = 5$ case. This figure shows that u_{rms}/U_c for all

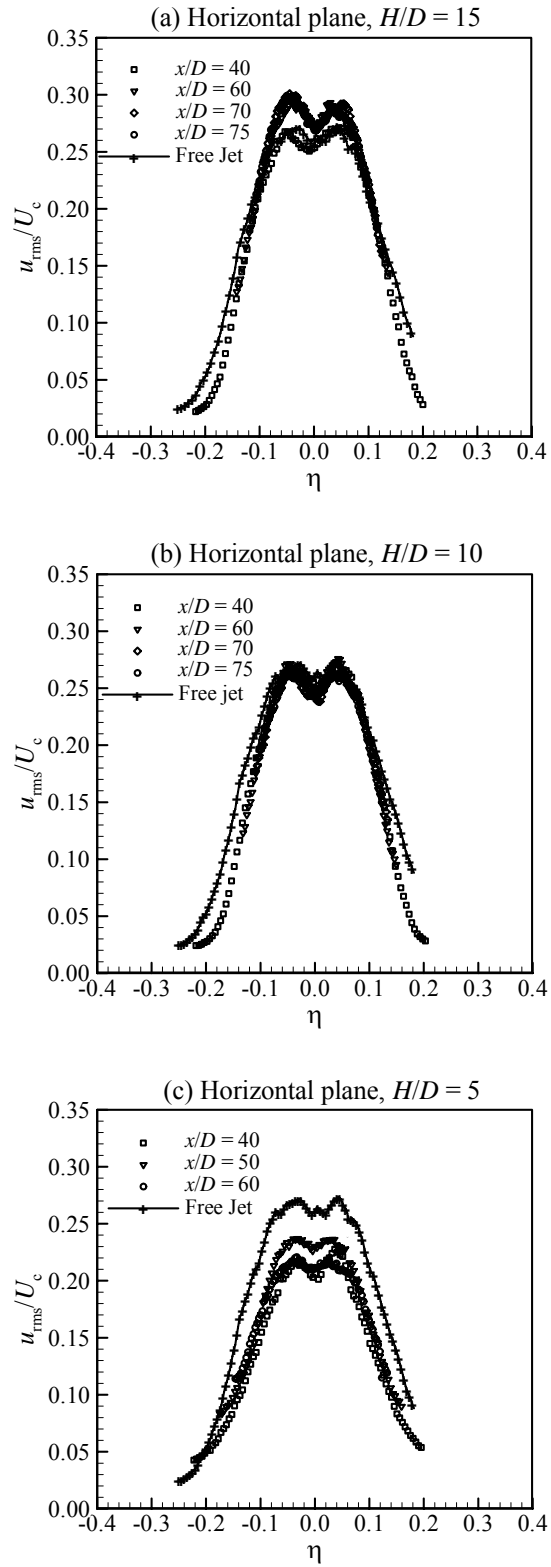


Figure 5.26: Downstream development of the relative axial turbulence intensity u_{rms}/U_c profiles on the horizontal plane for the shallow water jet cases; (a) $H/D = 15$, (b) $H/D = 10$, and (c) $H/D = 5$.

the shallow jet profiles is generally smaller than the free jet profile. Moreover, u_{rms}/U_c near the jet axis increases in the axial direction from $x/D = 40$ to 50, then decreases again from $x/D = 50$ to 60 and matches the profile at $x/D = 40$. This behaviour may be explained by the high rate of increase of the mean centreline velocity U_c for $x/D > 45$ as shown in Figure 5.10 which is used for normalising the axial turbulence intensity u_{rms} .

Figure 5.27(a) and (b) provides a comparison of the relative axial turbulence intensity u_{rms}/U_c for the shallow profiles ($H/D = 15, 10,$ and 5) at specific axial locations. At $x/D = 40$, Figure 5.27(a) shows that the u_{rms}/U_c profiles for the $H/D = 15$ and 10 cases are slightly affected by the vertical confinement. They look slightly narrower than the free jet profile. For the $H/D = 5$ case, the relative axial turbulence intensity u_{rms}/U_c looks much smaller compared to the other shallow cases which indicates that the effect of the confinement is profound in this case. However, u_{rms}/U_c seems to have higher values at the peripheries ($|z/D| > 6.7$) compared to the other shallow cases. As the flow proceeds downstream, Figure 5.27(b) shows that the relative axial turbulence intensity for the $H/D = 10$ case is also inhibited by the confinement. Also, the off-axis peaks disappear and the profile develops a flat top for the $H/D = 5$ case. For the $H/D = 15$ case, the profile looks similar to the free case although the free jet does not look symmetrical as it should be.

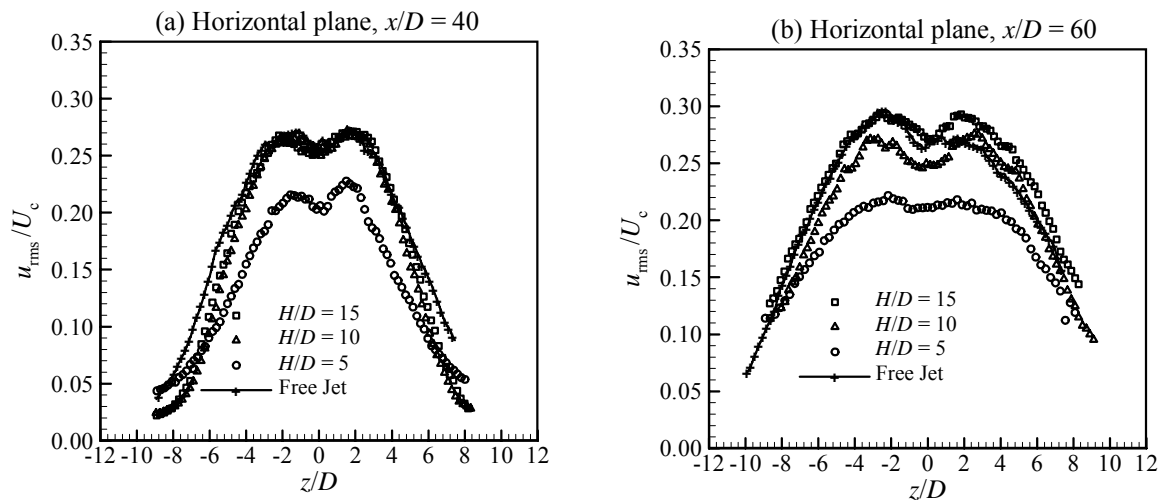


Figure 5.27: Behaviour of the relative axial turbulence intensity u_{rms}/U_c of free and shallow jet cases on the horizontal plane at axial locations; (a) $x/D = 40$, and (b) $x/D = 60$.

Vertical turbulence intensity v_{rms}/U_c

Figures 5.28(a), (b), and (c) illustrate the downstream development of the relative vertical turbulence intensity v_{rms}/U_c for the shallow water jet cases ($H/D = 15, 10, \text{ and } 5$). The v_{rms}/U_c profiles for the $H/D = 15$ case, shown in Figure 5.28(a), display similar behaviour as the axial turbulence intensity profiles shown in Figure 5.24(a) except near the boundaries, where the vertical fluctuations rapidly decrease as the boundaries are approached. At $x/D = 40$, the relative turbulence intensity for the shallow case is slightly greater than the free jet case over most of the depth. At locations further downstream, the v_{rms}/U_c peak broadens near the jet axis. It can also be seen that the profiles at $x/D = 70$ and 75 look similar at these locations. The relative vertical turbulence intensity is almost uniform in the region $-0.28 < y/H < 0.20$ with $v_{rms}/U_c \approx 0.22$.

Figure 5.28(b) shows the development of the relative vertical turbulence intensity v_{rms}/U_c for the $H/D = 10$ case. The shallow and free jet profiles at $x/D = 40$ and 60 agree reasonably well except near the boundaries where v_{rms}/U_c is smaller than the free jet data and is expected to reach zero. These profiles are uniform over most of the depth with a magnitude approximately equal to 0.203 . At $x/D = 70$ and 75 , Figure 5.28(b) shows that the two profiles are similar with a smaller v_{rms}/U_c in the core region ($-0.40 < y/H < 0.40$) compared to those at $x/D = 40$ and 60 . The relative vertical turbulence intensity in this region is approximately equal to 0.195 while it is almost zero near the boundaries.

Profiles for the relative vertical turbulence intensity v_{rms}/U_c for the $H/D = 5$ case are shown in Figure 5.28(c). It is obvious that the vertical fluctuations for this case are much smaller than the free jet data and the previous shallow cases shown in Figures 5.28(a) and (b). It is interesting to see that the data for all the profiles near the solid wall ($y/H < -0.30$) collapse to a single profile. In this region, the vertical fluctuations decrease rapidly as the solid wall is approached. Moreover, in the region $-0.2 < y/H < 0.16$, v_{rms}/U_c is almost uniform and equal to 0.155 for the profiles at $x/D = 30$ and 40 , and 0.167 for the profiles at $x/D = 50$ and 60 . Above $y/H = 0.16$, there

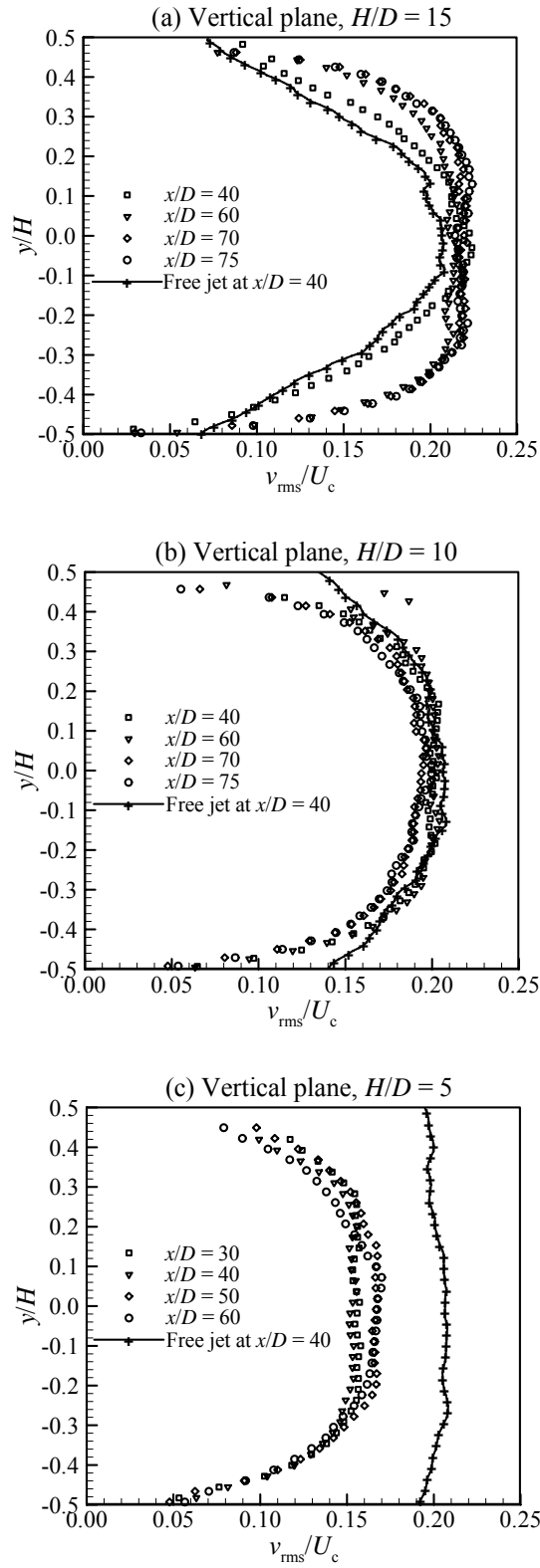


Figure 5.28: Downstream development of the relative vertical turbulence intensity v_{rms}/U_c profiles on the vertical plane for the shallow water jet cases; (a) $H/D = 15$, (b) $H/D = 10$, and (c) $H/D = 5$.

is no clear systematic trend for the profiles in the axial direction. However, it can be seen that the vertical fluctuations decrease rapidly in this region as the free surface is approached. From these results, it is observed that the profiles of v_{rms}/U_c at $x/D = 50$ and 60 collapse onto a single line in the region $-0.5 < y/H < 0.1$ while they are slightly different near the free surface. On the contrary, the trend of u_{rms}/U_c profiles at the same locations (see Figure 5.24(c)) is opposite to v_{rms}/U_c profiles. They collapse to a single line near the boundaries but they are slightly different in the core region. However, both u_{rms}/U_c and v_{rms}/U_c profiles show good agreement near the solid wall at these locations.

The relative vertical turbulence intensity v_{rms}/U_c for the $H/D = 15$, 10 , and 5 cases are compared to the free jet profile at axial locations $x/D = 40$ and 60 in Figures 5.29(a) and (b), respectively. Note that the width of the shallow jet profiles shown in these figures corresponds to the water depth H of each case. Figure 5.29(a) shows that v_{rms}/U_c for the $H/D = 15$ case is larger than the free jet profile while the $H/D = 10$ case is almost the same in the core region ($|y/D| < 4$) but rapidly decreases as the boundaries are approached. For the $H/D = 5$ case, v_{rms}/U_c looks uniform over most of the depth ($|y/D| < 1.2$) and $\sim 28\%$ smaller ($v_{\text{rms}}/U_c \approx 0.15$) than the free jet case. Then it decreases rapidly as it approaches the boundaries. The lower values of v_{rms}/U_c for this case may be attributed to the vertical confinement, since the decay of the mean centreline velocity at this location is the same as the free jet (see Figure 5.10).

At $x/D = 60$, v_{rms}/U_c becomes almost equal to the free jet case near the centreline for the $H/D = 15$ case. Also, the cone-top shape shown in Figure 5.29(a) broadens and becomes flat near the jet axis at this location, but deviates from the free jet profile as the boundaries are approached. For the $H/D = 10$ case, v_{rms}/U_c becomes slightly smaller than the free jet case in the core region compared to Figure 5.29(a) which may be attributed to the increase in the mean centreline velocity. Figure 5.29(b) also shows that the flat-top shape for the $H/D = 5$ case shown in Figure 5.29(a) has changed to an elongated-top shape.

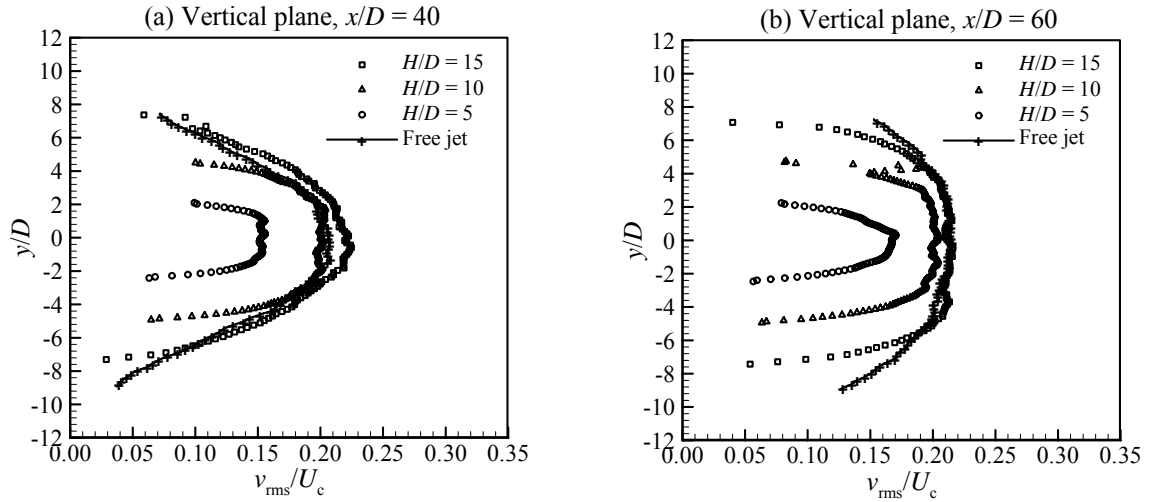


Figure 5.29: Behaviour of the relative vertical turbulence intensity v_{rms}/U_c of free and shallow jet cases on the vertical plane at axial locations; (a) $x/D = 40$, and (b) $x/D = 60$.

Horizontal turbulence intensity w_{rms}/U_c

The relative horizontal turbulence intensity w_{rms}/U_c on the horizontal plane for the $H/D = 15$, 10, and 5 cases are shown in Figures 5.30(a), (b) and (c) at different axial locations. The turbulence intensity is plotted against the non-dimensional coordinate $\eta = z/(x - x_0)$ in these figures. Figure 5.30(a) shows that the horizontal turbulence intensity profiles for the $H/D = 15$ case and the free jet at $x/D = 40$ agree reasonably well although the profile for the shallow case looks slightly narrower. At downstream locations, w_{rms}/U_c increases near the jet centreline ($|\eta| < 0.08$) but matches the free jet profile for $|\eta| > 0.08$. This figure also shows that the profiles at $x/D = 70$ and 75 look similar with w_{rms}/U_c equal to ~ 0.23 at the jet axis.

Figure 5.30(b) shows the horizontal turbulence intensity w_{rms} normalised by the local mean centreline velocity U_c for the $H/D = 10$ case plotted against the non-dimensional coordinate η . The overall agreement between the free jet and the shallow profiles at $x/D = 40$ and 60 is satisfactory although the profiles for the shallow case look slightly narrower. The behaviour of the profiles at locations further downstream is similar to the profiles for the deepest case shown in Figure 5.30(a). The difference is that the “cone top” shape of the profiles becomes a “flat top” shape at $x/D = 70$ and 75. The two

profiles at these locations are generally wider than the free jet profile. They look similar in the outer region, while there is some scatter near the top of the curves in the region $-0.08 < \eta < 0.04$.

Figure 5.30(c) shows the relative horizontal turbulence intensity w_{rms}/U_c profiles for the $H/D = 5$ case at $x/D = 30, 40, 50,$ and 60 plotted against the non-dimensional coordinate η . The profiles at $x/D = 30$ and 40 agree reasonably well with each other. However, w_{rms}/U_c looks smaller than the free jet profile at these locations in the region $|\eta| < 0.19$, but larger at the jet peripheries ($|\eta| > 0.19$). At $x/D = 50$ and 60 , w_{rms}/U_c has increased in the downstream direction and the two curves collapse onto a single line with a maximum value located at the jet axis equal to 0.24 as compared to 0.21 for the free jet data. This is equivalent to $\sim 14\%$ increase from the free jet data because of the confinement. It can be concluded that the increase in the horizontal turbulence intensity w_{rms} is even more significant than 14% in light of the fact that the centreline velocity U_c has increased 23% at $x/D = 60$ (see Figures 5.10, 5.14 and 5.15(b)).

The effect of the degree of confinement on the relative horizontal turbulence intensity w_{rms}/U_c profiles at two axial locations is depicted in Figures 5.31(a) and (b). Figure 5.31(a) shows that the w_{rms}/U_c profiles for the $H/D = 15$ and 10 cases are still similar at $x/D = 40$, but slightly narrower than the free jet case for $|z/D| > 5$. For the $H/D = 5$ case, w_{rms}/U_c is smaller than the free jet case in the region $|z/D| < 6.5$, but larger for $|z/D| > 6.5$. This result indicates that the horizontal fluctuations decrease in the core of the jet with a corresponding increase at the jet peripheries.

At $x/D = 60$, Figure 5.31(b) shows that the horizontal fluctuations broaden at downstream locations. The w_{rms}/U_c profiles for the $H/D = 15$ and 10 cases are similar at the peripheries ($|z/D| > 4$), but w_{rms}/U_c is slightly larger than the free jet near the jet centreline for the $H/D = 15$ case and smaller for the $H/D = 10$ case. The behaviour of the latter case may be due to the mean centreline velocity which is larger than the free jet

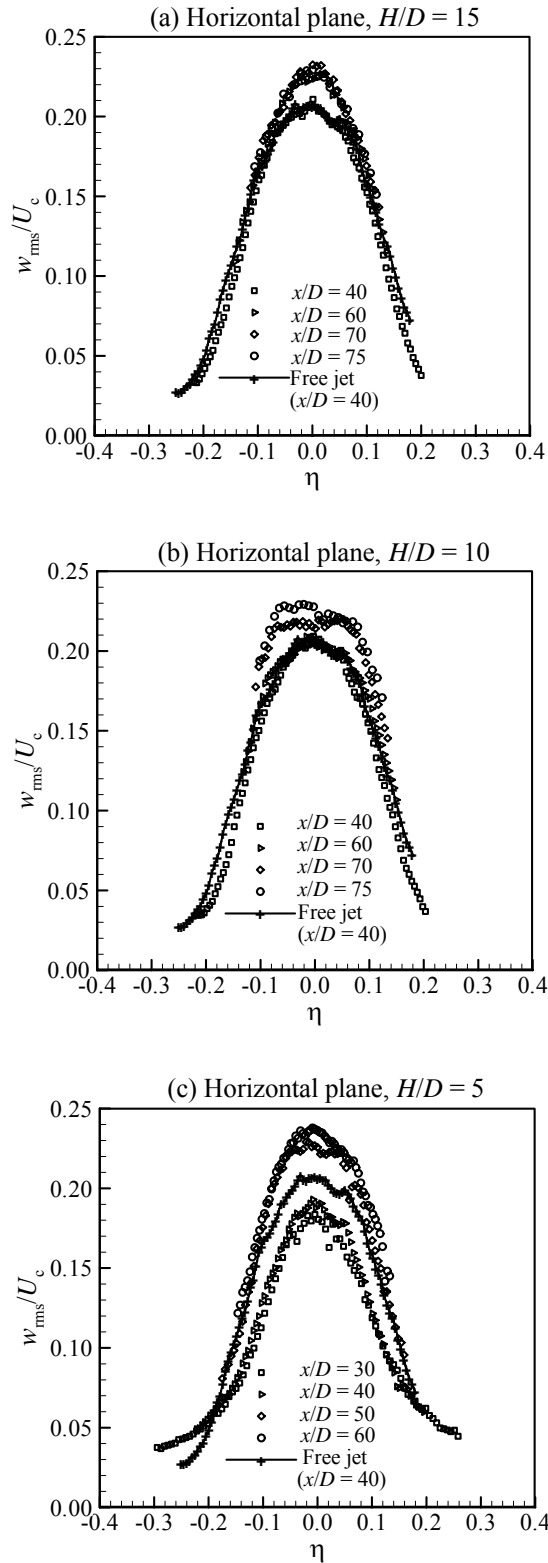


Figure 5.30: Downstream development of the relative horizontal turbulence intensity w_{rms}/U_c profiles on the horizontal plane for the shallow water jet cases; (a) $H/D = 15$, (b) $H/D = 10$, and (c) $H/D = 5$.

case at this location (see Figure 5.10). For the $H/D = 5$ case, the horizontal turbulence fluctuations seem to increase near the jet axis ($|z/D| < 5$), but match the free jet at the peripheries.

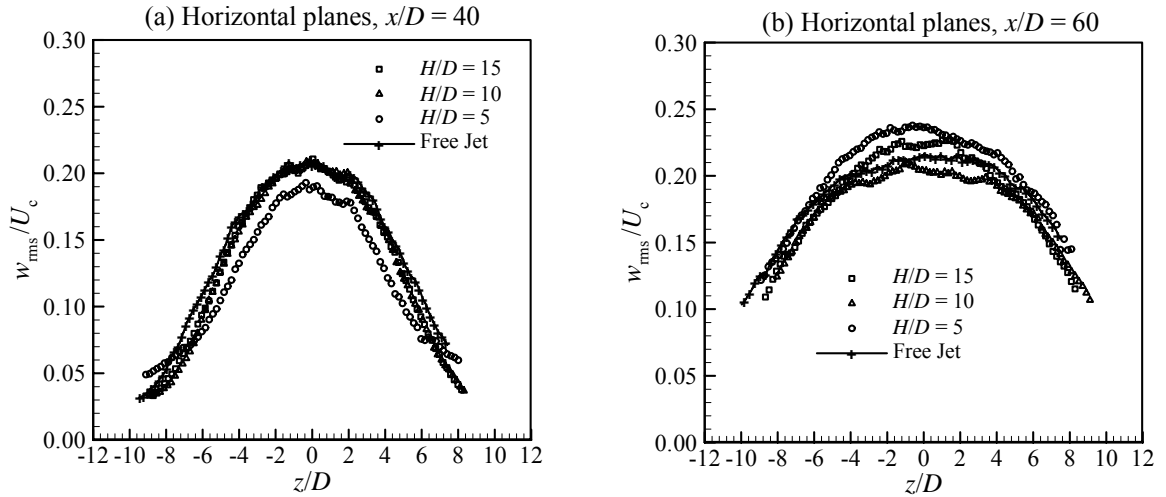


Figure 5.31: Behaviour of the relative horizontal turbulence intensity w_{rms}/U_c of free and shallow jet cases on the horizontal plane at axial locations; (a) $x/D = 40$, and (b) $x/D = 60$.

Reynolds shear stress $\langle uv \rangle$

The Reynolds shear stress $\langle uv \rangle / U_c^2$ profiles on the vertical plane for the shallow cases $H/D = 15$, 10, and 5 are shown in Figures 5.32(a), (b), and (c), respectively, at different axial locations. Figure 5.32(a) shows that the data for the $H/D = 15$ case are symmetric above and below the jet axis. The Reynolds stress profile at $x/D = 40$ agrees reasonably well with the free jet data although the relative axial and vertical turbulence intensities were slightly different (see Figures 5.24(a) and 5.28(a)). The maximum absolute value of $\langle uv \rangle / U_c^2$ at this location is 0.022 located at $y/H = \pm 0.20$. Further downstream, the magnitude of the peaks of $\langle uv \rangle / U_c^2$ decreases and their locations are shifted closer to the boundaries. Figure 5.32(a) shows that the profiles of $\langle uv \rangle / U_c^2$ look similar at $x/D = 70$ and 75. The maximum absolute value of $\langle uv \rangle / U_c^2$, which is located at $y/H = \pm 0.28$, is equal to ~ 0.012 .

The effect of the vertical confinement on the Reynolds shear stress for the $H/D = 10$ case is profound as shown in Figure 5.32(b). Although the Reynolds stress profile for the shallow case has the same features as the free jet profile at $x/D = 40$, $\langle uv \rangle / U_c^2$ is generally smaller than the free jet case. At locations further downstream, $\langle uv \rangle / U_c^2$ is increasingly attenuated until the two peaks above and below the jet centreline disappear. At $x/D = 70$ and 75 , the profile is close to zero over the entire depth. The lower levels of $\langle uv \rangle$ for this case are not due to low u_{rms} and v_{rms} levels, but from a decreased correlation in the turbulent fluctuations u' and v' . In other words, the axial and vertical fluctuations are only weakly correlated at these locations, which indicate that the momentum exchange by the Reynolds stress is significantly reduced by the vertical confinement. The two curves at these locations look similar with some scatter which may indicate that self-similarity has been achieved.

Figure 5.32(c) shows the evolution in the axial direction of the Reynolds shear stress $\langle uv \rangle / U_c^2$ profiles for the $H/D = 5$ case. It is clear that the Reynolds stress profile is somewhat symmetrical at $x/D = 30$ although $\langle uv \rangle / U_c^2$ is much smaller than the free jet data at this location. At $x/D = 40$, $\langle uv \rangle / U_c^2$ becomes almost zero over the entire depth. Farther away, $\langle uv \rangle$ is positive below the jet axis with a mild peak at $y/H = -0.23$. The Reynolds stress is almost zero above the jet axis. This indicates that almost no turbulent momentum transport occurs above the jet axis. In the region below the jet axis, it is clear that the sign of the fluctuating velocity components (u' and v') became the same. From a quadrant analysis prospective, this case lies in the first or third quadrant which indicates outward motion of high speed fluid or the motion associated with ejections of low-speed fluid away from the wall. Thus the first- and third-quadrant events contribute to the positive Reynolds shear stress (negative production) (Kim *et al.*, 1987).

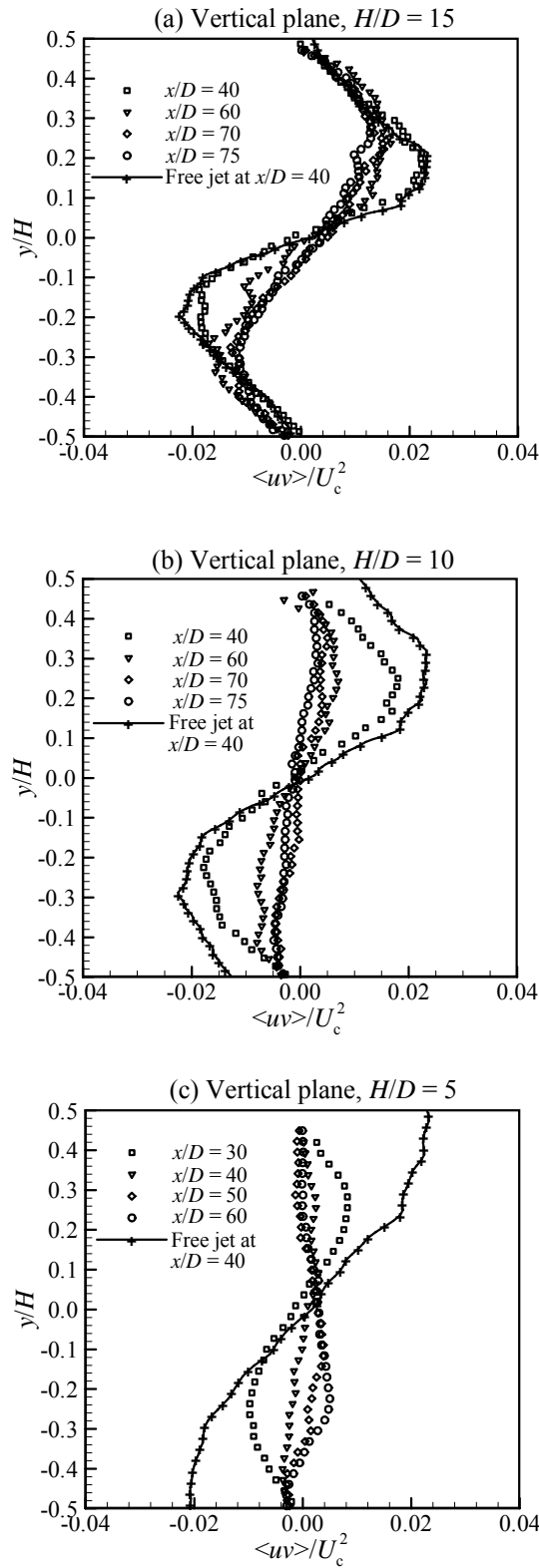


Figure 5.32: Downstream development of the relative Reynolds shear stress $\langle uv \rangle / U_c^2$ profiles on the vertical plane for the shallow water jet cases; (a) $H/D = 15$, (b) $H/D = 10$, and (c) $H/D = 5$.

The effect of the vertical confinement on the Reynolds shear stress $\langle uv \rangle / U_c^2$ is shown at axial locations $x/D = 40$ and 60 in Figures 5.33(a) and (b), respectively. It is clear from Figure 5.33(a) that the $\langle uv \rangle / U_c^2$ profile for $H/D = 15$ is not affected by the vertical confinement at $x/D = 40$ compared to the free jet case. For the $H/D = 10$ case, the $\langle uv \rangle / U_c^2$ profile matches the free jet case near the jet axis ($|y/D| < 1.2$), but the magnitude of the peaks is smaller ($\langle uv \rangle / U_c^2 \approx 0.018$) and their locations are slightly closer to the jet axis. For the $H/D = 5$ case, the effect of the vertical confinement is profound. The Reynolds shear stress $\langle uv \rangle / U_c^2$ is inhibited by the confinement and becomes almost zero over the entire depth. Further downstream ($x/D = 60$), Figure 5.33(b) shows that the turbulent momentum transport for all shallow jet cases is increasingly inhibited as the confinement increases. This figure shows that the magnitude of the peaks for the $H/D = 15$ and 10 decreases and their locations are shifted closer to the jet axis as the confinement increases. For the $H/D = 5$ case, the structure of the Reynolds stress $\langle uv \rangle$ changes at this location and becomes positive below the centreline of the jet with a mild peak at $y/D = -1.15$, while $\langle uv \rangle$ becomes almost zero above the jet axis. The behaviour of $\langle uv \rangle$ below the jet axis indicates that both the velocity fluctuation components have the same sign.

Reynolds shear stress $\langle uw \rangle$

The downstream evolution of the Reynolds shear stress $\langle uw \rangle$ on the horizontal plane for the shallow cases $H/D = 15$, 10 , and 5 is shown in Figures 5.34(a), (b) and (c). Figure 5.34(a) shows the axial development of the Reynolds shear stress $\langle uw \rangle / U_c^2$ profiles for the $H/D = 15$ case. It is interesting to see that the free and shallow water jet profiles collapse reasonably well onto a single curve although the axial and horizontal fluctuations shown in Figures 5.26(a) and 5.30(a) are different than the free jet data. This indicates that momentum transport in the horizontal plane is not affected by the vertical confinement although its effect is clear on the vertical transport of momentum (see Figure 5.32(a)).

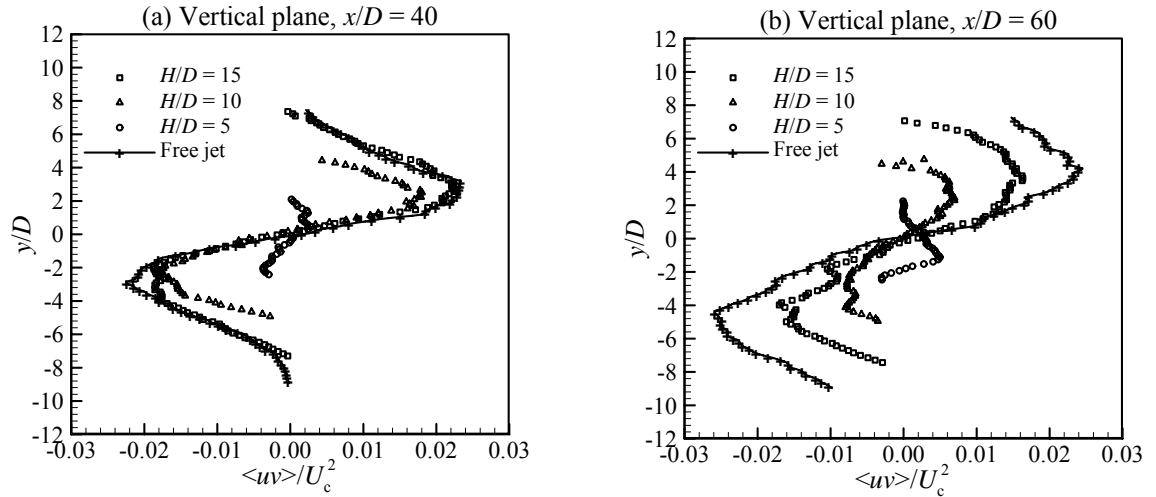


Figure 5.33: Behaviour of the Reynolds shear stress $\langle uv \rangle / U_c^2$ of free and shallow jet cases on the vertical plane at axial locations; (a) $x/D = 40$, and (b) $x/D = 60$.

Horizontal profiles of the Reynolds stress $\langle uw \rangle$ measured on a plane containing the centreline of the jet for the $H/D = 10$ case are shown in Figure 5.34(b). In contrast to the horizontal turbulence intensity shown in Figure 5.30(b), the data are more similar to the free jet data at all axial locations and especially near the jet centre. Figure 5.34(b) shows that the profiles of $\langle uw \rangle / U_c^2$ collapse reasonably well onto a single curve at $x/D = 70$ and 75 with a peak value of ± 0.027 which is greater than the free jet value (0.022). These peaks are located at $|\eta| \approx 0.062$ which is the same as the free jet data.

The Reynolds shear stress $\langle uw \rangle$ data for the $H/D = 5$ case plotted in Figure 5.34(c) show more scatter in the outer region of the jet ($|\eta| > 0.033$) while all the shallow and free jet data collapse onto a single line in the inner region of the jet ($|\eta| < 0.033$). The profiles at $x/D = 30$ and 40 are similar with a peak value equal to ± 0.017 located at $|\eta| \approx 0.047$, compared to ± 0.022 located at $|\eta| \approx 0.062$ for the free jet data. At $x/D = 50$ and 60, the profiles look similar with $\langle uw \rangle / U_c^2 = \pm 0.020$ located at $|\eta| \approx 0.054$.

A comparison between the Reynolds shear stress $\langle uw \rangle$ profiles for the $H/D = 15$, 10, and 5 cases at two axial locations is shown in Figures 5.35(a) and (b). As shown in

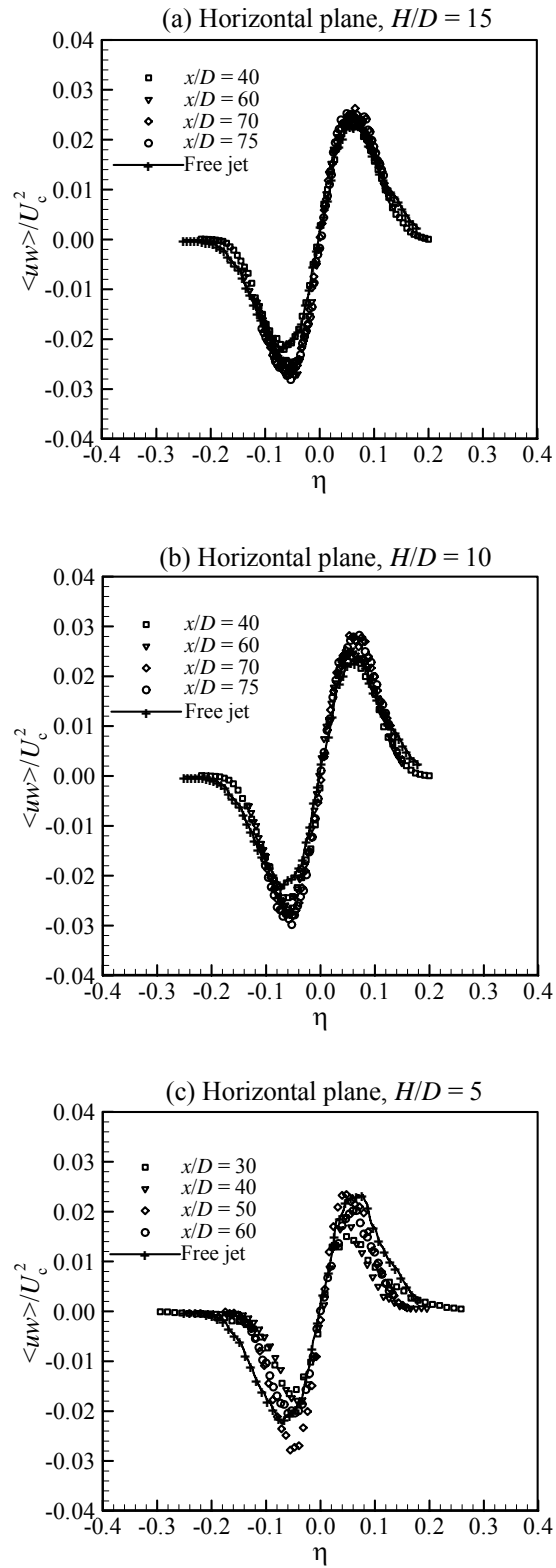


Figure 5.34: Downstream development of the relative Reynolds shear stress $\langle uw \rangle / U_c^2$ profiles on the vertical plane for the shallow water jet cases; (a) $H/D = 15$, (b) $H/D = 10$, and (c) $H/D = 5$.

Figure 5.35(a), the $H/D = 15$ profile is almost the same as the free jet profile at $x/D = 40$, but is slightly narrower for $|z/D| > 4.9$. The behaviour of the $H/D = 10$ profile is very similar to the $H/D = 15$ profile except that there is a slight shift of the peaks towards the jet axis ($|z/D| \approx 2.5$ compared to 2.7 for the free jet). The effect of the confinement is more apparent on the $H/D = 5$ case at this location. The $H/D = 5$ profile matches the free jet profile near the jet axis ($|z/D| < 0.9$), but becomes narrower in the outer region with a smaller absolute peak ($\langle uv \rangle / U_c^2 = 0.019$) compared to the free jet case located at $|z/D| \approx 1.83$.

Further downstream ($x/D = 60$), Figure 5.35(b) shows that the $H/D = 15$ and 10 profiles are similar with their peak locations slightly shifted towards the jet axis ($|z/D| \approx 3.4$ compared to 4.4 for the free jet). Moreover, the Reynolds stress $\langle uv \rangle$ for the two cases becomes smaller than the free jet case in the outer region ($|z/D| > 4.4$). The behaviour of the $H/D = 5$ case at this location is similar to the behaviour shown in Figure 5.35(a). Its profile matches the free jet profile near the jet axis ($|z/D| < 2.6$), but becomes narrower in the outer region with a smaller peaks ($\langle uv \rangle / U_c^2 \approx 0.020$) located at $|z/D| \approx 3.6$ compared to the free jet case (0.022).

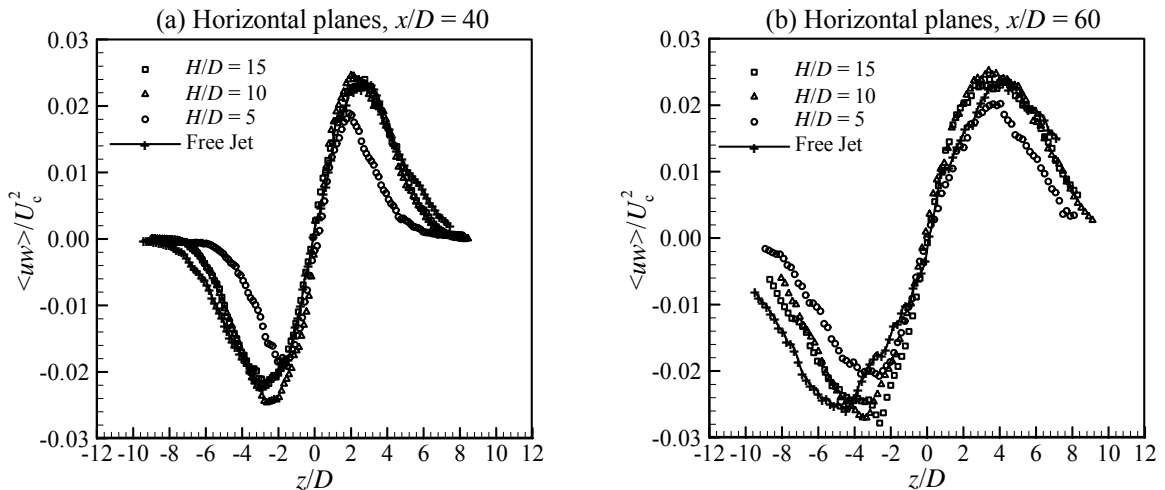


Figure 5.35: Behaviour of the Reynolds shear stress $\langle uv \rangle / U_c^2$ of free and shallow jet cases on the horizontal plane at axial locations; (a) $x/D = 40$, and (b) $x/D = 60$.

5.4 SHALLOW WATER JETS - COHERENT STRUCTURES

This section reports on the characteristics of large-scale structures in shallow water jets issuing from a round (9 mm) nozzle. Specifically, it focuses on identifying the characteristics of large vortical structures at different degrees of vertical confinement $H/D = 15, 10,$ and $5,$ while the horizontal confinement is negligible. The measurements were taken on two orthogonal planes (vertical and horizontal) along the jet axis. For the vertical plane, the measurement plane extends from the solid wall to the free surface. Measurements were taken at several axial distances downstream of the jet exit in the region where the vertical confinement started to be significant.

5.4.1 Correlation between the Velocity Fields

The spatial resolution of the PIV data is high while the temporal resolution is crude. The lower temporal resolution corresponds to the rather large time delay between each pair of images which greatly limits the high frequency response of the measurements. The large time delay between samples can be an advantage when the snapshots of the flow are required to be statistically independent and therefore uncorrelated. Ideally, the delay should be several orders of magnitude greater than the temporal integral scale (timescales which provide measures of the lifetime of the turbulence). This is particularly important for the POD analysis technique used here (method of snapshots) because the spatial correlation components C_{ij} are calculated from the snapshots as described in Section 4.2.2. For this reason, all image pairs were acquired at a sampling rate of 1 Hz. This is slow enough that the images are expected to be uncorrelated. This can be illustrated clearly by plotting the correlation of the velocity field at any time j with the velocity fields at all other times i ($i = 1$ to M) of a data set. Figure 5.36 shows the variation of the correlation C_{ij} of the velocity field at time $j = 1000$ s with the velocity field at times i . For clarity, it shows only the correlation values of velocity fields in the range of 100 s before and after the velocity field at time j . It is clear from this figure that all the correlation values are very small ($|C_{ij}| < 0.1$) compared with the peak at $i = 1000$ s ($C_{jj} = 0.365 \text{ m}^2/\text{s}^2$), which represents the correlation of the velocity field with itself.

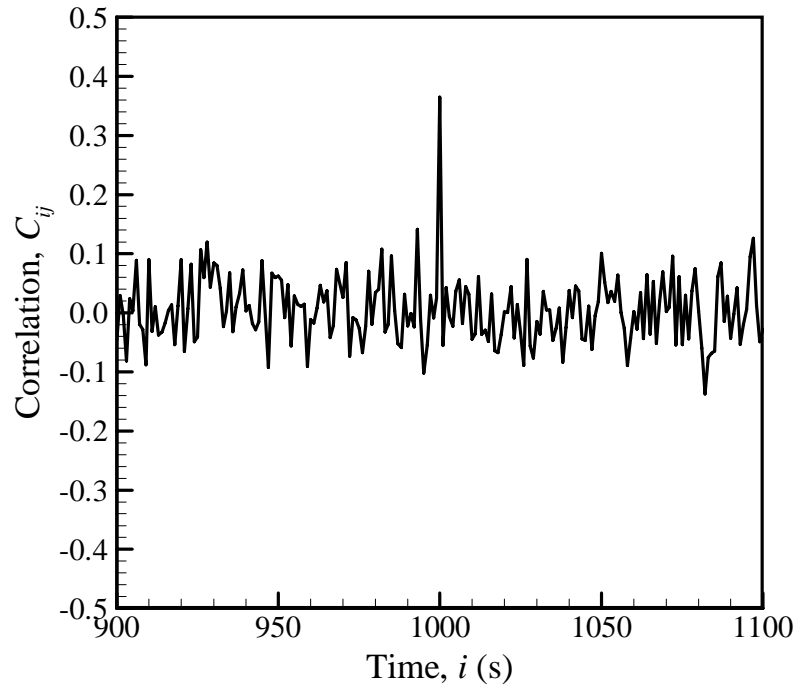


Figure 5.36: Variation of the correlation C_{ij} of the velocity field $j = 1000$ with the velocity field number i . Note that i and j also represent time of the velocity fields. For clarity, only the correlation values of one hundred velocity fields before and after the velocity field $j = 1000$ are shown.

5.4.2 Energy Content of Large-Scale Structures

Several methods for structure eduction are available and the choice of a particular one can be dependent on what information is sought. The choice depends not only on the definition of the structure, but also on the experimental and/or numerical capabilities available. It is evident that the selected technique for eduction should lead to an understanding of the dynamics of the structures. In this study, the POD was used for exposing coherent structures. The POD technique was applied to the PIV data using the method of snapshots as described in Section 4.2.2. The analysis was performed on two thousand velocity fields for each set in order to educe a large number of structures and allow a reliable statistical study. In order to maintain a common ground for comparison, the analysis was performed by fixing the energy content of the exposed structures. The exact fraction of the turbulent kinetic energy present in the large-scale motion is

virtually impossible to determine. Uijttewaal and Booij (1999) experimentally investigated the influence of shallowness on the development of a mixing layer and on the strength and size of large-scale structures. The turbulent kinetic energy of the large-scale structures was estimated to be more than 50% of the total energy. Fiedler (1988) gave estimates of the energy contained by large-scale structures in the near-exit and far regions of a free jet to be ~50% and ~10%, respectively. Since turbulence has a wide spectrum of eddy sizes and since there is no demarcation that clearly separates large eddies from smaller ones, the definition of large-scale structures adopted in this study is based on the range of the largest exposed structures that contain a specified amount of energy. Shinneeb *et al.* (2006) investigated large vortices in the near-exit region of a round turbulent jet using POD. Ten modes were used to reconstruct the velocity fields. This recovered 48% of the kinetic energy which is almost equal to the estimation of Fiedler (1988). In order to estimate the energy recovered using 10 modes, a sample from each set of the present data was reconstructed using 10 modes. It was found that the energy contained in the reconstructions varied from ~30% to ~50% of the total turbulent kinetic energy. Thus, the number of modes used for the POD reconstruction was selected based on a target of 40% energy content. Table 5.2 lists the total number of structures exposed by POD and the number of modes used for the reconstruction of the velocity fields.

5.4.3 Ensemble Size for the POD Analysis

The choice of the number of snapshots is important because it is directly linked with the size of the temporal correlation matrix. The number of snapshots should be as large as reasonably possible for an accurate computation of the POD eigenfunctions (Cazemier *et al.*, 1998). This can be assessed by checking the convergence of the eigenvalues with respect to the number of snapshots M . When the result begins to converge, the statistics obtained using that number of snapshots are valid. Figure 5.37 shows the effect of sample size M on the eigenvalue spectra. In this figure, the eigenvalue problem was calculated for ensembles of different sizes taken from a single data set. It is apparent that

Table 5.2: Number of educed structures, modes, percentage of kinetic energy contained in the modes used for the reconstruction of the velocity fields, and ratio of positive to negative vortices. The POD analysis was applied to two thousand velocity fluctuation fields for each case*.

Case Name	Number of identified vortices	Number of modes used for the reconstruction	Energy contained in the modes	Ratio of positive to negative vortices
FJ02	30,257	25	40.13%	0.962
FJ03	13,725	15	40.22%	0.974
FJ04	7,150	10	39.74%	0.981
SJ12	20,504	17	40.04%	1.010
SJ13	11,465	14	40.53%	0.929
SJ14	7,796	10	40.66%	0.930
SJ17	15,710	15	40.56%	1.005
SJ18	7,088	10	40.79%	0.982
SJ19	3,702	7	40.19%	0.966
SJ22	14,584	17	40.09%	0.961
SJ23	8,529	11	40.23%	0.964
SJ24	6,231	8	41.52%	0.868
SJ27	15,858	15	40.75%	0.979
SJ28	9,039	11	40.74%	1.005
SJ29	3,395	6	40.39%	1.057
SJ32	20,792	26	40.16%	0.938
SJ33	9,875	13	41.05%	0.912
SJ34	5,228	6	39.62%	0.758
SJ37	42,188	27	40.47%	0.917
SJ38	12,169	20	40.28%	0.989
SJ39	5,407	4	39.13%	1.030

* See Table 5.1 for more information about location, water depth, and measurement plane orientation of these fields.

there is no significant difference between the spectra for the first ten modes when the sample size is greater than 1200 snapshots. In this work, the ensemble size used for the POD analysis was 2000 snapshots.

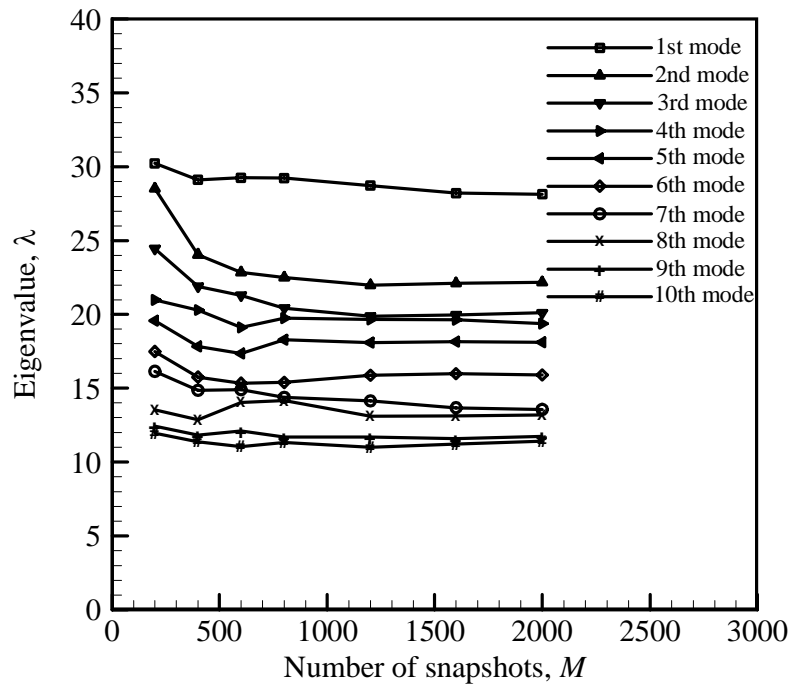


Figure 5.37: The effect of sample size M on the eigenvalue spectra for the first ten modes. The eigenvalue problem was calculated for ensembles of different sizes taken from a single data set.

5.4.4 Vortex Definition and Identification Method

Experimental studies to date differ in their descriptions of coherent structures, perhaps due to the difficulty involved in identifying them. The extraction of deterministic features from a turbulent flow has been a challenging problem. Kim (1983) used a conditional sampling technique based on numerical data. He admitted the subjectivity of the method due to the arbitrary choice of detection functions and threshold values. Therefore, it is important to discuss the method used to identify and measure vortical structures in this thesis before presenting the results.

The definition of a vortex has been an area of discussion and a number of different definitions, varying between mathematical and physical descriptions, have been offered (Jeong & Hussain, 1995, Pemberton *et al.*, 2002). The majority of vortex identification methods can be classified into the following groups; *Vorticity Maxima*, *Pressure Minimum*, *Closed or Spiral Streamlines*, and *Statistical Identification Methods* (Pemberton *et al.*, 2002). In the present study, the concept of using *closed streamlines* to identify vortices proposed by Robinson (1991) is adopted. It states that a vortex exists when instantaneous streamlines mapped onto a plane normal to the core exhibit a roughly circular or spiral pattern when viewed in a reference frame moving with the centre of the vortex core. According to this definition, the velocity vectors will demonstrate circular streamlines in two-dimensional velocity fields.

Agrawal & Prasad (2002b) proposed an automated technique for identifying and measuring vortices in two-dimensional velocity fields based on the closed streamline concept (see Section 4.3 for details). They tested the technique by seeding a real PIV velocity field with forty-four Rankine vortices of known location, rotational sense, and circulation. The Rankine vortices were distributed randomly in the velocity field. Although the streamlines of the individual Rankine vortices are closed, this situation was changed after superimposing the velocities from all the vortices. It was confirmed that the locations of all vortices were correctly identified using this technique. As well, it was found that the vortex core size of 50% of the resulting vortices corresponded exactly to the input vortex radius, while the measured radius of the remaining vortices was larger than their prescribed cores. Unfortunately, the difference in size was not quantified. However, it should be pointed out that the streamline pattern of a vortex in a real turbulent flow may be affected by the proximity of other vortices, which is likely the reason for the difference between the measured and exact radii used in the simulation.

Even though this technique can identify and measure vortical structures in two-dimensional velocity fields, the definition of a vortex core boundary is still a question that should be answered. The existence of a number of vortices in a velocity field with random circulations will disturb the closed streamline pattern around any vortex. This

raises an important question; what percentage of velocity vectors in a path around the centre of a candidate vortex need to have monotonically varying direction in order to be considered a closed streamline in the presence of other vortices? Agrawal & Prasad (2002b) argued that the vortex core is a region of high vorticity which is less likely to be affected by the presence of other vortices close to it, whereas beyond its edge is a region of lower vorticity which can be more easily affected by the proximity of other vortices. Based on this argument, it is reasonable to assume that the region of high-vorticity bounded by the largest closed streamline would correspond to a vortex core. They have also demonstrated that for vortices in a turbulent jet, circulation increases with r within the core of the vortex (r represents the radial position measured from the centre of the vortex), and may increase or decrease beyond the core depending upon the presence of other vortices close to it.

In this work, the procedures used to identify and measure properties of vortical structures are based on the concepts described above. As described in Section 4.3, a streamline can be considered closed if the direction of at least 75% of the velocity vectors surrounding the identified centre varies monotonically. The selection of this threshold $T = 75\%$ is supported by Figure 5.38 which illustrates the effect of the threshold T on the mean vortex radius R_{mean} and circulation Γ_{mean} . Each figure shows three curves extracted at three different axial locations of the same set of data. These mean values are calculated from the vortices that exist in four-grid-unit intervals of the axial distance x indicated. Figure 5.38(a) shows the behaviour of the mean radius R_{mean} with the threshold T . This figure demonstrates sensitivity of the measured mean radius R_{mean} to the threshold T . As the threshold decreases, R_{mean} increases. It is interesting to observe that the thresholds 75% and 80% give almost the same mean radius R_{mean} for all cases. The same behaviour can be seen in Figure 5.38(b), which shows the corresponding variation of mean circulation Γ_{mean} with the threshold. The linear increase of the mean circulation with increasing mean radius at thresholds 90%, 85%, and 80% is consistent with the findings of Agrawal & Prasad (2002b) discussed above, who found that circulation increases linearly with radius within the vortex core. Furthermore, it can be seen that the circulation is almost constant at thresholds 75% and 80%, which is

consistent with the mean radius result shown in Figure 5.38(a). This indicates that the threshold has a weak effect on R_{mean} and Γ_{mean} in the range 75 - 80%. This behaviour was also confirmed by inspecting other sets of data. As the threshold becomes very small, the identified vortices become larger. Thus, it can be concluded that thresholds in the range 75 - 80% are likely to give a good estimation of vortex sizes. In this work, the preference was for a 75% threshold after visual inspection of individual vortices.

In summary, identifying and measuring coherent structures in a velocity field are challenging tasks. In this work, the technique described in Section 4.3 was applied to the POD reconstruction of the fluctuating velocity fields. Vortical structures with a radius smaller than three grid units or a circulation less than $0.1 \text{ cm}^2/\text{s}$ were eliminated. The total number of structures identified in each data set is shown in Table 5.2. It should be noted that all the results presented in this work correspond to vortices in the x - y and x - z planes.

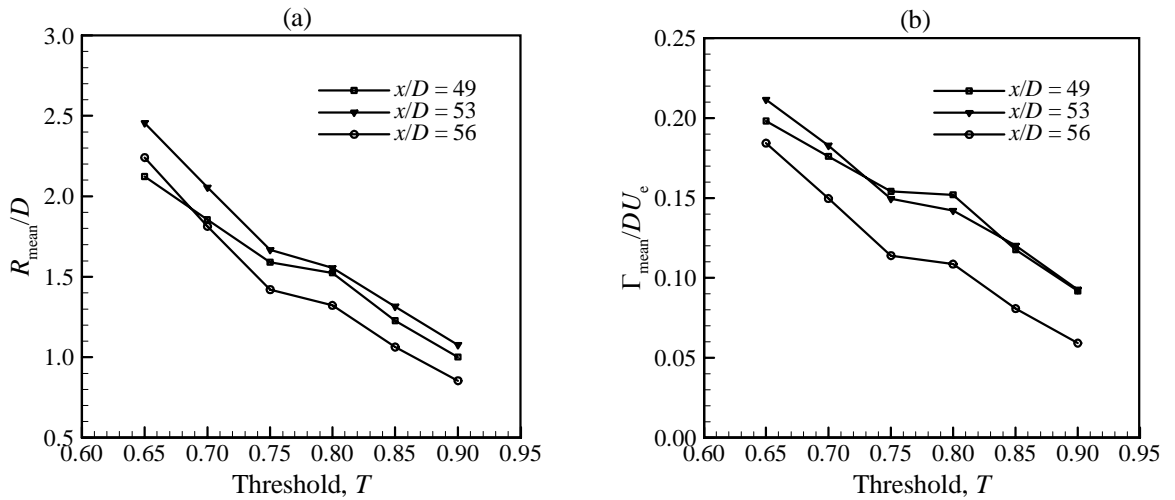


Figure 5.38: Illustration of the effect of the threshold T on (a) the mean size R_{mean} , and (b) the mean circulation Γ_{mean} of vortices. These mean values are calculated from the vortices that exist in sixteen-grid-unit intervals of the axial distance x indicated.

5.4.5 Examples of POD Reconstructed Velocity Fields

Selected examples of POD reconstructed velocity fluctuation fields for the deepest and shallowest jet cases are shown in Figure 5.39 and 5.40, respectively. Each figure shows two fields representing both vertical and horizontal planes. In these plots, only every fifth vector is shown in both directions. These velocity fields contain ~40% of the fluctuating velocity energy. Locations are normalised by the jet exit diameter D . Note that the solid wall and the free surface for vertical planes are at $y/D = -7.5$ and 7.5 in Figure 5.39(a), and $y/D = -2.5$ and 2.5 in Figure 5.40(a), respectively. These figures show several vortical structures of different sizes. Red and blue circles in these plots represent positive and negative rotational sense, respectively. All velocity fields confirm the existence of both positive and negative vortices in the shallow jet flow.

Figures 5.39(a) and (b) show two velocity fields for the deepest case ($H/D = 15$) on vertical and horizontal planes, respectively. These figures demonstrate that the vortex size in both planes is comparable and these vortices occupy only a relatively small region of the velocity fields. In contrast, the biggest vortex on the vertical plane for the shallowest case ($H/D = 5$) shown in Figure 5.40(a) almost spans the entire depth of the water layer, although its size is relatively smaller than the deeper water case. This figure also shows two pairs of vortices of opposite sign overlapping. This result suggests that the vertical confinement may force adjacent vortices to pair, which is consistent with the reduced number of vortices identified in this case (see cases SJ32, SJ33, and SJ34 in Table 5.2). The effect of the vertical confinement on the size of vortices in the horizontal plane is illustrated in Figure 5.40(b). It is clear that the vortices in this case are allowed to increase in size since they are not restricted by any physical boundaries. It is also clear that, as a result of the vertical confinement, the vortices shown in this field are generally bigger than the vortices in the previous examples.

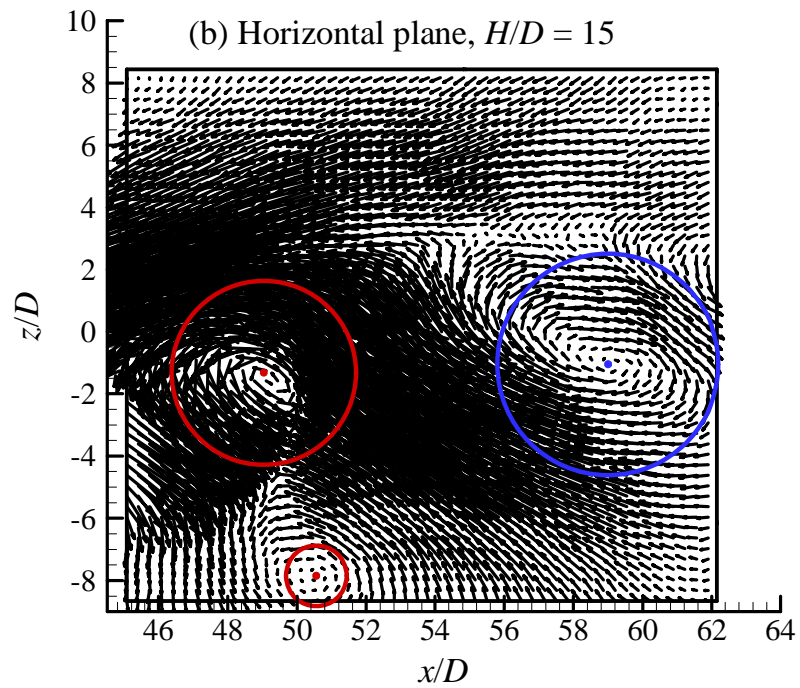
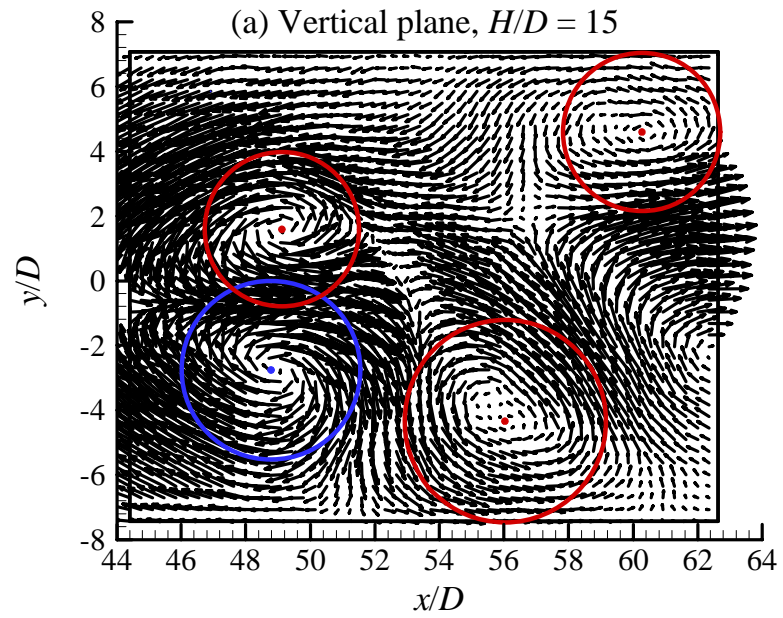


Figure 5.39: Examples of POD reconstructed velocity fluctuation fields for the $H/D = 15$ case; (a) Vertical plane, and (b) Horizontal plane. The circles represent the size of identified vortices. Red and blue circles represent positive and negative rotational sense, respectively.

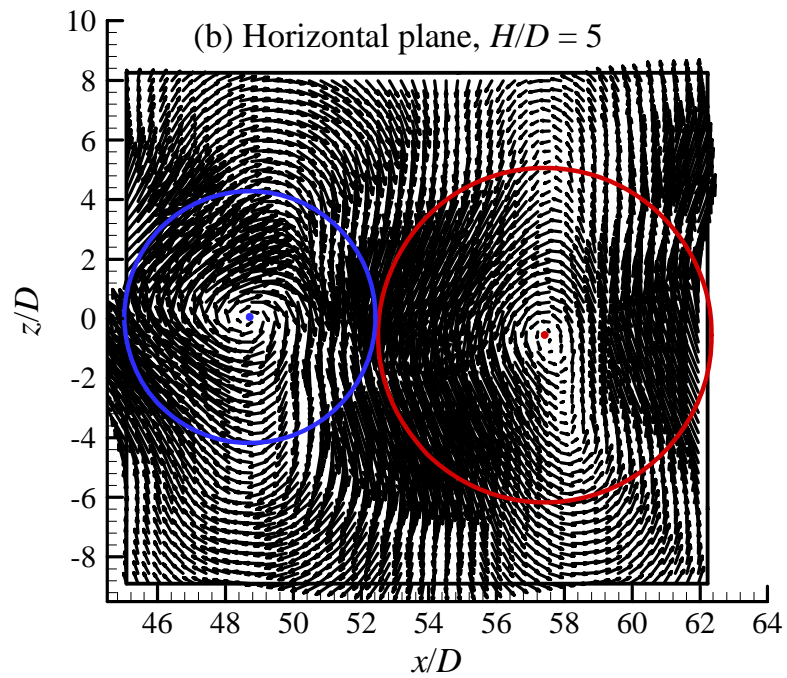
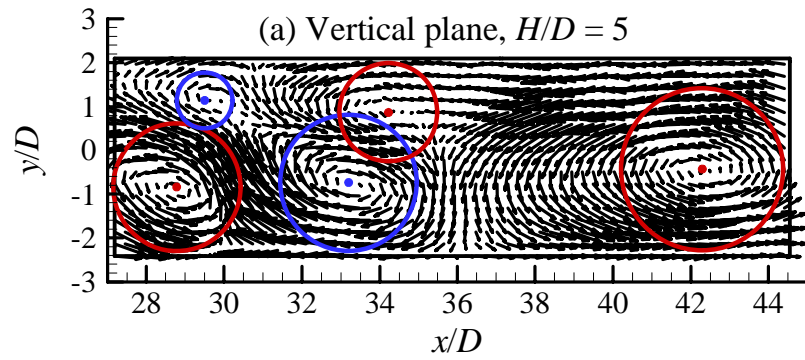


Figure 5.40: Examples of POD reconstructed velocity fluctuation fields for the $H/D = 5$ case; (a) Vertical plane, and (b) Horizontal plane. The circles represent the size of identified vortices. Red and blue circles represent positive and negative rotational sense, respectively.

It is interesting to note that the observations drawn from the vortices shown in Figures 5.39 and 5.40 reflect the general behaviour of the vortices under the effect of the confinement. A complete analysis of the effect of the vertical confinement is performed in Section 5.4.6. This section presents a statistical study that is based on all the identified vortices from all the velocity fields and provides a deeper look at their characteristics.

5.4.6 Quantitative Investigation of Coherent Structures

To understand the behaviour of vortical structures at different degrees of confinement, a statistical study was performed, which included the distribution of vortex size and circulation in the axial direction, the distribution of the number of vortices in the axial direction, and the distribution of the mean radius and circulation in the axial direction. Figure 5.41 shows the spatial distribution of the vortical structure centres from all 2000 fields for two different sets of data. In this figure, positions of the centres of all vortices (normalised by the jet exit diameter D) are plotted as points. Figure 5.41(a) shows the

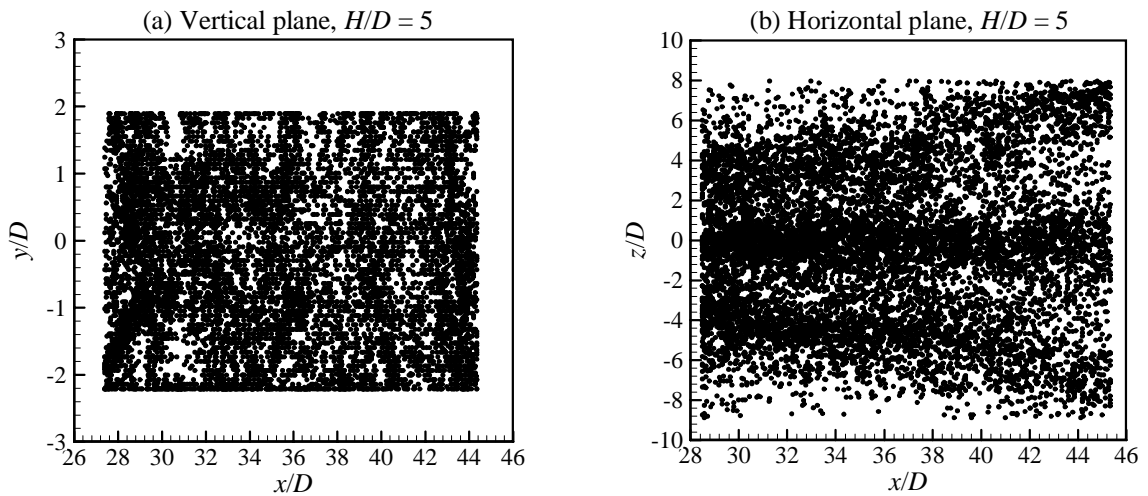


Figure 5.41: Two examples showing the centre positions of identified vortices of two sets of data extracted from 2000 velocity fields on; (a) a vertical plane, and (b) a horizontal plane of the shallowest case $H/D = 5$. Note that $y/D = z/D = 0$ represents the centreline of the jet.

distribution of the centres of vortices identified in a vertical plane for $H/D = 5$, while Figure 5.41(b) shows the corresponding horizontal plane at the same axial location. It is clear that the vortices can be found everywhere throughout the velocity field. The same behaviour can be seen in all reconstructed velocity fields analysed in this study (figures not included for brevity). An interesting observation can be seen in Figure 5.41(b). It shows three bands which indicate the preferred sites of the vortical structures in the horizontal plane; one along the jet axis and two at the sides of the jet.

Figure 5.42 shows the distribution of vortices in the axial direction x . Figure 5.42(a) shows the number of structures for the free jet and the $H/D = 15, 10$, and 5 cases in the vertical plane. In this figure, the horizontal axis represents the axial direction x normalised by the jet exit diameter D and the vertical axis represents the number of vortical structures. Each point on these curves represents the number of structures contained in a sixteen-grid-unit interval ($\sim 1.1D$) of the axial distance x . Figure 5.42(a) also shows that the number of identified vortices for the $H/D = 15$ case is relatively larger than the free jet case while the $H/D = 10$ case is comparable to the free jet case. For the $H/D = 5$ case, the number of identified vortices is relatively smaller than the free jet case. This figure also shows that the number of the vortices for all cases decreases in the axial direction. The effect of the vertical confinement on the horizontal plane for $H/D = 15, 10$, and 5 is illustrated in Figure 5.42(b). The free jet curve is also plotted for comparison. The number of vortices for all shallow cases for $x/D > 25$ is comparable to the free jet case although the number for the $H/D = 5$ case is slightly smaller. For the region $10 < x/D < 25$, Figure 5.42(b) shows that the number of structures for the shallow jet case $H/D = 5$ is much larger than the free jet. Then, the number of structures drops rapidly to become almost the same as the other cases. This indicates that the number of structures for the shallowest case ($H/D = 5$) increases significantly in the beginning, then drops as shown in Figure 5.42(b).

Additional insight is gained by plotting the distribution of vortex radius R and rotational sense with axial position (Figure 5.43). The relative error of the vortex size R was roughly estimated to be 10 to 30%, where the uncertainty is larger for small R . Both R

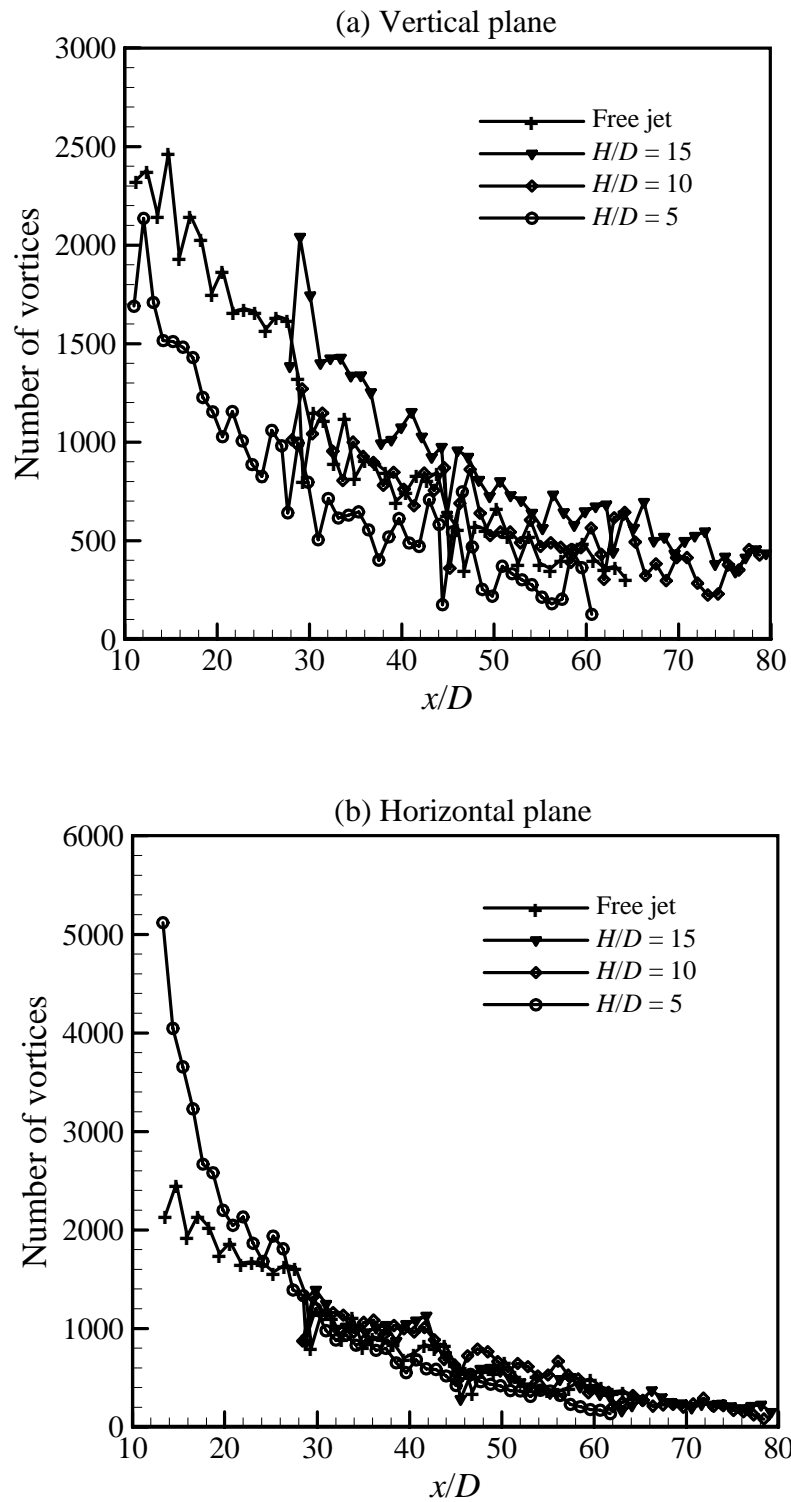


Figure 5.42: Variation of the number of vortices in the normalised axial direction x/D for the free and shallow jet cases on (a) the vertical plane, and (b) the horizontal plane.

and x are normalised by the jet exit diameter D . Note that the sign of R/D corresponds to the rotational sense of the vortex, where positive R/D represents positive rotational sense. This figure contains two sets of data (2000 velocity fields each) for the shallow case $H/D = 5$; one for the vertical plane (Figure 5.43(a)) and the other one for the horizontal plane (Figure 5.43(b)). It should be noted that the “pointed ends” on these figures occur because large vortical structures cannot be identified near the right and left edges of the velocity field. Also, the band near $R/D = 0$ corresponds to the minimum resolvable vortex size of $R/D < 0.21$ as discussed in Section 5.4.4. These figures reveal that the jet contains a substantial number of eddies of both signs. Figure 5.41(a) clearly shows that the jet has a wide spectrum of vortex sizes at each axial location, where the large vortices span the entire water depth ($\sim 5D$). Moreover, the distribution of positive vortical structures is a mirror-image of the negative ones. Note that the biggest vortex size R cannot exceed $2.5D$ in the vertical plane because of the confinement. Figure 5.43(b) shows the same characteristics except the range of vortex sizes is larger than in Figure 5.43(a). Obviously, the vortices can increase in size in the horizontal direction because there is minimal lateral confinement.

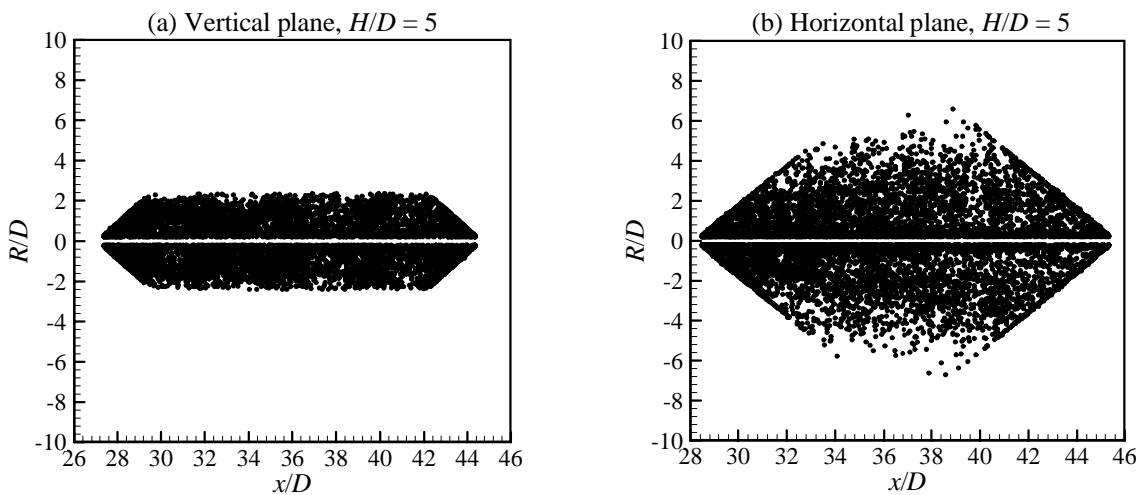


Figure 5.43: The distribution of vortex size R in the axial direction x . Each figure represents data extracted from 2000 velocity fields on (a) a vertical plane, and (b) a horizontal plane of the shallowest case ($H/D = 5$). Note that positive R/D represents positive rotational sense.

More information may be extracted from data similar to those shown in Figure 5.43 by sorting the vortical structures on the basis of size and rotational sense. Figure 5.44 shows the percentage of vortical structures as a function of vortex radius R and rotational sense. Figure 5.44 consists of four plots which show the size distribution of vortices for free and shallow jets in the vertical plane. In these figures, positive R indicates that the vortex is turning counter-clockwise. It should be noted that these plots were obtained by separately counting vortices of each rotational sense in a velocity field and dividing by the total number of vortices. The bin size of the vortex radius R used to construct all profiles in Figure 5.44 is $\sim 0.07D$. The results shown in Figure 5.44 were obtained after removing the “pointed ends” in Figure 5.43 to avoid biasing the results towards small values of R/D . This amounts to restricting the range of x/D considered to account for the difficulty in identifying large structures near the edges of a field-of-view. Two general characteristics can be identified in all of these plots. First, the number of vortices generally decreases as the size increases. Second, the plots are all symmetrical about $R/D = 0$ indicating that the size distribution is the same for each rotational sense. The ratio between the number of positive and negative vortices for all cases is given in Table 5.2. Although most of the ratios shown in Table 5.2 are close to unity, it is observed that the ratio of the vortices identified on the vertical plane decreases in the downstream direction. The decrease in the ratio means an increase in the number of negative (clockwise) rotating vortices compared to the positive ones.

Figure 5.44(a) presents the vortex size distribution at three axial locations for the free jet. Each profile is extracted from a set of data contained two thousand velocity fields. The purpose of plotting these profiles is to show the effect of the axial location on the size distribution of the vortical structures. It is clear that small vortices have generally higher population in all profiles and the number decreases as the vortex size increases. The number of small vortices decreases slightly with increasing axial distance and there is a corresponding increase in the number of larger vortices. Note that the largest identified vortices have sizes $|R/D| \approx 8$. As the vertical confinement increases, Figures 5.44(b), (c), and (d) show that the size of the largest identified vortices decreases to $|R/D| \approx 7.5$, 5, and 2.5, corresponding to $H/D = 15$, 10, and 5, respectively. In other words, the largest

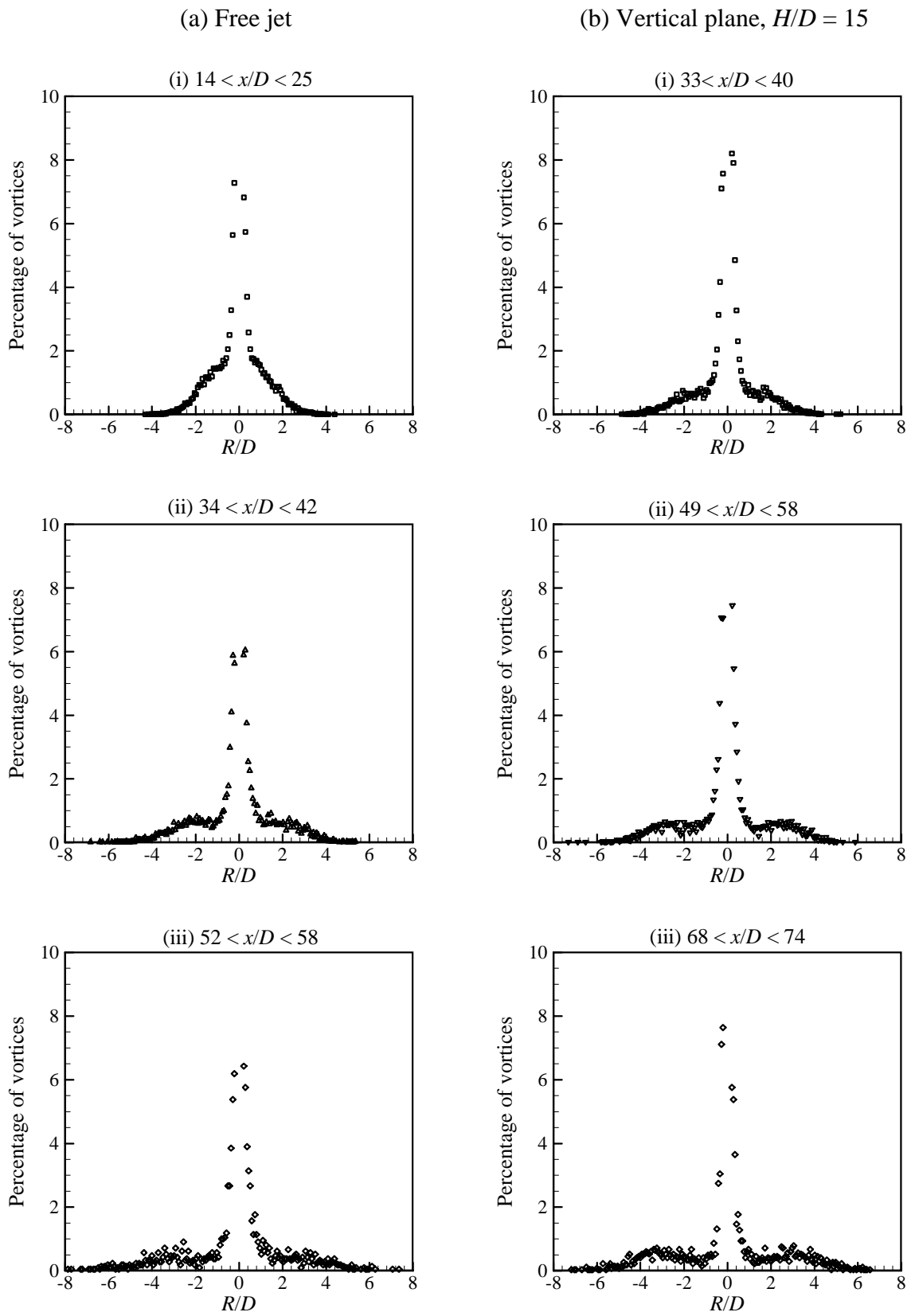
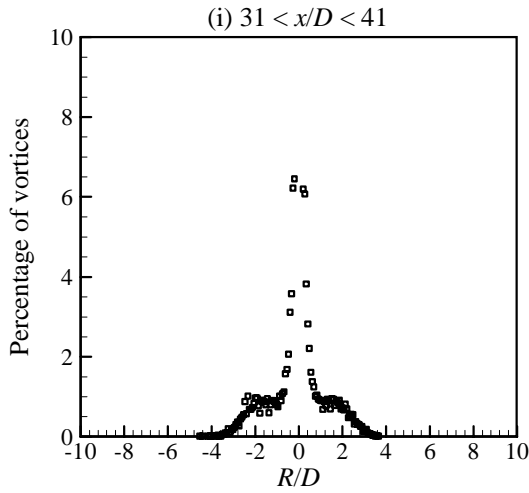


Figure 5.44: For caption see next page.

(c) Vertical plane, $H/D = 10$



(d) Vertical plane, $H/D = 5$

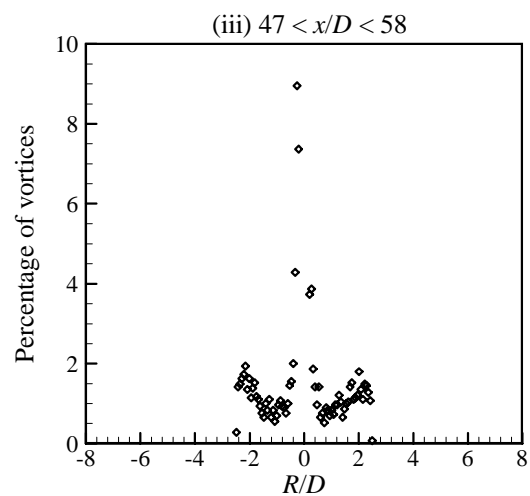
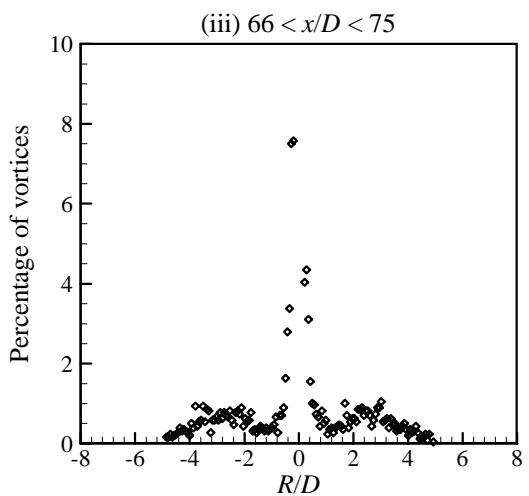
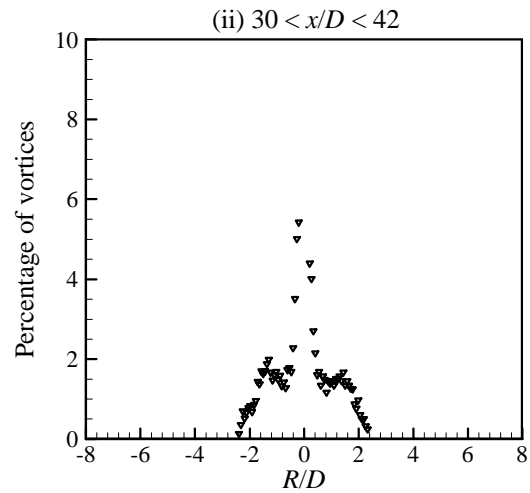
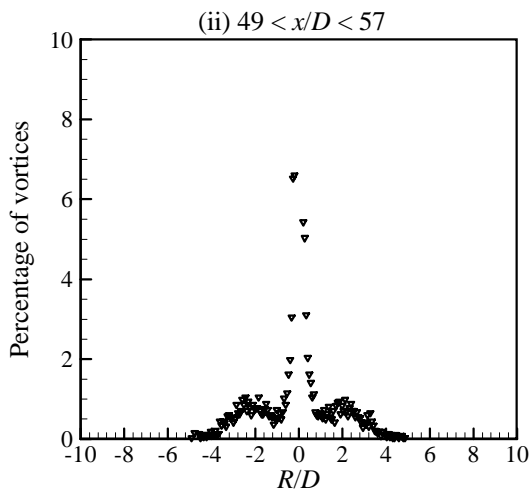
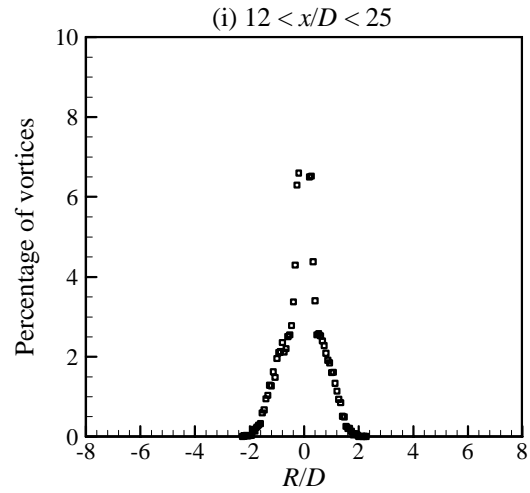


Figure 5.44: Percentage of vortices for (a) the free jet, and shallow jets on the vertical plane of depths; (b) $H/D = 15$, (c) $H/D = 10$, and (d) $H/D = 5$. Each figure shows three profiles (i), (ii), and (iii) taken at different ranges of axial distances.

size R spans the entire layer depth. Furthermore, it is observed that the percentage of small vortices increases slightly in the downstream direction where the confinement is still mild as shown by comparing plots (ii) and (iii) of Figure 5.44(a) with plots (i) and (ii) of Figure 5.44(b).

Another interesting feature can be seen in Figure 5.44(d), which shows three profiles for the shallowest case ($H/D = 5$). It shows that the percentage of small vortices seems to decrease in the axial direction in the beginning because of the confinement as shown by comparing the free and shallowest jet profiles in Figures 5.44(a) and (d). This is accompanied with an increase of the number of large vortices (both signs) in the downstream direction. Then, small resolved vortices started appearing again with a relatively larger number of negative (clockwise) sign without positive partners as shown in plot (iii) in Figure 5.44(d). This behaviour is also observed in Figures 5.44(b) and (c) which indicates that the decrease in the ratio of positive to negative vortices is due to an increase in the number of small vortices. This is a clear indication of the dramatic effect of the confinement on the turbulence structure. It should be noted that most small vortices are likely to be identified near the boundaries. This increase of the negative small vortices may be explained by the formation of vortices near the solid wall.

In order to obtain a clearer perception of the effect of confinement on the size distribution of the structures, Figures 5.45 illustrates the size distribution of vortical structures on the horizontal plane for the $H/D = 10$ and 5 cases. The results of the $H/D = 15$ case look similar to the $H/D = 10$ case and, for brevity, are not included. Figure 5.45(a) depicts the distribution of the vortical structures at three adjacent fields-of-view represented by plots (i), (ii), and (iii) for the $H/D = 10$ case. Figure 5.45(a) shows that there is a significant change in the size distribution of the vortices for this case compared to the free jet case at the same axial locations (Figure 5.44(a)). Plot (i) in Figure 5.45(a) shows that the percentage of small vortices at this axial location is smaller than the free jet case with a corresponding increase of vortex sizes in the range $1 < |R/D| < 4$. At locations further downstream, plot (ii) shows that the percentage of

(a) Horizontal plane, $H/D = 10$

(b) Horizontal plane, $H/D = 5$

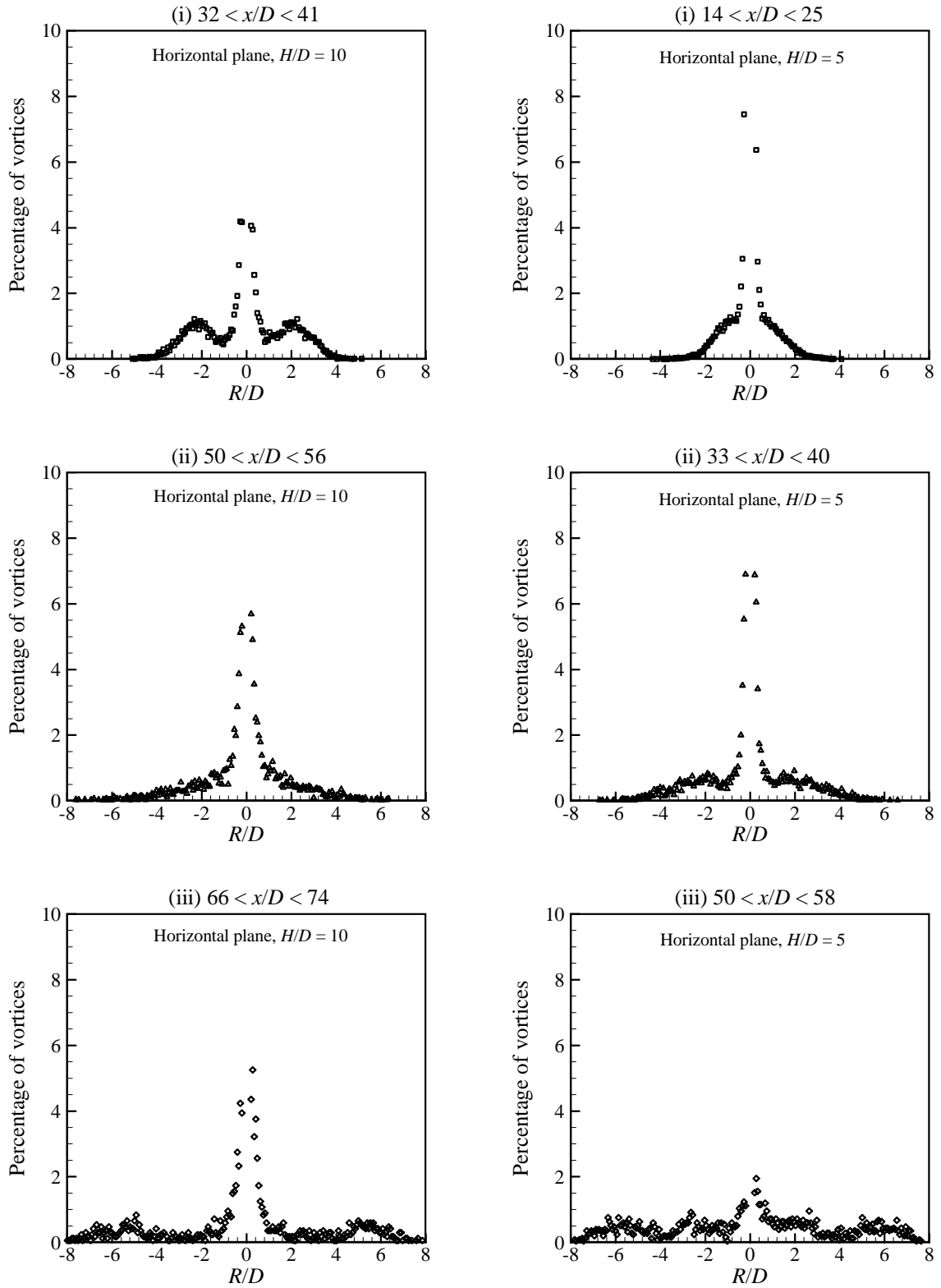


Figure 5.45: Percentage of vortices for the shallow jets on the horizontal plane of depths; (a) $H/D = 10$ and (b) $H/D = 5$. Each figure shows three profiles (i), (ii), and (iii) taken at different ranges of axial distances.

small vortices increases but they are slightly less than the free jet case. Generally, both shallow and free jet profiles look similar at these locations. Plot (iii) in Figure 5.45(a) shows that the percentage and range of larger vortices ($|R/D| > 4$) increase in the axial direction with a corresponding reduction in the percentage of moderate sizes in the range $1 < |R/D| < 4$.

Figure 5.45(b) shows three axial locations for the $H/D = 5$ case. By comparing the three profiles for the $H/D = 5$ case to the free jet case, the effect of the confinement is clear on the size distribution of vortices. Although there is a little difference between the profiles shown in plots (i) in Figures 5.44(a) and 5.45(b) for the free and shallow cases, respectively, the effect of the confinement on the size distribution is observable in Figure 5.45(b) plot (ii). This plot shows that the fraction of small vortices is larger than the free jet case while the range of vortex sizes is almost the same ($|R/D| \approx 6.7$). At locations further downstream, the percentage of small vortices ($|R/D| < 0.7$) decreased significantly with a corresponding increase in the fraction of larger vortices particularly those in the range ($4 < |R/D| < 8$). This indicates that large vortices become more frequent for the $H/D = 5$ case at these locations which may be attributed to the dominance of the pairing process because of the confinement. This observation may also be supported by the reduction of the number of vortices (see Table 5.2, cases SJ38 and SJ39). This is in contrast to the increase of negative (clockwise) small vortices observed on the vertical plane at the same locations which were attributed to the formation of vortices near the solid wall.

Figure 5.46 shows the behaviour of mean vortex size R_{mean} in the axial direction on vertical and horizontal planes. These mean values were calculated from the vortices that exist in sixteen-grid-unit intervals ($\sim 1.1D$) of the axial distance x . Figure 5.46(a) shows clearly that the mean size of vortices calculated on the vertical plane for all shallow cases is comparable to the mean size of the free jet case although it is slightly bigger in the free jet. It should be noted that the size of vortices of the shallowest case ($H/D = 5$) on the vertical plane is restricted by the depth of the water layer. Figure 5.46(b) shows

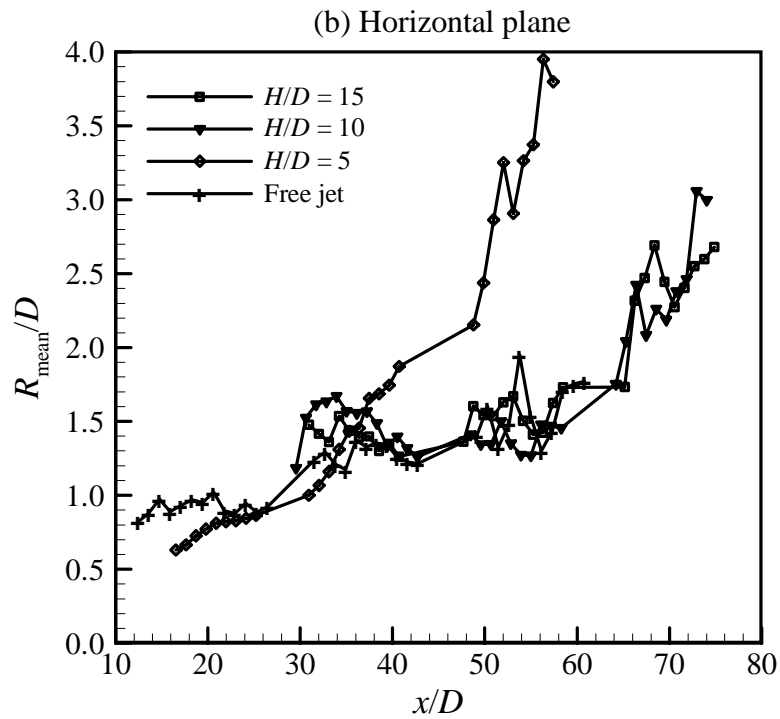
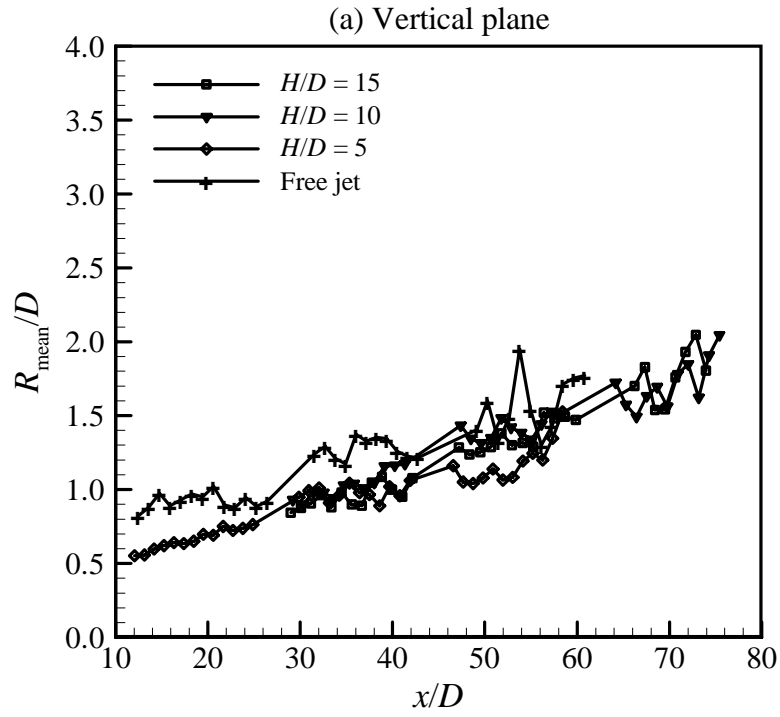


Figure 5.46: Variation of the normalised mean radius R_{mean}/D of vortices in the normalised axial direction x/D on (a) the vertical plane, and (b) the horizontal plane.

that the mean size of the structures calculated on the horizontal plane for the same water depths generally increases in the axial direction. It can also be seen that the mean size for the shallowest case ($H/D = 5$) increases with the same rate as the other cases until $x/D \approx 40$, then with a higher rate beyond that location. Note that the last point on the curves represents vortices near the right edge of the velocity field. The decreasing trend of the mean size indicated by the last point is because large vortical structures cannot be identified near the edge of the velocity field.

Figures 5.47 and 5.48 show the distribution of circulation Γ associated with the vortices in the axial direction x on vertical and horizontal planes, respectively. The measurement error in Γ was estimated to be 23 to 37% (see Section 3.4). In these figures, the circulation Γ is normalised by DU_e . Each figure consists of two plots which represent two adjacent fields-of-view. Both figures are extracted from the shallowest water jet data ($H/D = 5$). It should be noted that the data set is very large and only selected examples can be presented. The selection of these fields-of-view is because they clearly show the effect of the vertical confinement on the flow structure.

Figure 5.47(a) indicates that the circulation magnitude captured in this field-of-view ($28 < x/D < 44$) varies from a weak to a relatively larger circulation ($|\Gamma/DU_e| < 0.5$) at each axial location. At further downstream locations ($44 < x/D < 60$), Figure 5.47(b) shows that the circulation magnitude is slightly damped by the vertical confinement. Furthermore, the reduction of the number of the points that represent vortex circulations is apparent. On the other hand, Figures 5.48(a) and (b) show that the vortices identified in the horizontal plane generally contain more energy. Moreover, the reduction of the circulation magnitude, shown in Figure 5.47(b) due to the vertical confinement, is associated with a significant increase of the circulation magnitude on the horizontal plane as shown in Figure 5.48(b). This figure illustrates that the range of the circulation magnitude widens to $|\Gamma/DU_e| \approx 1.5$. These results are in agreement with the reduction of the axial and vertical turbulence intensities on the vertical plane and an increase of the

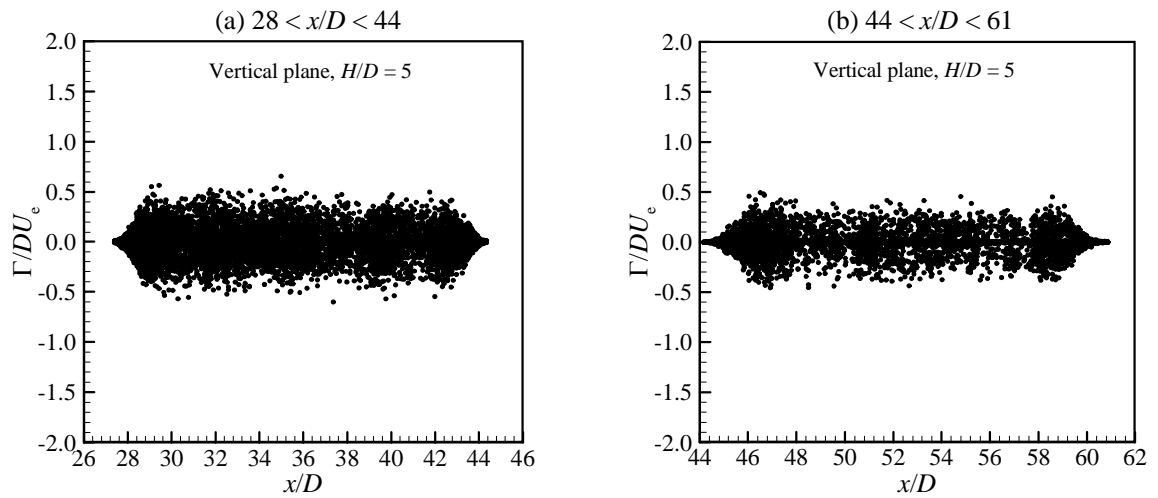


Figure 5.47: Distribution of vortex circulation Γ of the shallowest case ($H/D = 5$) extracted from 2000 velocity fields on a vertical plane of two adjacent fields-of-view (a) $28 < x/D < 44$, and (b) $44 < x/D < 61$. Note that positive Γ/DU_e represents positive rotational sense.

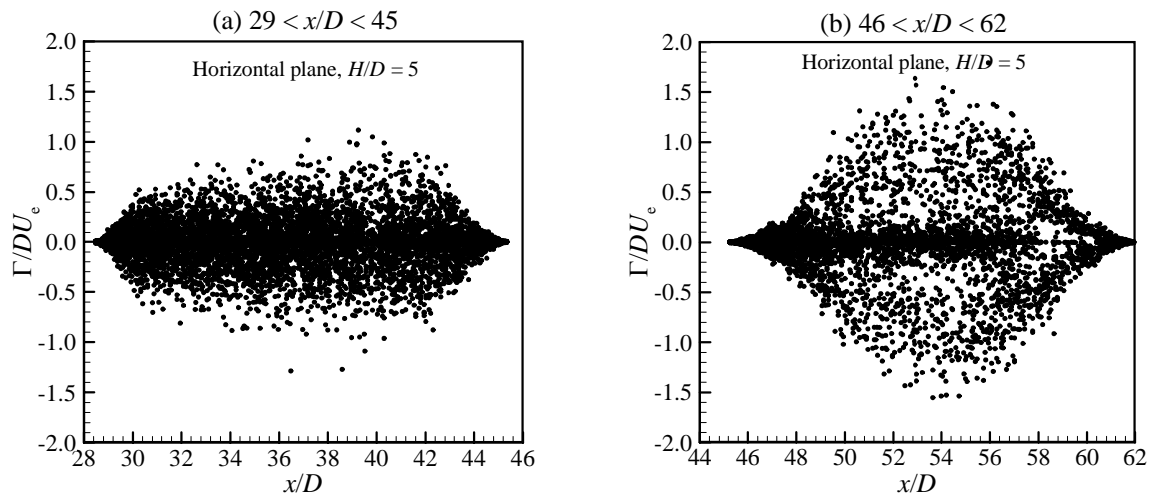


Figure 5.48: Distribution of vortex circulation Γ of the shallowest case ($H/D = 5$) extracted from 2000 velocity fields on a horizontal plane of two adjacent fields-of-view (a) $29 < x/D < 45$, and (b) $46 < x/D < 61$. Note that positive Γ/DU_e represents positive rotational sense.

horizontal turbulence intensity on the horizontal plane. Also, the smaller values of the Reynolds stress $\langle uv \rangle$ on the vertical plane is consistent with the reduction in the number and strength of the vortices on the vertical plane.

The behaviour of the mean circulation Γ_{mean} of vortices in the axial direction on the vertical and horizontal planes is shown in Figure 5.49. In this figure, the axial location x is normalised by D and the circulation is normalised by DU_e . Figure 5.49(a) illustrates the behaviour of the normalised mean circulation $\Gamma_{\text{mean}}/DU_e$ on the vertical plane for shallow jet cases $H/D = 15, 10,$ and 5 , in addition to the free jet case. It is apparent that the mean circulation for all free and shallow jets fluctuates within a small range and the confinement seems to have almost no effect on the mean circulation calculated on the vertical plane. Figure 5.49(b) shows a different behaviour of the normalised mean circulation $\Gamma_{\text{mean}}/DU_e$ on the horizontal plane. Although the mean circulation demonstrates similar behaviour to the previous figure in the beginning ($x/D < 49$), it suddenly increases at a downstream location which is determined by the degree of vertical confinement. The effect of the confinement is more profound on the shallowest case ($H/D = 5$) where the mean circulation increases at a very high rate until $\Gamma_{\text{mean}}/DU_e \approx 0.46$. For $H/D = 15$ and 10 , the mean circulation seems to increase at downstream locations. Unfortunately, these locations are near the right edge of the velocity field and, therefore, this behaviour cannot be investigated farther downstream. The decreasing trend of the mean circulation observed in the last point of the curves is because large vortical structures cannot be identified near the edge of the velocity field.

The circulation associated with vortical structures of different sizes is shown in Figure 5.50. In this figure, the horizontal axis represents normalised circulation Γ/DU_e and the vertical axis represents the normalised vortex radius R/D . Once again, the sign of the vortex radius corresponds to the rotational sense of the vortices. This figure consists of six plots; (a) & (b) represent the distribution of vortices for the free jet in two adjacent fields-of-view, (c) & (d) represent the distribution of vortices for the shallowest jet ($H/D = 5$) on the vertical plane in two adjacent fields-of-view, and (e) & (f) represent the

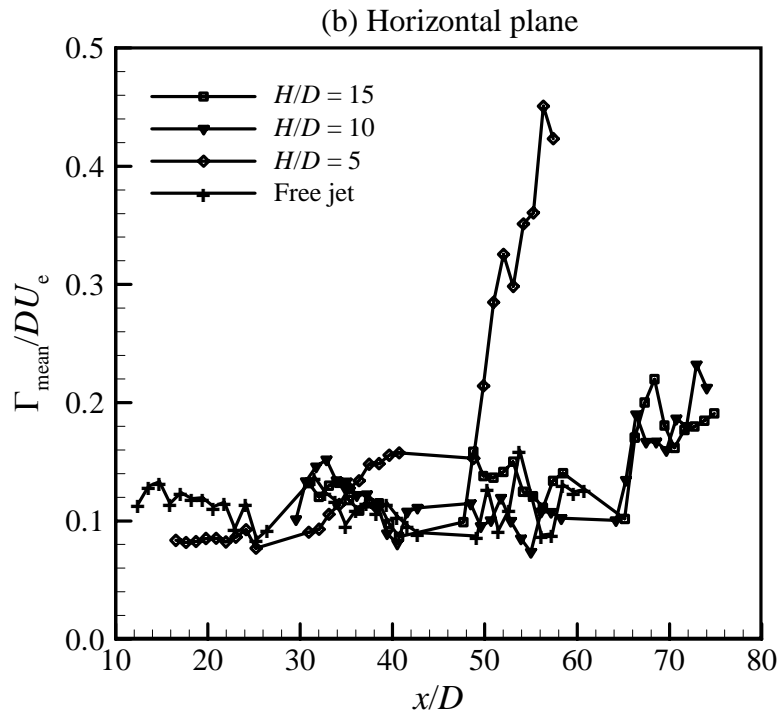
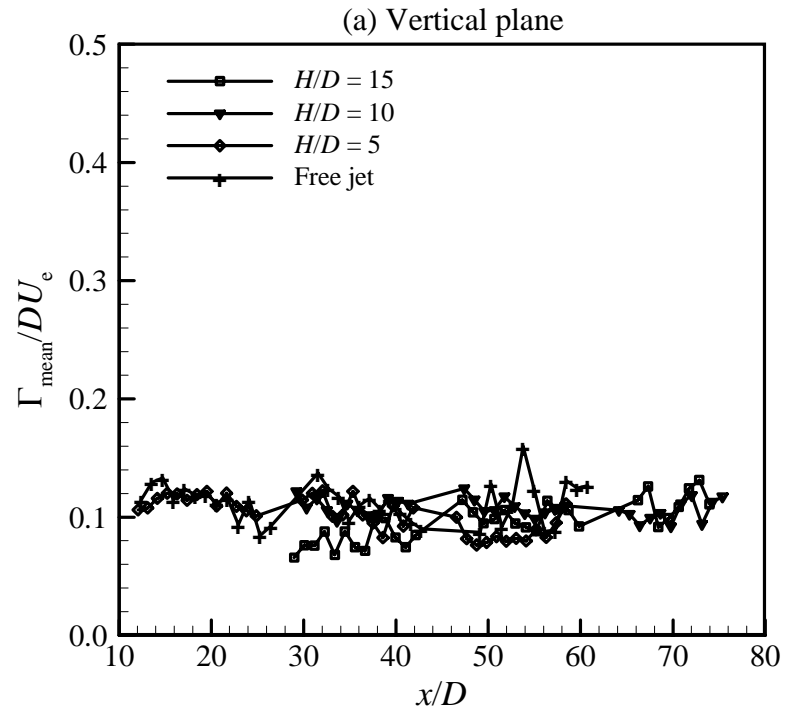


Figure 5.49: Variation of the normalised mean circulation $\Gamma_{\text{mean}}/DU_e$ of vortices in the normalised axial direction x/D on (a) the vertical plane, and (b) the horizontal plane.

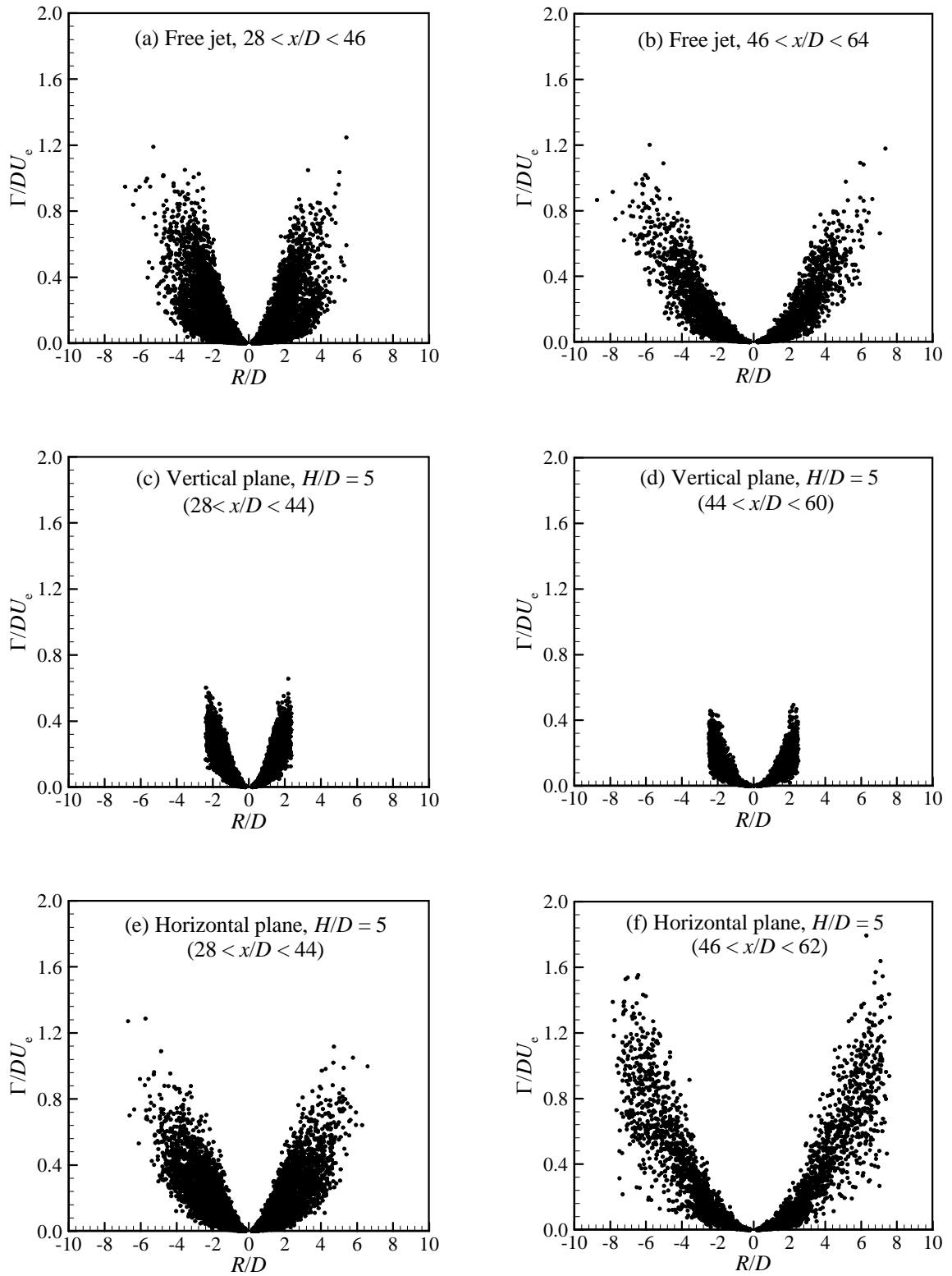


Figure 5.50: Distribution of normalised circulation Γ/DU_e associated with the identified vortices of different sizes at two adjacent fields-of-view for the free jet (a) and (b), the shallowest jet case ($H/D = 5$) on the vertical plane (c) and (d), and the shallowest jet case on the horizontal plane (e) and (f).

distribution of vortices for the shallowest jet ($H/D = 5$) on the horizontal plane in two adjacent fields-of-view. The purpose of these figures is to show the effect of the vertical confinement on flow structure for the shallow jet case as they evolve in the axial direction by comparing it to the free jet case. Figures 5.50(a) and (b) illustrate clearly that the vortices increase in size with the downstream direction although the range of vortex strengths seems to be preserved. These observations are consistent with the mean size R_{mean} and circulation Γ_{mean} results shown in Figures 5.46 and 5.49. It can be seen that the maximum circulation magnitude $|\Gamma/DU_e|$ reaches 1.2 although most of them are below 1.0. Owing to the effect of the confinement, the range of vortex sizes and strengths in the vertical plane decreases significantly as shown in Figures 5.50(c) and (d) compared by the free jet results. In addition, the strengths of all vortex sizes seem to be slightly weaker in the axial direction because of the confinement. Conversely, Figures 5.50(e) and (f) show that the range of vortex sizes and strengths in the horizontal plane is much wider than in the vertical plane. Moreover, the range of vortex sizes and strengths in the horizontal plane increases significantly in the axial direction as can be seen by comparing Figures 5.50(e) and (f). The maximum absolute value of normalised circulation $|\Gamma/DU_e|$ reaches ~ 1.6 (see Figure 5.50(f)). Generally speaking, the above results indicate that larger vortices have a higher value of circulation while smaller values of circulation are associated with smaller eddies. Furthermore, it is clear that the circulation magnitude $|\Gamma/DU_e|$ is directly proportional to $(R/D)^2$ and the constant of proportionality is a function of the axial location x/D . It is interesting to observe that the constant of proportionality for the free jet data shown in Figure 5.50(b) and the shallow jet data shown in Figure 5.50(f) is the same (0.025).

Chapter 6

CONCLUSIONS AND RECOMMENDATIONS

6.1 CONCLUSIONS

This work focused on the effect of vertical confinement on a horizontal jet issuing from a round nozzle of diameter $D = 9$ mm. Three different degrees of confinement ($H/D = 15, 10,$ and 5) were investigated. The horizontal confinement in the water tank was negligible. In order to show the effect of the vertical confinement, the shallow water jet results were compared to the free jet results obtained in the same experimental rig. The velocity field measurements were made using the particle image velocimetry (PIV) technique. The jet exit velocity was 2.5 m/s and the Reynolds number based on the exit condition was $22,500$. Measurements were made on vertical (x - y) and horizontal (x - z) planes at different axial locations downstream of the jet exit. The velocity, turbulence intensity, and turbulent shear stress profiles were compared to the free jet results to characterise the effect of the confinement. The mean axial velocity, turbulence intensity, and spread rate along the centreline of all the shallow jet cases were also obtained.

The characteristics of large-scale vortical structures in shallow water jets were also investigated. The proper orthogonal decomposition (POD) method was applied to the two-dimensional PIV data to expose vortical structures. The position, size, and strength of these vortices were identified and measured by the method described in Section 4.3. This method is based on the concept of using closed streamlines to identify vortices. The

largest closed streamline bounding the structure was considered the vortex core.

This study shows that the flow structure underwent significant changes because of the vertical confinement. Specific conclusions may be summarised as follows:

1. The vertical confinement has a clear effect on the decay rate of the mean centreline velocity. For the $H/D = 15$ case, the decay rate of the mean centreline velocity is constant and equal to the free jet decay ($K_d = 5.90$). For the $H/D = 10$ and 5 cases, the decay rate of the mean centreline velocity is the same as the free jet case until $x/D = 44$ and 55, respectively. Then, the centreline velocity started decaying at a slower rate compared to the free jet case. Although this behaviour was not observed in the $H/D = 15$ case, it is expected that the mean centreline velocity of this case will also eventually decay with a slower rate but at a larger x/D than was measured. The slower decay rate may be explained by the conservation of mass which demands an increase in the jet velocity compared to the free case because the cross-sectional area of the jet becomes constrained by the boundaries.
2. The vertical confinement has a significant effect on the jet spread. All shallow jet cases underwent a constriction in the horizontal mid-plane compared to the free jet case. However, the $H/D = 15$ case spreads linearly with a growth rate $K_s = 0.072$ compared to 0.096 for the free jet, while the $H/D = 10$ and 5 cases spread with slower, non-linear growth rates. The departure of the jet width curves from the free jet case occurs at approximately $x/D \approx 29, 25,$ and 12 for the $H/D = 15, 10,$ and 5 cases, respectively.
3. The confinement has a profound effect on the axial velocity profiles in the vertical plane. As the flow evolves downstream, the jet spreads to the boundaries and the axial velocity above and below the jet centreline increases rapidly. For the shallow cases $H/D = 10$ and 5, the axial velocity in the vertical plane becomes almost uniform over the entire depth, with a mild peak below the centreline of the jet for the $H/D = 5$ case. In contrast, the axial velocity profiles in the horizontal plane are

Gaussian and look similar to each other. However, they are slightly narrower than the free jet profile which is consistent with the slower spread rate of the shallow jet cases.

4. The mean vertical velocity profiles show that vertical entrainment has stopped at locations $x/D > 40, 30,$ and 20 for $H/D = 15, 10,$ and $5,$ respectively, because of the confinement and only vertical outward flow from the axis occurs. Conversely, the mean horizontal velocity profiles show that the inward horizontal flow at the jet peripheries increases while the outward lateral flow near the jet centreline decreases. This indicates that fluid is taken from the sides to the jet centreline and then diverted upward and downward from the jet axis. This explains the rapid increase of the axial velocity above and below the jet centreline and the reduction of the jet width in the horizontal plane.
5. For the $H/D = 10$ and 5 cases, the mean vertical velocity becomes negative over most of the depth at downstream locations, indicating that the flow is always directed downward towards the solid wall. This behaviour is similar to the behaviour of a round turbulent wall jet observed by Law & Herlina (2002) which indicates the dominance of the wall jet characteristics for these shallow jet cases. It was explained by the existence of secondary vortices near the wall that suck the fluid downward towards the wall and then divert it horizontally away from the vertical mid-plane parallel to the wall. This behaviour indicates the three-dimensionality of the jet in this region.
6. The vertical confinement generally has a mild effect on the turbulence intensities ($u_{rms}/U_c, v_{rms}/U_c, w_{rms}/U_c$) along the jet centreline for the $H/D = 15$ and 10 cases, but a profound effect on the $H/D = 5$ case. The decrease of u_{rms}/U_c and v_{rms}/U_c at downstream locations may be attributed to the corresponding increase of the mean centreline velocity. In contrast to the behaviour of the $H/D = 15$ and 10 cases, the relative axial and vertical turbulence intensities for the $H/D = 5$ case seem to be suppressed by the vertical confinement with a corresponding increase of w_{rms}/U_c .

This increase is confirmed by the large increase in the ratio $w_{\text{rms}}/u_{\text{rms}}$ compared to the ratio $v_{\text{rms}}/u_{\text{rms}}$ which seems to be constant. This behaviour may be explained by the energy removed from the axial and vertical fluctuations being transferred to the horizontal fluctuations.

7. As the flow proceeds downstream, the effect of the vertical confinement becomes more significant and suppresses the axial and vertical turbulence intensities compared to the free jet case. The reduction of the turbulence intensities increases as the degree of the confinement increases. The data on the vertical plane show that u_{rms} and v_{rms} are inhibited near the jet axis in the downstream direction. However, the axial velocity fluctuations increase near the boundaries until they become close to the values near the jet axis. The vertical fluctuations decrease rapidly as the boundaries are approached. The axial turbulence intensity on the horizontal plane displays similar behaviour near the jet axis as the profiles on the vertical plane. However, the horizontal profiles are generally narrower than the free jet profiles which is consistent with the mean axial velocity profiles. In contrast to the axial and vertical fluctuations, the horizontal fluctuations increase in the downstream direction which may be explained by the transfer of kinetic energy from the axial and vertical fluctuations to the horizontal component.

8. The Reynolds shear stress $\langle uv \rangle$ results show that mixing efficiency of the fluid in the vertical plane is significantly affected by the vertical confinement. In other words, the momentum transport is increasingly inhibited as the flow proceeds in the axial direction and as the degree of the confinement increases. Moreover, the confinement changed the structure of the Reynolds stress $\langle uv \rangle$ for the shallowest case ($H/D = 5$) which becomes positive below the jet centreline at downstream locations. This indicates that both the velocity fluctuation components (u', v') have the same sign. In contrast, the momentum transport in the horizontal plane is only slightly affected by the confinement as shown by the Reynolds stress $\langle uw \rangle$ profiles. For the $H/D = 15$ and 10 cases, the profiles are almost the same as the free jet profile, but are slightly narrower at the jet peripheries. However, the momentum

transport for the $H/D = 5$ case is more affected by the confinement. The profiles become narrower in the outer region with a slightly smaller peak ($\langle uw \rangle / U_c^2 = 0.020$ compared to 0.022 for the free jet).

9. The POD analysis results show that centres of the identified vortices are distributed throughout the velocity fields, which indicates that they exist everywhere in the velocity fields.
10. The POD results extracted from the vertical plane show that the free jet case has a larger number of vortical structures than the $H/D = 5$ case, a comparable number to the $H/D = 10$ case, and a smaller number than the $H/D = 15$ case. In addition, the number of vortices identified in the horizontal plane for all cases for $x/D > 25$ is comparable to the free jet case. For the region $10 < x/D < 25$, the number of structures for the shallowest jet case ($H/D = 5$) is much larger than the free jet and drops rapidly to become almost the same as the other cases at $x/D \approx 25$. It can be concluded that the number of vortices increases when the effect of the confinement is still mild, then starts decreasing in the downstream direction because of the pairing process.
11. For all free and shallow cases on the vertical and horizontal planes, the number of vortices decreases rapidly in the axial direction.
12. The jet flow has a wide spectrum of vortex sizes ranging from the smallest resolved vortices ($R/D \approx 0.2$) to vortices on the same order of magnitude as the jet width. The large vortices identified in the vertical plane are restricted by the water depth, while they are allowed to increase in size in the horizontal plane because there is negligible lateral confinement. The largest vortex size identified in this research was $R/D \approx 10$.
13. The distribution of vortex sizes shows that small vortices are more numerous in all fields-of-view and the number decreases as the size increases. In addition, the percentage of small vortices generally decreases with decreasing water depth. Also,

the number of small vortices decreases slightly with increasing axial distance and there is a corresponding increase in the number of larger vortices. However, the number of small vortices for the shallowest case on the horizontal plane decreases significantly at downstream locations with a corresponding increase in the number of large vortices and significant increase in their size.

14. The mean size of vortices for the shallow cases calculated on the vertical plane does not highlight the size difference for the different cases. It shows that the mean size of vortices is comparable to the mean size of the free jet case, although it is slightly larger in the free jet, and increases with the same rate as the free jet in the axial direction. The failure of the mean size to differentiate between different cases may be attributed to the existence of small vortices in the vertical plane at all axial locations, which is used in calculating the mean radius. The mean size of the vortical structures calculated on the horizontal plane for the same water depths generally increases in the axial direction with a relatively higher rate compared to the vertical plane. Beyond certain locations determined by the degree of the confinement, the mean size increases with a much higher rate which is in agreement with the reduction of the number of small vortices at downstream locations particularly for the shallowest case.
15. The population of vortical structures of either rotational sense is almost identical for all vortex sizes. This distribution was changed in the downstream direction such that small negative vortices increase significantly without positive partners. This imbalance seems to increase as the degree of the vertical confinement increases. However, the data extracted from the horizontal plane do not demonstrate such an imbalance. This increase of the negative small vortices on the vertical plane may be attributed to the formation of vortices near the solid wall.
16. The distribution of the circulation associated with the vortices shows that the circulation magnitude varies from a weak to a relatively larger circulation at each axial location. Moreover, the circulation magnitude calculated on the vertical plane

is slightly damped by the vertical confinement at downstream locations ($|\Gamma/DU_e| < 0.7, 0.5, \text{ and } 0.4$ for $H/D = 15, 10, \text{ and } 5$, respectively compared to 1.2 for the free jet) while the mean circulation seems to be constant for all free and shallow jet cases. The reduction of the vortex circulation on the vertical plane is associated with an increase of the circulation magnitude on the horizontal plane. This is particularly significant for the $H/D = 5$ case where the range of the circulation magnitude widens to $|\Gamma/DU_e| \approx 1.6$ compared to 1.2 for the free jet case. This behaviour is in agreement with the reduction of the axial and vertical turbulence intensities on the vertical plane. Similarly, the mean circulation $\Gamma_{\text{mean}}/DU_e$ is almost constant in the beginning, and then suddenly increases with a very high rate at different downstream locations. This behaviour is clearly observed in the $H/D = 5$ case where the circulation starts increasing with a very high rate at $x/D > 49$ until $\Gamma_{\text{mean}}/DU_e$ reaches ~ 0.46 . This increase of the circulation for the shallowest case is consistent with the high rate of increase of the horizontal turbulence intensity w_{rms} .

17. Pairing and tearing processes occur frequently in all free and shallow jet cases. However, the rate of occurrence of these processes increases because of the confinement. The occurrence of the pairing process is supported by the increase of vortex sizes in the downstream direction with a corresponding decrease in the number of the small vortices. In addition, the occurrence of the tearing process is supported by the existence of small resolved vortices in all shallow cases particularly on the vertical plane. Also, the vortices whose sizes almost span the entire water depth are likely to become unstable since they are not allowed to increase in size. For the vortices identified in the horizontal plane, pairing and tearing processes occur frequently at the beginning. However, the pairing process becomes dominant farther downstream. This is supported by the rapid increase of vortex sizes with a significant decrease in the number of the small vortices.

18. In all cases the distribution of the vortices indicates that larger vortices have a higher value of circulation while smaller values of circulation are associated with smaller

eddies. It was found that the circulation magnitude $|\Gamma/DU_e|$ is directly proportional to $(R/D)^2$ and the constant of proportionality is a function of the axial location x/D .

6.2 CONTRIBUTIONS

This research was a very large-scale study. In total, 43,000 image pairs (~344 GB) were acquired. The analysis of the images and consequent analysis of the data demanded an additional ~150 GB. In addition, all analysis procedures were performed using codes developed in-house which included the PIV correlation analysis, the cellular neural network (CNN) for outlier rejection using a variable threshold technique, a Levenberg-Marquardt algorithm for non-linear curve fitting, the proper orthogonal decomposition (POD) technique, a vortex identification algorithm which identified vortex centres and measured their size and strength, and a code for performing the statistical investigation.

The main contributions of the present work to research may be summarised in three main areas:

1. Contribution to the PIV data analysis

- Developed a variable threshold technique that can be applied to any PIV post-analysis outlier identification algorithm. This technique is a practical procedure for selecting a threshold field in large data sets where there is significant variability in the properties of the vector field. In this way, it filters the data from outliers while saving vectors from being mistakenly rejected.

2. Contributions to the understanding of confined jets

- The PIV technique is applied for the first time to study shallow water jets in order to produce a better description of the flow structure. As well, the POD technique was also used for the first time for this flow.
- This work is the first quantitative study of large vortical structures in free and shallow water jets using spatial information. Also, this is the first study that investigates both mean flow field and coherent structures in shallow jets.

3. Contributions to the understanding of turbulence phenomena

- This is a pioneer investigation for exploring coherent structures based on spatial information rather than pointwise measurements. It is amazing to visualise and quantify the effect of the confinement on the large vortices.
- This work is believed to be the first experimental study that offers strong quantitative information of the distribution of size, rotational sense, and circulation of large vortices. Also, it provides strong evidence of the occurrence of pairing and tearing processes.
- The present investigation provides new information of the effect of the confinement on the velocity fields and mixing process in confined jets. In addition, this is the first time that it has been shown that jets contain an equal number of clockwise and counter-clockwise rotating vortices and that this balance is altered because of the confinement.

The present results also demonstrate the capabilities of the PIV measurement technique for investigating complex flow fields, particularly when combined with efficient analysis methods such as the POD technique, for extracting information from the measured velocity fields.

In general, this work contributes to expand the base data and knowledge available on shallow water jets and turbulence phenomena. Since the structure of this flow has not been extensively explored, the present results may be useful to furnish a solid foundation for future work and to suggest which points need deeper investigation.

6.3 RECOMMENDATIONS FOR FUTURE WORK

The principal parameter used for determining the effect of the vertical confinement in the current study was the depth of the water layer. Some recommendations for future work on shallow water jets are summarised below:

- The dynamics of coherent structures at locations farther downstream ($x/D > 80$) are not fully characterised. Some features of coherent structures in the far field were investigated in this study, but further analysis is still needed to confirm that the $H/D = 15$ results would display similar characteristics to the $H/D = 5$ case if measurements had been made further downstream.
- Further experimental work is needed to determine the jet behaviour at several vertical and horizontal planes parallel to the vertical and horizontal mid-planes investigated in this thesis. This could include planes near the free surface and the solid wall.
- The present analysis could be enhanced by investigating a range of Reynolds numbers. In many practical applications, Reynolds numbers are orders of magnitude higher than those studied in the laboratory, and there is always some risk when extrapolating laboratory results to real flows.
- Another variable that could be examined is the effect of buoyancy on the dynamics of coherent structures.
- Additional information on the flow patterns and the dynamics of large vortical structures could be obtained by considering simultaneous visualisations and velocity measurements. This could be done by applying the method of simultaneous PIV and LIF techniques. As well, the time-resolved PIV technique could give additional insight into the dynamics of the vortical structures.
- Some useful techniques such as holographic PIV offer the opportunity to extract three-dimensional velocity fields for the study of coherent structures. This will provide more insight into the physics of the flow field.
- More work is needed to refine the vortex identification algorithm of Agrawal & Prasad (2002) and clearly define the core boundary of the vortices.

REFERENCES

1. Abramovich, G.N. (1963), *The theory of turbulent jets*, MIT Press.
2. Adrian, R.J. (1988), *Statistical properties of particle image velocimetry measurements in turbulent flow*, In *Laser Anemometry in Fluid Mechanics III*, Springer-Verlag, Berlin Heidelberg, pp. 115-129.
3. Adrian, R.J. (1991), *Particle-imaging techniques for experimental fluid mechanics*, *Annu. Rev. Fluid Mech.*, v23, pp. 261-304.
4. Adrian, R.J., Christensen, K.T., and Liu, Z.-C. (2000), *Analysis and interpretation of instantaneous turbulent velocity fields*, *Exp. Fluids*, v29, n3, pp. 275-290.
5. Agrawal, A. and Prasad, A.K. (2002a), *Organizational modes of large-scale vortices in an axisymmetric turbulent jet*, *Flow, Turbulence and Combustion*, v86, n4, pp. 359-377.
6. Agrawal, A. and Prasad, A.K. (2002b), *Properties of vortices in the self-similar turbulent jet*, *Exp. Fluids*, v33, n4, pp. 565-577.
7. Agrawal, A. and Prasad, A.K. (2003), *Measurements within vortex cores in a turbulent jet*, *J. Fluids Engrg.*, *Transactions of the ASME*, v125, n3, pp. 561-568.
8. Anthony, D.G. and Willmarth, W.W. (1992), *Turbulence measurements in a round jet beneath a free surface*, *J. Fluid Mech.*, v243, pp. 699-720.
9. Aubry, N., Holmes, P., Lumley, J.L., and Stone, E. (1988), *The dynamics of coherent structures in the wall region of a turbulent boundary layer*, *J. Fluid Mech.*, v192, pp. 115-173.
10. Balasubramanian, V. and Jain, S.C. (1978), *Horizontal buoyant jets in quiescent shallow water*, *J. Environmental Engrg. Division*, v104, n. EE4, pp. 717-729.

11. Barker, J.M. (1998), *Flow structure dynamics of an impinging elliptic jet*, Ph.D. thesis, Clemson University, USA.
12. Beavers, G.S. and Wilson, T.A. (1970), *Vortex growth in jets*, J. Fluid Mech., v44, part 1, pp. 97-112.
13. Becker, H.A. and Massaro, T.A. (1968), *Vortex evolution in a round jet*, J. Fluid Mech., v31, part 3, pp. 435-448.
14. Berkooz, G., Holmes, P., and Lumley, J.L. (1993), *The proper orthogonal decomposition in the analysis of turbulent flows*, Annu. Rev. Fluid Mech., v25, pp. 539-575.
15. Bi, W., Sugii, Y., Okamoto, K., and Madarame, H. (2003), *Time-resolved proper orthogonal decomposition of the near-field flow of a round jet measured by dynamic particle image velocimetry*, Meas. Sci. Technol., v14, pp. L1-L5.
16. Boillot, A. and Prasad, A.K. (1996), *Optimization procedure for pulse separation in cross-correlation PIV*, Exp. Fluids, v22, n2, pp. 87-93.
17. Bonnet, J.P., Delville, J., Glauser, M.N., Antonia, R.A., Bisset, D.K., Cole, D.R., Fiedler, H.E., Garem, J.H., Hilberg, D., Jeong, J., Kevlahan, N.K.R., Ukeiley, L.S., and Vincendeau, E. (1998), *Collaborative testing of eddy structure identification methods in free turbulent shear flows*, Exp. Fluids, v25, pp. 197-225.
18. Bradshaw, P. (1987), *Turbulent secondary flows*, Annu. Rev. Fluid Mech., v19, pp. 53- 74.
19. Bronson, R. (1991), *Matrix methods: an introduction*, 2nd ed., Academic Press Inc., Ca.
20. Brown, G.L. and Roshko, A. (1974), *On density effects and large structure in turbulent mixing layers*, J. Fluid Mech., v64, part 4, pp. 775-816.
21. Browne, L.W., Antonia, R.A., and Chambers, A.J. (1984), *The interaction regions of a turbulent jet*, J. Fluid Mech., v149, pp.355-373.
22. Bugg, J.D. and Rezkallah, K.S. (1998), *An analysis of noise in PIV images*, J. Visualization, v1, n2, pp. 217-226.
23. Camussi, R. (2002), *Coherent structure identification from wavelet analysis of particle image velocimetry data*, Exp. Fluids, v32, n1, pp. 76-86.

24. Cantwell, B.J. (1981), *Organized motion in turbulent flow*, Annu. Rev. Fluid Mech., v13, pp. 457-515.
25. Cazemier, W., Verstappen, R.W.C.P., and Veldman, A.E.P. (1998), *Proper orthogonal decomposition and low-dimensional models for driven cavity flows*, Phy. Fluids, v10, n7, pp.1685.
26. Chen, D. and Jirka, G.H. (1993), *Mixing character and meandering mechanism of a plane jet bounded in shallow water layer*, Hydraulic Engrg. v93, pp. 2147-2152.
27. Citriniti, J.H. and George, W.K. (1999), *Organized structure dynamics in turbulent round jet*, IUTAM symposium on simulation and identification of organized structures in flows, Lyngby, Denmark, 25-29 May 1997, pp. 365-373.
28. Cizmas, P.G., Palacios, A., Brien, T.O., and Syamlal, M. (2003), *Proper orthogonal decomposition of spatio-temporal patterns in fluidized beds*, Chemical Engineering Science, v58, pp. 4417-4427.
29. Clift, R., Grace, J.R., and Weber, M.E. (1978), *Bubbles, Drops, and Particles*, Academic Press Inc., London
30. Crow, S.C., and Champagne, F.H. (1971), *Orderly structure in jet turbulence*, J. Fluid Mech., v48, n5, pp. 547-592.
31. Dahm, W.J.A. and Dimotakis, P.E. (1985), *Measurements of entrainment and mixing in turbulent jets*, AIAA Paper, AIAA-85-0056, pp. 1216-1223.
32. Dahm, W. J. A. and Dimotakis, P. E. (1990), *Mixing at large Schmidt number in the self-similar far field of turbulent jets*, J. Fluid Mech., v217, pp. 299-330.
33. Davies, P.O.A.L., Fisher, M.J., and Barratt, M.J. (1963), *The characteristics of the turbulence in the mixing region of a round jet*, J. Fluid Mech., v15, pp. 337-367.
34. Davis, M.R. and Davies, P.O.A.L. (1979), *Shear fluctuations in a turbulent jet shear layer*, J. Fluid Mech., v93, pp. 281-303
35. Davis, M.R. and Winarto, H. (1980), *Jet diffusion from a circular nozzle above a solid plane*, J. Fluid Mech., v101, part 1, pp. 201-221.
36. Dimotakis, P.E., Miake-Lye, R.C., and Papanтониου, D.A. (1983), *Structure and dynamics of round turbulent jets*, Phy. Fluids, v26, n11, pp. 3185-3192.
37. Dracos, T., Giger, M., and Jirka, G.H. (1992), *Plane turbulent jets in a bounded fluid layer*, J. Fluid Mech., v241, pp. 587-614.

38. Ferdman, E., Otugen, M.V., and Kim, S. (2000), *Effect of initial velocity profile on the development of round jets*, J. Propulsion and Power, v16, n4, pp. 676-686.
39. Fiedler, H.E. (1988), *Coherent structures in turbulent flows*, Prog. Aerospace Sci., v25, pp. 231-269.
40. Foss, J.F. and Jones, J.B. (1968), *Secondary flow in a bounded rectangular jet*, Trans. of the ASME, J. Basic Engrg., pp. 241-248.
41. Gad-el-Hak, M. (2000), *Flow control: passive, active, and reactive flow management*, Cambridge University Press, UK.
42. Ganapathhisubramani, B., Longmire, E.K., and Marusic, I. (2002), *Investigation of three dimensionality in the near field of a round jet using stereo PIV*, J. Turbulence, v3, pp. 1-10.
43. George, W.K. (1989), *The self-preservation of turbulent flows and its relation to initial conditions and coherent structures*, Advances in Turbulence, Hemisphere Pub. Corp., New York, pp. 39-73.
44. Govindarajan, R. (2002), *Universal behavior of entrainment due to coherent structures in turbulent shear flow*, Phy. Rev. Letters, The American Physical Society, v88, n13, pp.1-4.
45. Golub, G.H. and Van Loan, C.F. (1983), *Matrix computations*, Johns Hopkins Univ. Press, Baltimore.
46. Graftieaux, L., Michard, M., and Grosjean, N. (2001), *Combining PIV, POD and vortex identification algorithms for the study of unsteady turbulent swirling flows*, Meas. Sci., v12, pp. 1422-1429.
47. Green, S.I. (1995), *Fluid vortices*, Kluwer Academic Publishers, The Netherlands.
48. Guezennec, Y.G. and Kiritsis, N. (1990), *Statistical investigation of errors in particule image velocimetry*, Exp. Fluids, v10, pp.138-146.
49. Hart, D. (2000), *PIV error correction*, Exp. Fluids, v29, pp. 13-22.
50. Hill B.J. (1972), *Measurement of local entrainment rate in the initial region of axisymmetric turbulent air jets*, J. Fluid Mech., v51, pp. 773-779.
51. Hinze, J.O. (1975), *Turbulence*, 2nd edn, McGraw Hill, New York

52. Holdeman, J.D. and Foss, J.F. (1975), *The initiation, development, and decay of the secondary flow in a bounded jet*, Trans. of the ASME, J. Basic Engrg., pp. 343-352.
53. Holmes, P., Lumley, J.L., and Berkooz, G. (1996), *Turbulence, coherent structures, dynamical systems and symmetry*, Cambridge University Press, NY, USA.
54. Huang, H., Dabiri, D., and Gharib, M. (1997), *On errors of digital particle image velocimetry*, Meas. Sci. Tech., v8, pp.1427-1440.
55. Hussain, A.K.M.F. (1983), *Coherent structures – reality and myth*, Phys. Fluids, v26, n10, pp. 2816-2850.
56. Hussain, A.K.M.F. (1984), *Coherent structures and incoherent turbulence*, Turbulence and Chaotic Phenomena in Fluids, pp. 453-460.
57. Hussain, A.K.M.F. (1986), *Coherent structures and turbulence*, J. Fluid Mech., v173, pp. 303-356.
58. Hussain, A.K.M.F. and Clark, A.R. (1981), *On the coherent structure of the axisymmetric mixing layer: a flow-visualization study*, J. Fluid Mech., v104, pp. 263-294.
59. Hussain, A.K.M.F., Zedan, M.F. (1978a), *Effects of the initial condition on the axisymmetric free shear layer: Effect of the initial fluctuation level*, Phys. Fluids, v21, n9, pp.1475-1481.
60. Hussain, A.K.M.F., Zedan, M.F. (1978b), *Effects of the initial condition on the axisymmetric free shear layer: Effects of the initial momentum thickness*, Phys. Fluids, v21, n7, pp.1100-1112
61. Hussein, H.J., Capp, S.P., and George, W.K. (1994), *Velocity measurements in a high-Reynolds-number, momentum-conserving, axisymmetric, turbulent jet*, J. Fluid Mech., v258, pp. 31-75.
62. Jeong, J. and Hussain, F. (1995), *On the identification of a vortex*, J. Fluid Mech., v285, pp. 69-94.
63. Johnston, A.J., Nguyen, N. and Volker, R.E. (1993), *Round buoyant jet entering shallow water in motion*, J. Hydr. Engrg., v119, n12, pp. 1364-1381.

64. Johnston, A.J., Phillip, C. R. and Volker, R.E. (1994), *Modeling horizontal round buoyant jet in shallow water*, J. Hydr. Engrg., v120, n1, pp. 41-59.
65. Johnston, A.J. and Volker, R.E. (1993), *Round buoyant jet entering shallow water*, J. Hydr. Res., v31, n1, pp. 121-138.
66. Johnston, A.J. and Volker, R.E. (1994), *Round buoyant jet in shallow water: bed shear velocity*, J. Hydr. Res., v32, n2, pp. 233-250.
67. Keane, R. and Adrian, R.J. (1990), *Optimization of particle image velocimeters. Part I: Double pulsed systems*, Meas. Sci. Tech., v1, pp. 1202-1205.
68. Keane, R. and Adrian, R.J. (1991), *Optimization of particle image velocimeters. Part II: Multiple pulsed systems*, Meas. Sci. Tech., v2, pp. 963-974.
69. Kim, J. (1983), *On the structure of wall-bounded turbulent flows*, Phys. Fluids, v26, pp. 2088-2097.
70. Kim, J., Moin, P., and Moser, R. (1987), *Turbulence statistics in fully developed channel flow at low Reynolds number*, J. Fluid Mech., v177, pp. 133-166.
71. Knystautas, R. (1964), *The turbulent jet from a series of holes in line*, Aeronautical Quarterly, v15, pp. 1-28 .
72. Kostas, J., Soria, J., and Chong, M.S. (2001), *PIV measurements of backward step flow*, 4th international symposium on particle image velocimetry, Germany, Sep. 17-19.
73. Kuang, J., Hsu, C., and Qiu, H. (2001), *Experiments on vertical turbulent plane jets in water of finite depth*, J. Engg. Mech., v127, n1, pp. 18-26.
74. Lau, J.C. and Fisher, M.J. (1975), *The vortex sheet structure of turbulent jets*, J. Fluid Mech., v67, n1, pp. 299-337.
75. Launder, B.E. and Rodi, W. (1981), *Turbulent wall jet*, Prog. Aerospace Sci, v19, n2-4, pp. 81-128.
76. Launder, B.E. and Rodi, W. (1983), *The turbulent wall jet – measurements and modeling*, Annu. Rev. Fluid Mech., v15, pp. 429-459.
77. Law, A.W.-K. and Herlina (2002), *An experimental study on turbulent circular wall jets*, J. Hydr. Engrg., v128, n2, pp. 161-174.
78. Liang, D., Jiang, C., and Li, Y. (2003), *Cellular neural network to detect spurious vectors in PIV data*, Exp Fluids, v34, pp. 52-62.

79. Liepmann, D. and Gharib, M. (1992), *The role of streamwise vorticity in the near-field entrainment of round jets*, J. Fluid Mech., v245, pp. 643-668.
80. Liepmann, D. and Gharib, M. (1994), *The vorticity and entrainment dynamics of near-field jets*, ASME Free-surface Turbulence, FED-v181, pp. 53-58.
81. List, E. J. (1982), *Turbulent jets and plumes*, Ann. Rev. Fluid Mech., v14, pp. 189-212.
82. Longmire, E.K. and Eaton, J.K. (1992), *Structure of a particle-laden round jet*, J. Fluid Mech., v236, pp.217-257.
83. Lourenco, L. and Krothapalli, A. (1995), *On the accuracy of velocity and vorticity measurements with PIV*, Exp. Fluids, v18, pp. 421-428.
84. Nauka, Moscow, pp. 166-178.
85. Madnia, C.K. and Bernal, L.P. (1994), *Interaction of a turbulent round jet with the free surface*, J. Fluid Mech., v261, pp. 305-332.
86. Malmstrom, T.G., Kirkpatrick, A.T., Christensen, B., and Knappmiller, K.D. (1997), *Centreline velocity decay measurements in low-velocity axisymmetric jets*, J. Fluid Mech., v246, pp. 363-377.
87. Maxwell, W.H.C. and Pazwash, H. (1975), *Axisymmetric shallow submerged jets*, J. Hydr. Engrg., ASCE, v99, n4, pp. 637-652.
88. Maxworthy, T. (1972), *The structure and stability of vortex rings*, J. Fluid Mech., v51, part 1, pp. 15-32.
89. Maxworthy, T. (1974), *Turbulent vortex rings*, J. Fluid Mech., v64, part 2, pp. 227-239.
90. McCabe, A. (1967), *An experimental investigation of a plane subsonic jet with an aspect ratio of three*, Proc. Instn. Mech. Engrs, v182, part 3H, pp. 342-346.
91. Michalke, A. and Freymuth, P. (1966), *The instability and the formation of vortices in a free boundary layer*, AGARD, Conf. Proc. n4, paper 2.
92. Milojevic, D. (1990), *Lagrangian stochastic-deterministic (LSD) predictions of particle dispersion in turbulence*, Part. Part. Syst. Charact., v7, pp. 181-190.
93. Moore, C.J. (1977), *The role of shear layer instability waves in jet exhaust noise*, J. Fluid Mech., v80, part 2, pp. 321-367.

94. Mungal, M.G. and Hollingsworth, D.K. (1989), *Organized motion in a very high Reynolds number jet*, Phys. Fluids, vA1, n10, pp. 1615-1623.
95. Newman, B.G., Patel, R.P., Savage, S.B., and Tjio, H.K. (1972), *Three-dimensional wall jet originating from a circular orifice*, Aeronautical Quarterly, v23, pp. 188-200.
96. Panchapakesan, N.R., and Lumely, J.L. (1993), *Turbulence measurements in axisymmetric jets of air and helium, Part 1. Air jet*, J. Fluid Mech., v246, pp. 197-223.
97. Pemberton, R.J., Turnock, S.R., Dodd, T.J. and Rogers, E. (2002), *A novel method for identifying vortical structures*, J. Fluids and Structures, v16, n8, pp. 1051-1057.
98. Petersen, R.A. (1978), *Influence of wave dispersion on vortex pairing in a jet*, J. Fluid Mech., v89, n3, pp. 469-495.
99. Prasad, A.K., Adrian, R.J., Landreth, C.C., and Offutt, P.W. (1992), *Effect of resolution on the speed and accuracy of particle image velocimetry interrogation*, Exp. Fluids, v13, pp. 105-116.
100. Press, W.H., Teukolok, S.A., Vetterling, W.T., and Flannery, B.P. (c1998), *Numerical recipes in C, 2nd ed.*, Cambridge Univ. Press, Cambridge, NY.
101. Raffel, M., Willert, C., and Kompenhans, J. (1998), *Particle image velocimetry: a practical guide*, Springer-Verlag, Berlin Heidelberg, Germany.
102. Rajaratnam, N. (1976), *Turbulent Jets*, Elsevier Scientific Publishing Company, Amsterdam.
103. Rajaratnam, N. and Humphries, J.A. (1984), *Turbulent non-buoyant surface jets*, J. Hydr. Research., v22, n2, pp. 103-115.
104. Rajaratnam, N. and Pani, B.S. (1974), *Three-dimensional turbulent wall jets*, J. Hydr. Div., v100, n HY1, pp. 69-83.
105. Ricou, F.P. and Spalding, D.B. (1961), *Measurements of entrainment by axisymmetrical turbulent jets*, J. Fluid Mech., v11, pp. 21-32.
106. Robinson, S.K. (1991), *Coherent motions in the turbulent boundary layer*, Ann. Rev. Fluid Mech., v23, pp. 601-639.
107. Rodi, W. (1982), *Turbulent buoyant jets and plumes*, Pergamon Press Ltd., Headington Hill Hall, Oxford, England.

108. Romano, G.P. (2002), *The effect of boundary conditions by the side of the nozzle of a low Reynolds number jet*, Exp. Fluids, v33, n2, pp. 323-333.
109. Roshko, A. (1976), *Structure of turbulent shear flows: A new look*, AIAA J., v14, n10, pp. 1349-1357.
110. Schlichting, H. (1979), *Boundary layer theory*, 7th ed., McGraw-Hill Inc., NY.
111. Sforza, P.M. and Herbst, G. (1970), *A study of three-dimensional, incompressible, turbulent wall jets*, AIAA J., v8, n2, pp. 276-282.
112. Shinneeb, A.-M., Bugg, J.D., Balachandar, R. (2002), *PIV measurements in a confined jet*, In ASME Fluids Engineering Division Summer Meeting, Montreal, July 14-18.
113. Shinneeb, A.-M., Bugg, J.D., and Balachandar, R. (2004a), *Variable threshold outlier identification in PIV data*, Meas Sci Technol, v15, pp. 1722-1732.
114. Shinneeb, A.-M., Balachandar, R., and Bugg, J.D., (2004b), *PIV measurements in shallow water jets*, In Canadian Society of Civil Engineering, 1st Water and Environment Speciality Conference, June 2-5, Saskatoon, Saskatchewan, Canada.
115. Shinneeb, A.-M., Bugg, J.D. and Balachandar, R. (2006), *Investigation of vortical structures in the near-exit region of a round turbulent jet using PIV and POD*, submitted to Exp. Fluids.
116. Sirovich, L. (1987), *Turbulence and the dynamics of coherent structures. Part I: Coherent structures*, Quarterly of Applied Math., v45, n3, pp. 561-571.
117. Sobey, R.J., Johnston, J. and Keane, R.D. (1988), *Horizontal round buoyant jet in shallow water*, J. Hydr. Engrg., v114, n8, pp. 910-929.
118. Swearn Jr., T.F., Ramberg, S.E., Plesniak, M.W., and Stewart, M.B. (1989), *Turbulent surface jet in channel of limited depth*, J. Hydr. Engrg., v115, n12, pp. 1587-1606.
119. Townsend, A.A. (1956), *The structure of turbulent shear flow*, Cambridge Univ. Press, Cambridge, NY.
120. Tso, J. (1984), *Coherent structures in a fully developed turbulent axisymmetric jet*, Ph.D. thesis, The Johns Hopkins Univ.
121. Tso, J. and Hussain, F. (1989), *Organized motions in fully developed turbulent axisymmetric jet*, J. Fluid Mech., v203, pp. 425-448.

122. Tso, J., Kovasznay, L.S.G., and Hussain, A.K.M.F. (1981), *Search for large-scale coherent structures in the nearly self-preserving region of a turbulent axisymmetric jet*, J. Fluids Engrg., Transactions of the ASME, v103, pp. 503-508.
123. Uijttewaal, W.S.J. and Booiij, R. (1999), *Influence of shallowness on growth and structures of a mixing layer*, Engng. Turbulence Modelling and Expts. - 4, Elsevier Sci. Ltd., The Netherlands.
124. Van Dyke, M. (1982), *An album of fluid motion*, The Parabolic Press, Stanford, California, USA.
125. Viets, H. and Sforza, P.M. (1972), *Dynamics of bilaterally symmetric vortex rings*, Phys. Fluids, v15, n2, pp. 230-240.
126. Walker, D.T., Chen, C.-Y., and Willmarth, W.W. (1995), *Turbulent structure in free-surface jet flows*, J. Fluid Mech., v291, pp. 223-261.
127. Westerweel, J., Dabiri, D., and Gharib, M. (1997), *The effect of a discrete window offset on the accuracy of cross-correlation analysis of digital PIV recordings*, Exp. Fluids, v23, pp. 20-28.
128. Widnall, S.E. (1975), *The structure and dynamics of vortex filaments*, Annu. Rev. Fluid Mech., v7, pp. 141-165.
129. Widnall, S.E. and Sullivan, J.P. (1973), *On the stability of vortex rings*, Proc. R. Soc. Lond., vA332, pp. 335-353.
130. Widnall, S.E., Bliss, D.B., and Tsai, C.-Y. (1974), *Instability of short waves on a vortex ring*, J. Fluid Mech., v66, n Part 1, pp. 35-47.
131. Willert, C.E. and Gharib, M. (1991), *Digital particle image velocimetry*, Exp. Fluids, v10, pp. 181-193.
132. Winant, C.D. and Browand, F.K. (1974), *Vortex pairing: the mechanism of turbulent mixing-layer growth at moderate Reynolds number*, J. Fluid Mech., v63, part 2, pp. 237-255.
133. Wygnanski, I., and Fiedler, H. (1969), *Some measurements in the self-preserving jet*, J. Fluid Mech., v38, part 3, pp.577-612.
134. Xu, G. and Antonia, R.A. (2002), *Effect of different initial conditions on a turbulent round free jet*, Exp. Fluids, v33, n5, pp. 677-683.

135. Yoda, M., Hesselink, L., and Mungal, M.G. (1992), *The evolution and nature of large-scale structures in the turbulent jet*, Phys. Fluids, v4, n4, pp. 803-811.
136. Yoda, M., Hesselink, L., and Mungal, M.G. (1994), *Instantaneous three-dimensional concentration measurements in the self-similar region of a round high-Schmidt-number jet*, J. Fluid Mech., v279, pp. 313-350.
137. Young, W.C. (1989), *Roark's formulas for stress and strain*, 6th ed., McGraw-Hill Inc., USA.
138. Yule, A. J. (1978), *Large-scale structure in the mixing layer of a round jet*, J. Fluid Mech., v89, part 3, pp. 413-432.
139. Zhou, X. and Hitt, D.L. (2004), *Proper orthogonal decomposition analysis of coherent structures in a transient buoyant jet*, J. Turbulence, v5, n028, pp. 1-21.

APPENDIX A

AXIAL DEVELOPMENT OF SELECTED VELOCITY PROFILES

The purpose of this appendix is to provide a clearer presentation of some phenomena which are ambiguous because of the superimposing of a number of profiles in one figure. Figure A.1 displays individual profiles of the mean horizontal velocity W for the $H/D = 15$ case at different axial locations (shown in Figure 20(a)). These profiles show that the outward lateral flow region near the jet centreline is shrinking in the downstream direction, indicating that the horizontal mid-plane of the jet undergoes a constriction.

Figure A.2 displays individual profiles of the mean horizontal velocity W for the $H/D = 5$ case at different axial locations (shown in Figure 20(c)). These profiles show that, although the outward flow is relatively weak and constrained to a small region near the jet axis, it narrows in the downstream direction until the mean flow is toward the jet centreline at $x/D \approx 40$. Further downstream, it expands again in the axial direction as can be seen at $x/D = 50$ and 60 . This behaviour is accompanied by first increasing the inward velocity at the sides of the jet until it reaches a maximum value at $x/D = 40$, then decreasing of the inward velocity ($|\eta| < 0.03$) as shown by the velocity profiles at $x/D = 50$ and 60 .

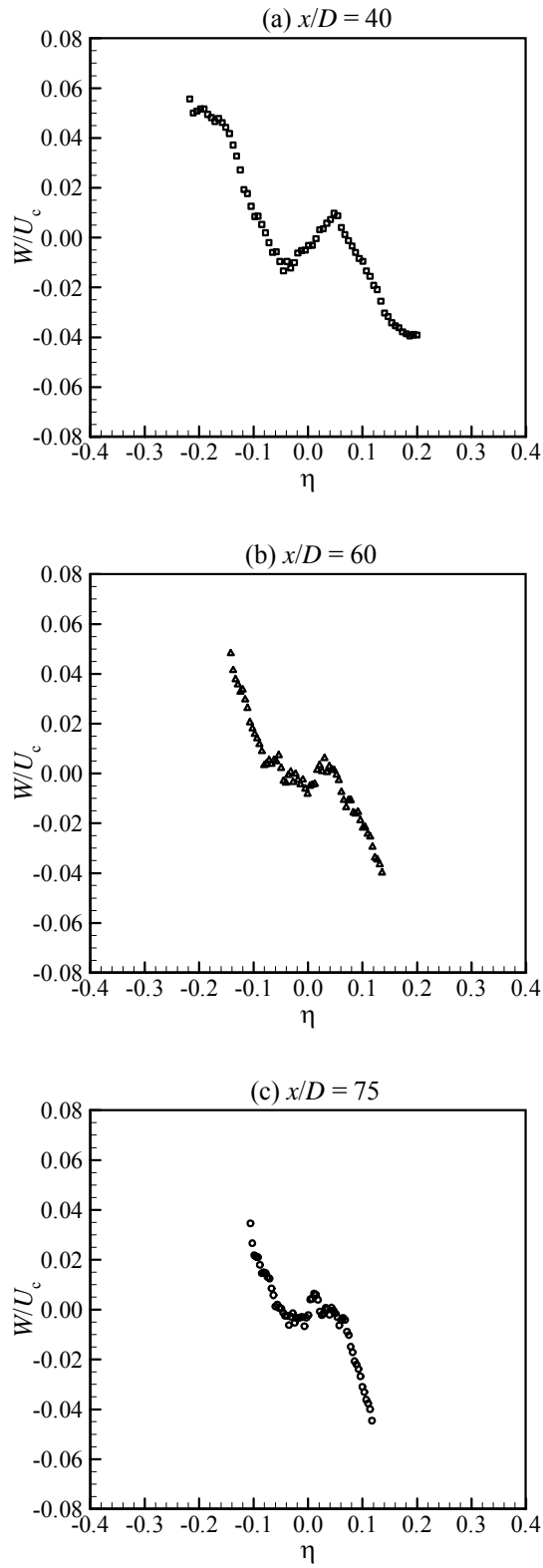


Figure A.1: Downstream development of the normalised mean horizontal velocity W/U_c profiles on the horizontal plane for the $H/D = 15$ case; (a) $x/D = 40$, (b) $x/D = 60$, and (c) $x/D = 75$.

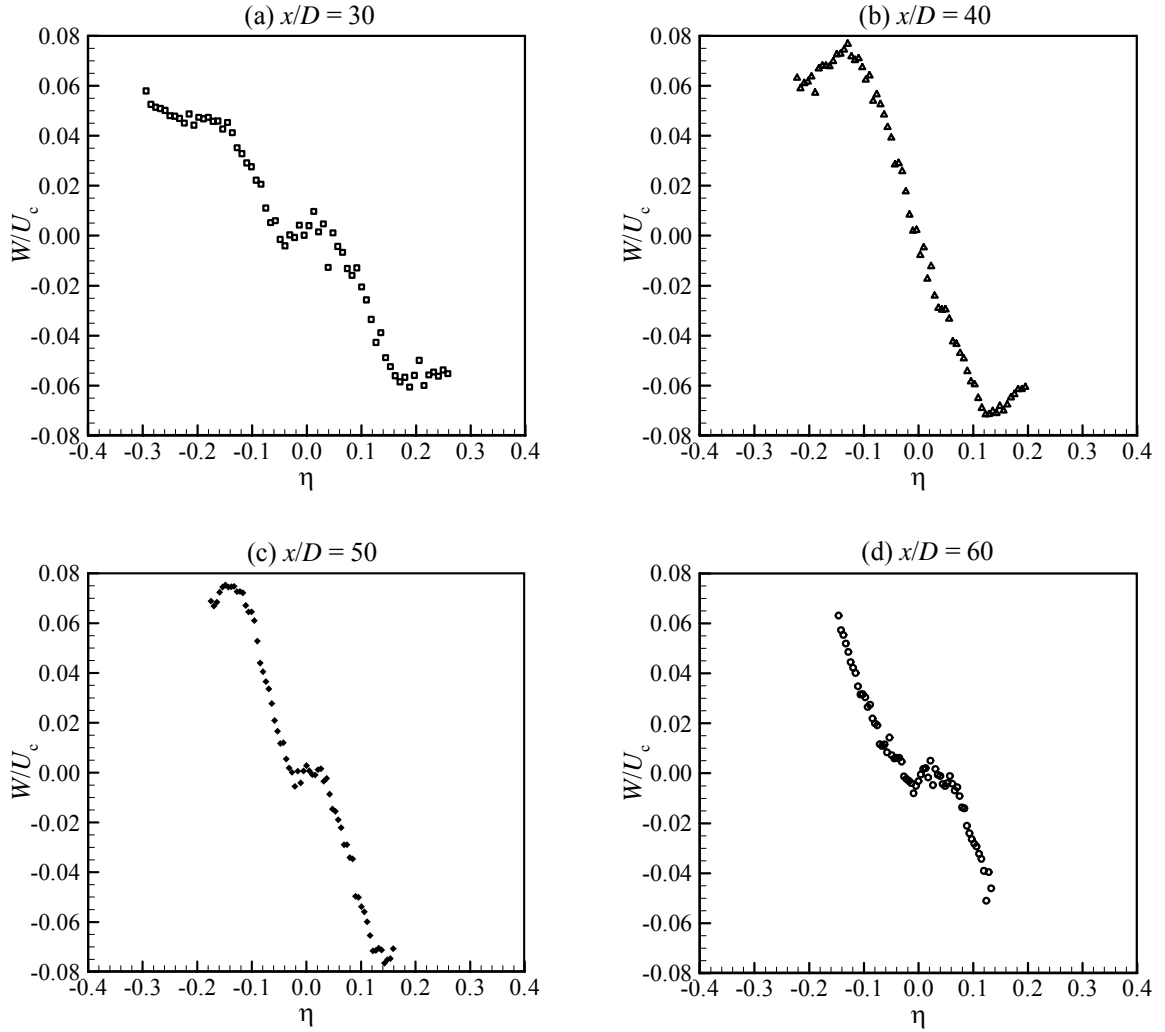

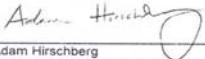


Figure A.2: Downstream development of the normalised mean horizontal velocity W/U_c profiles on the horizontal plane for the $H/D = 5$ case; (a) $x/D = 30$, (b) $x/D = 40$, (c) $x/D = 50$, and (d) $x/D = 60$.

APPENDIX B

COPYRIGHT PERMISSIONS

A.1 Permission of Figures 2.2 and 2.3

		 CAMBRIDGE UNIVERSITY PRESS
PUBLICATION PERMISSION		
March 29, 2006		
AbdulMonsif Shinneeb 57 Campus Drive Department of Mechanical Engineering University of Saskatchewan Saskatoon S7N 5A9 Canada		40 West 20th Street New York, NY 10011-4211 USA Telephone 212 924 3900 Fax 212 691 3239
<hr/>		
References		
Journal:	Journal of Fluid Mechanics, Vol. 173 1986	
Author:	A.K.M. Fazle Hussain	
Title:	Coherent structures and turbulence	
Selection/pp:	Figure 12(b) and (c)	
Additional:		
Use		
Reprint Title:	Confinement effects in shallow water jets	
Publisher:	University of Saskatchewan	
Format:	dissertation / thesis	
Quantity:		
Avail. Date	2006	
Rights/Acknowledgement		
Permission is granted for nonexclusive rights throughout the world in the English language for interior text editorial use in the format described above, including non-profit editions for the visually and physically impaired. Please fully acknowledge our material and include the phrase "Reprinted with the permission of Cambridge University Press."		
Restrictions		
This permission does not allow the reprinting of any material copyrighted by or credited in our publication to another source; Cambridge disclaims all liability in connection with the use of such material without proper consent.		
<input type="checkbox"/> This permission is restricted to the indicated format only; for additional uses you must re-apply for permission.		
<input type="checkbox"/> This permission requires that you obtain the written consent of one author of our material, without which this grant is not valid.		
<hr/>		
Authorization:	 Adam Hirschberg Rights and Permissions Coordinator	

Date: Wed, 26 Apr 2006 10:22:27 -0400
 From: "Adam Hirschberg" <ahirschberg@cambridge.org> **Block Address**
 Subject: **Your permission request**
 To: abs189@mail.usask.ca

Reply Reply All Forward Print Delete

April 26, 2006

RE: Journal of Fluid Mechanics, 1986
 Figure 12, page 334

Dear Mr. Shinneeb,

You have our permission to use this figure in your thesis. Please cite Cambridge in your work. Please know that it is not necessary to submit a request for a single figure. Thanks.

Sincerely,

Adam

Adam Hirschberg
 Rights and Permissions Coordinator
 Cambridge University Press
 40 W. 20th St.
 New York, NY 10011-4211

tel.: 212-337-5088 (direct)
 tel.: 212-924-3900 (general)
 fax: 212-691-3239 (general)
 email: ahirschberg@cambridge.org
 web: www.cambridge.org/us

A.2 Permission of Figure 2.4

Date: Thu, 01 Jun 2006 10:57:22 +0100
 From: "Jones, Jennifer (ELS-OXF)" <J.Jones@elsevier.co.uk> **Block Address**
 Subject: **RE: Obtain Permission**
 To: "abs189@mail.usask.ca" <abs189@mail.usask.ca>

Reply Reply All Forward Print Delete

Dear AbdulMonsif Shinneeb

We hereby grant you permission to reproduce the material detailed below at no charge **in your thesis, in print and on the University of Saskatchewan web site** subject to the following conditions:

1. If any part of the material to be used (for example, figures) has appeared in our publication with credit or acknowledgement to another source, permission must also be sought from that source. If such permission is not obtained then that material may not be included in your publication/copies.
2. Suitable acknowledgment to the source must be made, either as a footnote or in a reference list at the end of your publication, as follows:
 "Reprinted from Publication title, Vol number, Author(s), Title of article, Pages No., Copyright (Year), with permission from Elsevier".
3. Reproduction of this material is confined to the purpose for which permission is hereby given.
4. This permission is granted for non-exclusive world **English** rights only. For other languages please reapply separately for each one required. Permission excludes use in an electronic form other than as specified above.
5. This includes permission for the Library and Archives of Canada to supply single copies, on demand, of the complete thesis. Should your thesis be published commercially, please reapply for permission.

Yours sincerely

Jennifer Jones
 Rights Assistant

Your future requests will be handled more quickly if you complete the online form at www.elsevier.com/permissions <http://www.elsevier.com/permissions>

-----Original Message-----
 From: abs189@mail.usask.ca [mailto:abs189@mail.usask.ca]
 Sent: 31 May 2006 19:43
 To: permissions@elsevier.com
 Subject: Obtain Permission

This Email was sent from the Elsevier Corporate Web Site and is related to Obtain Permission form:

Product: Customer Support
Component: Obtain Permission
Web server: <http://www.elsevier.com>
IP address: 10.10.24.149
Client: Mozilla/4.0 (compatible; MSIE 6.0; Windows NT 5.1; SV1; .NET CLR 1.1.4322; .NET CLR 2.0.50727)
Invoked from: http://www.elsevier.com/wps/find/obtainpermissionform.cws_home?isSubmitted=yes&navigateXmlFileName=/store/prod_webcache_act/framework_support/obtainpermission.xml

Request From:
Mr. AbdulMonsif Shinneeb
University of Saskatchewan
57 Campus Drive
S7N 5A9
Saskatoon, Saskatchewan
Canada

Contact Details:
Telephone: (306) 966 - 5455
Fax: (306) 966-5427
Email Address: abs189@mail.usask.ca

To use the following material:
ISSN/ISBN:
Title: Progress in Aerospace Science
Author(s): H. E. Fiedler
Volume: 25
Issue: N/A
Year: 1988
Pages: 231 - 269
Article title: Coherent structures in turbulent flows

How much of the requested material is to be used:
I would like to request a permission to use Figure 17, page 250 in my Ph.D. thesis. The figure shows the dominant modes in axisymmetric jet flow.

Are you the author: No
Author at institute: No

How/where will the requested material be used: [how_used]

Details:

The aforementioned figure will be used in my thesis. My thesis will be electronically submitted to the library at the University of Saskatchewan and a hard copy of the same work will be printed out as well.






Additional Info: I would be grateful if you could give me a written permission to use the aforementioned figure in my thesis.

- end -

For further info regarding this automatic email, please contact:
WEB APPLICATIONS TEAM (esweb.admin@elsevier.co.uk)

A.3 Permission of Figure 2.5

Date: Thu, 13 Apr 2006 19:12:11 -0400
From: cmvandyke@cox.net **Block Address**
Subject: **Re: Copyright permission-Parabolic press**
To: "Abdul-Monsif Shinneeb" <abs189@mail.usask.ca>

 Reply  Reply All  Forward  Print  Delete

Mr. Shinneeb-

While we often suggest that the person wishing to use the image contact the original source as cited in the Album, in your case you have permission to reproduce the figure for your PhD thesis. For many images my father received permission to use the image(s) but does not have the ability to confer rights to their further use.

-Christopher Van Dyke

>
> From: Abdul-Monsif Shinneeb <abs189@mail.usask.ca>
> Date: 2006/04/10 Mon PM 01:08:26 EDT
> To: cmvandyke@cox.net
> Subject: Copyright permission-Parabolic press
>
> Dear Sir/Madam
>
> My name is AbdulMonsif Shinneeb. I am a graduate student in the
> Mechanical Engineering Department at the University of Saskatchewan,
> Canada. I would like to request a permission to use Figure 102, page
> 60
> (from "An album of fluid motion" by Milton Van Dyke, 1982) in my Ph.D.
> thesis. The figure shows the "Instability of an axisymmetric jet".
>
> I would be grateful if you could give me a written permission to use
> the aforementioned figure in my thesis. My thesis will be
> electronically submitted to the library at the University of
> Saskatchewan and a hard copy of the same work will be printed out as
> well.
>
> Thank you for your cooperation. I look forward to hearing from you.
>
> Sincerely,
> A. Shinneeb
> Ph.D. candidate
> Mechanical Engineering Department
>
>

A.4 Permission of Figures 2.6 and 2.7

Date: Thu, 30 Mar 2006 10:21:54 -0500
From: "Adam Hirschberg" <ahirschberg@cambridge.org> **Block Address**
Subject: **Permission request**
To: abs189@mail.usask.ca

Reply Reply All Forward Print Delete

March 30, 2006

AbdulMonsif Shinneeb
Department of Mechanical Engineering
University of Saskatchewan
Saskatoon
S7N 5A9
Canada

RE: Journal of Fluid Mechanics
Dorian Liepmann and Morteza Gharib
v245, pp. 643-668
Figures 5 and 12

Dear Mr. Shinneeb,

You have our permission to use these figures in your thesis provided you credit us in your work.

Sincerely,

Adam

Adam Hirschberg
Rights and Permissions Coordinator
Cambridge University Press
40 W. 20th St.
New York, NY 10011-4211

tel.: 212-337-5088 (direct)
tel.: 212-924-3900 (general)
fax: 212-691-3239 (general)
email: ahirschberg@cambridge.org
web: www.cambridge.org/us
